University of California

Ernest O. Lawrence
Radiation Laboratory

$\pi^+ p$ 4-PRONG INTERACTIONS BETWEEN 3 AND 4 GeV/c

David Gordon Brown

(Ph. D. Thesis)

May 1968

DISCLAIMER

UCRL-18254

UNIVERSITY OF CALIFORNIA

Lawrence Radiation Laboratory
Berkeley, California

AEC Contract No. W-7405-eng-48

$\pi^+ p$ 4-PRONG INTERACTIONS BETWEEN 3 AND 4 GeV/c

David Gordon Brown

(Ph. D. Thesis)

May 1968

$\pi^+ p$ 4-PRONG INTERACTIONS BETWEEN 3 AND 4 GeV/c

Contents

$\pi^+ p$ 4-PRONG INTERACTIONS BETWEEN 3 AND 4 GeV/c

David Gordon Brown

Lawrence Radiation Laboratory
University of California
Berkeley, California

May 1968

ABSTRACT

The Lawrence Radiation Laboratory 72-inch hydrogen bubble chamber was exposed to a beam of π^+ mesons at incident momenta ranging from 2.95 to 4.08 GeV/c. The resulting film yielded 39 000 4-prong interactions which were processed using the FSD device and the Fog-Cloudy-Fair data reduction system.

Formation of $N^*(2850)$ and production of the dominant quasi-two-body final states were investigated. In particular the double resonance channels $N^{*++}\rho^\circ$, $N^{*++}f^\circ$, $N^{*++}\omega^\circ$, and $N^{*++}\eta^\circ$ were sufficiently free from background to allow consideration of their production mechanisms as seen in their cross-sections and angular distributions. One-meson-exchange models were found to account correctly for the general features of the first reaction although being inadequate to explain the fine structure of the experimental distributions.

I. INTRODUCTION

In an effort to further the understanding of the processes involved in multi-pion production in $\pi^+ p$ interactions, 4-prong events of the following three types have been studied at the five incident π^+ momenta 2.95, 3.19, 3.53, 3.74 and 4.08 GeV/c:

$$\pi^+ p \rightarrow \pi^+ p \pi^+ \pi^- \qquad (1)$$

$$\pi^+ p \rightarrow \pi^+ p \pi^+ \pi^- \pi^\circ \qquad (2)$$

$$\pi^+ p \rightarrow \pi^+ \pi^+ \pi^+ \pi^- n \qquad (3)$$

These are the only reactions accounting for any sizeable portion of the total 4-prong cross-section which may be kinematically constrained. The intermediate-energy region was thought to be advantageous because: a) The 4-prong cross-section is large, b) The momentum imparted to the final-state particles is sufficiently low that ionization information is very useful, c) One should be within the range of validity of t-channel exchange models but with s-channel resonance effects still in evidence. The analysis was performed on samples of 7300, 9300, and 2100 events of the respective reactions.

These were obtained in a run at the Bevatron in the spring of 1966. The 72-inch hydrogen bubble chamber was exposed to a separated π^+ beam to obtain .29μb/event of pion path length. The event sample was culled from a sample of 39 000 4-prongs measured by the FSD device and processed by the Fog-Cloudy-Fair system.

The analysis of the events had two distinct goals:

1. The I=3/2 $N^{*++}(2850)$ lies within the energy range of the experiment. An attempt was to be made to determine the cross-sections for the decay of this resonance into the

channels considered here.

2. It was known that reactions (1) and (2) were dominated by double resonance production - e.g. $N^{*++}\rho^{\circ}$ and $N^{*++}\omega^{\circ}$ respectively, and the cross-sections and angular distributions of these processes were to be studied.

In Section (II) the experimental procedure is outlined, i.e. the method by which the event sample and mb/event normalization were made. In the following section the total cross-sections and fundamental experimental distributions for the three reactions are described. In the last section double resonance production is investigated and the success with which these processes are described by one-meson-exchange models is examined.

II. EXPERIMENTAL PROCEDURE

The experiment was performed to obtain two things: an event sample, or "library" of processed events, and the mb/event ratio for events of that sample. In this section the methods used and problems encountered in carrying out this task are described in detail.

A. The Beam

The beam layout is shown in Fig. (1). It delivered a separated beam of π^+ mesons to the 72-inch hydrogen bubble chamber, momentum analyzed to ±1%. The beam line does not merit further attention except to comment that a) the momentum bite was larger than expected because of the relatively poor operating characteristics of the quadrupoles, and b) proton contamination was fairly severe at the higher energies and will be discussed at length in Section (C). Runs were made at 2.95, 3.19, 3.53, 3.74, and 4.08 GeV/c incident π^+ momentum. No un-due difficulty was experienced with any of the apparatus during the running of the experiment.

B. Data Processing

All of the film was scanned for 4-prong interactions between rakes 1 and 13 in the 72-inch bubble chamber.[39] These events were measured on the Flying Spot Digitizer (FSD) automatic measuring machine. If an event failed to pass through the reconstruction programs it was remeasured on either the Franckenstein device or (for one momentum--4.08 GeV/c) again on the FSD.

The fog-Cloudy-Fair system of computer programs was used to reconstruct the events from the measuring machine information, to constrain the events to those reactions of interest, and to output the data in a useful form.[40] Since in reactions (1) and (2) any of three

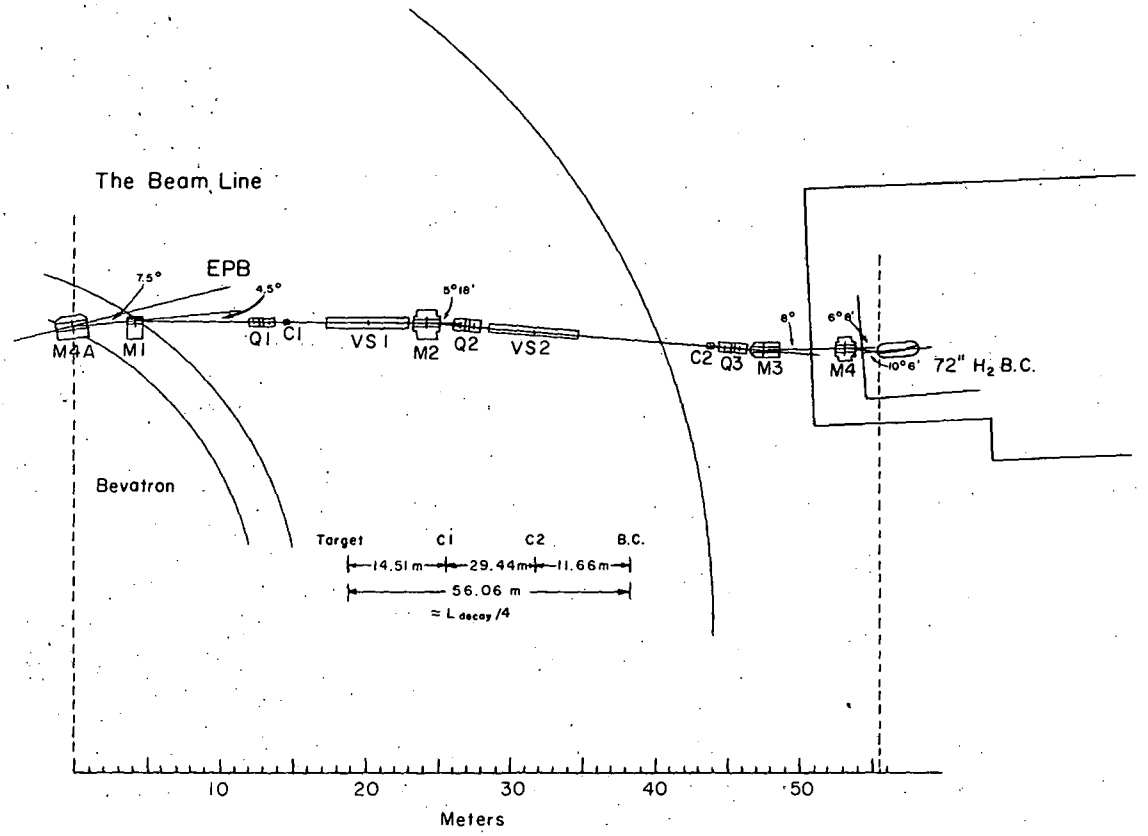

XBL 684-687

Fig. 1. The beam line used in this experiment.

positive outgoing tracks could be the proton, there were a total of seven hypothetical sets of mass assignments to be tried for each event. Also, as detailed in the next section, the events were constrained to the corresponding pp reactions in order to determine the proton contamination.

Events were lost at each stage of processing because of scanning, measurement, and tape-handling errors. These errors consist of such things as measuring the tracks of an event in a different order in two views or of punching in the wrong roll or frame number for an event or even of loosing the tapes from an evening's FSD run. Over 90% (92.3%) of the events survived processing (including events saved by remeasurement). No evidence was found that the missing events were a biased sample except for containing the "non-events" (such as a 2-prong event with crossing beam tracks at the origin making a fake "4-prong" event) for which a correction was made in the efficiency calculations.

C. Beam Contamination

The π^+ beam had fairly severe contamination problems, the principal contaminants being protons and μ mesons. In particular, the proton contamination was a source of concern because of the possibility of constraining pp 4-prong events to the πp interactions considered. The extent of proton contamination will be discussed below, and the μ-meson contamination will be mentioned in Section (D).

Two velocity separators and an accompanying mass-resolution slit were used to extract the π^+ component of the beam for this experiment. Fig. (2) shows separation curves taken at the highest momentum with 1) "B" a narrow solid-state counter placed just above the slit, and 2) "CFČ" and "CF", Čerenkov and paddle counters respectively, in series

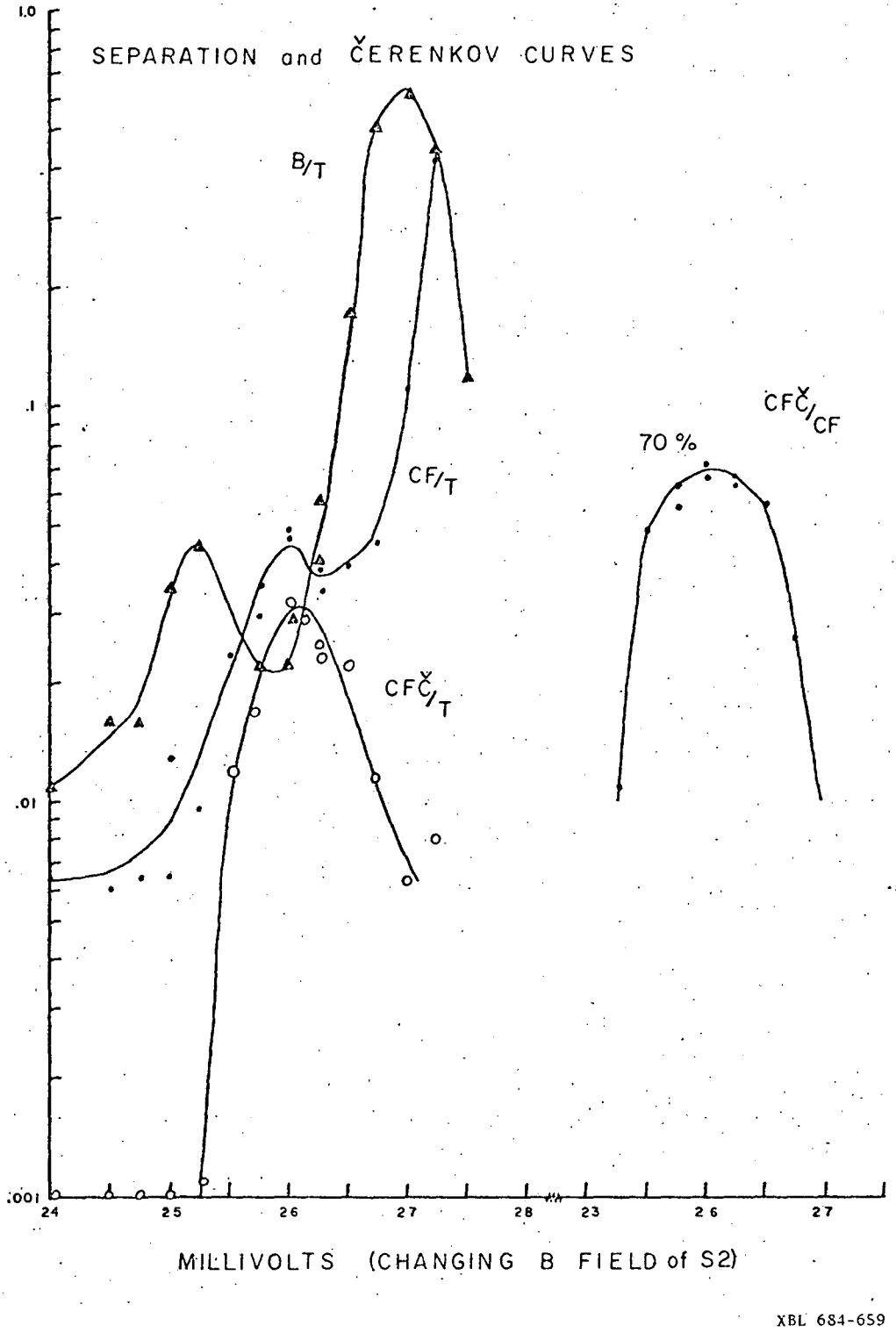

Fig. 2. Separation and Čerenkov curves used in estimating the proton contamination.

after the slit--all normalized by T the target monitor. At this momentum the proton and pion peaks are seen to be in the ratio of nearly 150 to 1 with the two peaks not being very well resolved. Of course, because of the $1/p^3$ behavior of the separation distance, much better resolution was obtained at the lower momenta. The Čerenkov counter was adjusted so as not to count the (relatively) slow protons; and hence (CF - CFČ)/CF is the percentage of protons in the beam after separation has occurred--i.e. roughly 30%.

In order to get a better quantitative understanding of the proton contamination. The measured 4-prong events were constrained to the following reactions:

$$pp \rightarrow pp\,\pi^+\pi^- \tag{4}$$

$$pp \rightarrow pp\,\pi^+\pi^-\pi^\circ \tag{5}$$

$$pp \rightarrow p\,\pi^+\pi^+\pi^-n \tag{6}$$

The ratio of the number of events constraining to these reactions, to those constraining to the corresponding pion beam hypotheses, when compared to the ratio of the respective cross-sections, was used to determine the fraction of protons in the pion+proton beam. That is, if N_π, N_p and $\sigma_{\pi p}$, σ_{pp} are the respective numbers of events (excluding events constraining to both pp and π^+p hypotheses) and cross-sections for these reactions and α the fraction of protons, then:

$$N_\pi = C(1-\alpha)\,\sigma_{\pi p},\quad N_p = C\,\alpha\,\sigma_{pp}$$

$$\frac{\alpha}{1-\alpha} = \frac{N_p\sigma_{\pi p}}{N_\pi\sigma_{pp}}$$

Also, using the number of events constraining to both pion and proton hypotheses and the ratio N_p/N_π, an estimate of the proton-event

Table I. Proton contamination of the π^+, p beam and good-event sample (G.E.S.) and muon contamination of the π^+, μ^+ beam.

Momentum	Using only the 4C fits		Using all of reactions 1-6		δ-ray results
GeV/c	% P beam	% P G.E.S.	% P beam	% P G.E.S.	% μ beam
2.95	2.7 ± .7	.032 ± .013	3.0 ± .8	.030 ± .008	5.7 ± 2.6
3.19	5.4 ± .8	.070 ± .017	6.0 ± 1.1	.10 ± .01	5.3 ± 2.4
3.53	5.7 ± .9	.14 ± .03	8.1 ± 1.4	.19 ± .02	4.8 ± 2.2
3.74	9.1 ± 1.2	.29 ± .05	10.7 ± 1.7	.45 ± .04	4.5 ± 2.1
4.08	25.0 ± 2.4	1.9 ± .2	22.1 ± 3.0	2.6 ± .1	4.1 ± 1.9

contamination of the final event sample may be obtained.

The results of this analysis are exhibited in Table I, the proton contamination having been found to vary from 3% at the lowest to 24% at the highest momentum. Note that by this method the proton contamination of the "good" beam, as defined by criteria detailed in Part (E), is determined. Off-momentum protons (e.g. degraded at the mass slit) are rejected by the momentum cut; so, their contamination is not relevant to the experiment. This accounts for the higher value given by the Čerenkov counter at 4.08 GeV/c.

D. Beam Normalization

Because of the beam contamination it was not sufficient merely to make a beam count in order to obtain the total pion path length. In particular it was felt desirable that a method be used which was independent of measurement of the proton contamination. This could be accomplished by normalizing to the δ-ray cross-section since large δ-rays are only produced by beam π's or μ's.[30] A scan for δ-rays with momenta greater than 18 MeV/c (i.e. sufficiently large that the delta-ray cross-section for production by a beam proton was negligible), and strong interactions on beam tracks with these δ-rays was made over about 20% of the film with the δ-ray initial momentum being measured (actually the cut was made on the initial radius of curvature and corresponds only approximately to 18 MeV/c). From the known cross-section for these δ-rays the total π^+, μ^+ track length could be obtained: and from the number of strong interactions occurring on these tracks and the total $\pi^+ p$ interaction cross-section, the mu-meson contamination could be estimated. Because of the paucity of data, this latter was done for the entire experiment, rather than for each momentum separately, with

Table II. Beam Normalization

Momentum GeV/c	mb/event ratios δ-ray normalization	σ_τ normalization
2.95	$(2.29 \pm .10) \times 10^{-3}$	$(2.48 \pm .13) \times 10^{-3}$
3.19	$1.19 \pm .04$	$1.07 \pm .05$
3.53	$1.26 \pm .05$	$1.15 \pm .06$
3.74	$1.54 \pm .05$	$1.45 \pm .09$
4.08	$1.32 \pm .04$	$1.15 \pm .09$

an assumed 1/p (lifetime effect) dependence upon incident momentum. Muon contamination is given in Table I, and Table II shows the figure obtained for the number of millibarns per event at each energy.

Since this was not the conventional way to determine the path length, an independent means was sought to confirm the delta-ray results. A scan was made for all strong interactions in a sample of the film, which, in conjunction with knowledge of the proton contamination, was used to normalize to the known $\pi^+ p$ total cross-section. The results from this method are shown in Table II and are seen to agree, within errors, with those obtained by the δ-ray method.

In both of the above methods the error quoted is not purely statistical--i.e. from the number of δ-rays or strong interactions discovered. It also stems from the uncertainty in the cross-sections used, in the necessary corrections for efficiencies and μ or proton contamination, and in the correction of these samples to the good-beam criteria detailed in Section (E).

E. The Event Sample

The "good-event" sample (G.E.S.) for reactions 1-3 was culled from the events which survived processing by the Fog-Cloudy-Fair System. The basic requirements determining the selection criteria were that the sample be as free from contamination, as unbiased, and as large (statistically significant) as possible. The events were screened in the following ways:

a. Good beam requirement: The beam momentum, entrance angles and entrance position were required to satisfy conditions ensuring that only good beam events would be considered. Also, events were required to lie within certain limits, in the beam

Table III. Cuts in the event sample.

Momentum (GeV/c)	2.95		3.19		3.53		3.74		4.08	
Events processed	3236	100%	8179	100%	8261	100%	6758	100%	9524	100%
-12<XVTX<108 cm.	45	1.39	104	1.27	72	.87	77	1.14	100	1.05
PE > .9 P_0	89	2.75	450	5.50	414	5.01	455	6.73	1160	12.18
$\lvert BETE-B_0\rvert < 3°$	10	.31	39	.48	17	.21	20	.30	25	.26
$\lvert ALFE-\alpha_0\rvert < 2°$	40	1.24	65	.79	53	.64	57	.84	74	.78
35<YEND<61.5 cm.	155	4.79	447	5.47	328	3.97	230	3.40	228	2.39
42<ZEND<58 cm.			1	.01						
TDAV < 60	137	4.23	319	3.90	339	4.10	184	2.72	324	3.40
ITER $\leq$ 8					1	.01				
M^* < 8, 15 (1C, 4C)	473	14.62	1533	18.74	1630	19.73	1350	19.98	2112	22.18
GM^* < 7	473	14.62	851	10.40	727	8.80	564	8.35	1283	13.47
Good event	1814	56.06	4370	53.43	4680	56.65	3821	56.54	4218	44.29

direction, in the chamber.

b. Good measure requirement: The parameter Tdav, which is a measure of the goodness of fit of a track through the digitized points along it, was used to remove events with poorly measured tracks.

c. Good fit requirement: Cuts were made on the Fair quantities Iter, M* and GM* which measure the ease with which the programs kinematically constrained an event, the goodness of the kinematic fit of constrained events, and the agreement of the measured and calculated ionization for the (FSD) measured tracks of an event.

Table III shows the precise upper and lower bounds of each cut and the percentage of events eliminated by each cut applied in succession.

Some of the events constrained to more than one hypothesis. These ambiguous events, amounting to 11% of the good event sample, were examined on the scan table. Roughly 30% of these could not be resolved by ionization information and were assigned on the basis of the lower M* value, with the greater reliability of 4C than 1C fits being taken into consideration.

The value of the ionization criteria (GM* cut) may be seen in the fact that the number of ambiguous events would have been doubled without its use. Also, it provided a means for ridding the sample of events which constrained incorrectly--e.g. multi-pi-zero events, which could fake a neutron event (reaction (3)) kinematically, would have a misidentified proton, and hence should fail the ionization test. Figure (3) shows the GM* distributions for one experiment (3.53 GeV/c) for the 4C fits which were (A) ambiguous, with the largest GM* and

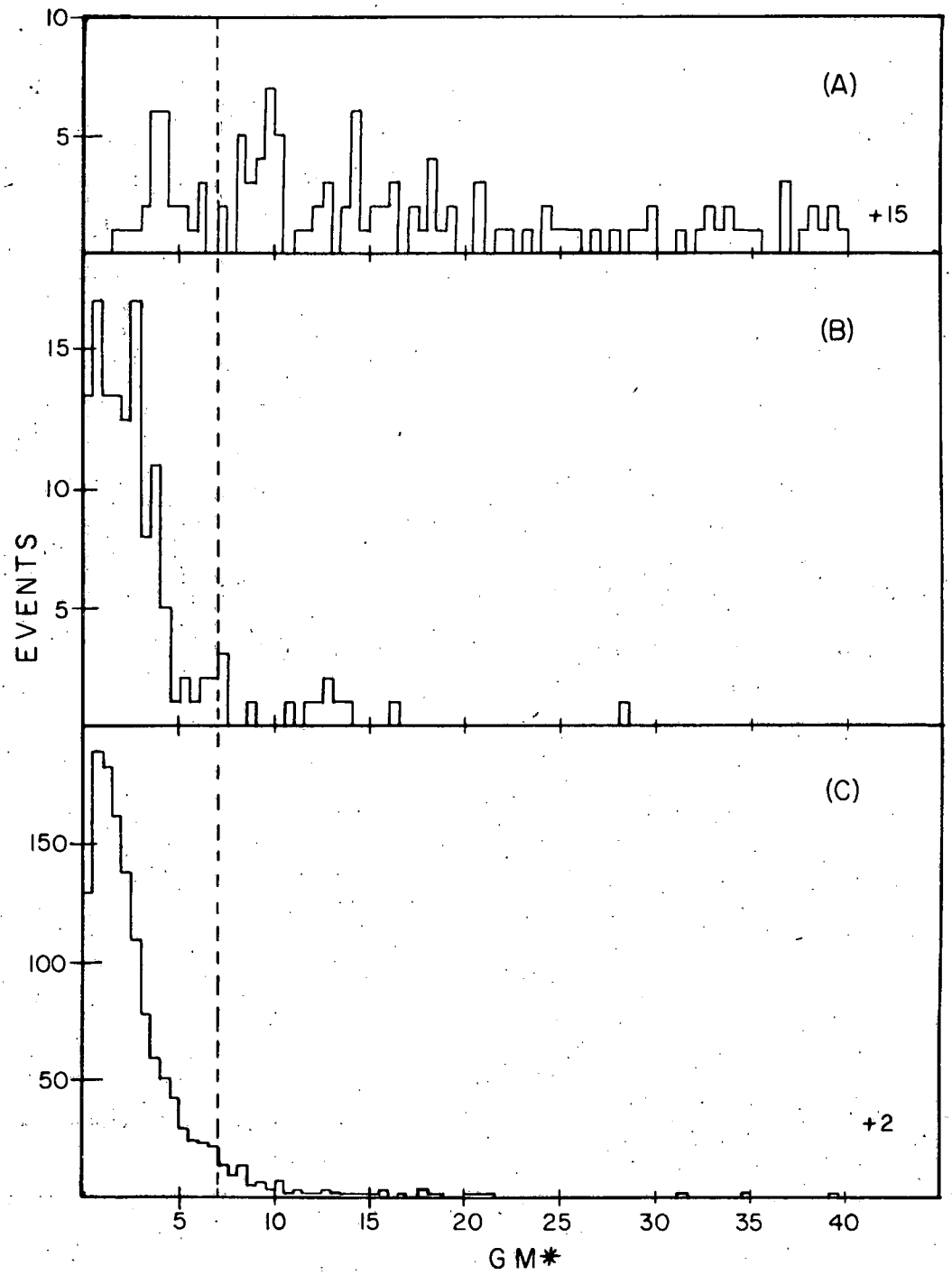

XBL 684-661

Fig. 3. GM* distributions for the ambiguous 4C - fit events for the permutation with (A) the highest and (B) the lowest GM*, and (C) for the unambiguous 4C fits.

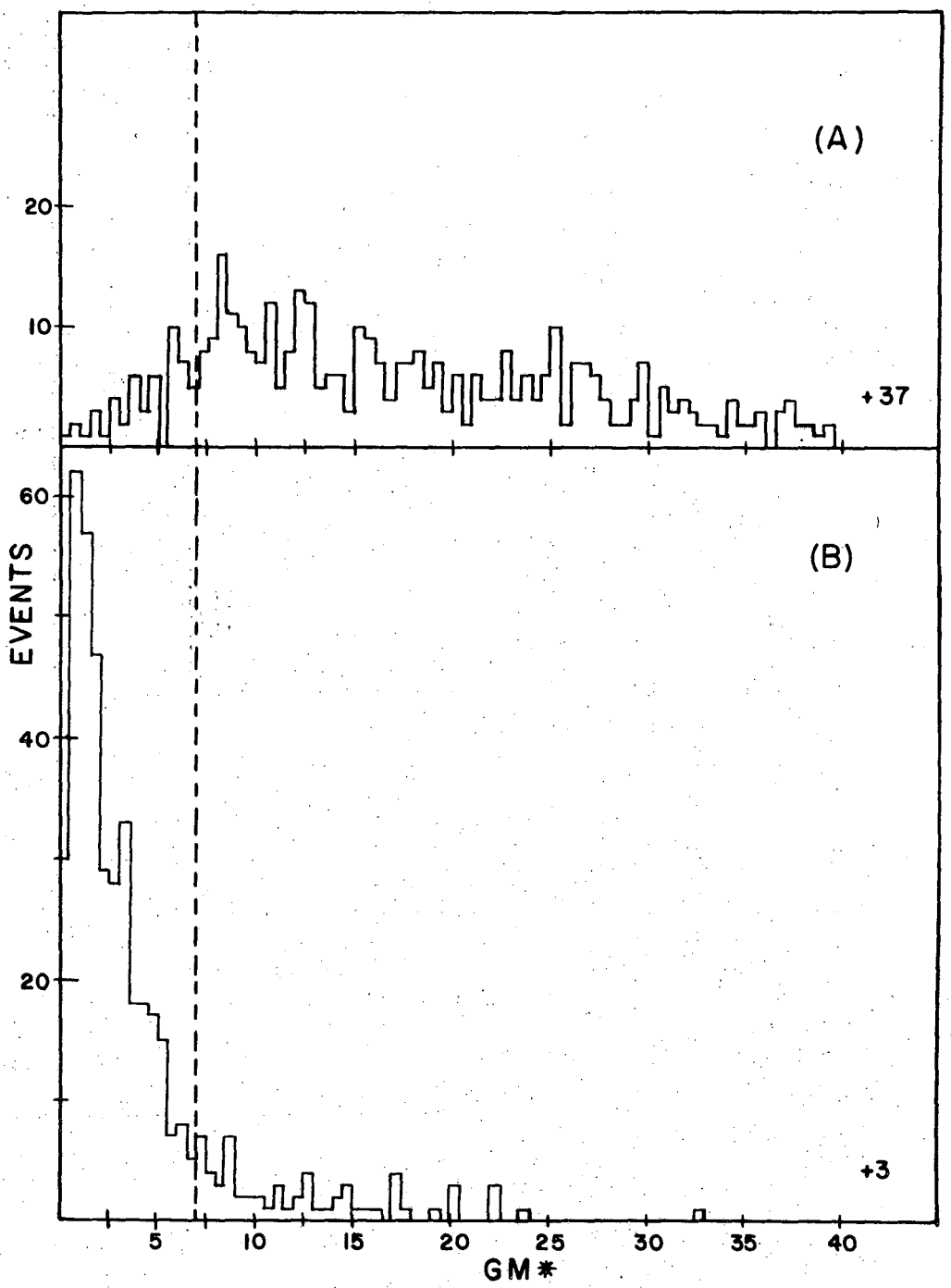

Fig. 4. GM* distributions for the events constraining to a permutation of both reactions (1) and (2) for (A) the best (lowest GM*) reaction (2) permutation which constrained and (B) the best reaction (1) permutation.

(B) ambiguous with the smallest GM*, and (C) which were unambiguous. This shows the extent to which GM* could be used to differentiate between the different hypotheses. Further, Fig. (4) shows the GM* distributions for the 4C-π° (reactions (1 and 2)) overlap events for (A) the best (by GM*) π° hypothesis which fit and (B) for the best 4C hypothesis fitting. Only those cases (96%) for which different tracks were fit as the proton under the two hypotheses were used. Clearly GM* offers a good method for choosing the correct hypothesis, and also, as expected, 4C fits are more reliable than 1C fits.

The ionization information was furnished by the FSD as the fraction (HM) of the scans of a given track for which a bubble was encountered.[31] Since the theoretical dependence of this upon a particle's velocity is well known, a similar number (HC) could be computed from the particle's known momentum and assumed mass, and normalized using the minimally-ionizing beam tracks. Corrections are of course made for the orientation of the track relative to the plane of the camera, and of the projection of the track relative to the scan direction. It was found that the measured ionization was also dependent upon position in the chamber, so corrections were made for this effect as well. GM* was then defined to be the average, for all of the tracks for which ionization information was received, of the quantity $(HC-HM)^2/DH^2$, where DH was the estimated error on the ionization measurement.

F. The mb/event Ratios

The remaining task is to adjust the previously found mb/event figures to the particular event sample chosen in Section (E). That is accomplished as follows:

$$\frac{\text{mb}}{(\text{event in sample})} = \frac{\text{mb}}{(\text{event on film})} \times \frac{\text{event on film}}{(\text{event in sample})}$$

Corrections for the physical cuts (1-6) have already been made; however, important corrections for inefficiencies in scanning and in the processing system and for the tails of the TDAV, M*, and GM* distributions remain.

Scanning efficiency was measured by comparing the results of the original scan with those of a rescan of a quarter of the rolls. Lists of the events found in the two scans were compared and events not on both of the lists segregated. These events were scanned once again and classified as (1) bad, (2) non-beam or (3) good events (typical examples of the first two classes of events would be a two prong event and an event from a low-momentum beam track). Events of the first type would not be processed by the system, so their fraction was subracted from the total number scanned. Likewise, events of the second type would fail the good beam requirement and were irrelevant to the efficiency calculation. The usual efficiency calculation was then made on the good events. There was, ofcourse, some difficulty in deciding whether an event should be assigned to type (2) or (3); however, this results in only a slight increase in the error on the calculated efficiency.

The efficiency of the system was simply the percentage of the events scanned for which Fair output was received. In view of the previous paragraph, however, the fraction of "bad" events was first subtracted from the "events scanned" catagory. The Tdav cut was similarly treated--i.e. the events eliminated were those improperly treated (poorly measured) by the system. The measurement errors for those events within the generous Tdav cuts, should simple result in a larger tail to the M* distribution (chi-square, for events which constrain) which is evaluated below.

The effects of the constraint criteria are somewhat more difficult to evaluate. The effects of the M* and GM* cuts would be easy to

calculate if these measures of the kinematic and ionization fits were in reality chi-square distributed. The relevant errors are not gausian distributed, however, but have proportionately greater tails to their distributions than expected, so that the related "chi-square" distributions also have exessive values for large chi-squares. Further, the distributions for different hypotheses overlap, and this effect--of "background" events also constraining to the reactions of interest--increases considerably with energy with the increase of the proton contamination and of the multiple-neutral production cross-sections.

A determination of the fraction of good events lost in the cut on the ionization measure, GM*, was made in a fairly straight-forward way. Samples of the events failing only the GM* test were scanned at each energy to check the ionization, and the percentage of good events estimated. This was not a completely unambiguous procedure because the FSD ionization measurement should be more reliable than that of a scanner, especially in the 1.2 to 1.5 GeV/c momentum range. Only a fairly small percentage of events fell within this ambiguous catagory however.

The effect of the M* cut was examined in the following ways:

1. The M* distributions at each energy were fit to chi-square + constant background distributions, to obtain estimates of the excess of events in the tails of the distributions.
2. The effects of the following abnormal conditions in artifically worsening the M* distribution were studied: a) high TDAV--poorly measured events, b) off-momentum beam--since the beam momentum was edited in the constraint programs, and c) XVTX near the end of the chamber--where measurements were less reliable.

Table IV. mb/event normalization and cross-sections for reactions 1-3 (4C, π°, n).

Momentum	Reaction	mb/event	G.E.S.	σ (mb)
2.95	4C	$(3.67 \pm .28) \times 10^{-3}$	798	$2.93 \pm .25$
	π°	$3.50 \pm .35$	850	$2.98 \pm .31$
	n	$3.37 \pm .34$	157	$.53 \pm .07$
			1805	$6.44 \pm .61$
3.19	4C	$1.73 \pm .12$	1683	$2.91 \pm .21$
	π°	$1.54 \pm .14$	2195	$3.38 \pm .31$
	n	$1.40 \pm .13$	421	$.59 \pm .06$
			4299	$6.88 \pm .56$
3.53	4C	$1.71 \pm .11$	1943	$3.33 \pm .24$
	π°	$1.60 \pm .15$	2280	$3.64 \pm .34$
	n	$1.44 \pm .13$	433	$.63 \pm .06$
			4656	$7.60 \pm .63$
3.74	4C	$2.26 \pm .15$	1498	$3.39 \pm .24$
	π°	$2.06 \pm .18$	1851	$3.79 \pm .35$
	n	$1.88 \pm .17$	488	$.84 \pm .09$
			3797	$8.03 \pm .66$
4.08	4C	$2.05 \pm .14$	1383	$2.83 \pm .21$
	π°	$1.78 \pm .16$	2125	$3.78 \pm .36$
	n	$1.57 \pm .15$	613	$.97 \pm .10$
			4121	$7.58 \pm .65$
Combined	4C	$(4.22 \pm .13) \times 10^{-4}$	7305	$3.09 \pm .10$
	π°	$3.84 \pm .16$	9301	$3.57 \pm .15$
	n	$3.48 \pm .15$	2072	$.72 \pm .03$
			18678	$7.37 \pm .26$

3. A sample of film was completely remeasured so that the effects of measurement errors could be better evaluated.

From these, a figure for the percentage of good events lost minus bogus events retained was determined at each energy for each of the three reactions.

The final values for the mb/event ratios are given in Table IV, along with the cross-sections which these imply for reactions (1-3).

III. EXPERIMENTAL RESULTS

The event samples and mb/event ratios having been obtained for the three reactions of interest, their cross-sections and invariant mass and momentum transfer distributions will be shown before proceeding to a more detailed analysis of the data. For the sake of completeness, these distributions are presented for all incident momenta and for all possible combinations of final-state particles. Invariant mass and momentum transfer distributions of course do not begin to exhaust the possible displays of the data which could be made, the associated triangle plots and Chew-Low plots in particular might be of interest. Further expansion of this section was not deemed practicable; however, and a few of the "most important" triangle and Chew-Low scatter plots appear in Section (IV).

The cross-sections for reactions (1-3) are shown in Figs. (5 and 7). Values from other experiments are included in order to give a better understanding of the energy dependence of the cross-sections. Those found in this experiment are seen to agree fairly well with earlier work, at least to within the rather substantial errors involved.

In particular, previous results indicated the possibility of a broad enhancement in the cross-section for reaction (1) in the region of the $N^*(2850)$. This was supported both by the general trend of the experimental cross-sections and by structure in the $M(\pi^+ p\ \pi^+\pi^-)$ invariant mass distribution of 8 Gev/c $\pi^+ p$ 6-prong events (Bardadin-Otwinowska et al.[24]). Quite striking confirmation of this has been obtained, although the evidence is not completely conclusive because of the large experimental errors. Despite the evident arbitrariness of any attempt to put a smooth curve through the experimental points and the difficulty

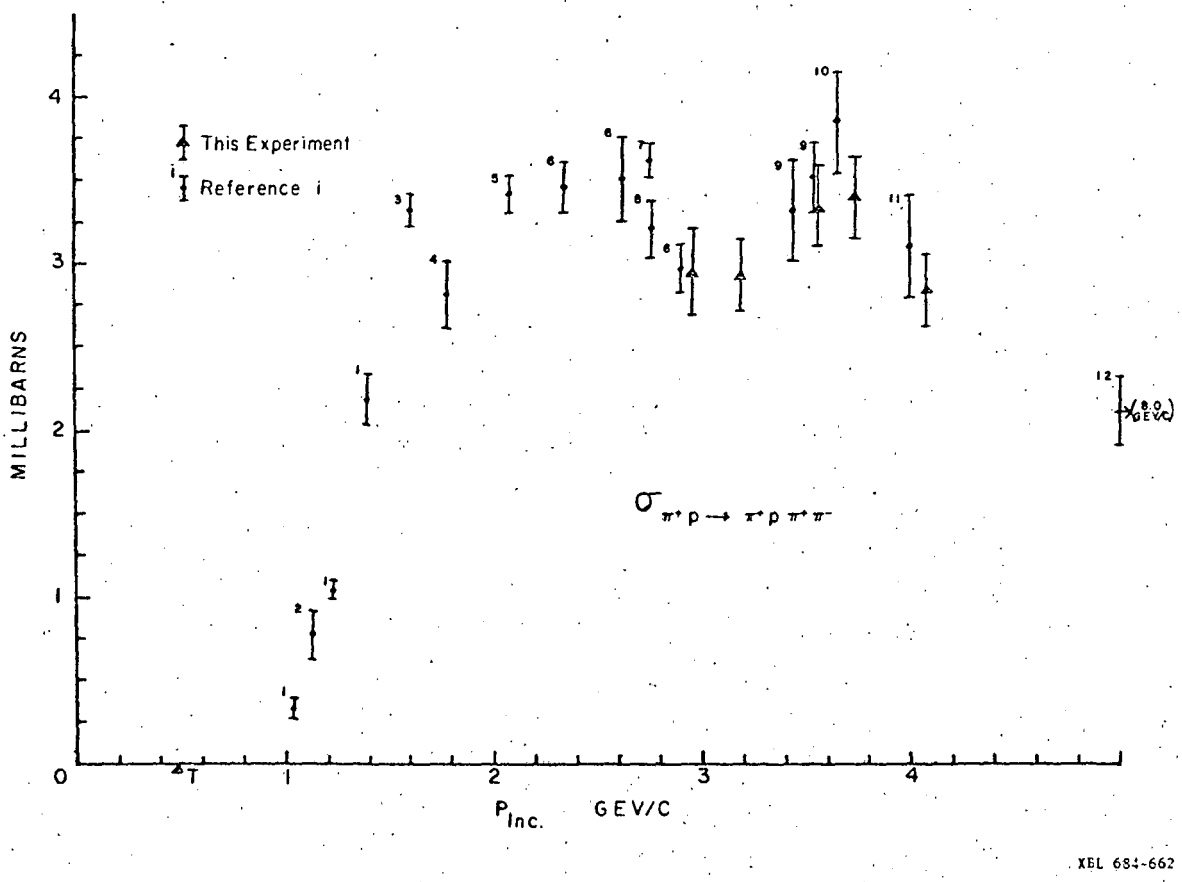

Fig. 5. Cross-section for reaction (1).

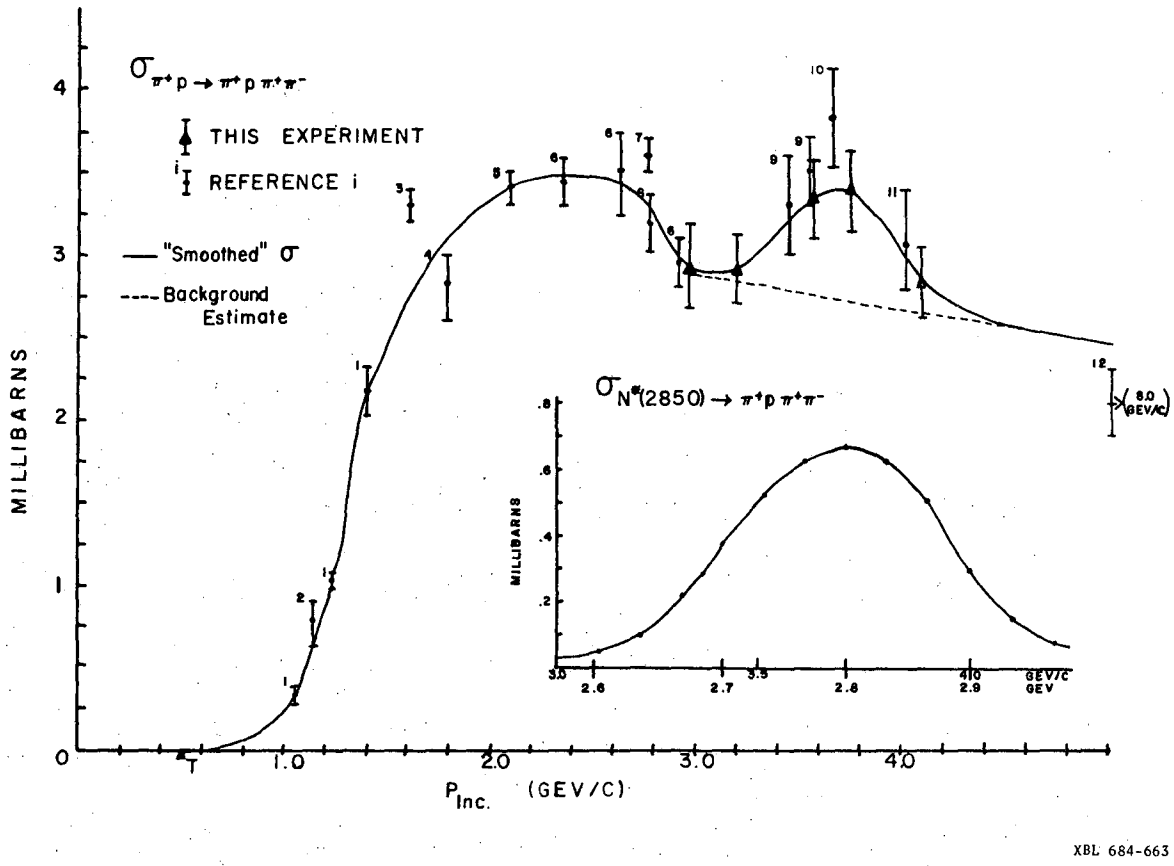

Fig. 6. Cross-section for reaction (1), with a smooth-line interpolation of the experimental points yielding an estimate of the cross-section for $N^*(2850)$ formation.

in drawing a suitable background, this has been done and is shown in Fig. (6). The resulting very crude estimate of the cross-section for formation of $N^*(2850)$ with subsequent decay into $\pi^+ p\ \pi^+\pi^-$ is exhibited in the inset to the figure. The resonance mass and width are seen to be roughly 2800 and 200 MeV respectively, which are not unreasonably far from the "8030" values of 2850 and 400 MeV. The height, however, is surprisingly large. It has been estimated as about .65 mb, which is 84% of the .77 ± .06 mb figure of Citron et al.[33] for the $N^*(2850)$ contribution to the total cross-section. Further evidence for the $N^*(2850)$ decay into $\pi^+ p\ \pi^+\pi^-$ will be seen in Section (B) in the $\pi^+ p\ \pi^+\pi^-$ invariant mass distribution of the $\pi^+ p\ \pi^+\pi^-\pi^\circ$ events.

The invariant mass and momentum transfer distributions are exhibited for each reaction in turn in the sections which follow together with some comments on their general features. The five distributions corresponding to the five incident momenta are displayed in perspective for every variable, with the number of events in the highest bin displayed for each histogram. Their sum is presented separately, with phase space curves (small triangles) included to give some idea of what a "background" might resemble. Also, for reactions (1) and (2) an effort has been made to take into account $N^{*++}\rho^\circ$ and $N^{*++}\omega^\circ$ production respectively (dots, with interpolated solid curve). Since there are substantial differences between the kinematic limits at the lowest and highest incident momenta, the background curves are not drawn for some average momentum but are the weighted sums of those generated at the five momenta.

No differentiation is made between (among) the two (three) outgoing positive pions so that for some distributions more than one combination must be histogrammed. For uniformity in normalization this is done for all the distributions. That is, in reactions (1) and (2) the curves

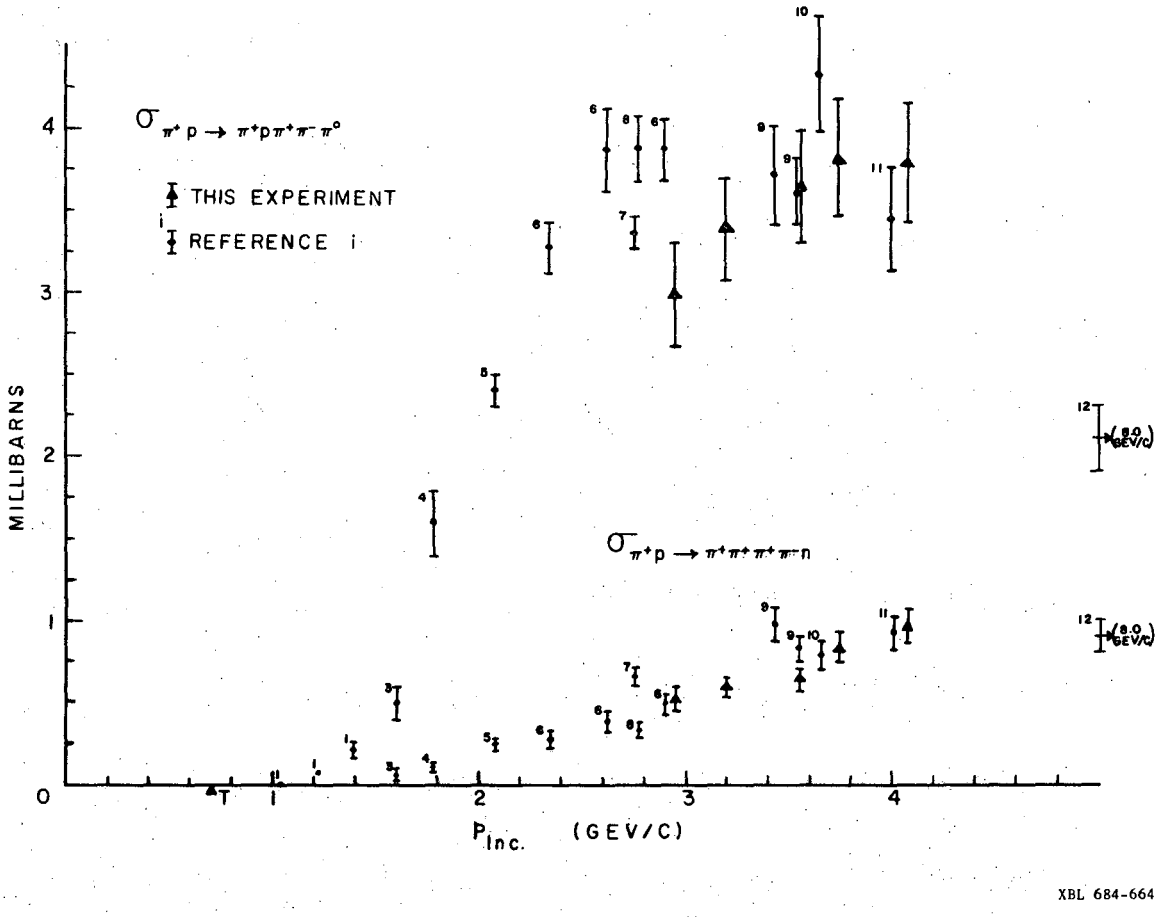

Fig. 7. Cross-sections for reactions (2) and (3).

are normalized to twice the number of events and in (3) to three times the number of actual events. Hence for an event contraining to reaction (3), invariant masses of the three distinct $\pi^+ n$ combinations are histogrammed in one distribution, and in another the unique value of $M(\pi^- n)$ is histogrammed three times.

A. $\pi^+ p \rightarrow \pi^+ p \pi^+ \pi^-$

Reaction (1) is the lone four-constraint (4C) fit reaction of the three (having no missing neutral), and as such its event sample is most to be trusted as free from spurious events. There are 7305 events in the entire sample divided 798, 1683, 1943, 1498, 1383 at each of the five incident momenta respectively. Its invariant-mass and momentum-transfer distributions are shown in Figs. (8-15). There are four 2-body and three 3-body combinations possible, not differentiating between the two π^+ mesons, and hence five momentum-transfer distributions.

The dotted curve is the phase space prediction, and the solid line is a combination of 40% $N^{*++}\rho^\circ$ with 60% phase space. The $N^{*++}\rho^\circ$ contribution is obtained from 100 000 events Monte-Carloed according to phase space times $e^{8t_{p,N^*}}$ and weighted by N^{*++} and ρ° Breit-Wigners, with the ρ° decay cosine (helicity frame) further weighted as $1/2\,(1+.6\cos\theta + .25(3\cos^2\theta-1))$ to take into partial account the observed ρ° decay anisotropy and asymmetry. The N^{*++} and ρ° parameters are given in Section (IV), their masses and widths being based on the UCRL-8030 values--i.e. $N^{*++}(1236, 120)$, ρ° (770, 130).

$N^{*++}(1236)$ and $\rho^\circ(770)$ production in the $\pi^+ p$ and $\pi^+\pi^-$ distributions respectively are the most dramatic features of the invariant mass distributions. Aside from an $f^\circ(1260)$ peak in the $\pi^+\pi^-$ distribution at the higher incident momenta and a rather striking peak at about 1700 MeV

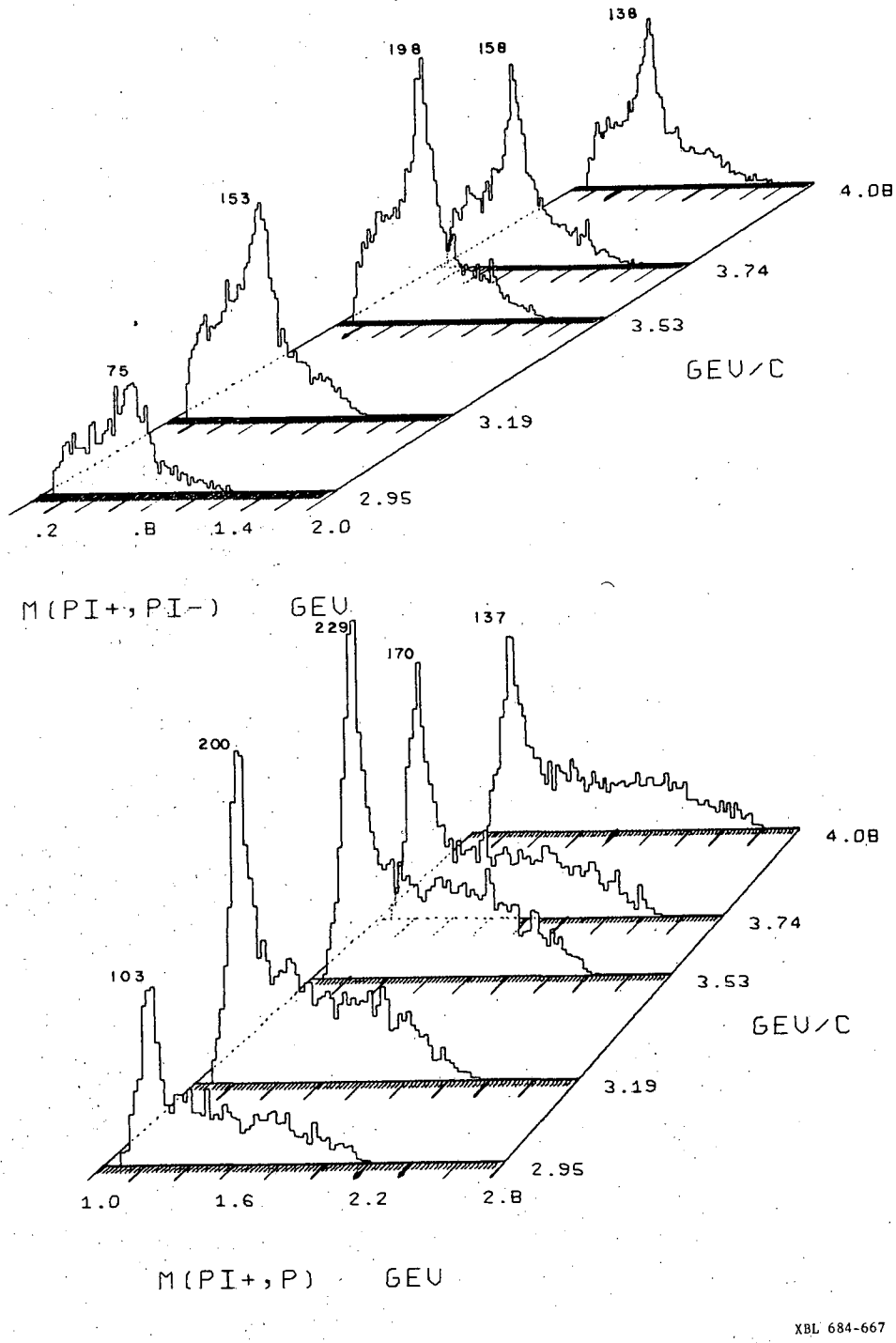

Fig. 8. Invariant mass and momentum transfer distributions of reaction (1) for the five momenta, in events/10 MeV($(MeV/c)^2$), with the number of events in the highest bin being given for each histogram.

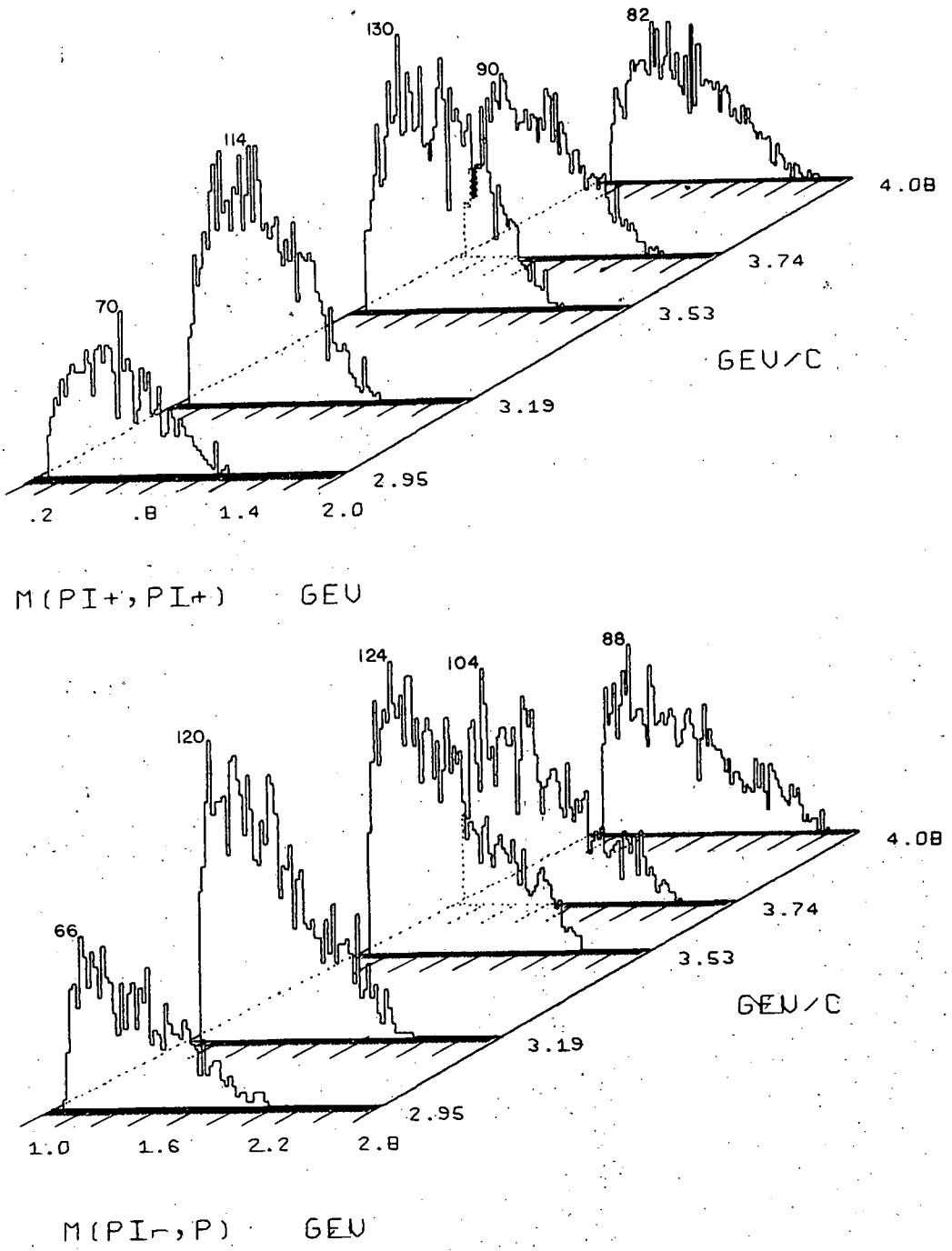

Fig. 9. Invariant mass and momentum transfer distributions of reaction (1) for the five momenta, in events/10 MeV ($(MeV/c)^2$), with the number of events in the highest bin being given for each histogram.

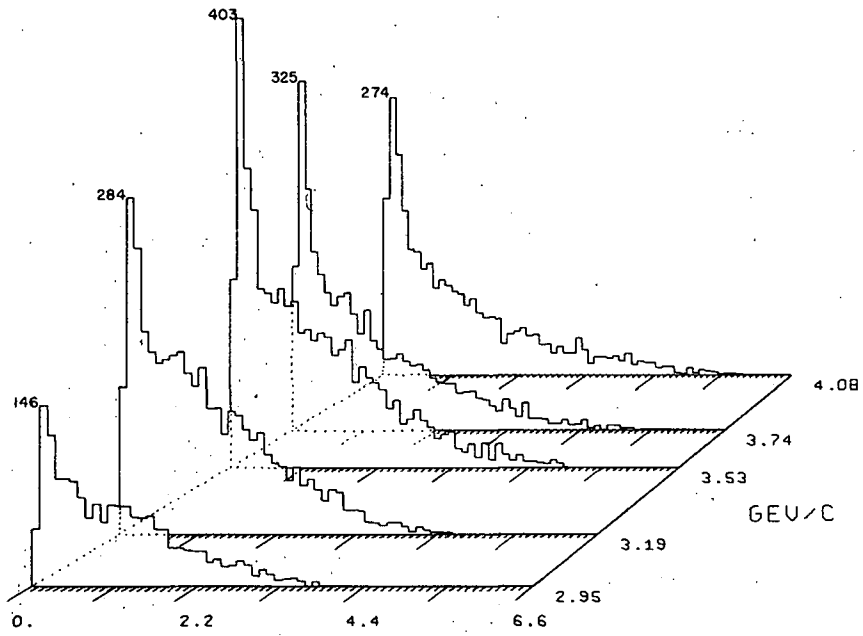

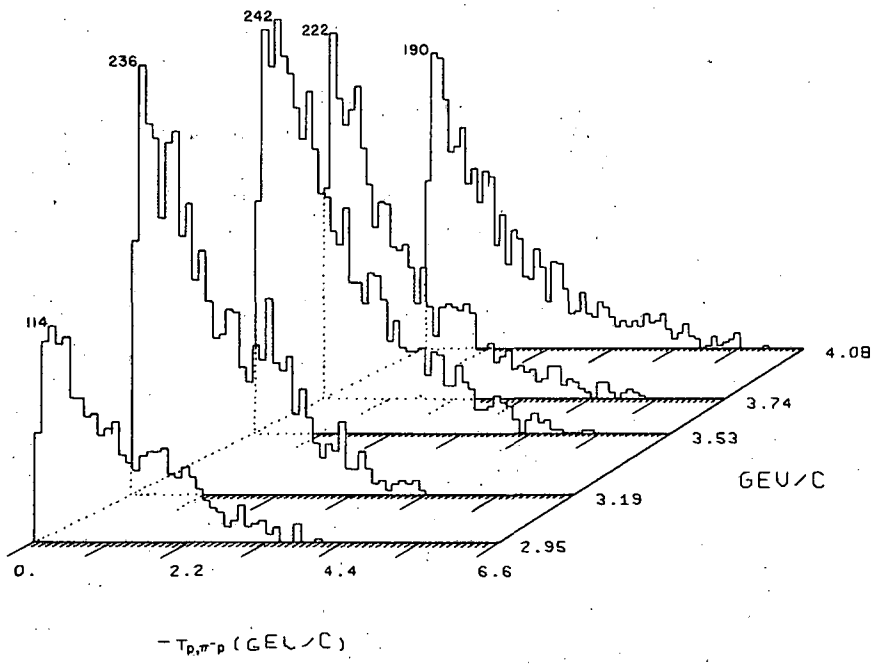

XBL 684-669

Fig. 10. Invariant mass and momentum transfer distributions of reaction (1) for the five momenta, in events/10 MeV $((MeV/c)^2)$, with the number of events in the highest bin being given for each histogram.

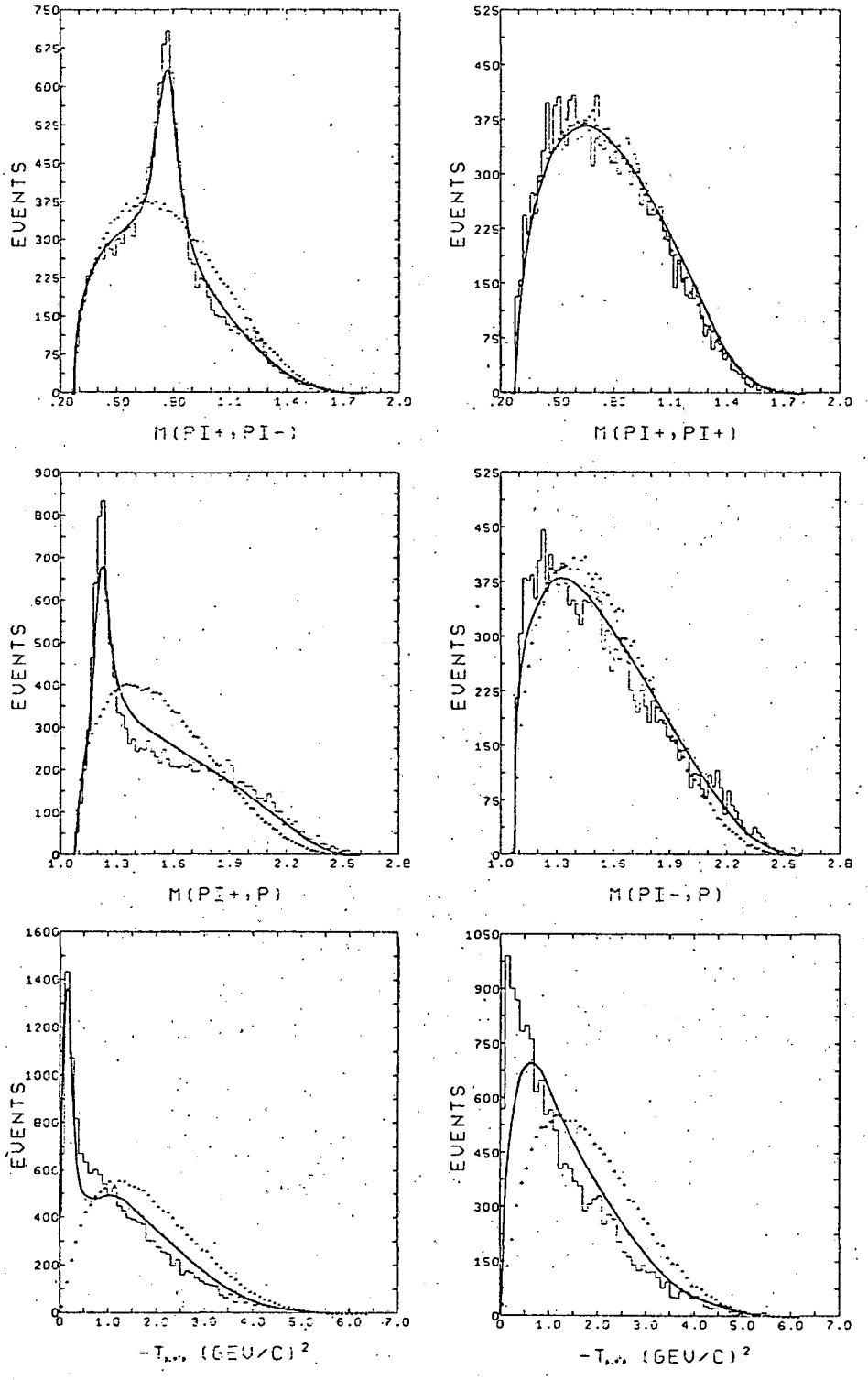

XBL 684-682

Fig. 11. Invariant mass and momentum transfer distributions of reaction (1) for all momenta combined, in events/10 MeV ((MeV/c)^2). The dotted curve is phase space; the solid curve represents 60% phase space and 40% $N^*\rho$ production.

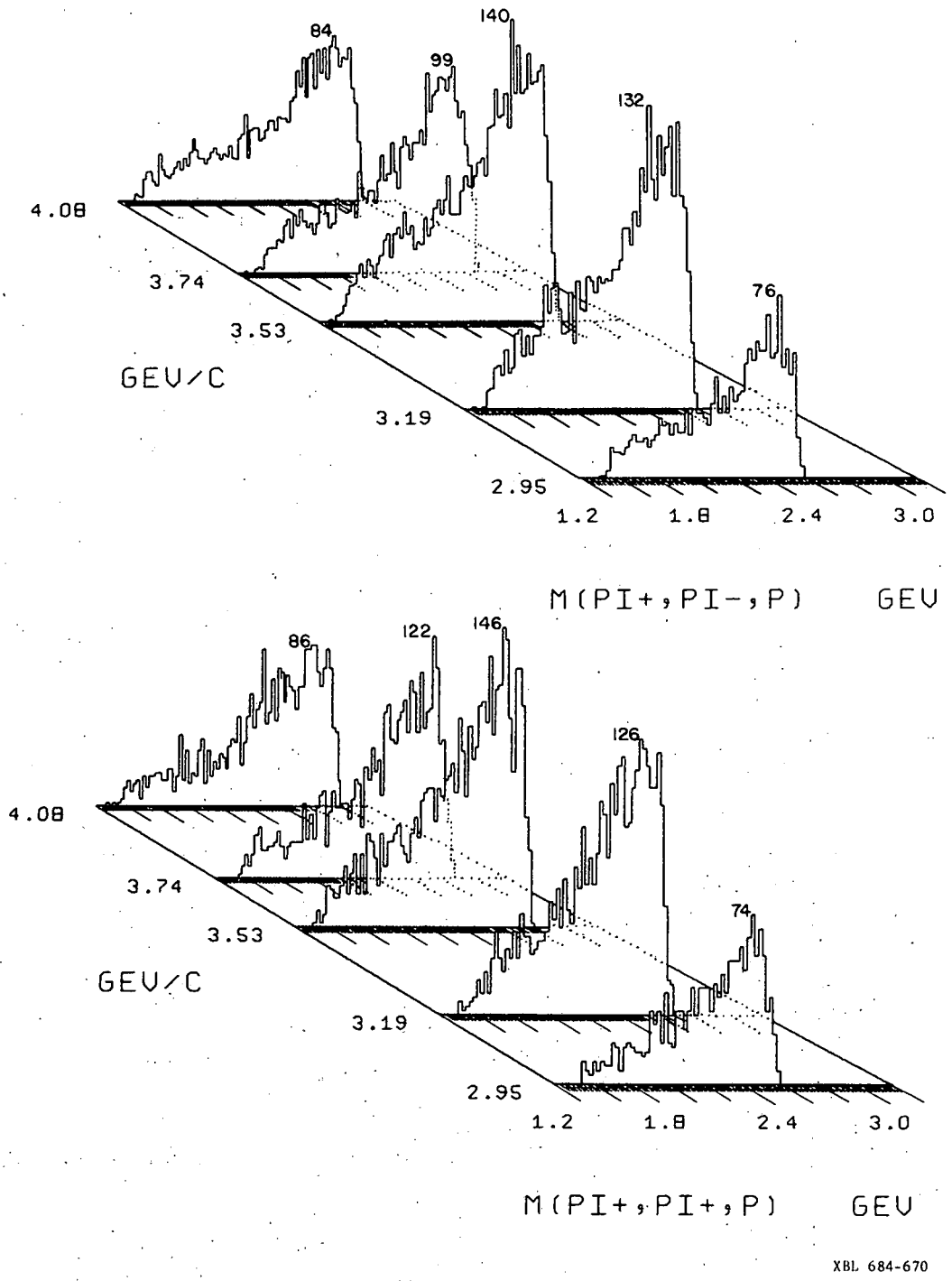

Fig. 12. Invariant mass and momentum transfer distributions of reaction (1) for the five momenta, in events/10 MeV ($(MeV/c)^2$), with the number of events in the highest bin being given for each histogram.

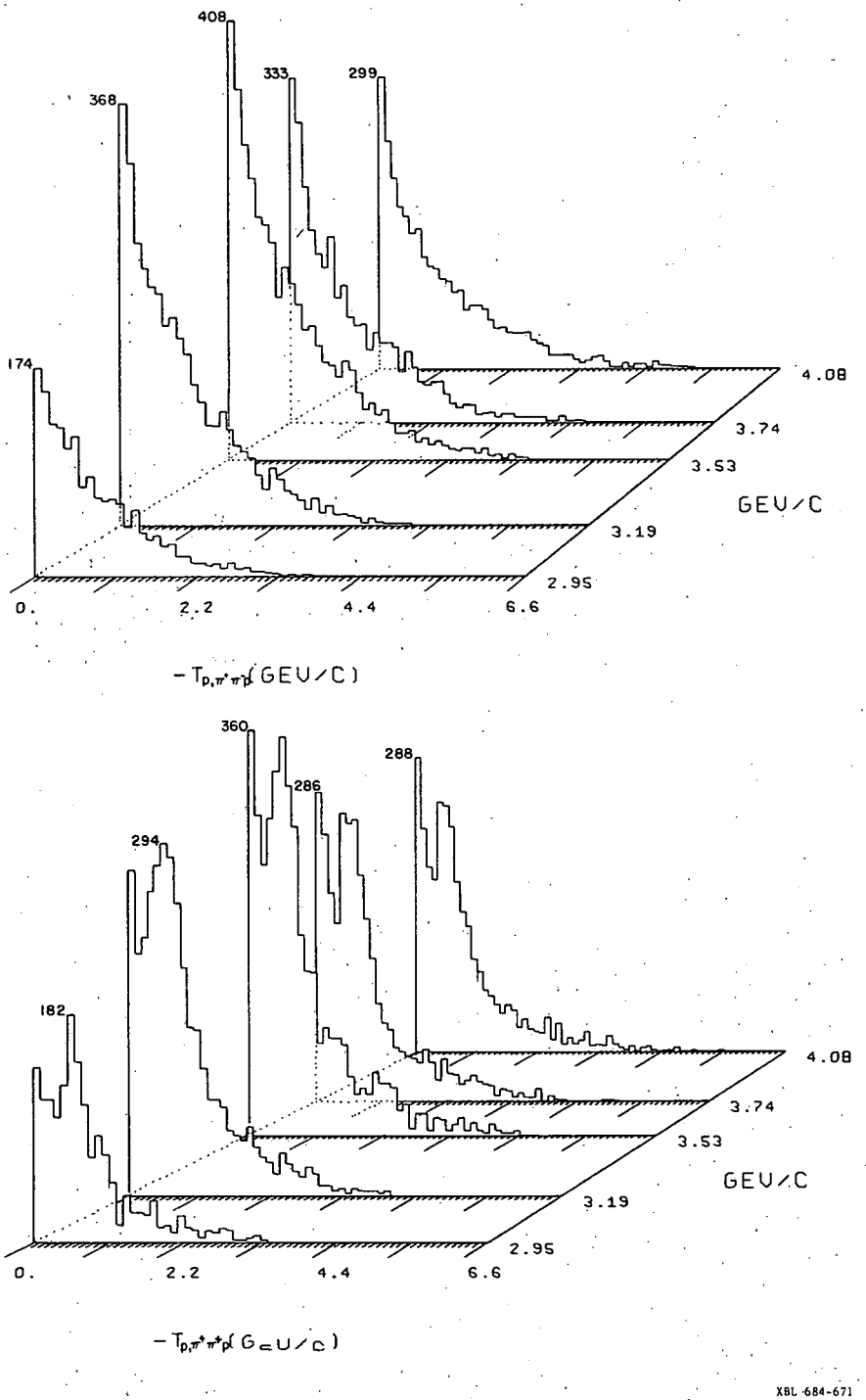

Fig. 13. Invariant mass and momentum transfer distributions of reaction (1) for the five momenta, in events/10 MeV ((MeV/c)^2), with the number of events in the highest bin being given for each histogram.

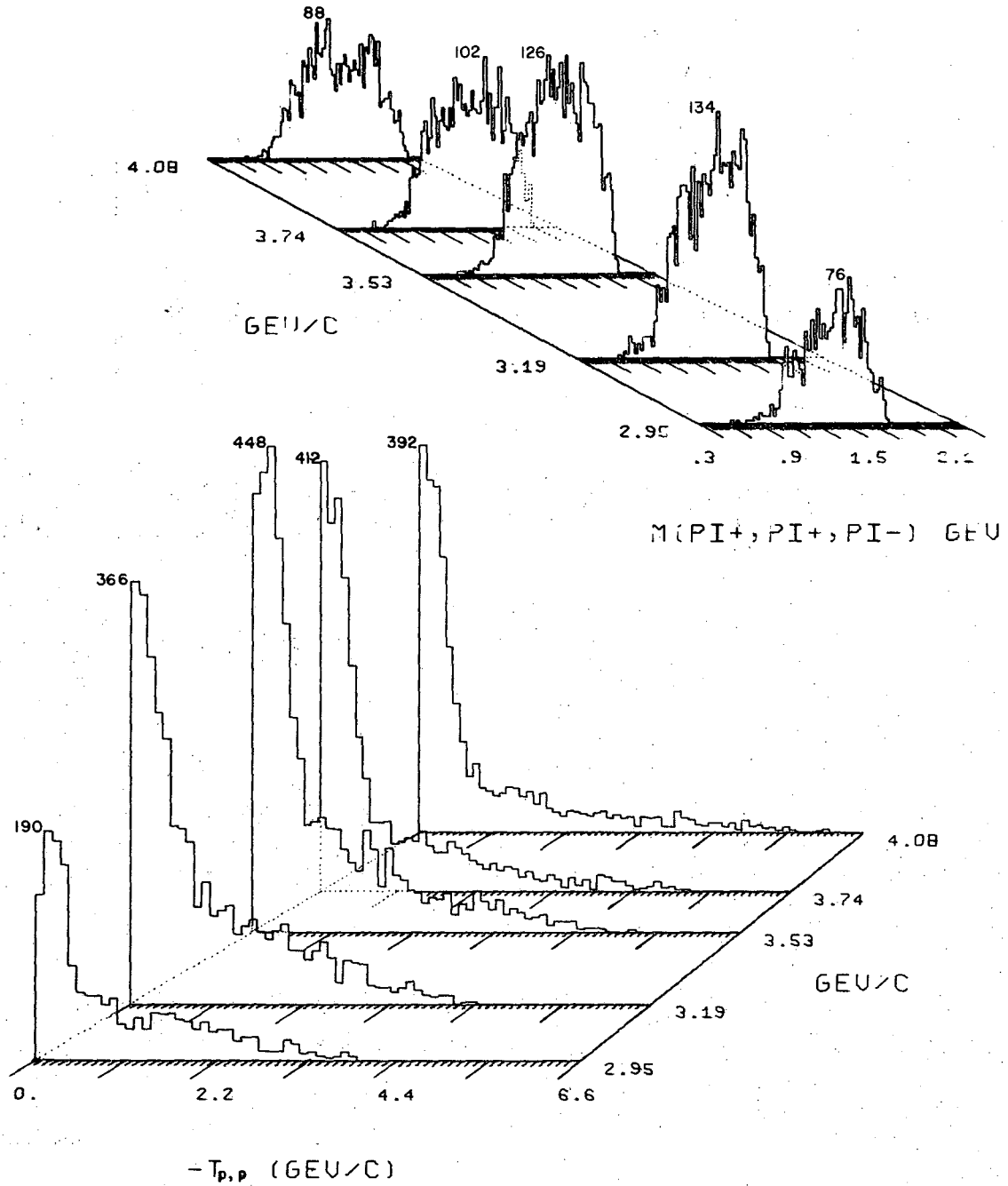

XBL 684-672

Fig. 14. Invariant mass and momentum transfer distributions of reaction (1) for the five momenta, in events/10 MeV ($(MeV/c)^2$), with the number of events in the highest bin being given for each histogram.

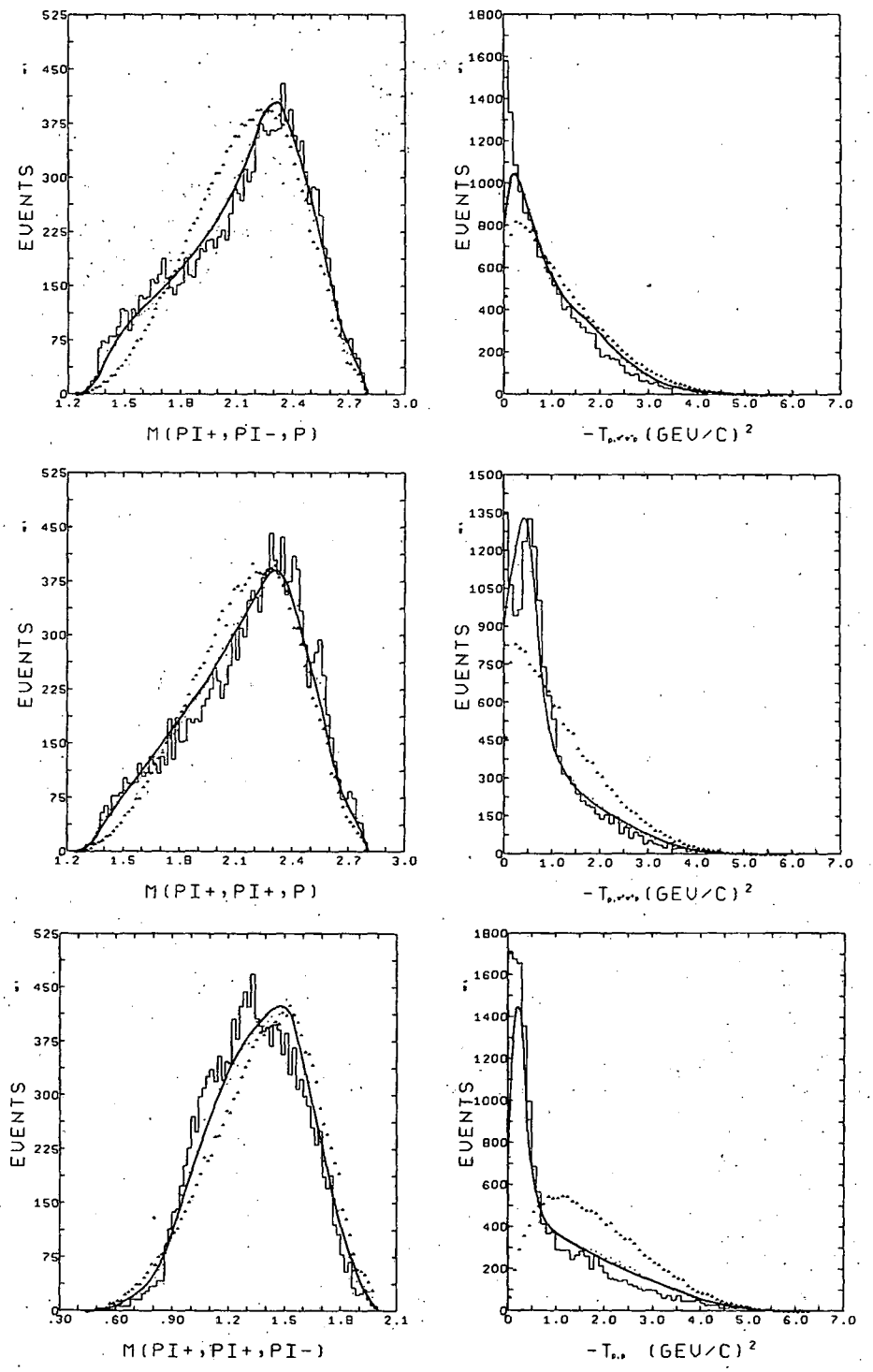

XBL 685-800

Fig. 15. Invariant mass and momentum transfer distributions of reaction (1) for all momenta combined, in events/10 MeV ((MeV/c)^2). The dotted curve is phase space; the solid curve represents 60% phase space and 40% $N^*\rho$ production.

in the $\pi^+\pi^-p$ distribution there is little other structure unambiguously associated with known resonances. In particular the three pion invariant mass distribution gives a rather confused, albeit enhanced, signal in the "A" region. When viewed against the "background" curve a shoulder in the A1 region and a broad A2 stand out prominently but certainly not with the narrow widths credited to them in the "8030"--i.e. of 80 and 90 MeV respectively.

The very peripheral nature of the processes involved in this reaction is evident from the momentum transfer distributions. Low values of the momentum transfer to the π^+p and $\pi^+\pi^+\pi^-$ systems are especially favored, but in all cases the distribution of momentum transfer between initial and final "particles" of like Baryon number is sharply peaked. Of course, these distributions are not independent. Because the proton is so much more massive than the pion, forward peaking in one distribution automatically requires a certain amount of forward peaking in the others. For example, the propagation of peaking in the t_{p,π^+p} distribution to the other momentum transfer distributions is clearly seen in the $N^*\rho^\circ$ contribution to the background curves of Figs. (11 and 15)--i.e. in the difference between the dotted (phase space) and solid (phase space + peripheral $N^*\rho$) background curves.

B. $\pi^+p \rightarrow \pi^+p\,\pi^+\pi^-\pi^\circ$

Reaction (2) has the largest cross-section of the three reactions. The event sample was composed of 9301 events, divided 850, 2195, 2280, 1851 and 2125 respectively at the five incident momenta. There are seven 2-body and 3-body combinations, and four 4-body combinations possible and hence eleven momentum transfer distributions. The invariant mass and momentum transfer distributions are shown in Figs. (16-34).

Again, phase space is indicated with a dotted line, and a solid line is drawn representing 80% phase space and 20% $N^{*++}\omega^{\circ}$ production (with an $e^{3t_{p,\pi^+p}}$ dependence).

$N^{*++}(1236)$ and $\omega^{\circ}(783)$ production in the π^+p and $\pi^+\pi^-\pi^{\circ}$ invariant mass distributions are the most striking features of the data. Other structure is present in the invariant mass distributions, however. In particular production of $\eta(549)$ is a well differentiated, if small, effect in the $\pi^+\pi^-\pi^{\circ}$ distribution. All of the two pion distributions, except $M(\pi^+\pi^+)$, show a pronounced hump at about 770 MeV indicating the presence of substantial $\rho(770)$ production. There is also some evidence of the B(1220) in the four-pion distribution. Some work on the B meson has already been published,[34] as well as a brief paper on the H enhancement.[35]

A further interesting feature of the mass histograms is the small "blip" at the upper end of the $M(\pi^+p\ \pi^+\pi^-)$ distribution mentioned previously. Unless attributable to some possible contamination effect, this seems to give further evidence for the decay of $N^*(2850)$ into the $\pi^+p\ \pi^+\pi^-$ channel.

The peripheral character of the reaction is again attested to by the sharp forward peaking in the momentum transfer distributions. It is very noticeably less marked, however, than for the distributions of reaction (1). The maximum peaking, in terms of an exponential slope, corresponds to less than an e^{3t} dependence.

C. $\pi^+p \rightarrow \pi^+\pi^+\pi^+\pi^-n$

Reaction (3) is distinguished by having three π^+ mesons among the five final state particles, so that for distributions involving one or two π^+, three combinations are possible for each event. This would tend

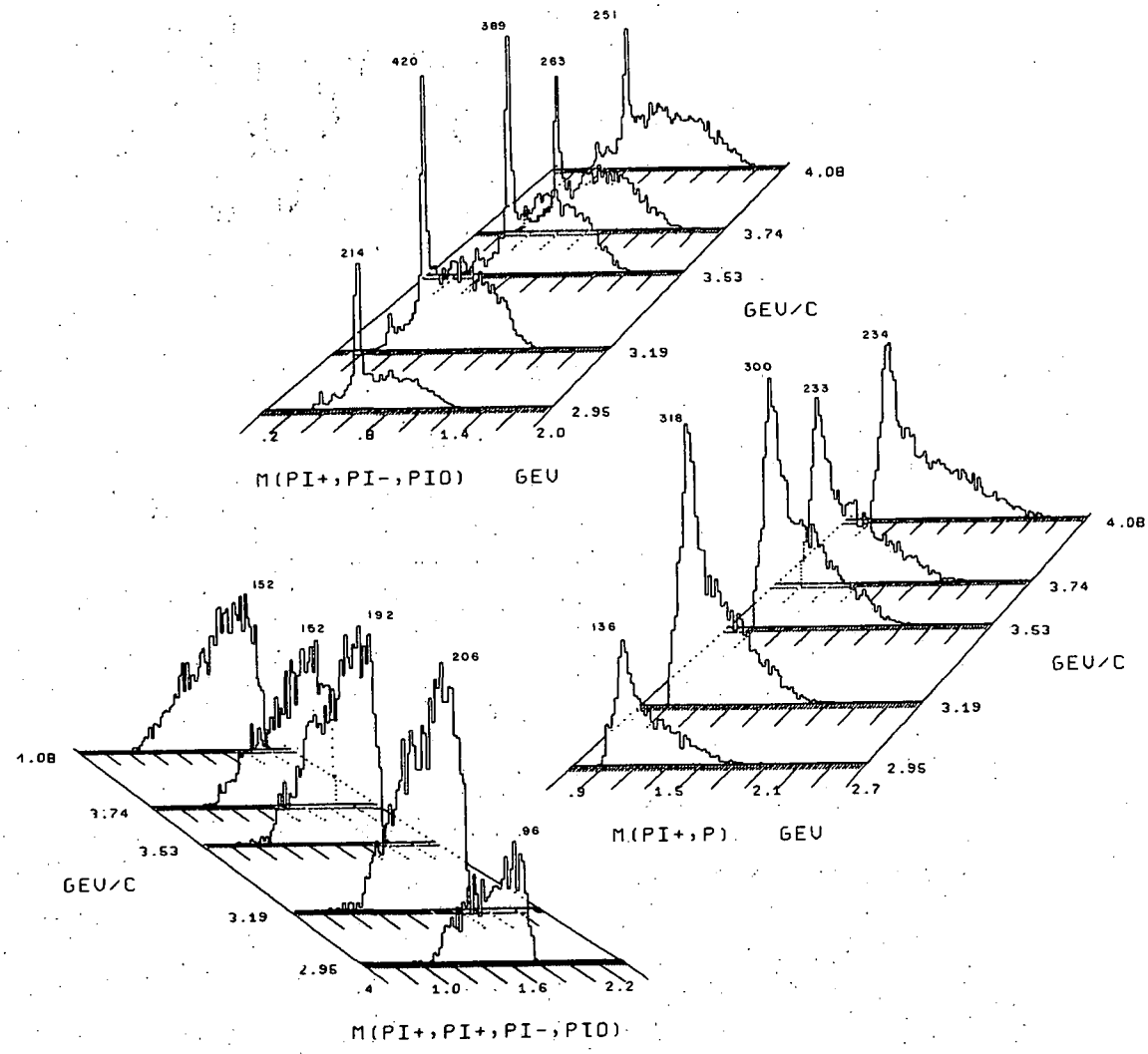

XBL 685-801

Fig. 16. Invariant mass and momentum transfer distributions of reaction (2) for the five momenta, in events/10 MeV $((MeV/c)^2)$, with the number of events in the highest bin being given for each histogram.

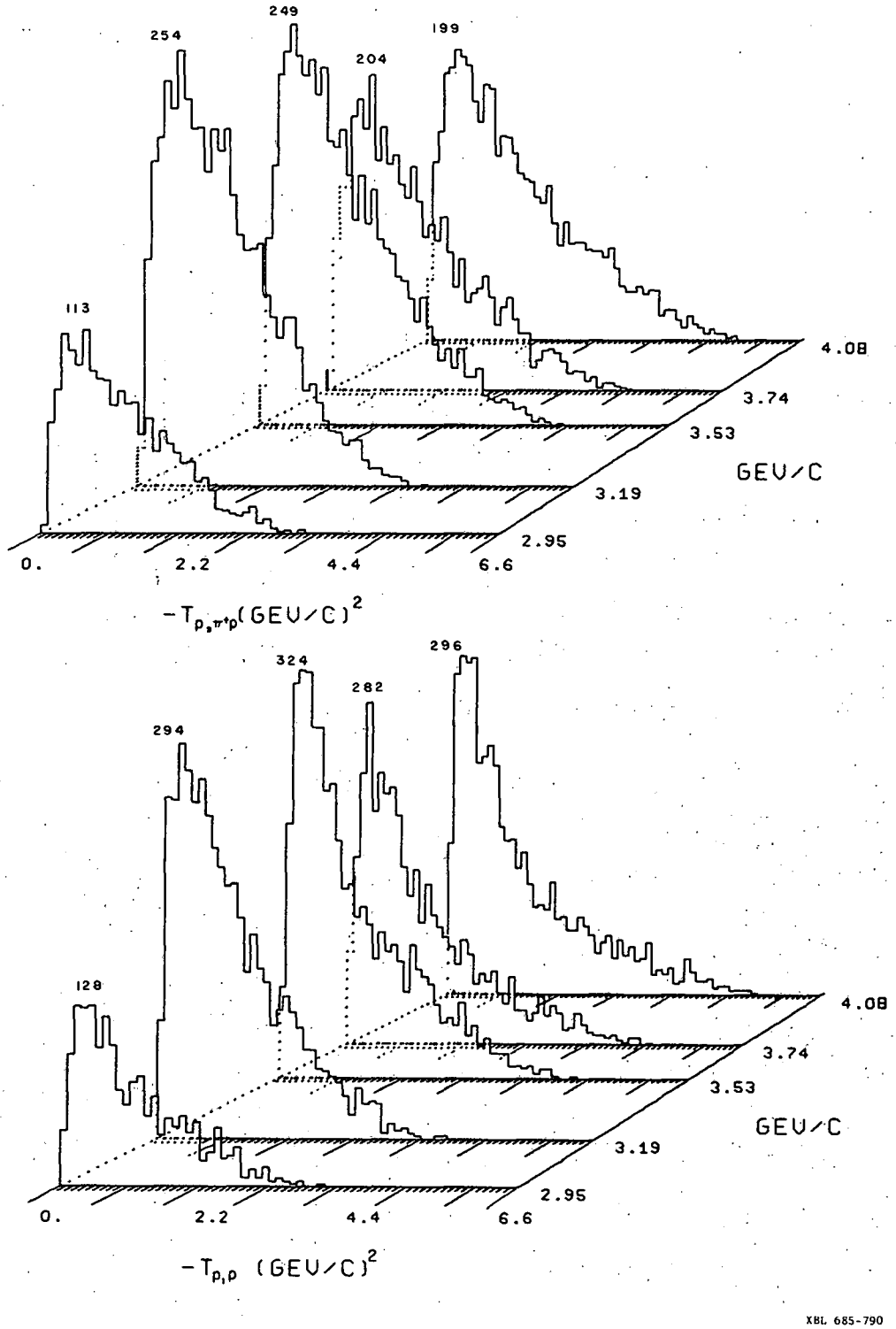

Fig. 17. Invariant mass and momentum transfer distributions of reaction (2) for the five momenta, in events/10 MeV $((MeV/c)^2)$, with the number of events in the highest bin being given for each histogram.

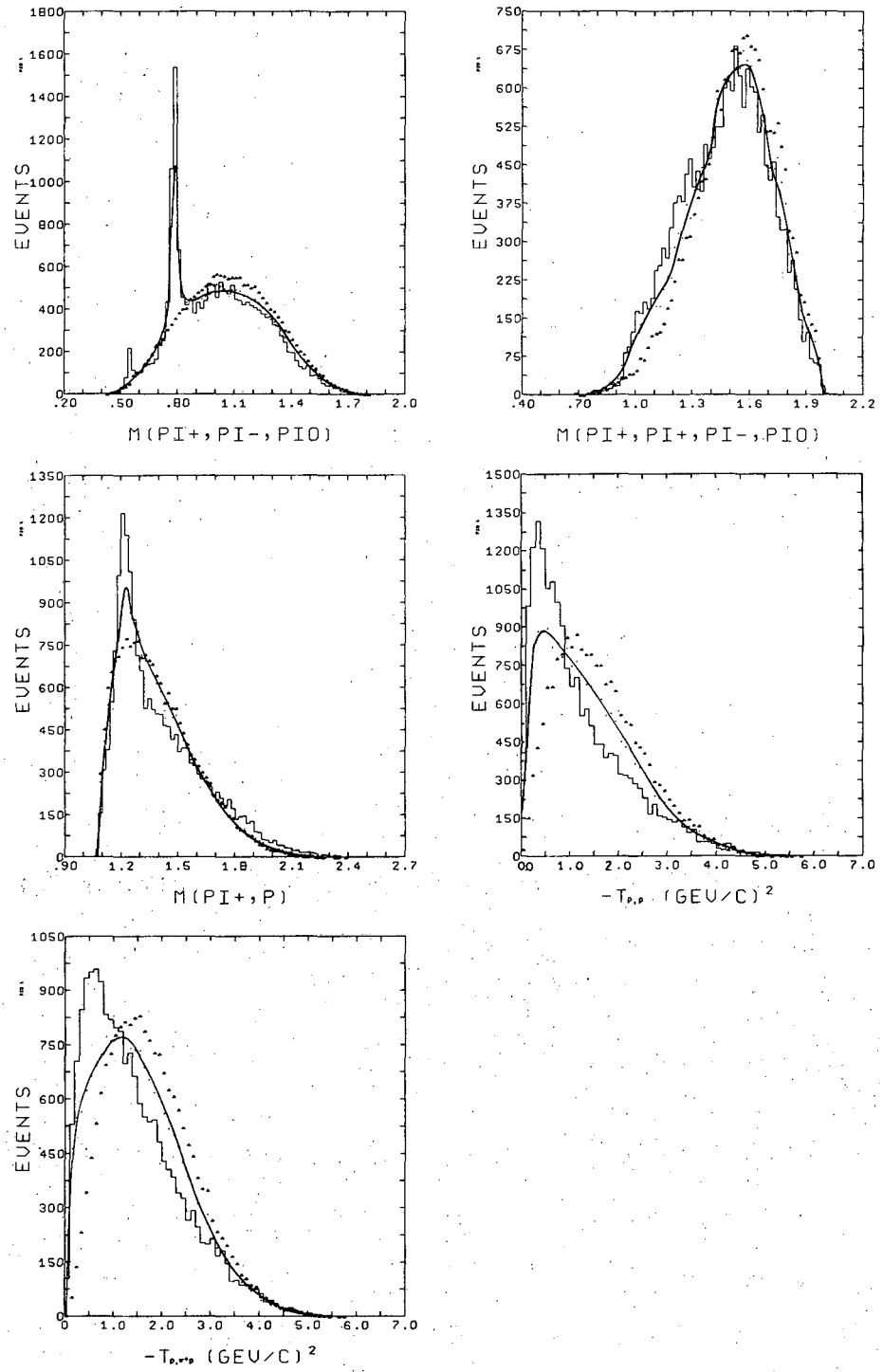

XBL 685-768

Fig. 18. Invariant mass and momentum transfer distributions of reaction (2) for all momenta combined, in events/10 MeV ((MeV/c)^2. The dotted curve is phase space; the solid curve represents 60% phase space and 40% $N^*\rho$ production.

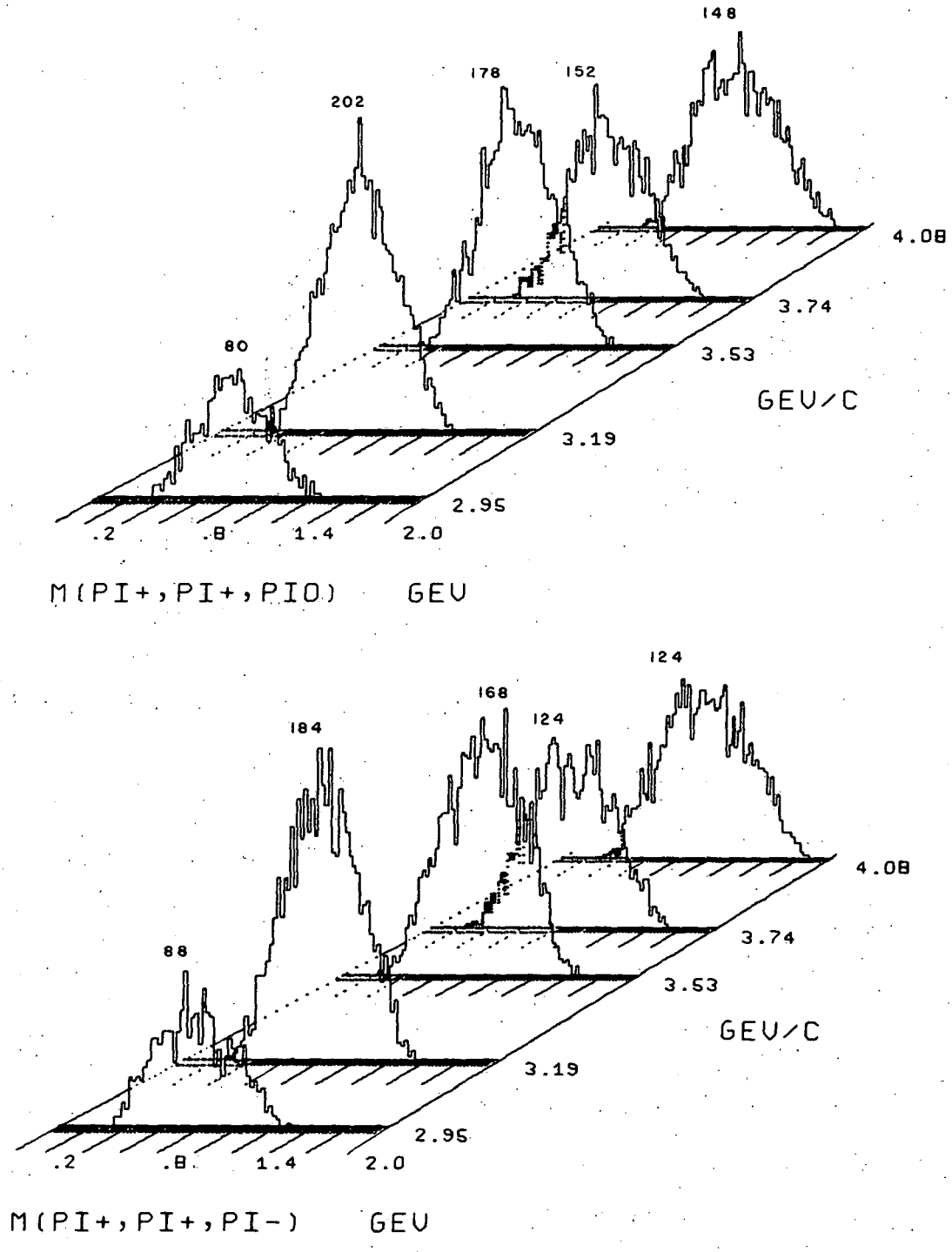

XBL 685-789

Fig. 19. Invariant mass and momentum transfer distributions of reaction (2) for the five momenta, in events/10 MeV ($(MeV/c)^2$), with the number of events in the highest bin being given for each histogram.

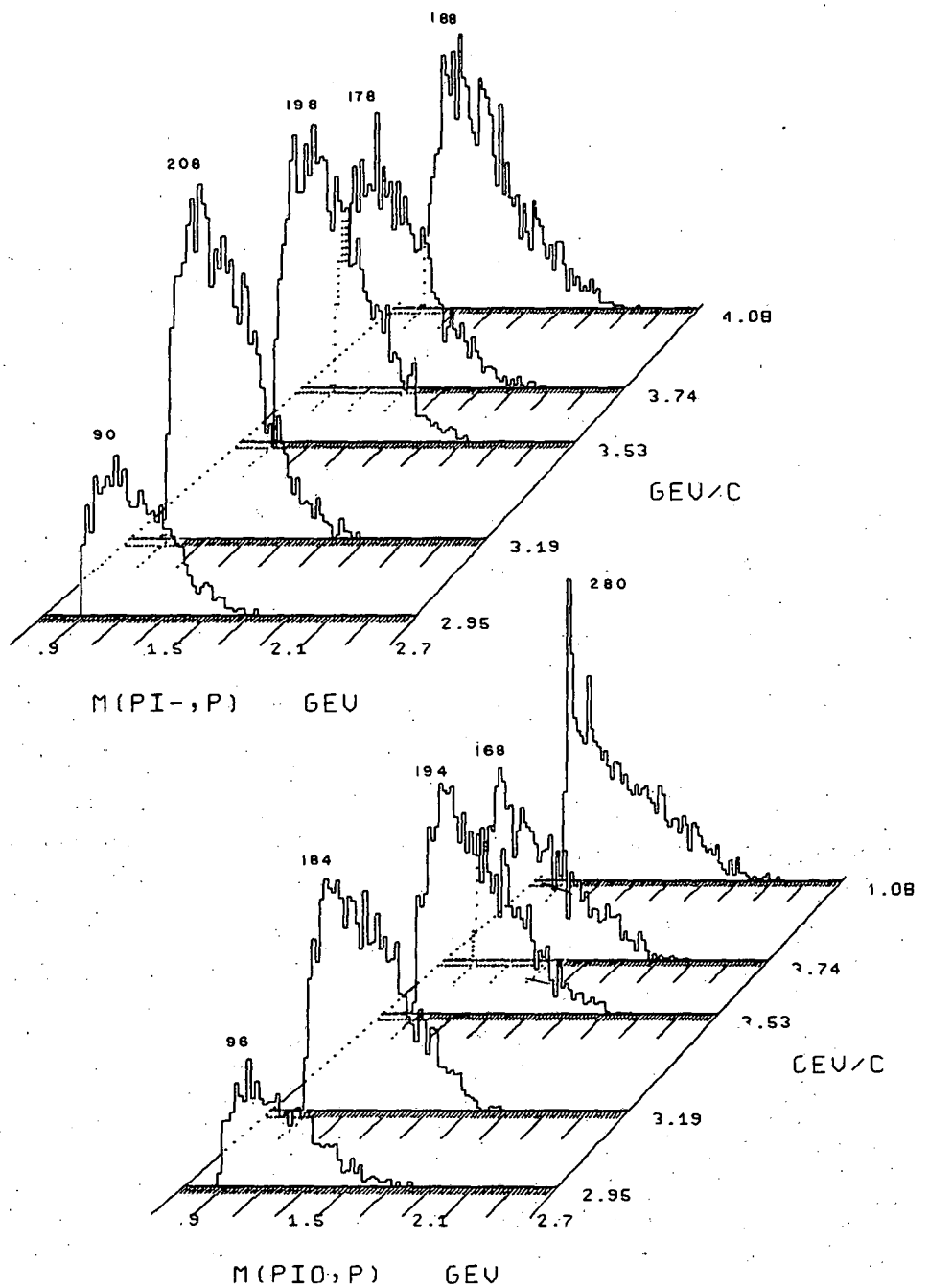

Fig. 20. Invariant mass and momentum transfer distributions of reaction (2) for the five momenta, in events/10 MeV $((MeV/c)^2)$, with the number of events in the highest bin being given for each histogram.

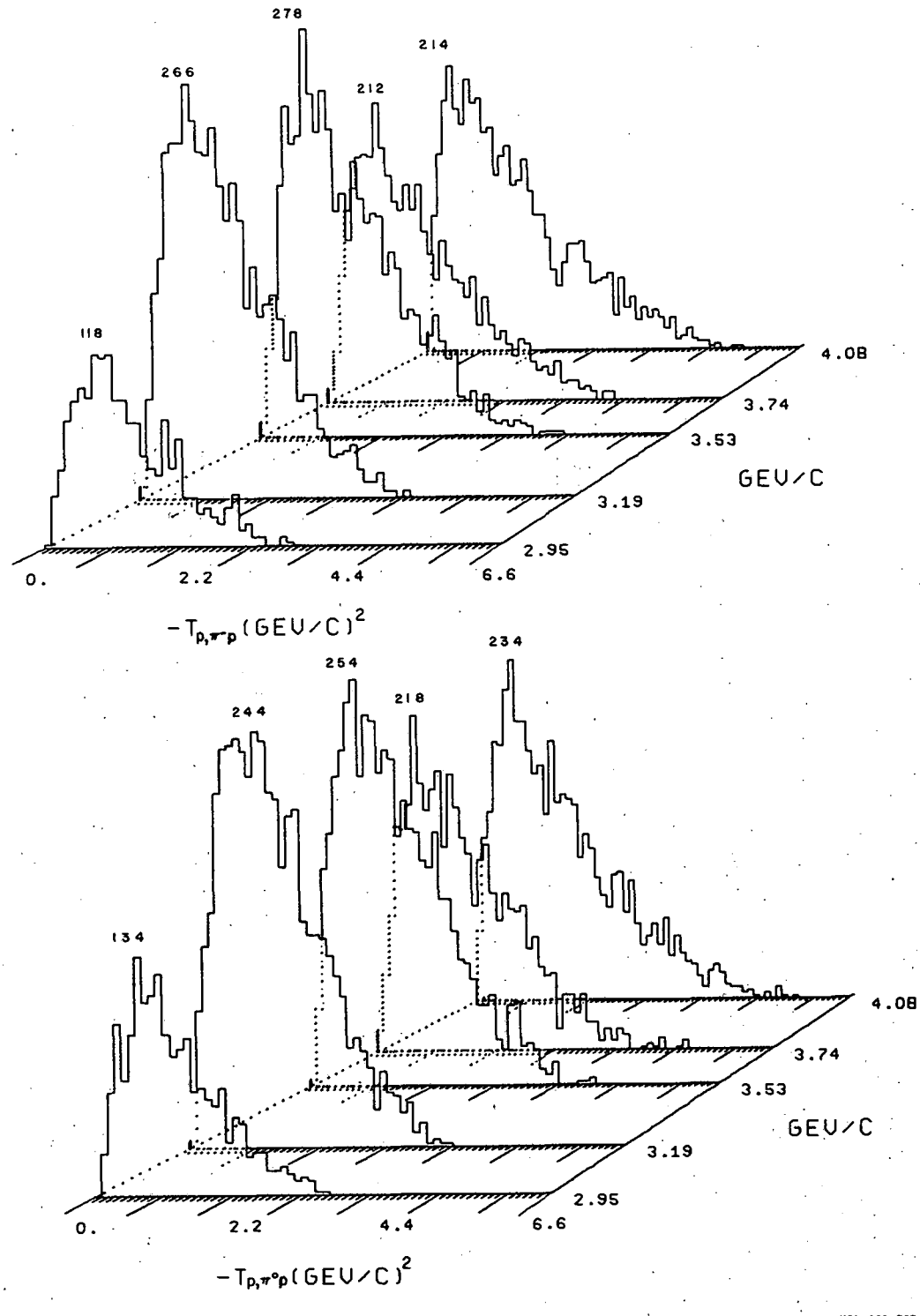

Fig. 21. Invariant mass and momentum transfer distributions of reaction (2) for the five momenta, in events/10 MeV ($(MeV/c)^2$), with the number of events in the highest bin being given for each histogram.

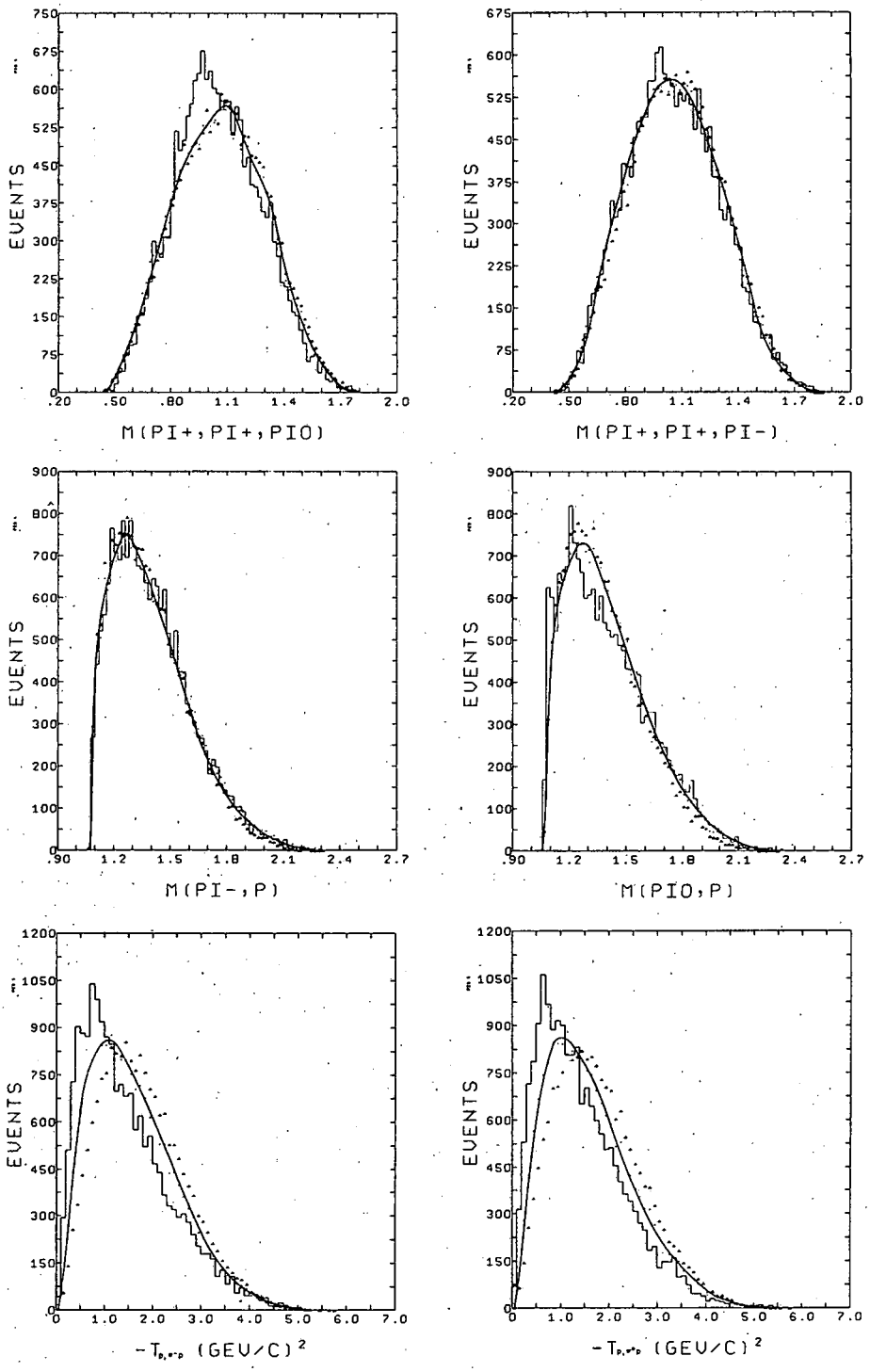

XBL 685-766

Fig. 22. Invariant mass and momentum transfer distributions of reaction (2) for all momenta combined, in events/10 MeV ((MeV/c)^2). The dotted curve is phase space; the solid curve represents 60% phase space and 40% $N^*\rho$ production.

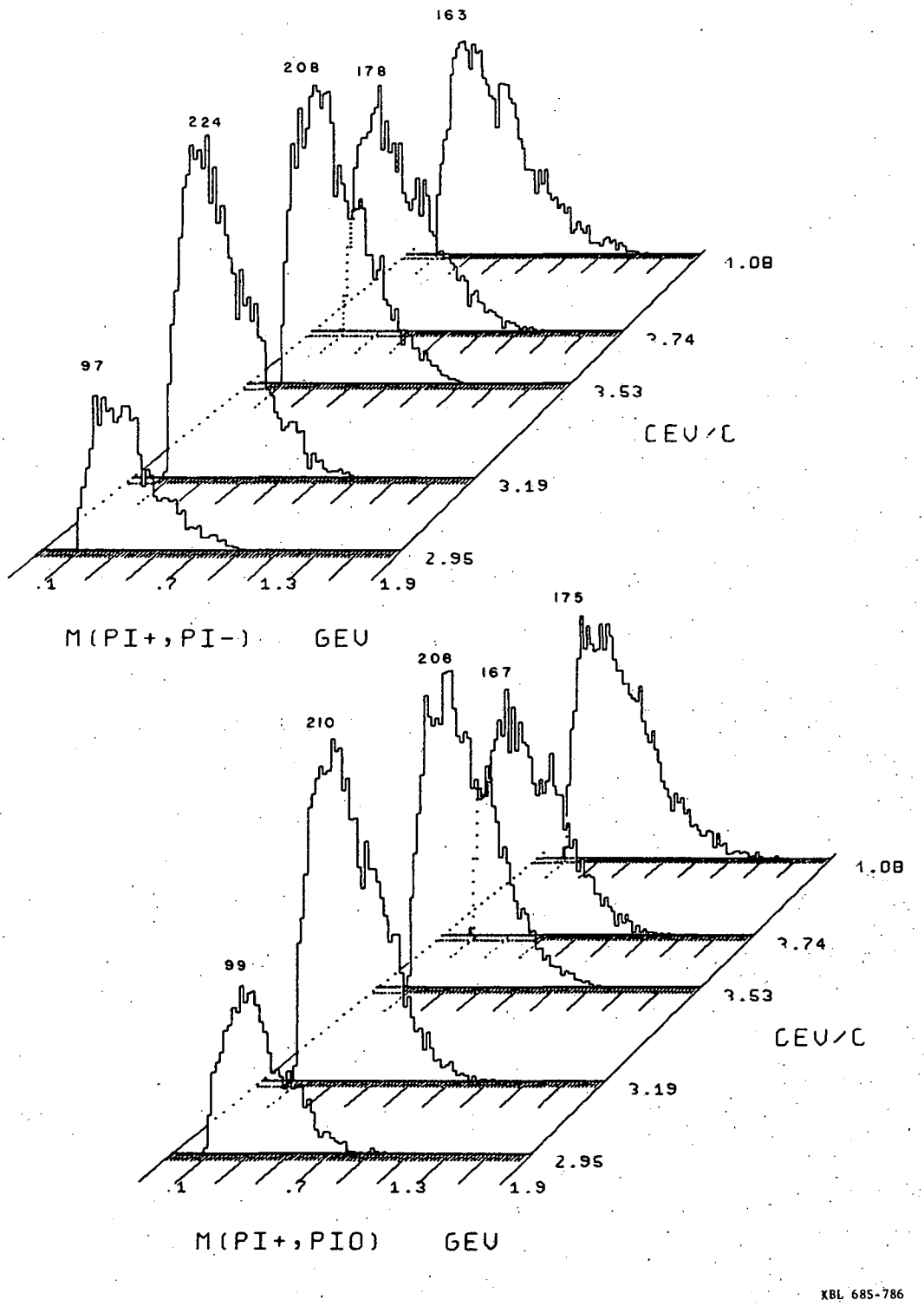

Fig. 23. Invariant mass and momentum transfer distributions of reaction (2) for the five momenta, in events/10 MeV $((MeV/c)^2)$, with the number of events in the highest bin being given for each histogram.

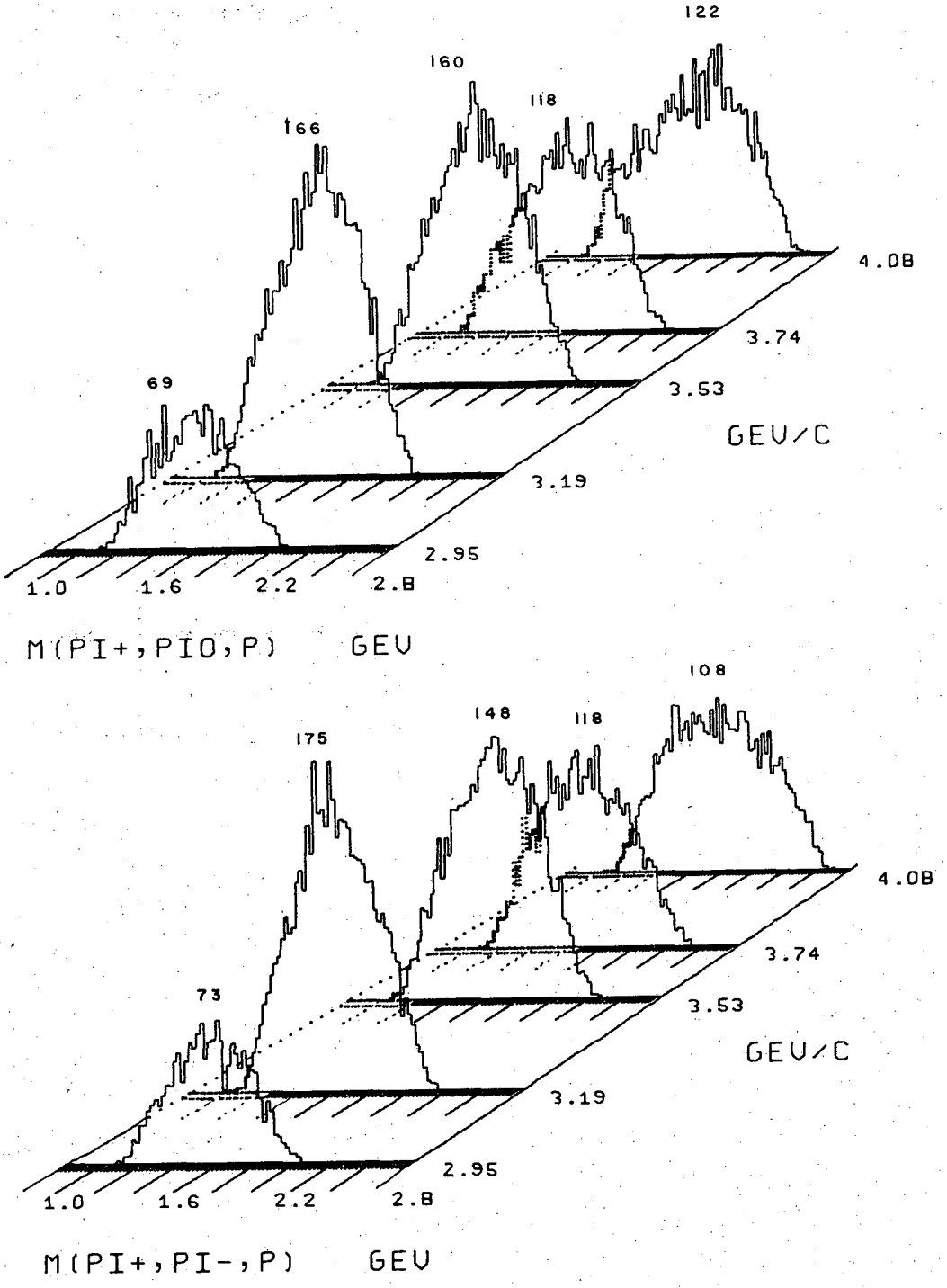

XBL 685-785

Fig. 24. Invariant mass and momentum transfer distributions of reaction (2) for the five momenta, in events/10 MeV ($(MeV/c)^2$), with the number of events in the highest bin being given for each histogram.

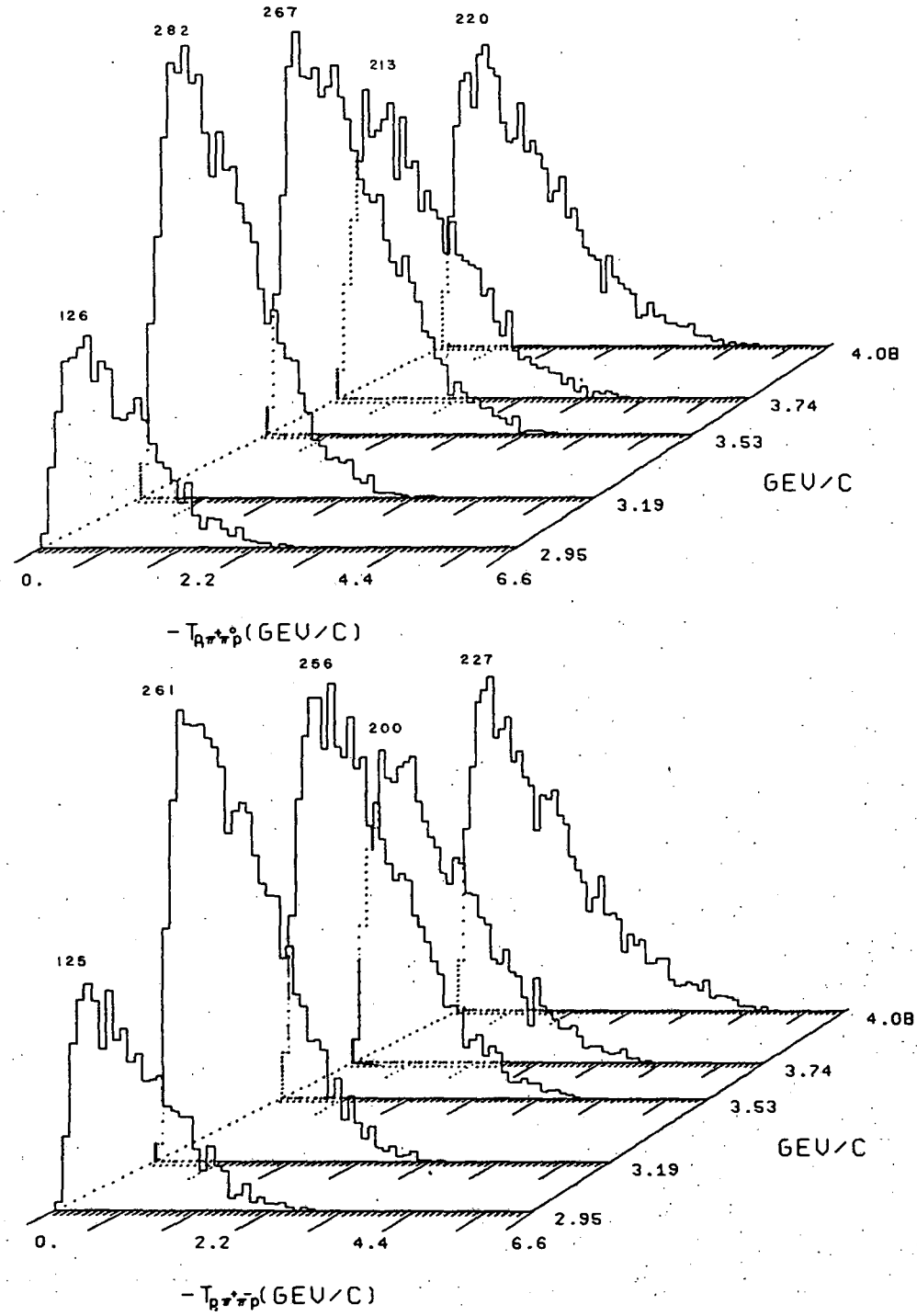

Fig. 25. Invariant mass and momentum transfer distributions of reaction (2) for the five momenta, in events/10 MeV $((MeV/c)^2)$, with the number of events in the highest bin being given for each histogram.

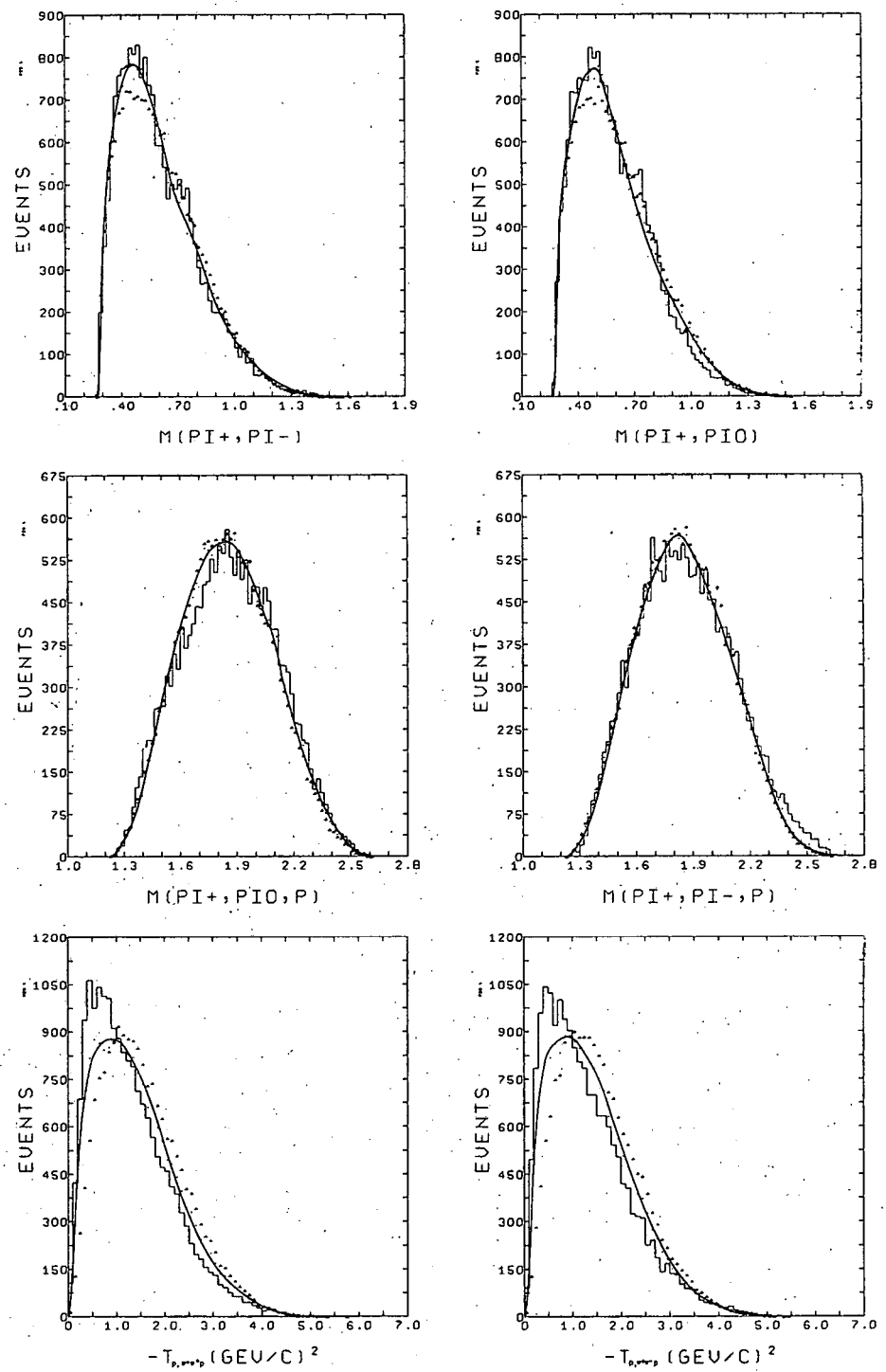

XBL 685-765

Fig. 26. Invariant mass and momentum transfer distributions of reaction (2) for all momenta combined, in events/10 MeV ((MeV/c)^2). The dotted curve is phase space; the solid curve represents 60% phase space and 40% N*ρ production.

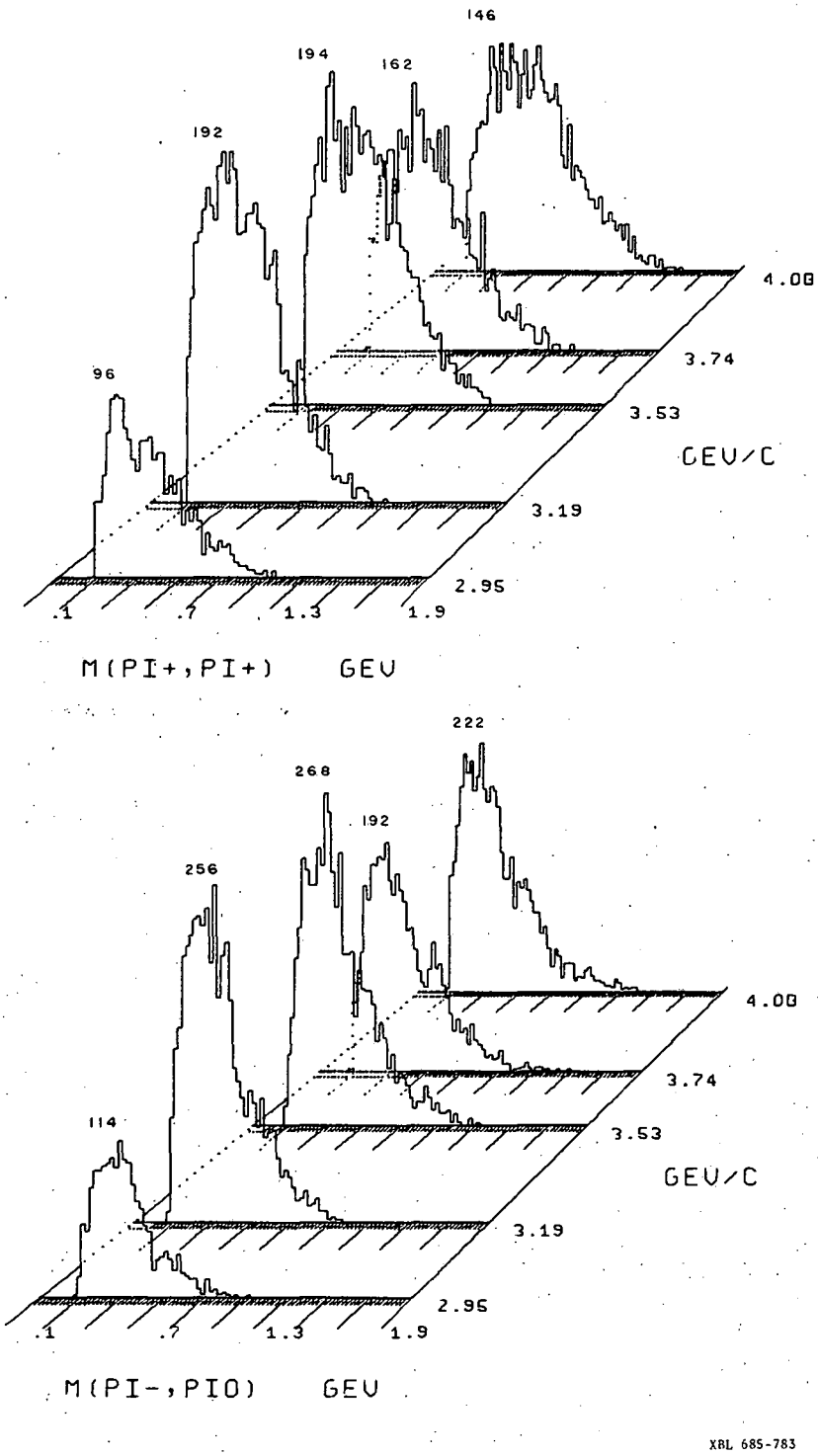

Fig. 27. Invariant mass and momentum transfer distributions of reaction (2) for the five momenta, in events/10 MeV $((MeV/c)^2)$, with the number of events in the highest bin being given for each histogram.

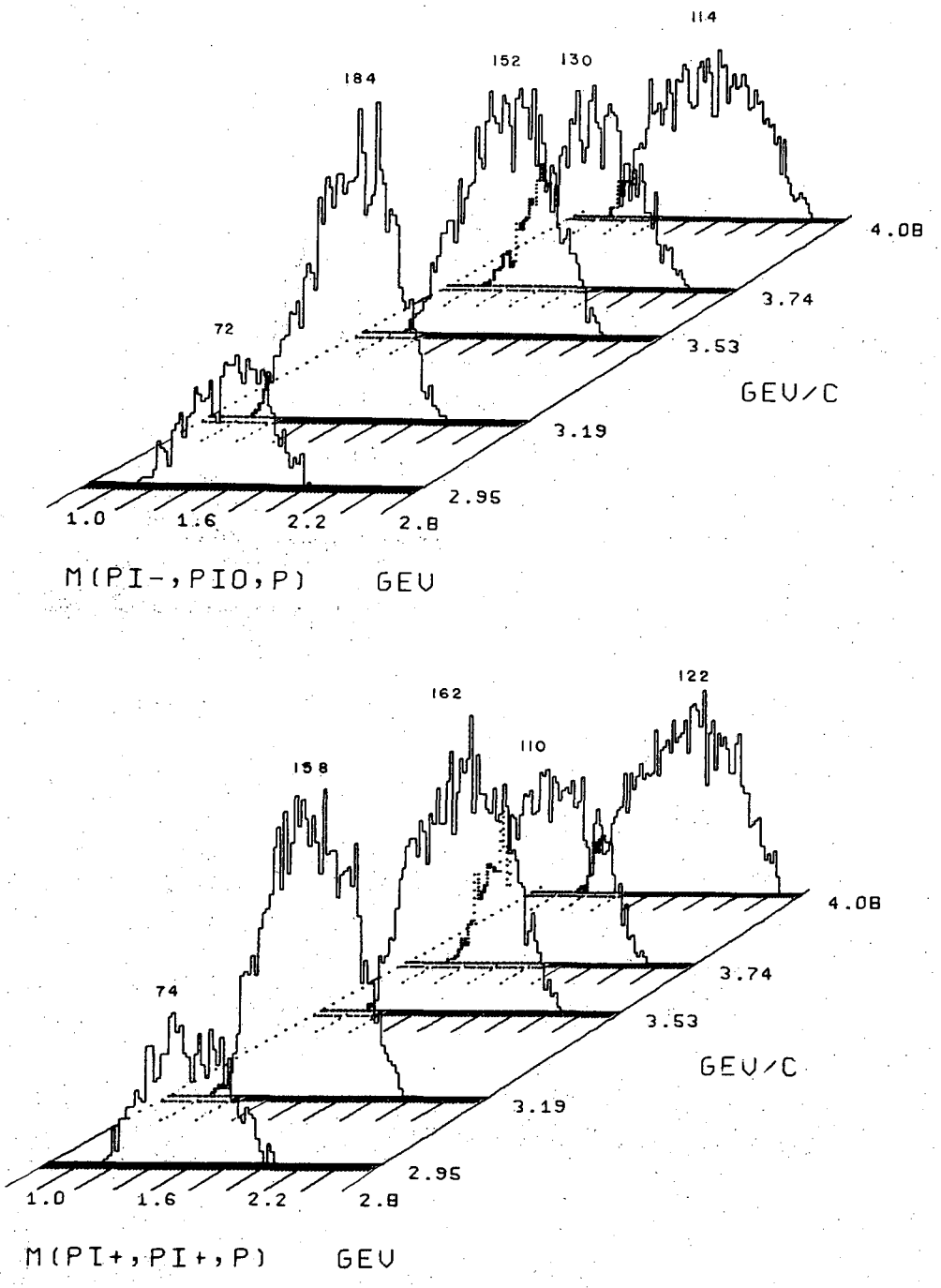

XBL 685-782

Fig. 28. Invariant mass and momentum transfer distributions of reaction (2) for the five momenta, in events/10 MeV $((MeV/c)^2)$, with the number of events in the highest bin being given for each histogram.

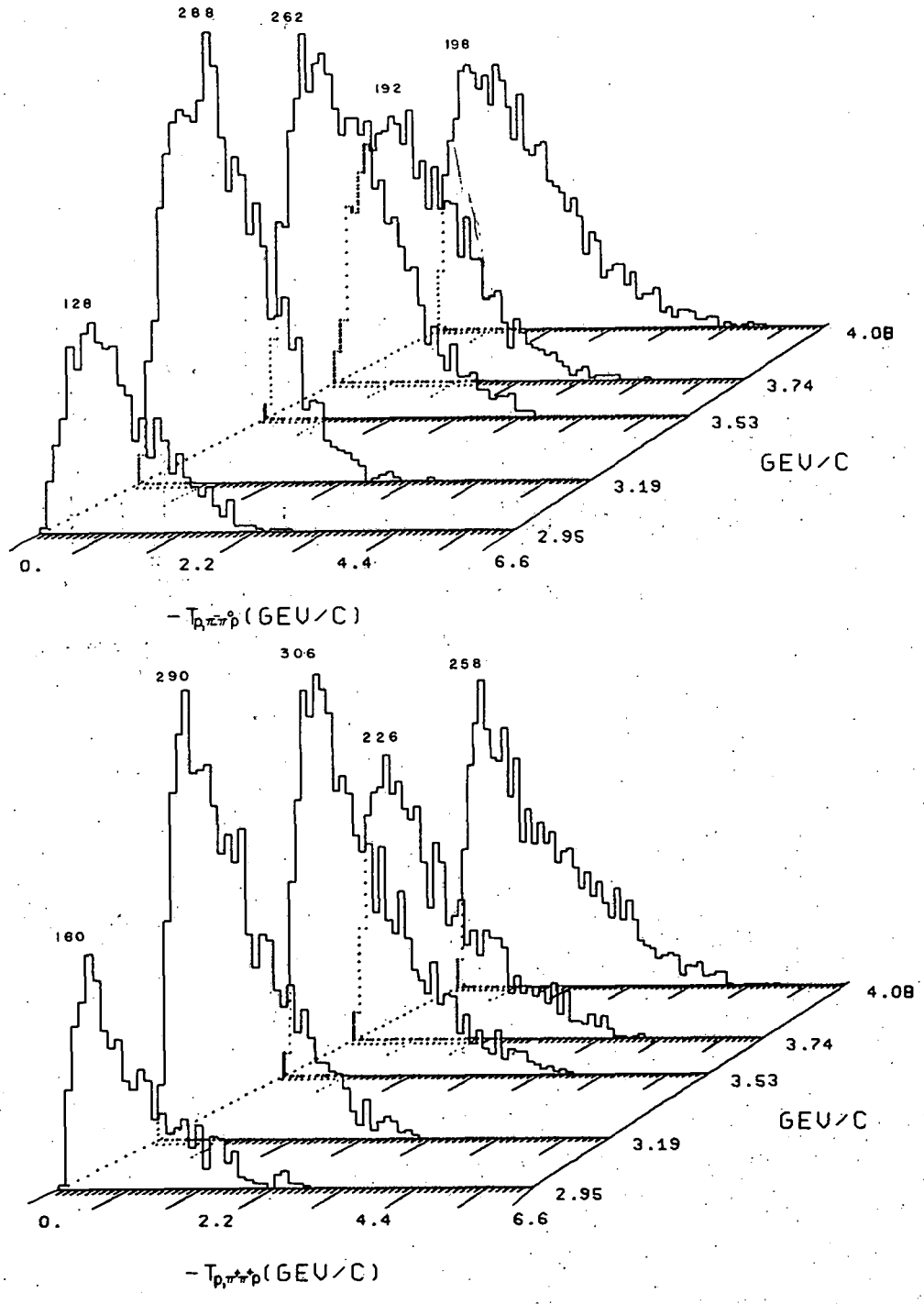

Fig. 29. Invariant mass and momentum transfer distributions of reaction (2) for the five momenta, in events/10 MeV $((MeV/c)^2$, with the number of events in the highest bin being given for each histogram.

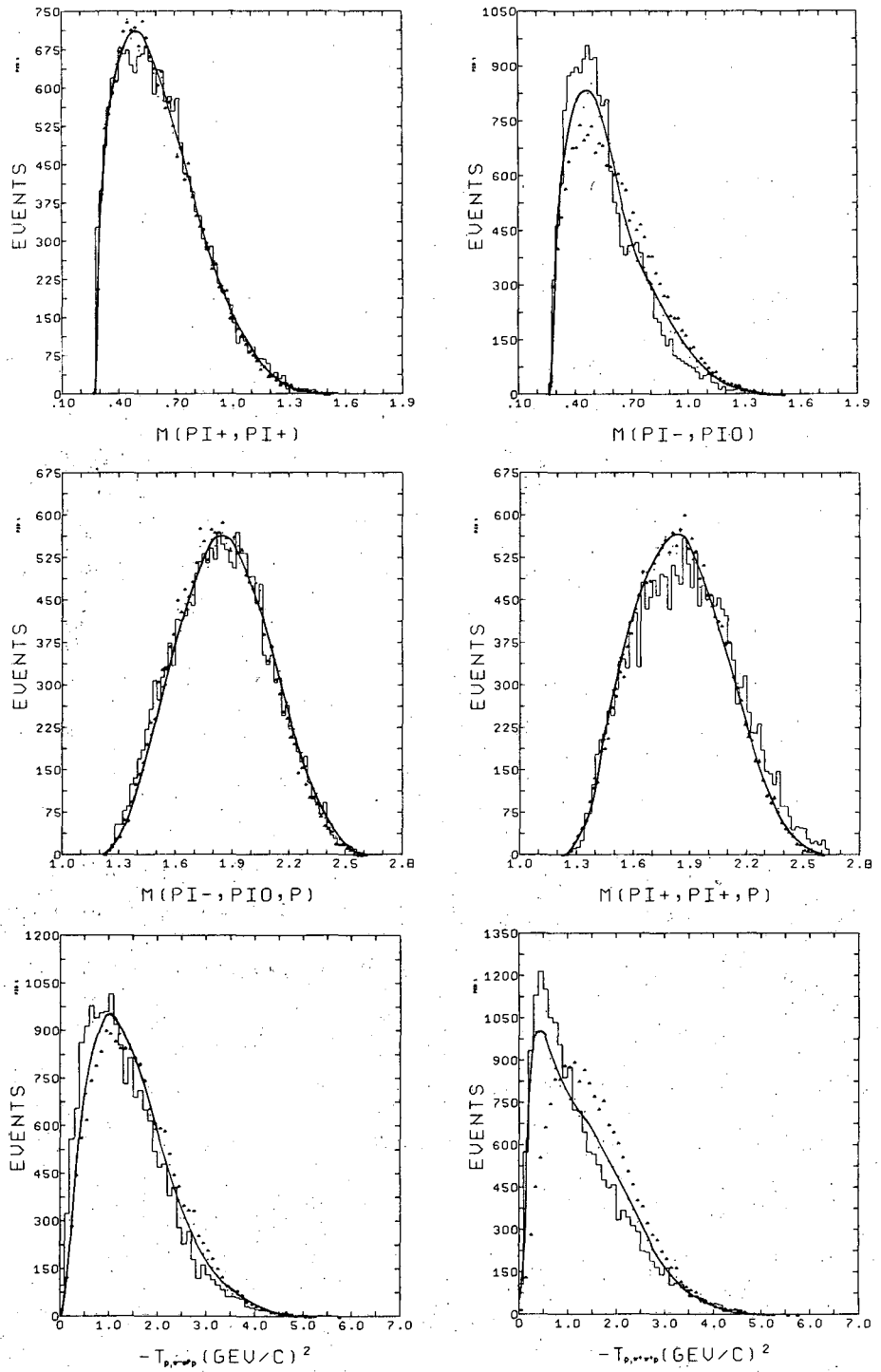

XBL 685-771

Fig. 30. Invariant mass and momentum transfer distributions of reaction (2) for all momenta combined, in events/10 MeV ((MeV/c)^2). The dotted curve is phase space; the solid curve represents 60% phase space and 40% $N^*\rho$ production.

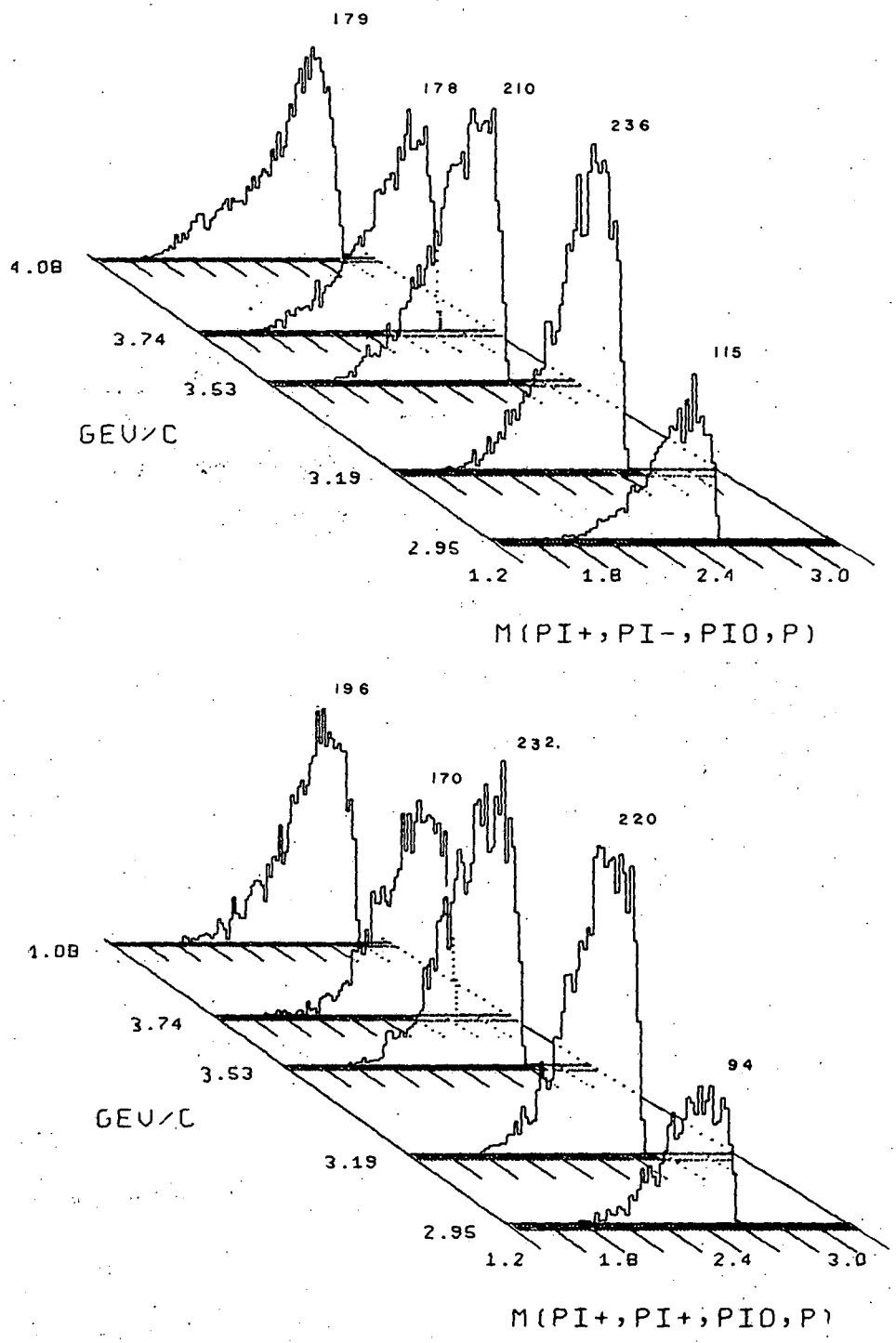

XBL 685-780

Fig. 31. Invariant mass and momentum transfer distributions of reaction (2) for the five momenta, in events/10 MeV ($(MeV/c)^2$), with the number of events in the highest bin being given for each histogram.

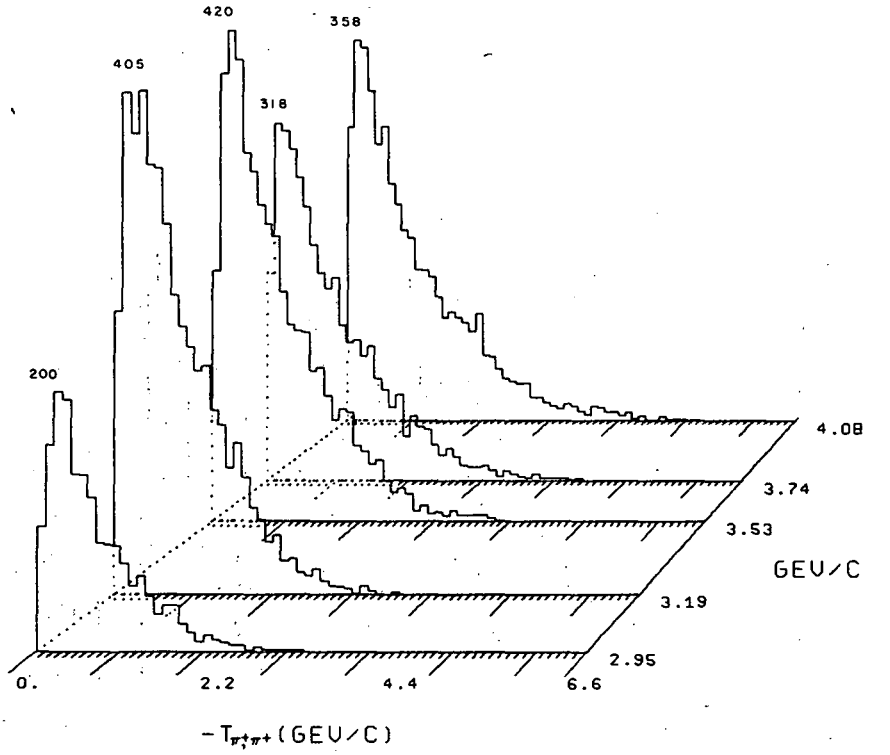

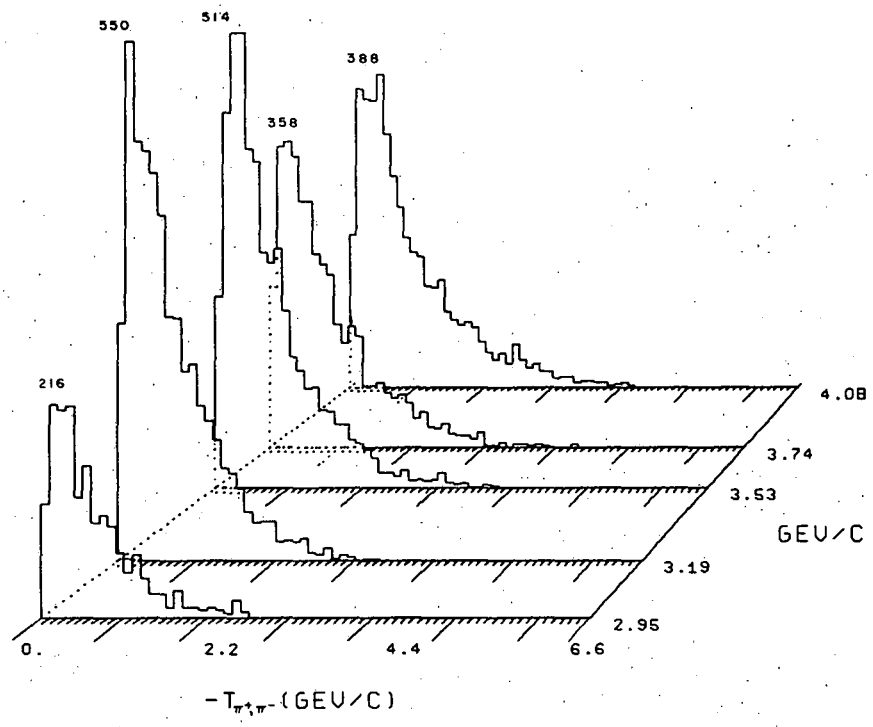

XBL 685-779

Fig. 32. Invariant mass and momentum transfer distributions of reaction (2) for the five momenta, in events/10 MeV $((MeV/c)^2)$, with the number of events in the highest bin being given for each histogram.

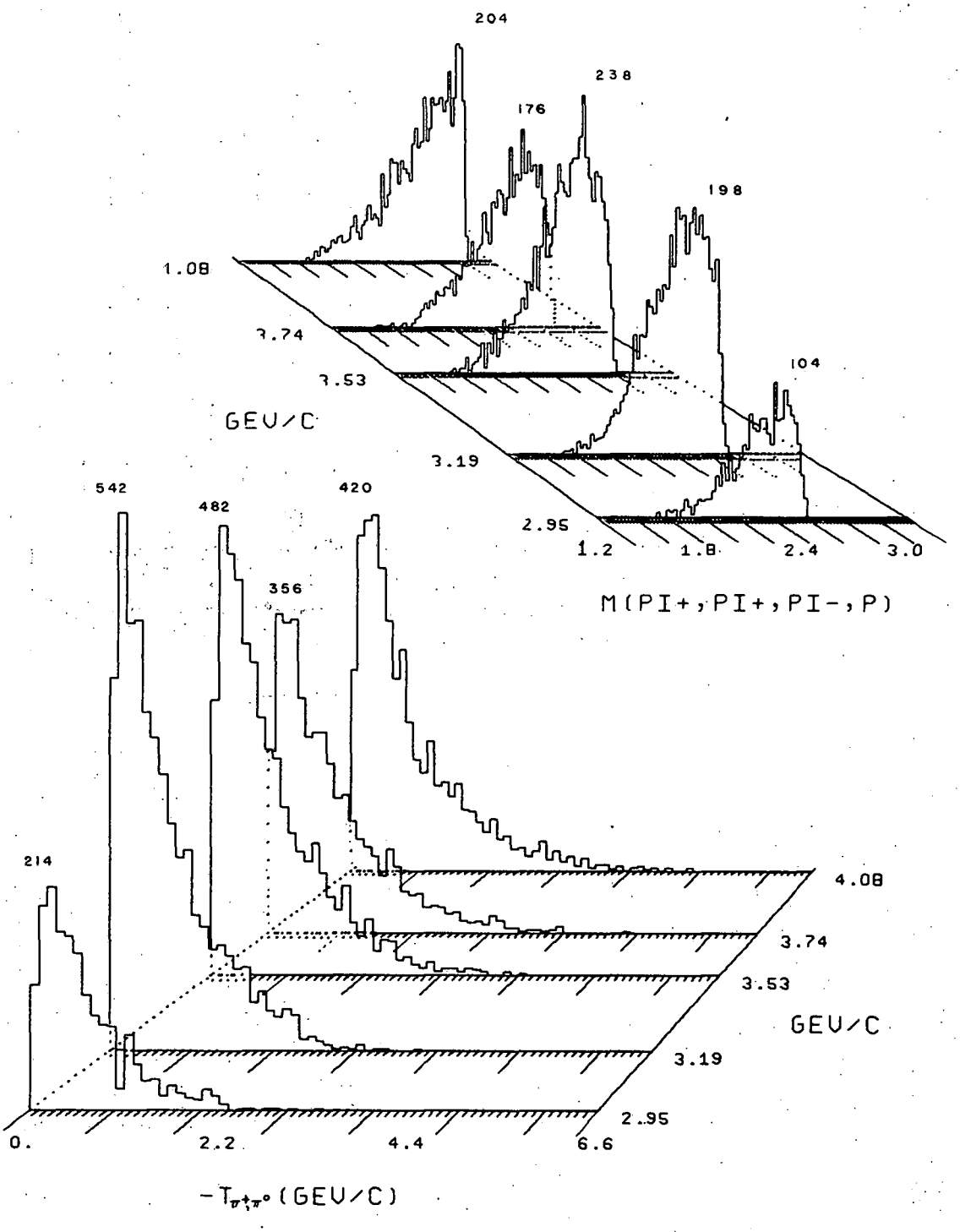

XBL 685-778

Fig. 33. Invariant mass and momentum transfer distributions of reaction (2) for the five momenta, in events/10 MeV ($(MeV/c)^2$), with the number of events in the highest bin being given for each histogram.

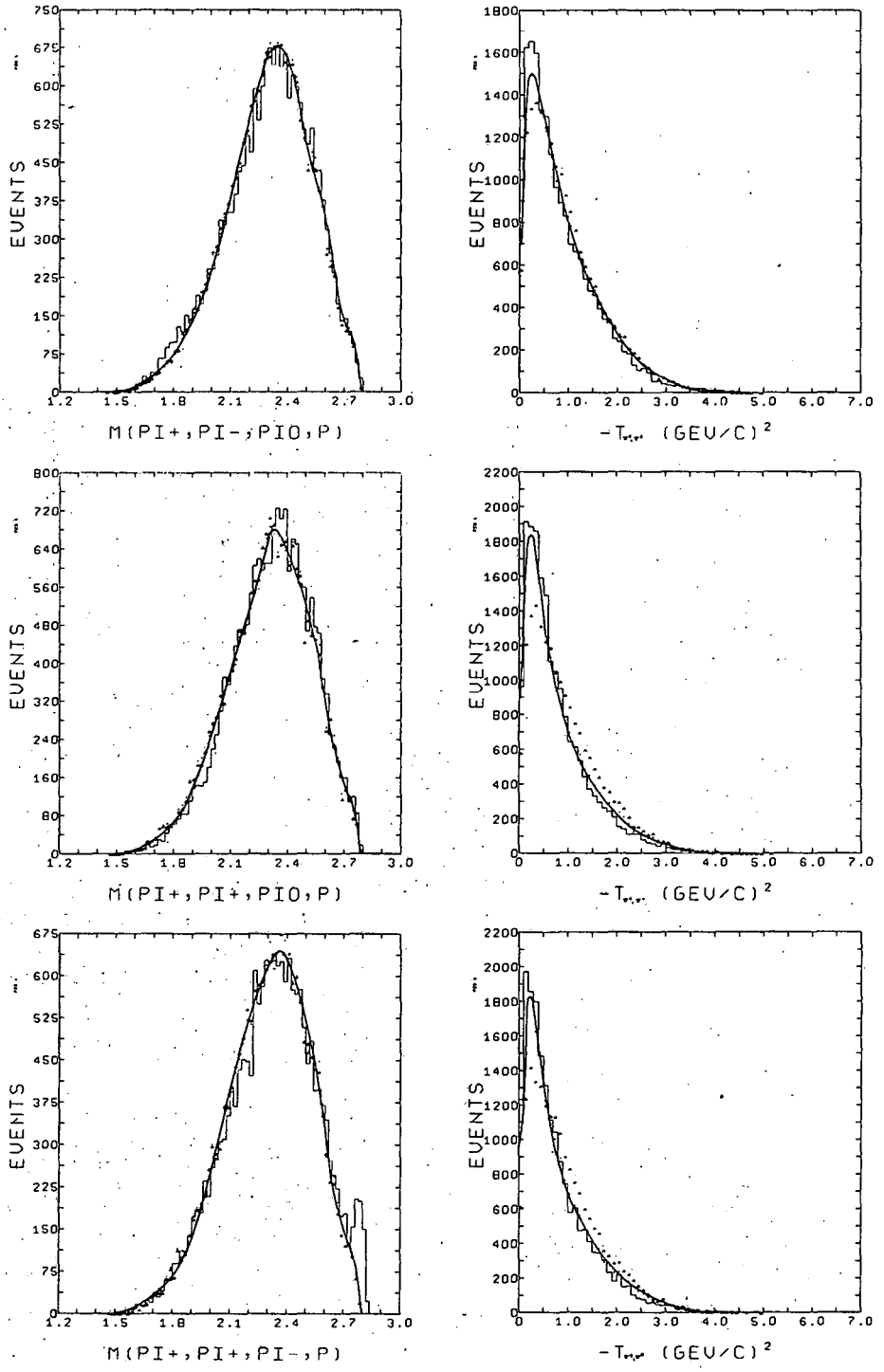

XBL 685-769

Fig. 34. Invariant mass and momentum transfer distributions of reaction (2) for all momenta combined, in events/10 MeV ((MeV/c)^2). The dotted curve is phase space; the solid curve represents 60% phase space and 40% $N^*\rho$ production.

to smear out any structure which might be present, as would the presence of a considerable contamination (~10%) of mis-constraining events. There are 2072 events in the entire event sample with 157, 421, 433, 448, 613 at the five incident π^+ momenta respectively. There are four 2-body and 3-body, and three 4-body combinations possible, and hence eleven invariant mass and seven momentum transfer distributions. They are displayed in Figs. (35-46).

$N^{*-}(1236)$ production in the π^-n invariant mass distribution gives the only very noticeable mass peak, accounting for about 40 ± 8% of the events. Otherwise the distributions seem to follow phase space rather closely. To estimate the percentage of the reaction associated with N^{*-} production, the π^-n invariant mass distribution was fit to (Breit-Wigner + constant) x phase space. (The form of Breit-Wigner used is detailed in Appendix B). Not too surprisingly the results were somewhat unsatisfactory:

1) M_o, Γ_o free--M_o=1.238±.008 GeV, Γ_o=2.59±.046 GeV, $\%N^{*-}$=45±3%, CL≃40%

2) Γ_o=.120 GeV--M_o=1.215±.003 GeV, $\%N^{*-}$=35±2%, CL≃1.4%

Different conventional forms of the energy dependent width of the B.W. were used and gave similar results, none simultaneously yielding values near those expected for both M_o and Γ_o --i.e. M_o=1.244 GeV, Γ_o=.120 GeV.

Forward peaking in the t distributions is less prominent than for the other two reactions. Only the $-t_{p,\pi^-n}$ and $-t_{p,n}$ distributions are appreciably different from phase space; and their peaking is not much greater than that given by phase space weighted by e^t. Of course peripheralism in most of the other -t distributions would be obscured because of the identical-π^+ ambiguity, as mentioned above.

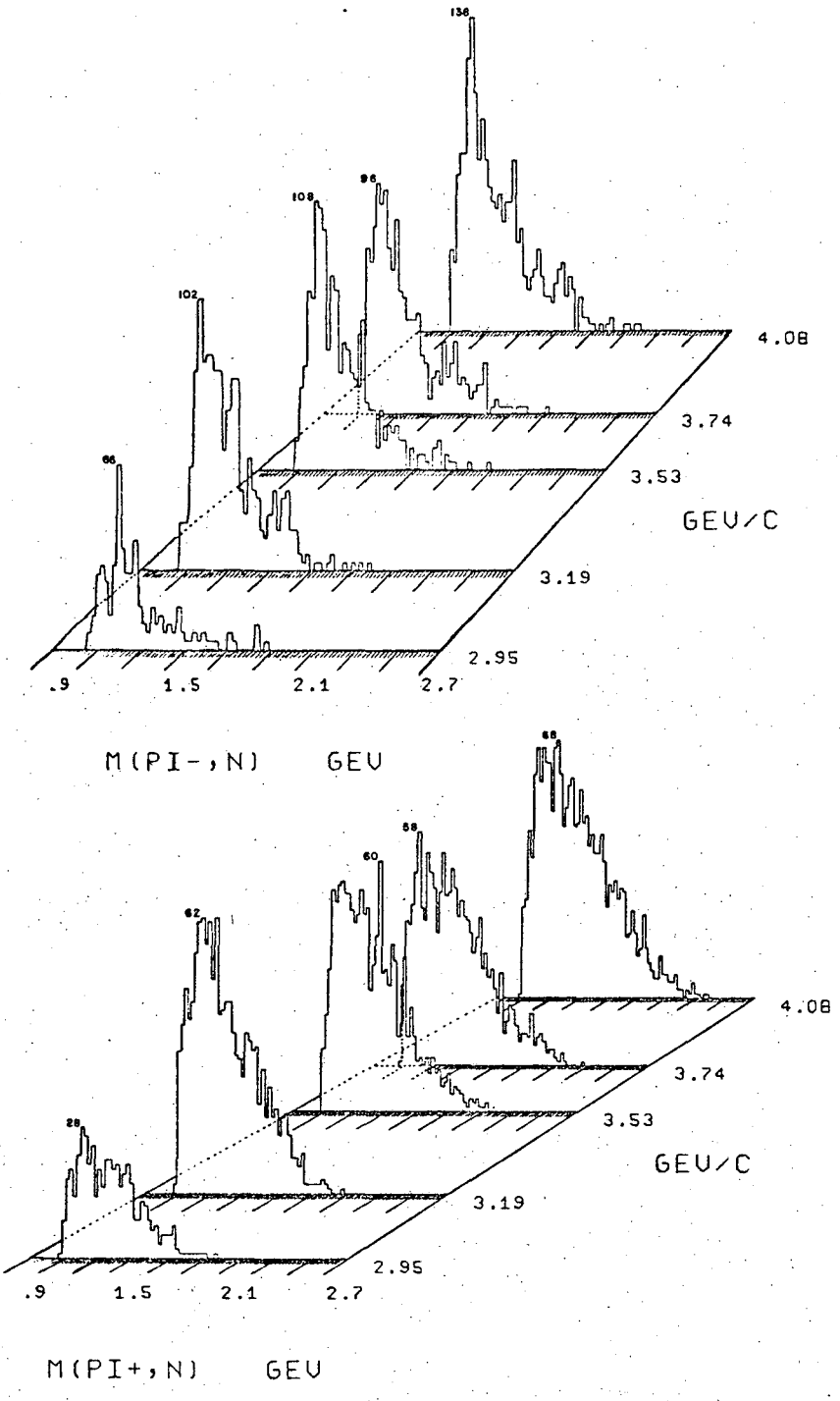

Fig. 35. Invariant mass and momentum transfer distributions of reaction (3) for the five momenta, in events/10 MeV ($(MeV/c)^2$), with the number of events in the highest bin being given for each histogram.

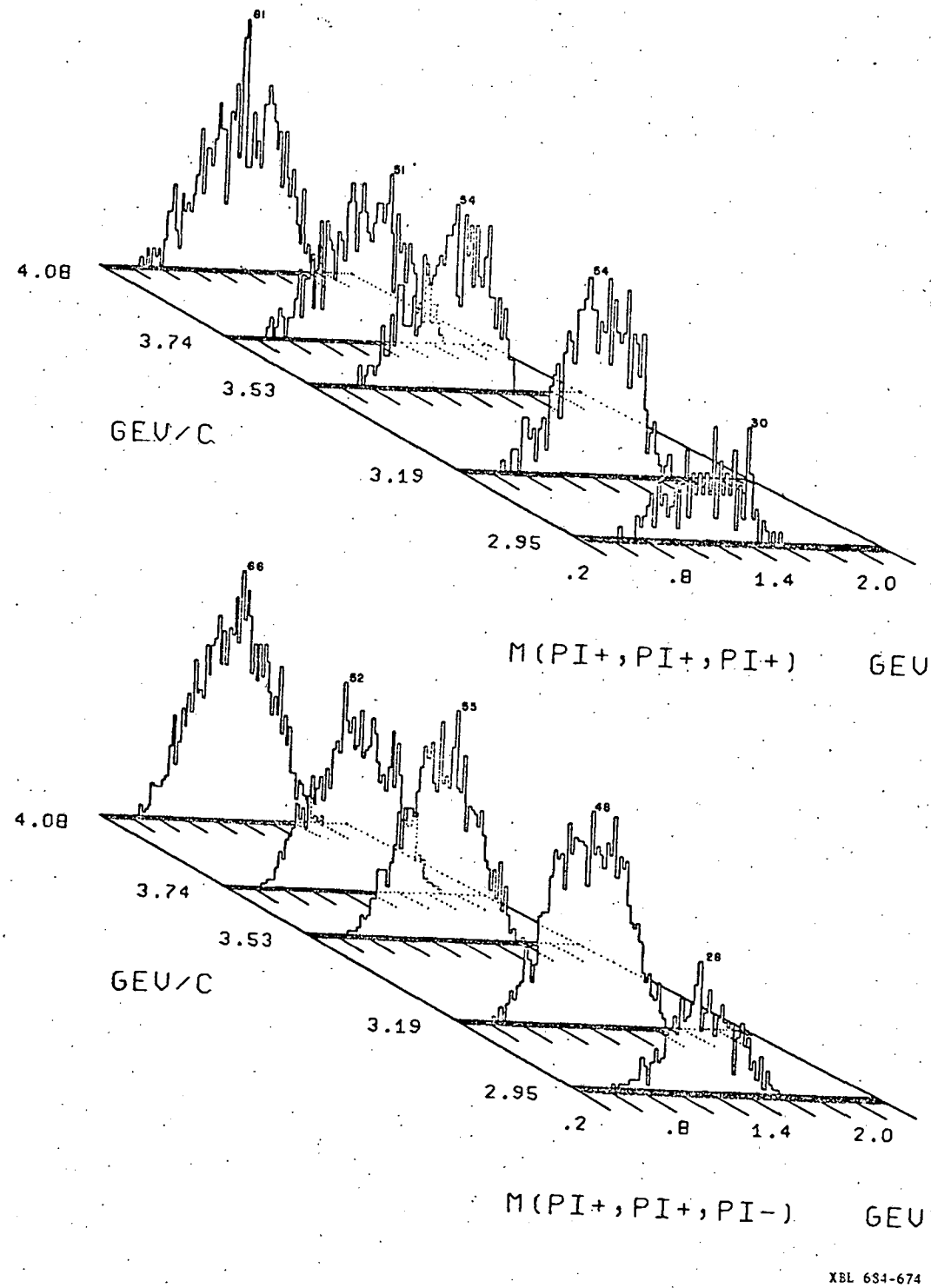

XBL 6S4-674

Fig. 36. Invariant mass and momentum transfer distributions of reaction (3) for the five momenta, in events/10 MeV ((MeV/c)^2), with the number of events in the highest bin being given for each histogram.

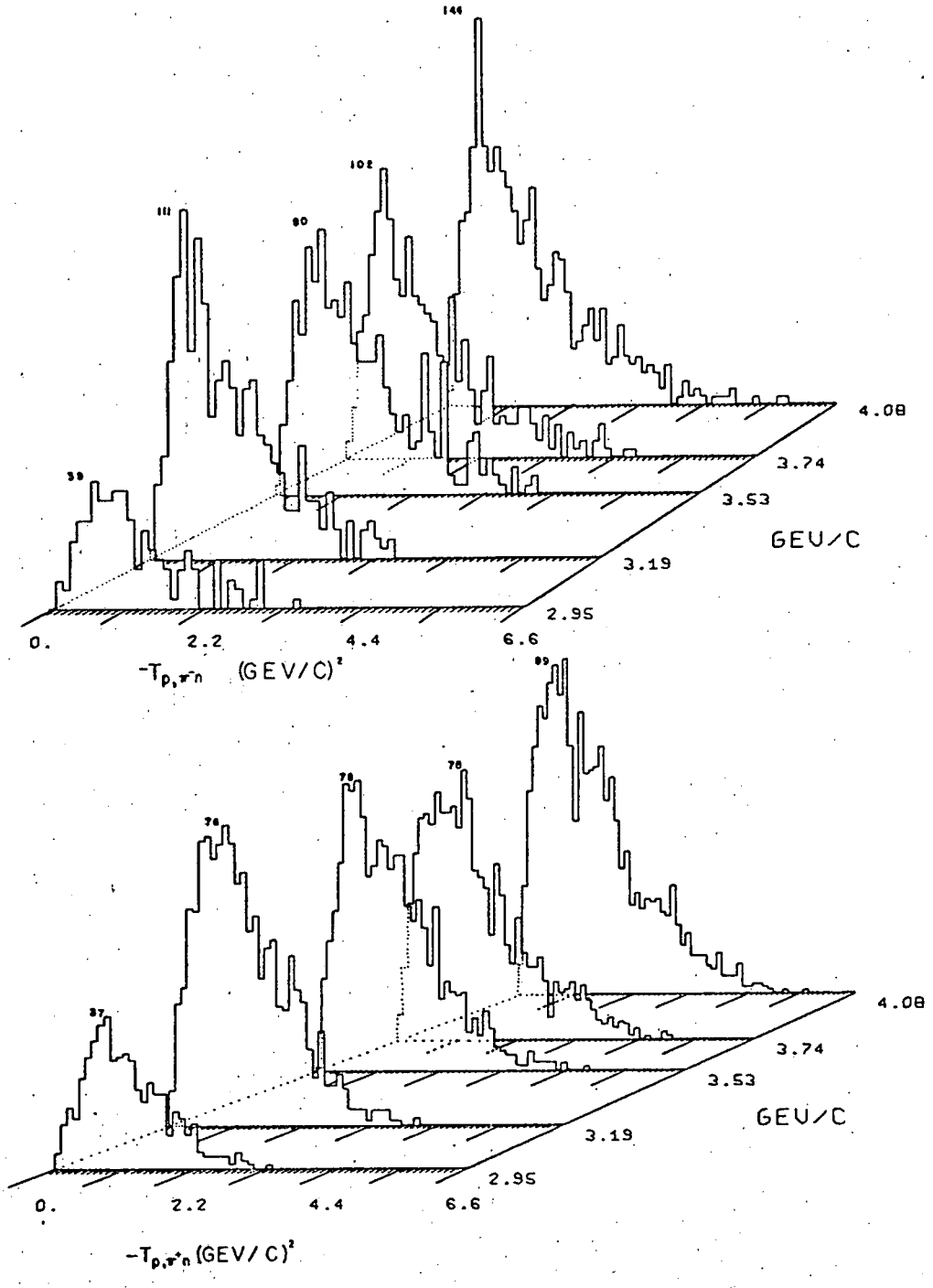

Fig. 37. Invariant mass and momentum transfer distributions of reaction (3) for the five momenta, in events/10 MeV ((MeV/c)^2), with the number of events in the highest bin being given for each histogram.

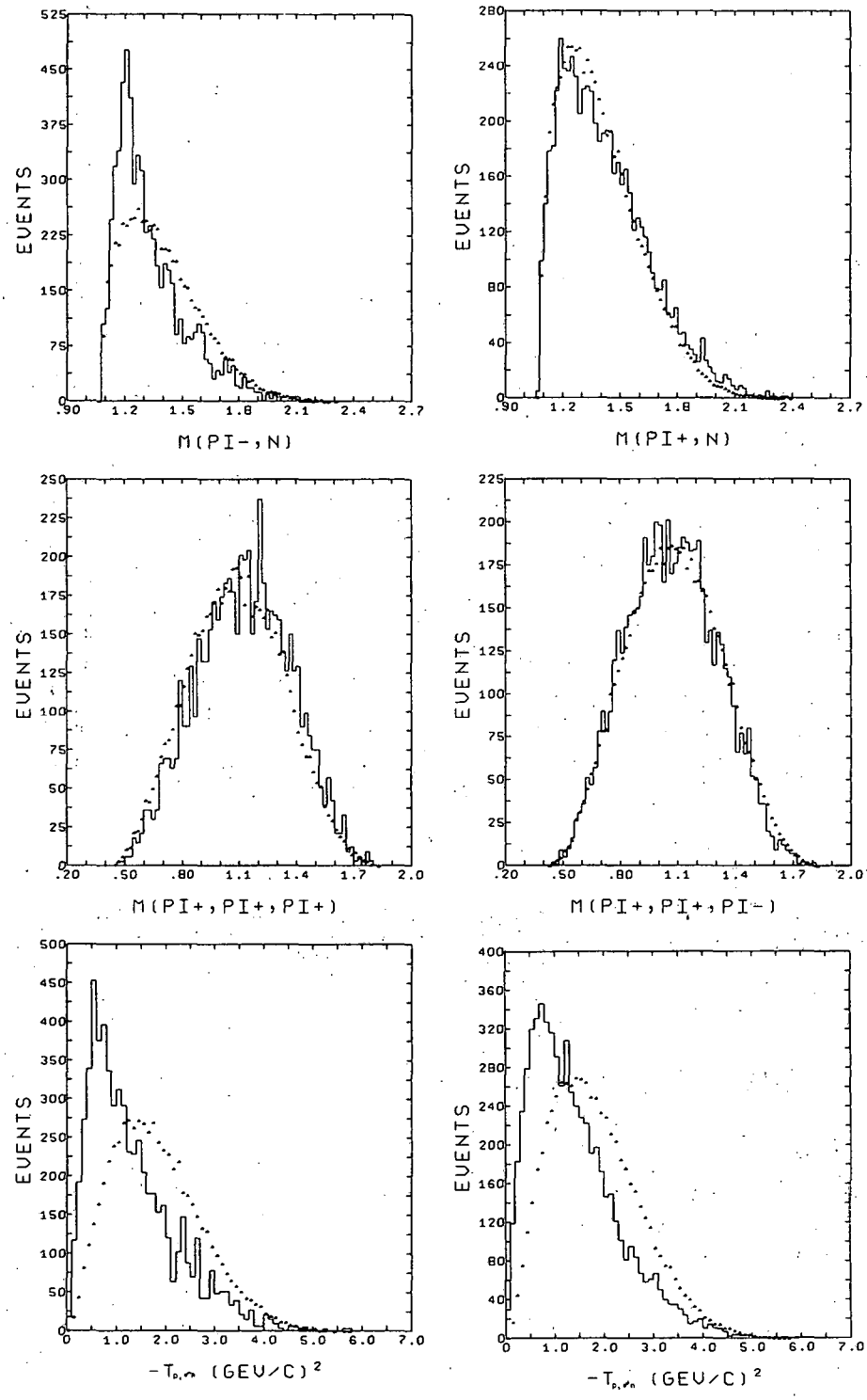

XBL 684-690

Fig. 38. Invariant mass and momentum transfer distributions of reaction (3) for all momenta combined, in events/10 MeV ((MeV/c)^2). The dotted curve is phase space.

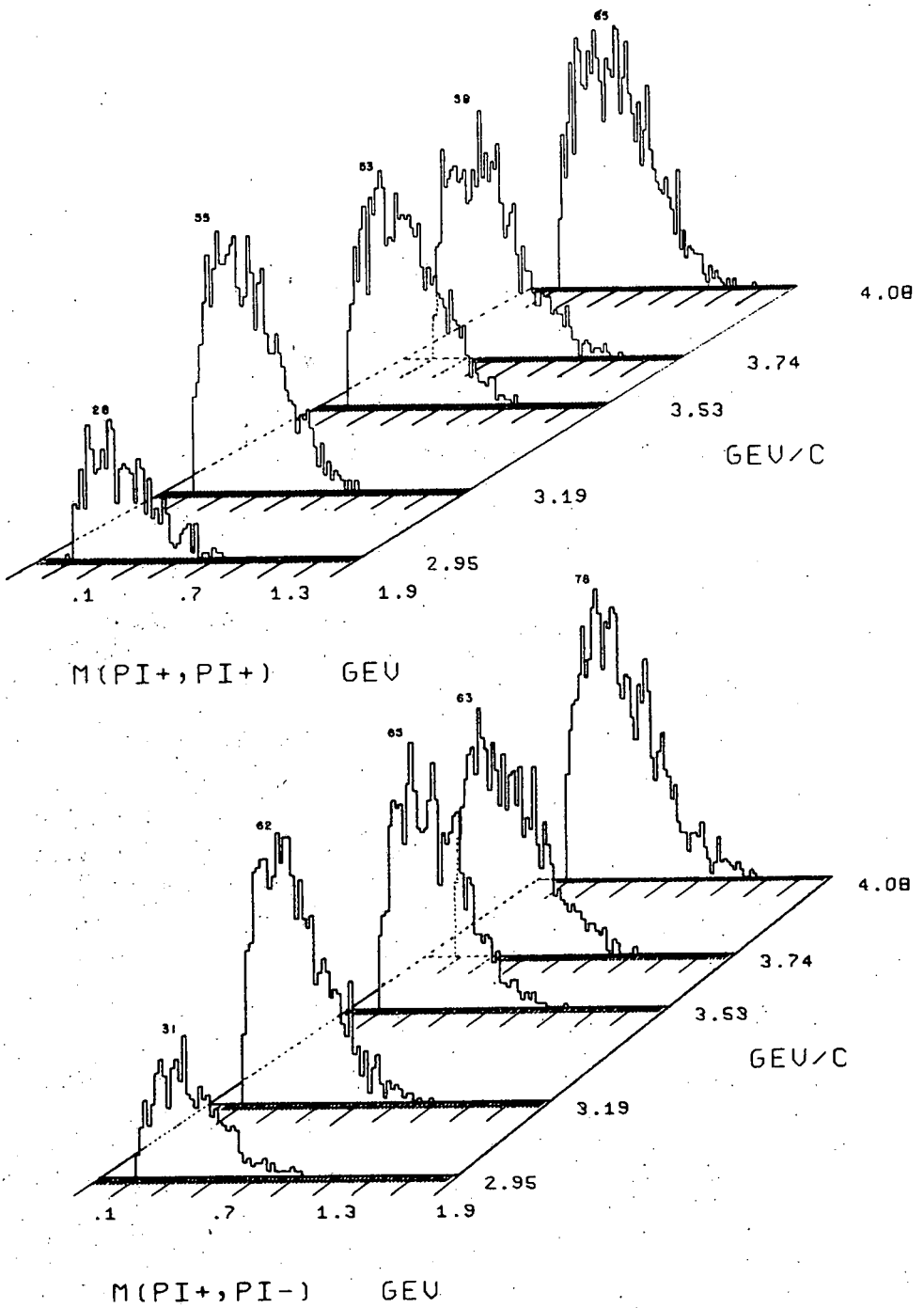

XBL 684-676

Fig. 39. Invariant mass and momentum transfer distributions of reaction (3) for the five momenta, in events/10 MeV ($(MeV/c)^2$), with the number of events in the highest bin being given for each histogram.

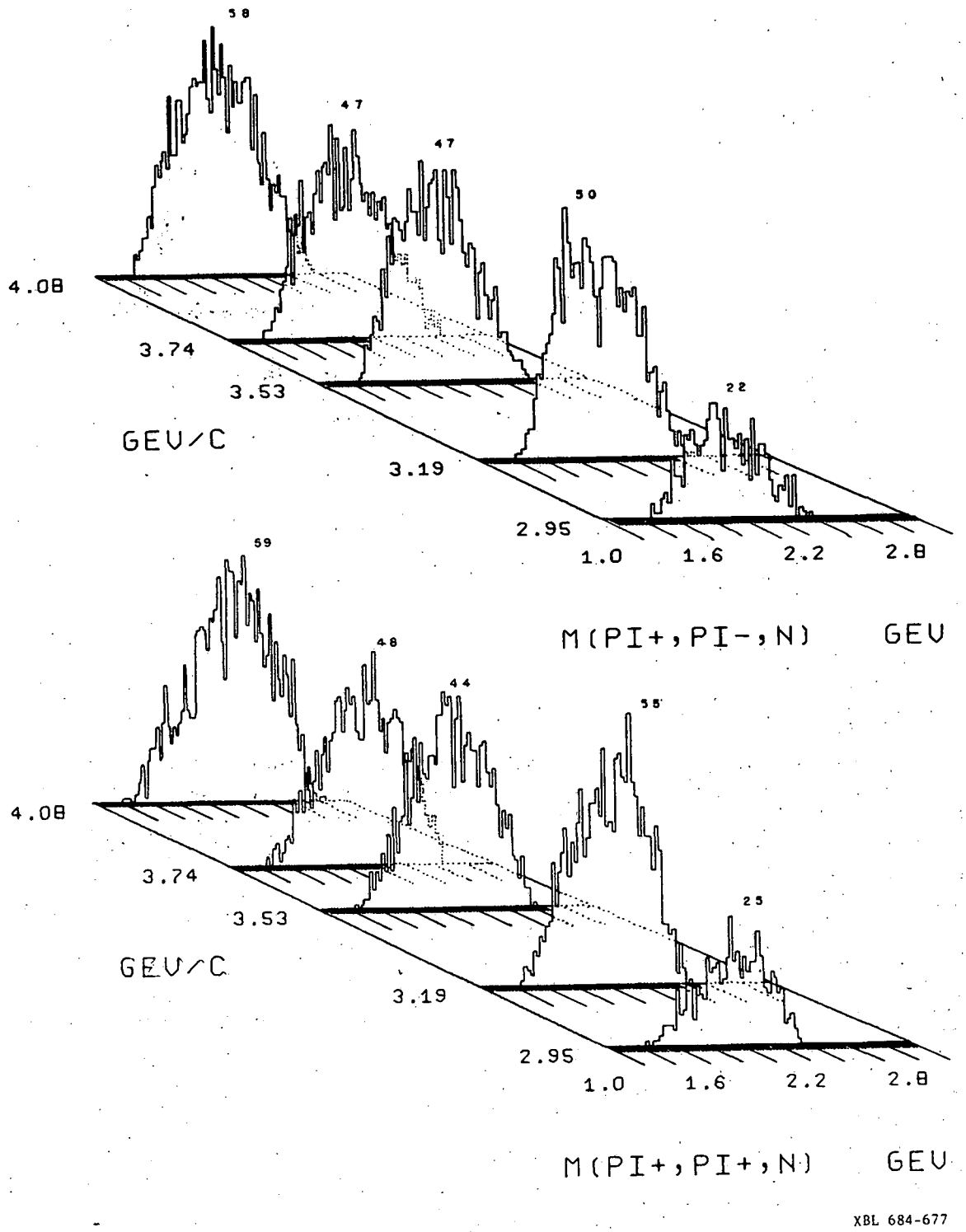

XBL 684-677

Fig. 40. Invariant mass and momentum transfer distributions of reaction (3) for the five momenta, in events/10 MeV ($(MeV/c)^2$), with the number of events in the highest bin being given for each histogram.

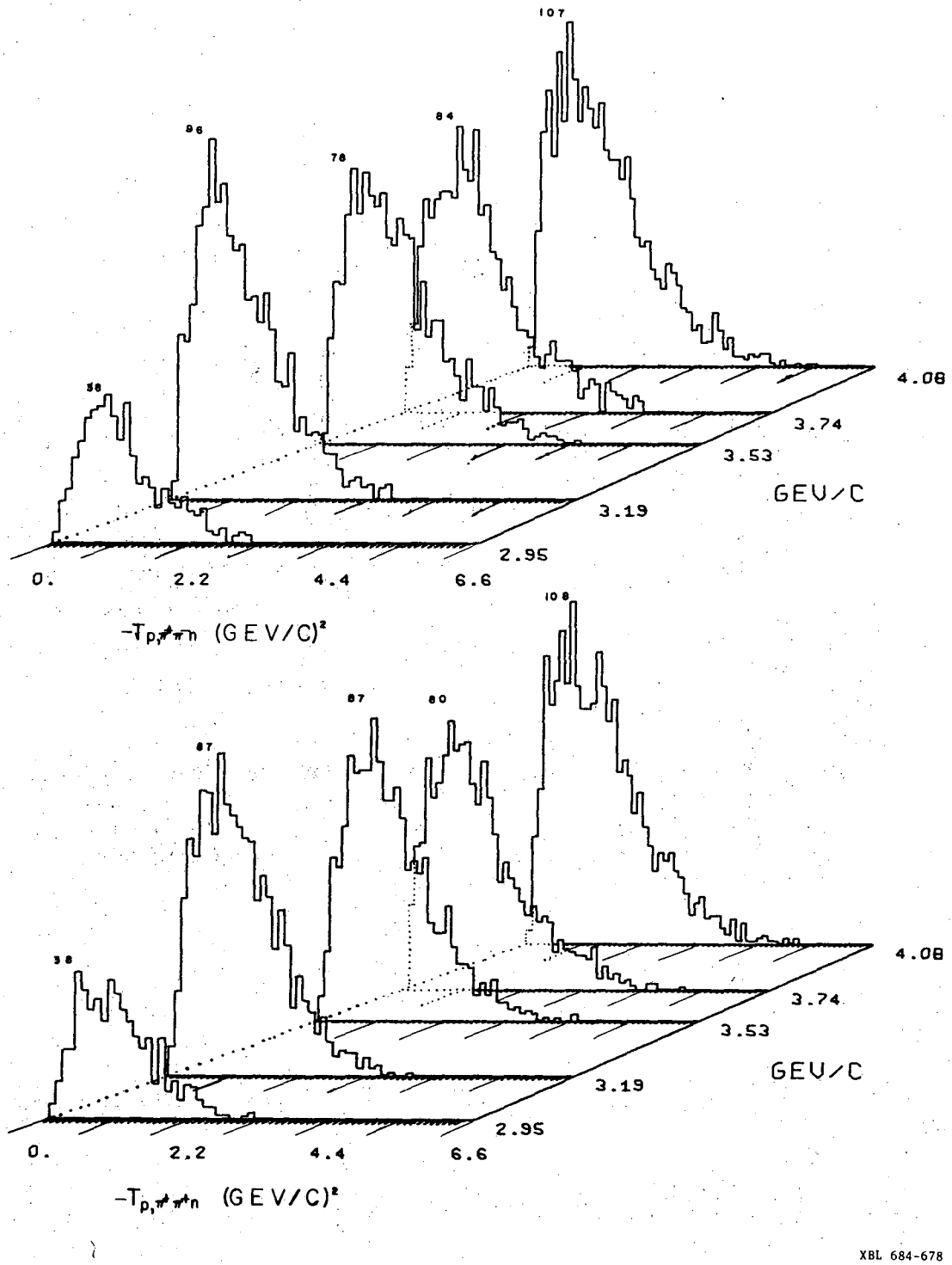

XBL 684-678

Fig. 41. Invariant mass and momentum transfer distributions of reaction (3) for the five momenta, in events/10 MeV ((MeV/c)^2), with the number of events in the highest bin being given for each histogram.

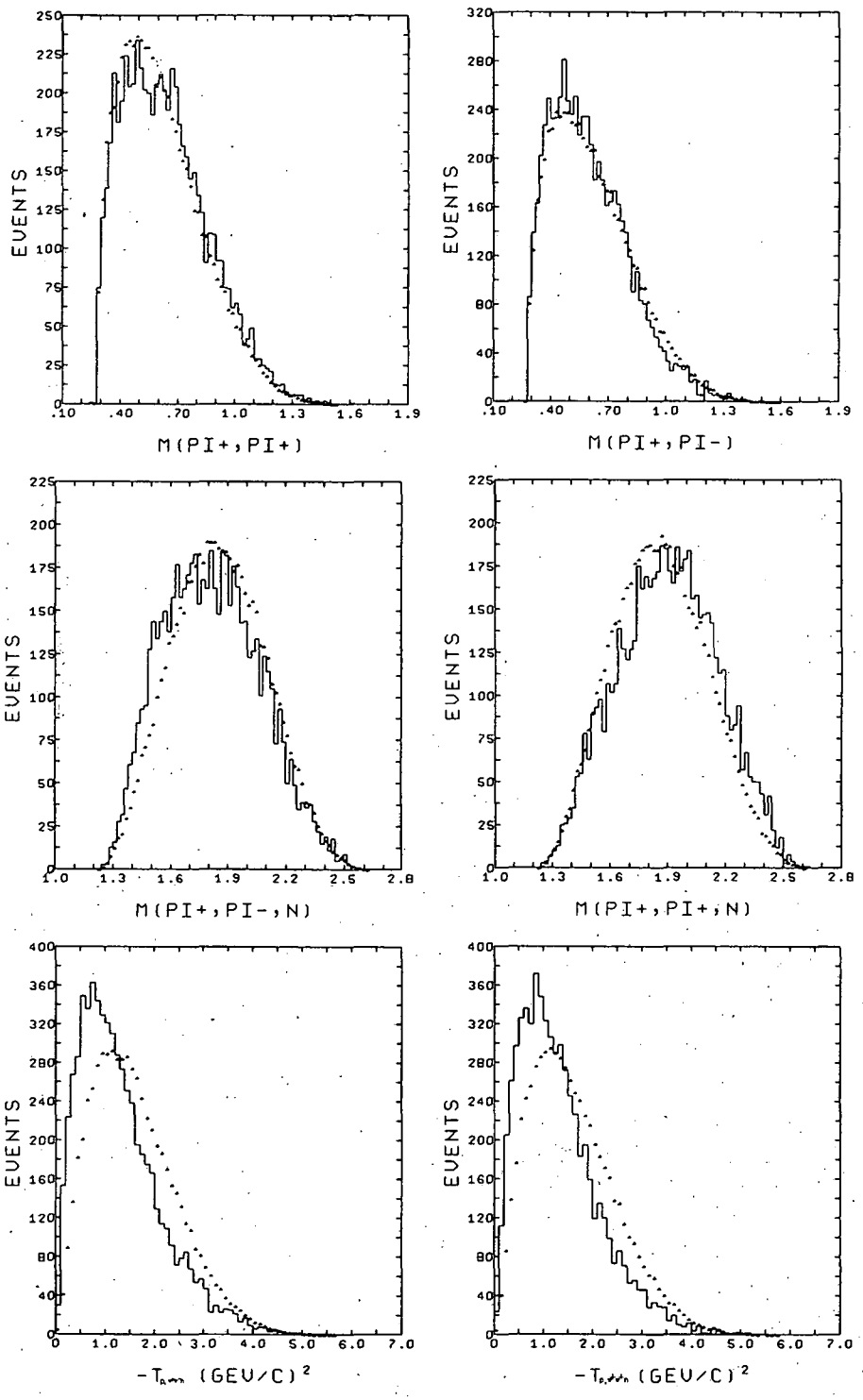

XBL 684-691

Fig. 42. Invariant mass and momentum transfer distributions of reaction (3) for all momenta combined, in events/10 MeV ($(MeV/c)^2$). The dotted curve is phase space.

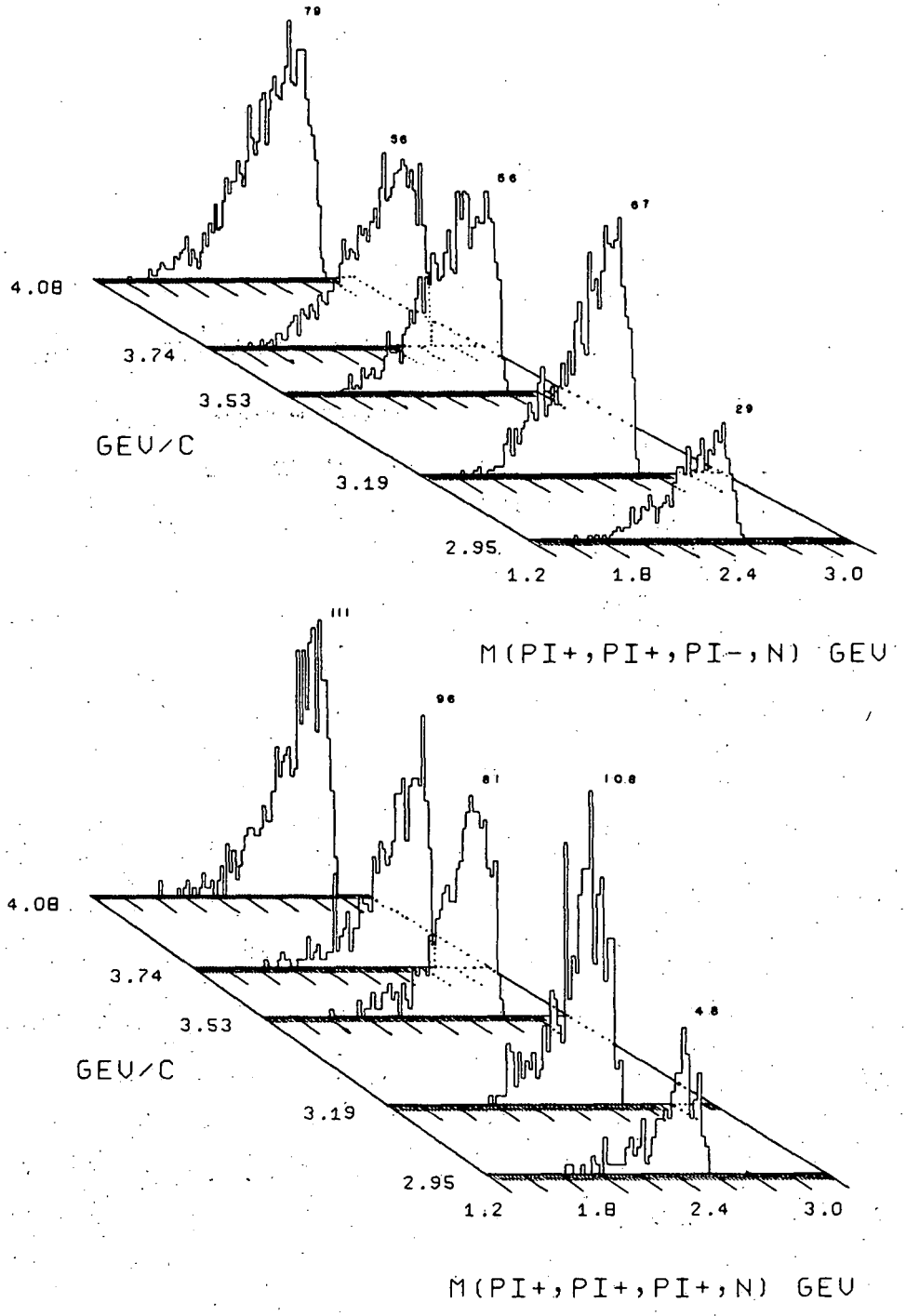

Fig. 43. Invariant mass and momentum transfer distributions of reaction (3) for the five momenta, in events/10 MeV $((MeV/c)^2)$, with the number of events in the highest bin being given for each histogram.

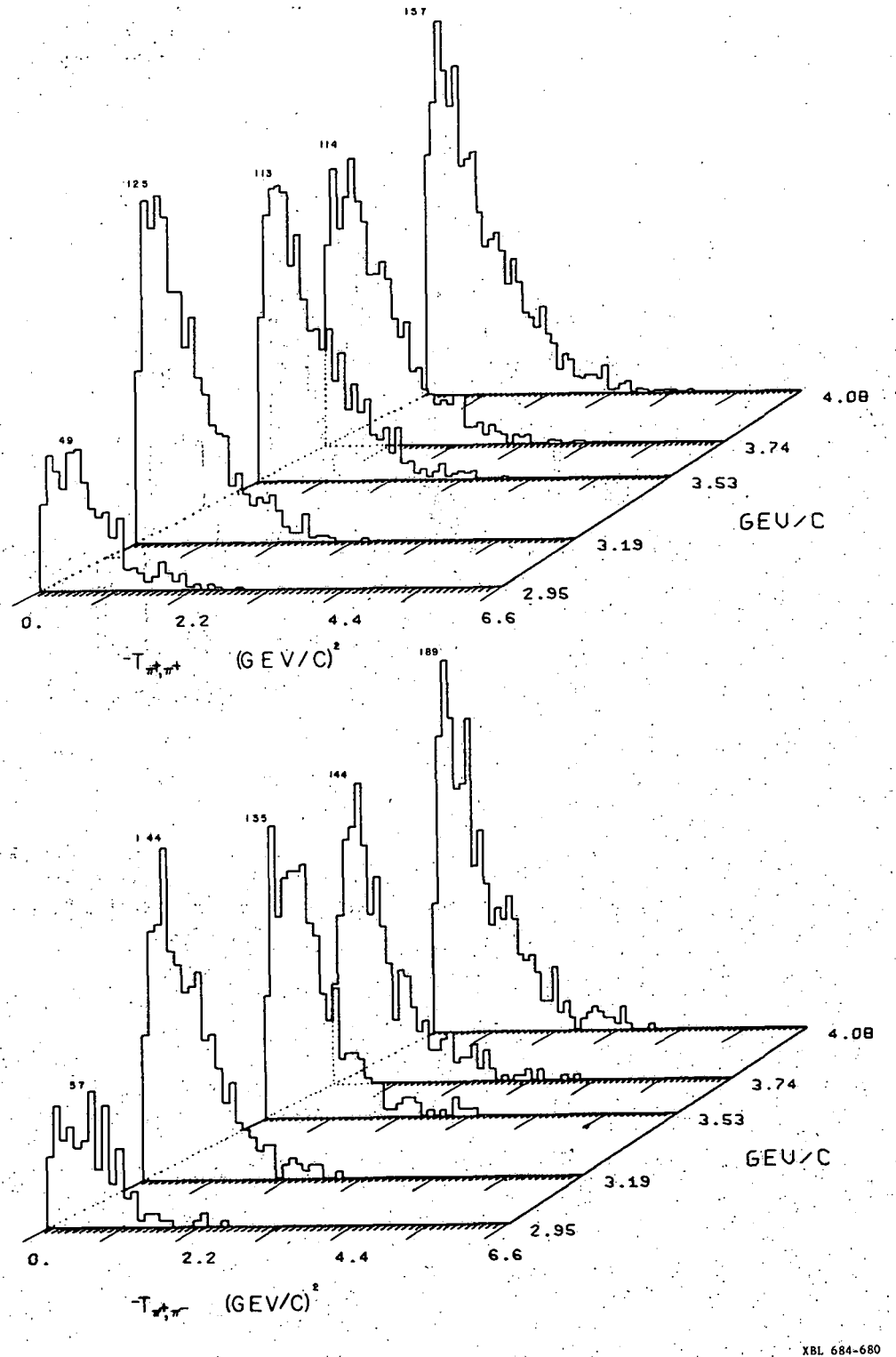

Fig. 44. Invariant mass and momentum transfer distributions of reaction (3) for the five momenta, in events/10 MeV ((MeV/c)^2), with the number of events in the highest bin being given for each histogram.

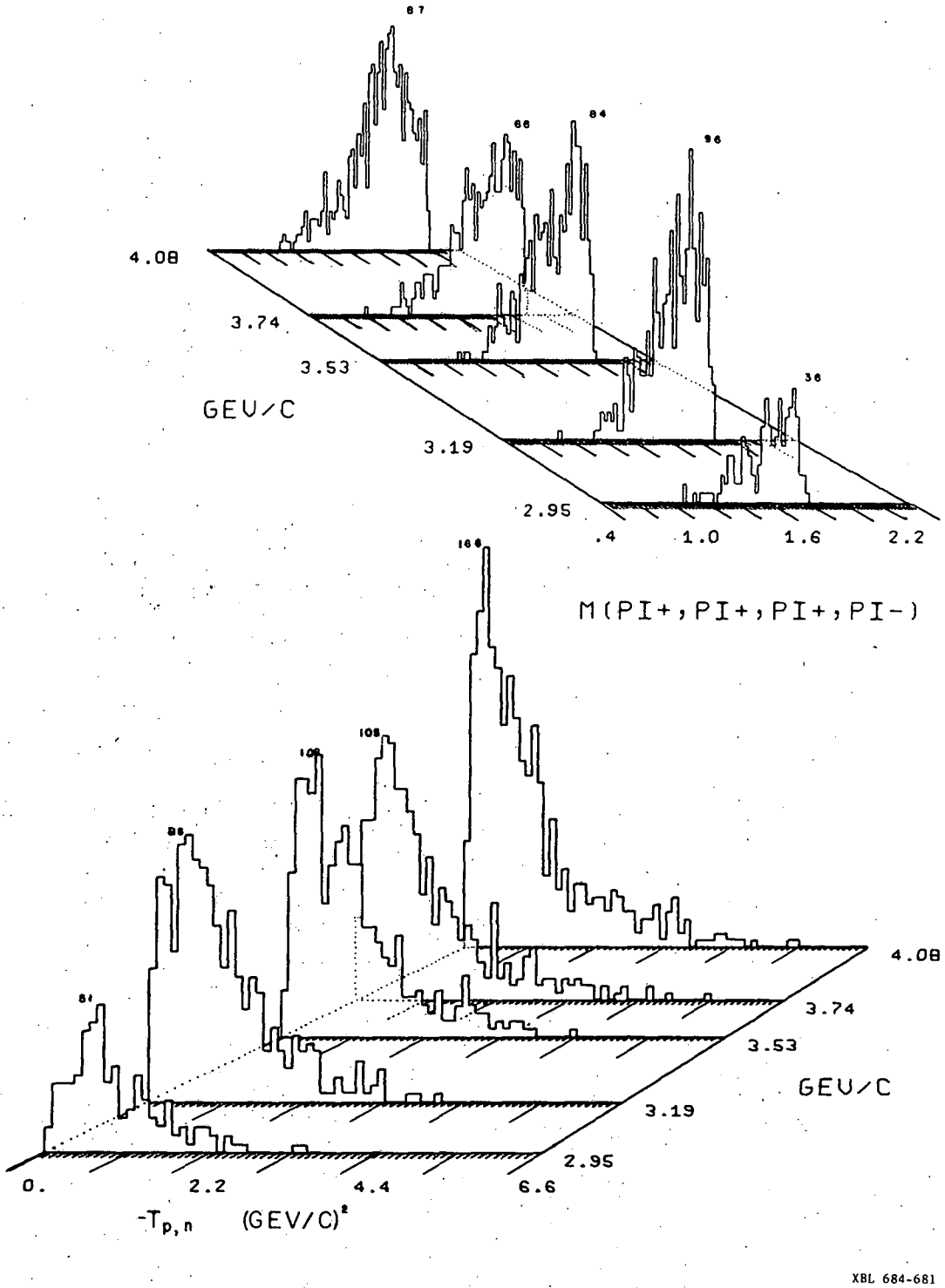

Fig. 45. Invariant mass and momentum transfer distributions of reaction (3) for the five momenta, in events/10 MeV ($(MeV/c)^2$), with the number of events in the highest bin being given for each histogram.

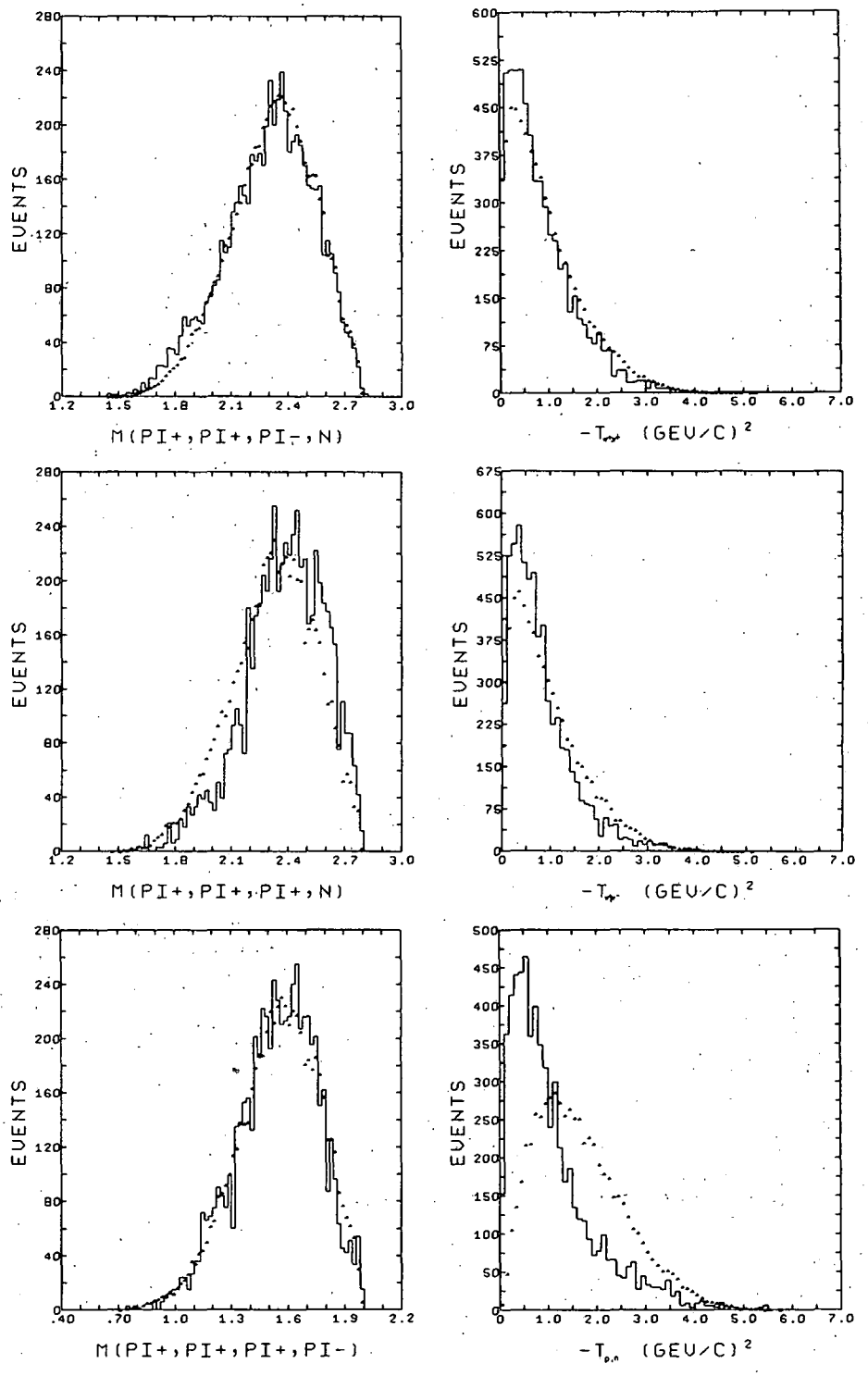

XBL 684-685

Fig. 46. Invariant mass and momentum transfer distributions of reaction (3) for all momenta combined, in events/10 MeV ((MeV/c)^2). The dotted curve is phase space.

IV. DOUBLE RESONANCE PRODUCTION

As noted in the previous section, reactions (1) and (2) are dominated by double resonance channels, in particular by $N^{*++}\rho^{\circ}$ and $N^{*++}\omega^{\circ}$ production respectively. These processes are of special interest because they are relatively free from background, and being quasi-two-body final states are subject to the traditional, fairly straight-forward methods of analysis. The additional final states of $N^{*++}f^{\circ}$ and $N^{*++}\eta^{\circ}$ share these qualifications, although they are produced less copiously, and will also be considered in this section. The relevant triangle and Chew-Low plots for reactions (1) and (2) are shown in Fig. (47) and give an indication of the prominence of these double resonance channels.[38]

The analysis of these reactions divides naturally into three levels of sophistication. Treated as strictly two body channels the relevant variables are the masses of the two systems, the momentum transfer from the incident to the outgoing B = 0 (or equivalently, B = 1) "particle", and the total c.m. energy. In this regard, the various momentum transfer distributions will be studied at some length and they and the respective cross-sections examined as a function of c.m. energy. Next, recognizing that the final state particles are unstable, the decay angular distributions in the appropriate rest frames are of interest. The particular parameters singled out in the following are the decay density matrix elements, in the helicity frame (shown in Fig. (48)). Finally, the possibility of correlations between the two decays is considered and the joint-density matrix elements examined.

Aside from presenting the experimental distributions there will be some comparison made of these with the theoretical predictions of certain one-meson-exchange models. In particular the one-meson exchange model

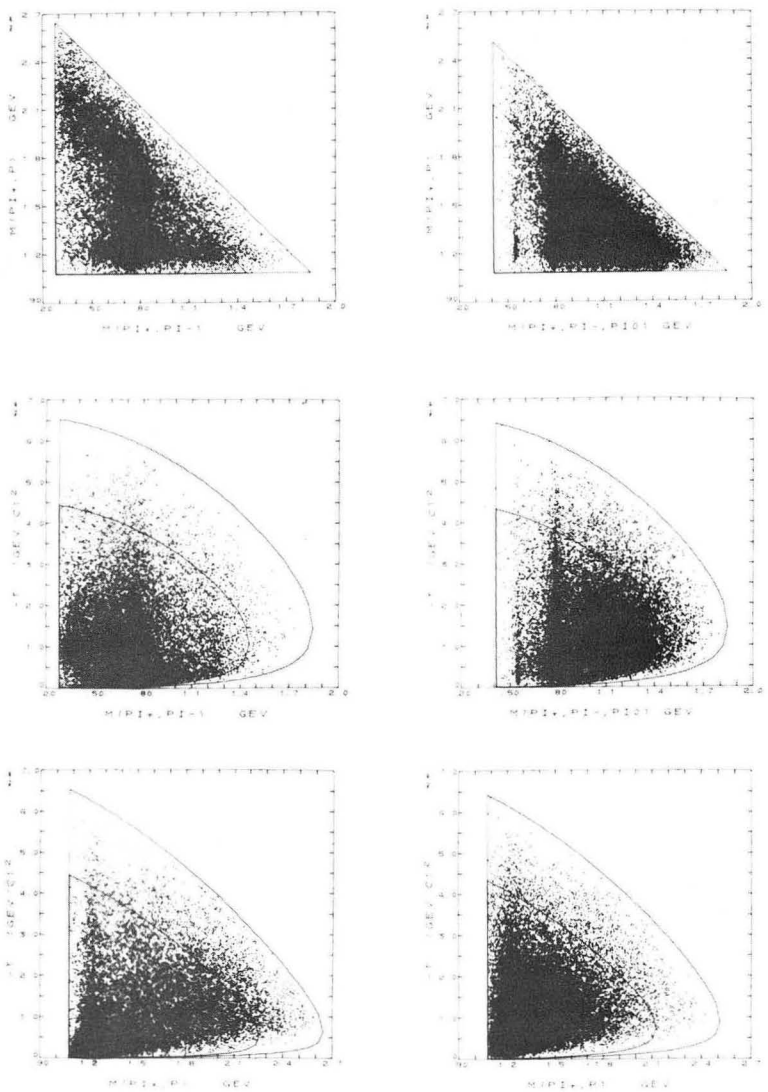

XBB 685-2612

Fig. 47. Triangle and Chew-Low plots for the di-particle systems of reactions (1) and (2) corresponding to the double resonance channels being studied. All events are plotted twice.

with absorption (OMEA) of Jackson and a form factor approach suggested by G. Wolf (OMEW) are used. The OMEA is especially useful because it may be used to predict the density matrix elements as well as the momentum transfer distributions. Following a suggestion of Jackson,[25] it has been altered slightly to take into account the effects of the finite widths of the resonances concerned. A brief description of these models and of the extraction of the parameters used with them is presented in Appendix (D).

It should be noted that the reference frame used here in the description of the decay distributions is not that commonly employed. It is customary to take the z-axis along the direction of the respective incident particle in the decay particle's rest frame. However, the helicity states (which constitute the basis used for the density matrix elements) are most easily described using axes with z along the direction of the transformation from the c.m. to the decay c.m. frame. The transformation which customarily is then used to rotate the density matrix into the canonical system is dependent upon the values of the masses of the final state particles, and is hence the source of some inconvenience and confusion when the finite widths of the resonances are taken into account. For ease in comparing the density matrices of this with other experiments, the experimental values are given for both systems.

One complicating aspect of these double resonance channels is the presence of the two positive pions, with one being assigned to each of the two final-state systems. This is a complication in two respects: 1) It introduces an ambiguity when both combinations lie within the chosen mass bands--e.g. $M(\pi_1^+ p)$ and $M(\pi_2^+ p)$ both "make" an $N^{*++}(1236)$

A. "JACKSON" FRAME

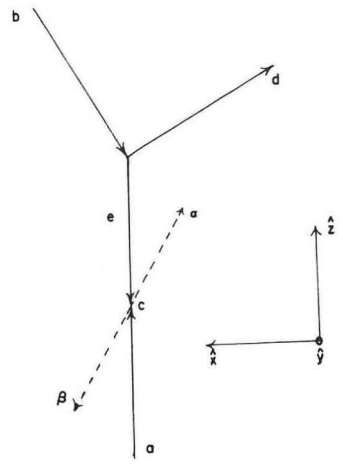

"c" REST FRAME

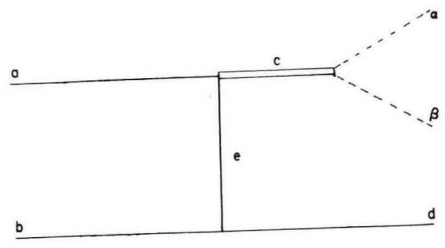

EXCHANGE DIAGRAM

$$\hat{Z} = \hat{a}$$

$$\hat{Y} = b\hat{x}d$$

$$\hat{X} = \hat{Y}x\hat{Z}$$

B. "HELICITY" FRAME

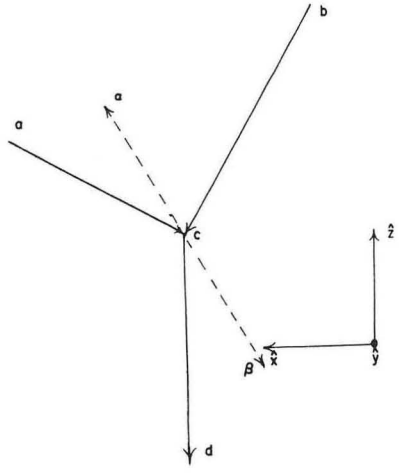

"c" REST FRAME

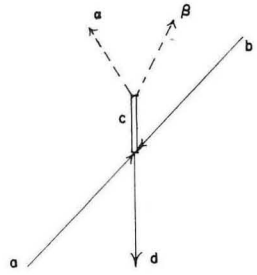

C.M. FRAME

$$\hat{Z} = -\hat{d}$$

$$\hat{Y} = b\hat{x}d$$

$$\hat{X} = \hat{Y}x\hat{Z}$$

XBL 684-686

Fig. 48. The reference frames used in the description of resonance decay angular distributions.

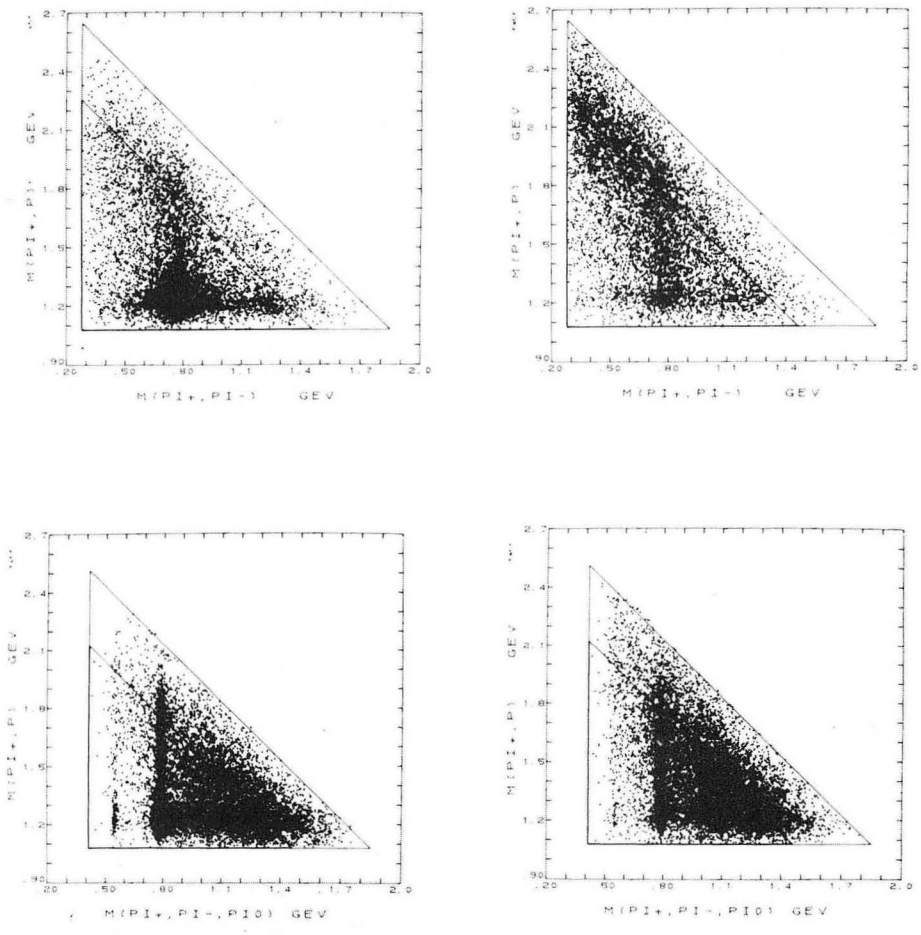

XBB 685-2614

Fig. 49. Triangle plots for the π^+p -- $\pi^+\pi^-$ (top) and π^+p -- $\pi^+\pi^-\pi^0$ (bottom) systems with the combination with the lesser (left) or greater (right) momentum transfer from the proton to the π^+p system being plotted.

and $M(\pi_2^+\pi^-)$ and $M(\pi_1^+\pi^-)$ a ρ° meson. 2) It increases the difficulty of estimating background when the reflection as well as the tails of the process enhance the neighboring region of the triangle plot. Fortunately, the peripheral nature of these reactions enables one to differentiate between the positive pions in a fairly reasonable manner. In this analysis the "correct" combination for the small percentage of ambiguous events has been chosen on the basis of the smaller momentum transfer.

Evidence that this is a reasonable procedure is presented in Fig. (49): Choosing the combination with the smaller momentum transfer is seen to enhance the $N^*\rho$ and $N^*\omega$ signals. These problems are discussed further with reference to the individual reactions in what follows.

A. $\pi^+p \rightarrow N^{*++}\rho^\circ$

$N^*\rho$ production accounts for roughly 40% of reaction (1). Its magnitude is seen in the $\pi^+\pi^-$ -- π^+p triangle plots of Fig. (50) and its highly peripheral character is obvious from the Chew-Low plots of Figs. (51 and 52). It is thought to proceed primarily via a pion-exchange mechanism, and detailed comparisons will be made between the experimental results and predictions of the one-pion-exchange-with-absorption (OPEA) model of Jackson (as described in Appendix (D)). As will be seen, the model describes most aspects of the data fairly well.

The $N^*\rho$ cross-sections were estimated from fits to the triangle plots of Fig. (50), with an attempt being made to represent the background with something slightly more realistic than pure phase space. A Monte Carlo program (Appendix (C)) was used to generate events according to six possible final states:

1) $\pi^+p \rightarrow \pi^+p\,\pi^+\pi^-$ (phase space) 2) $\pi^+p \rightarrow N^{*++}\rho^\circ$ (e^{8t})

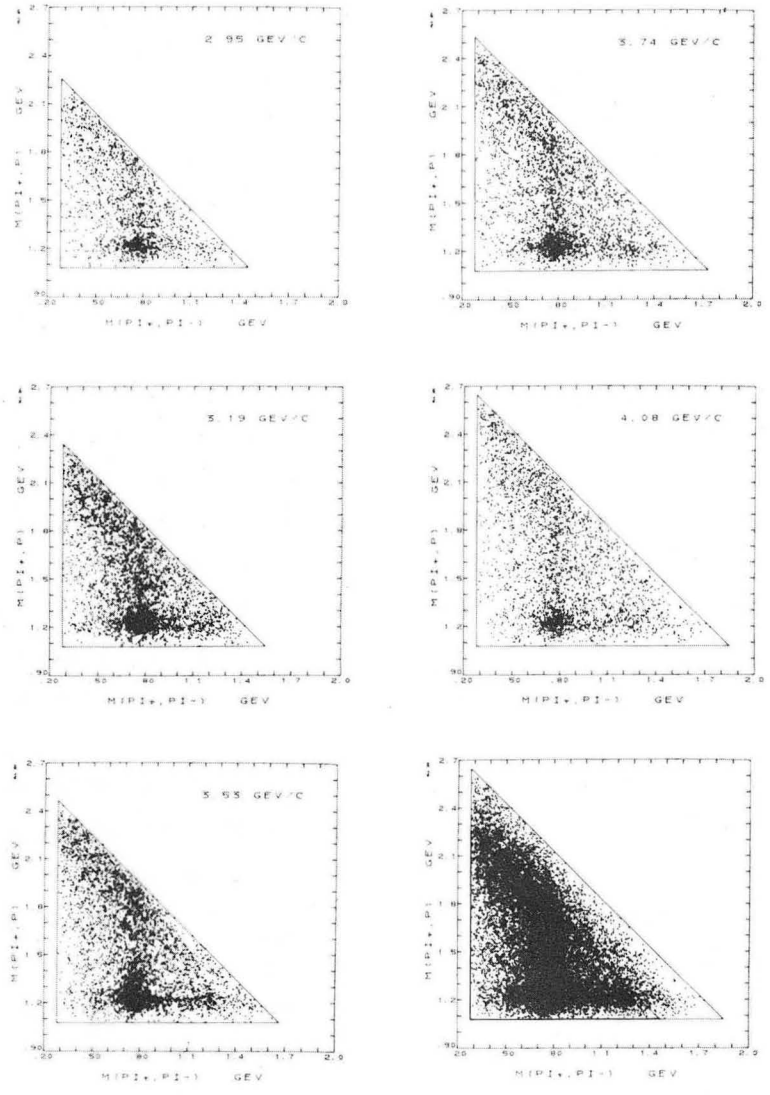

XBB 685-2613

Fig. 50. π^+p %% $\pi^+\pi^-$ triangle plots for reaction (1) for the individual momenta and their sum. Both combinations are plotted for each event.

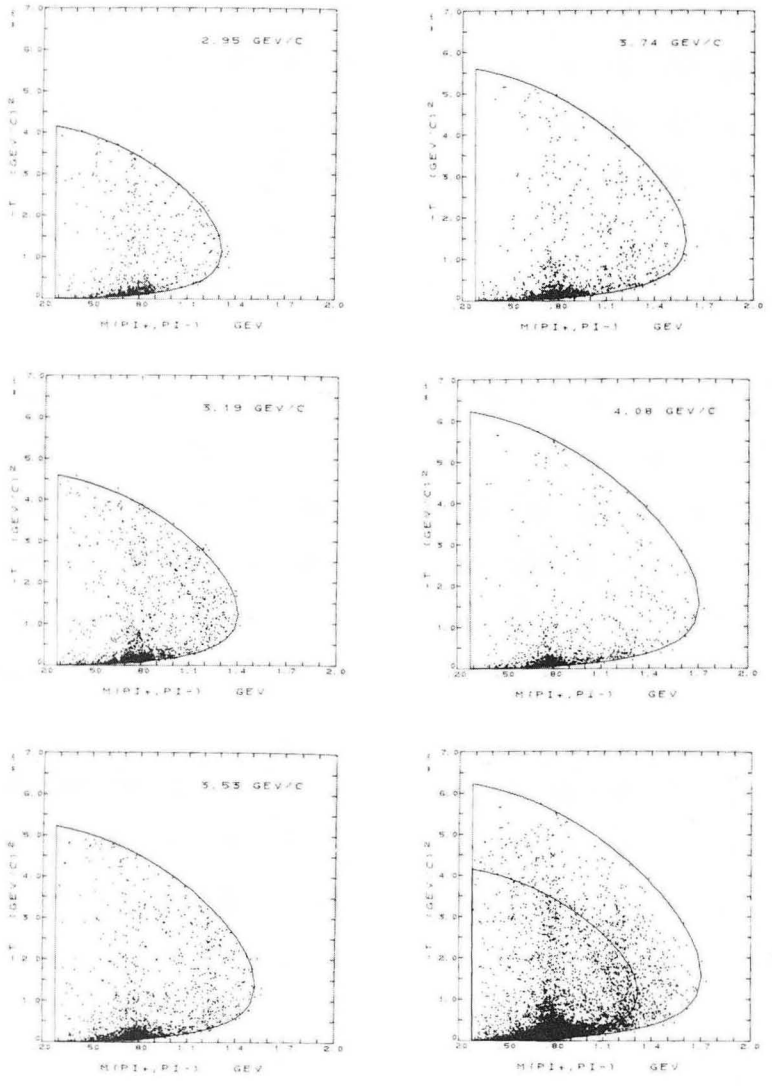

XBB 685-2611

Fig. 51. -t -- $\pi^+\pi^-$ Chew-Low plots for events of reactions (1) lying within the N^* mass band. One combination per event is plotted (ambiguities are resolved on the basis of the lower momentum transfer).

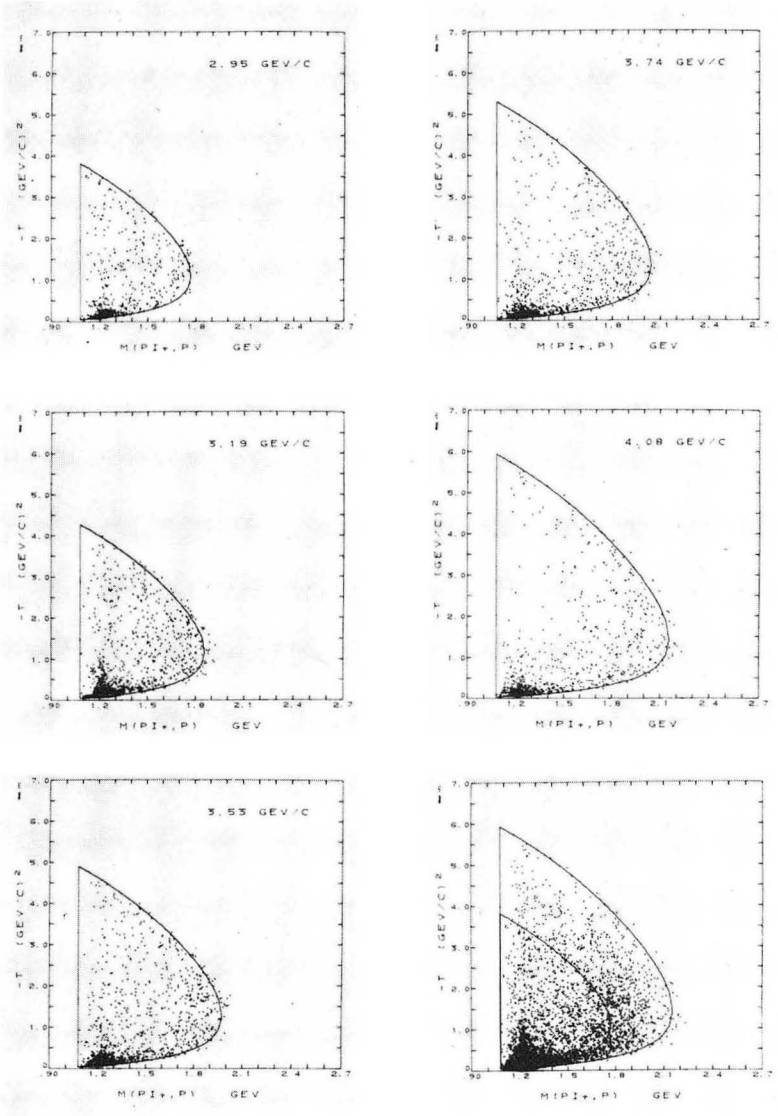

XBB 685-2615

Fig. 52. -t -- $\pi^+ p$ Chew-Low plots for events of reaction (1) lying within the ρ mass band. One combination per event is plotted (ambiguities are resolved on the basis of the lower momentum transfer).

3) $\pi^+ p \rightarrow N^{*++} f^\circ$ (e^{7t})

4) $\pi^+ p \rightarrow p\,A1$ (↳ $\pi^+ \rho^\circ$) (e^{10t})

5) $\pi^+ p \rightarrow p\,A2$ (↳ $\pi^+ \rho^\circ$) (e^{6t})

6) $\pi^+ p \rightarrow \pi^+ N^{*+}(1700)$ (↳ $\pi^- N^{*++}$) (e^{6t})

The resonance parameters used are based on those in the January 1968 UCRL-8030[27] and are listed in Appendix (B). The events were generated having the exponential momentum-transfer dependence shown in parenthesis (in the momentum transfer variable appropriate for each reaction) and then weighted according to resonance Breit-Wigners. The $\pi^+\pi^- - \pi^+ p$ scatter plots of these events were used in fitting the corresponding data distribution at each energy.

In interpreting the results of this analysis one must note the following: 1) Only the $\pi^+\pi^- - \pi^+ p$ distribution was fit, so that the resonance parameters and relative fractions of the latter three reactions are not to be taken seriously. They are only included in order to better parameterize the background. 2) The weighting of the (100 000) Monte Carlo events of the respective reactions resulted in the effective number of events in each fitting distribution being comparable to the number in the data distribution, so that the theoretical errors are important in lowering the chi-squares. Therefore, the only parameters in which one may hold a reasonable degree of confidence are the fractions of $N^{*++}\rho^\circ$ and $N^{*++}f^\circ$ production and, to a lesser degree, the total fraction of N^{*++} and ρ° present. These are shown in Table (V), and in Fig. (53) the corresponding cross-sections in millibarns are plotted.

Since the relative fraction of $N^*\rho$ is found to be nearly constant with energy, the structure of the $N^*\rho$ cross-section is just that of the total 4C cross-section. With the same reservations expressed previously, this leads to a peak value of .25 ± .1 mb for decay of the $N^{*++}(2850)$

Table V. Results of a fit to the experimental $\pi^+\pi^-$ -- π^+p triangle plot with events Monte-Carloed according to the six hypothetical reactions mentioned in the text.

Momentum GeV/c	CL	"Background" Reactions (%) P.S.	A1(ρ)	A2(ρ)	N*(N*)	N*ρ and N*f Production (%) N*ρ	N*f	N* and ρ Production (%) N*	ρ
2.95	.96	0.0±16.6	15.0±2.6	8.4±4.2	32.1±2.4	43.4±2.1	1.2±4.3	76.7±5.4	66.8±5.4
3.19	.05	7.2±5.6	8.3±4.5	9.6±3.4	34.2±1.9	39.3±1.1	1.4±3.9	74.9±4.5	57.2±5.7
3.53	.54	8.4±4.5	7.3±4.0	13.5±3.0	26.8±2.4	40.4±1.6	3.6±2.4	70.8±3.8	61.2±5.2
3.74	.98	10.9±3.5	10.1±3.2	11.8±2.3	20.8±2.2	41.9±1.2	4.6±1.7	67.3±3.0	63.8±4.1
4.08	.91	11.4±3.8	12.5±3.4	13.6±3.4	17.0±2.7	39.5±1.6	5.9±2.0	62.4±3.7	65.6±5.1
Combined	10^{-7}	12.8±1.8	10.1±1.7	10.1±1.7	24.3±1.3	39.2±.7	3.6±.8	67.1±1.7	59.4±2.5

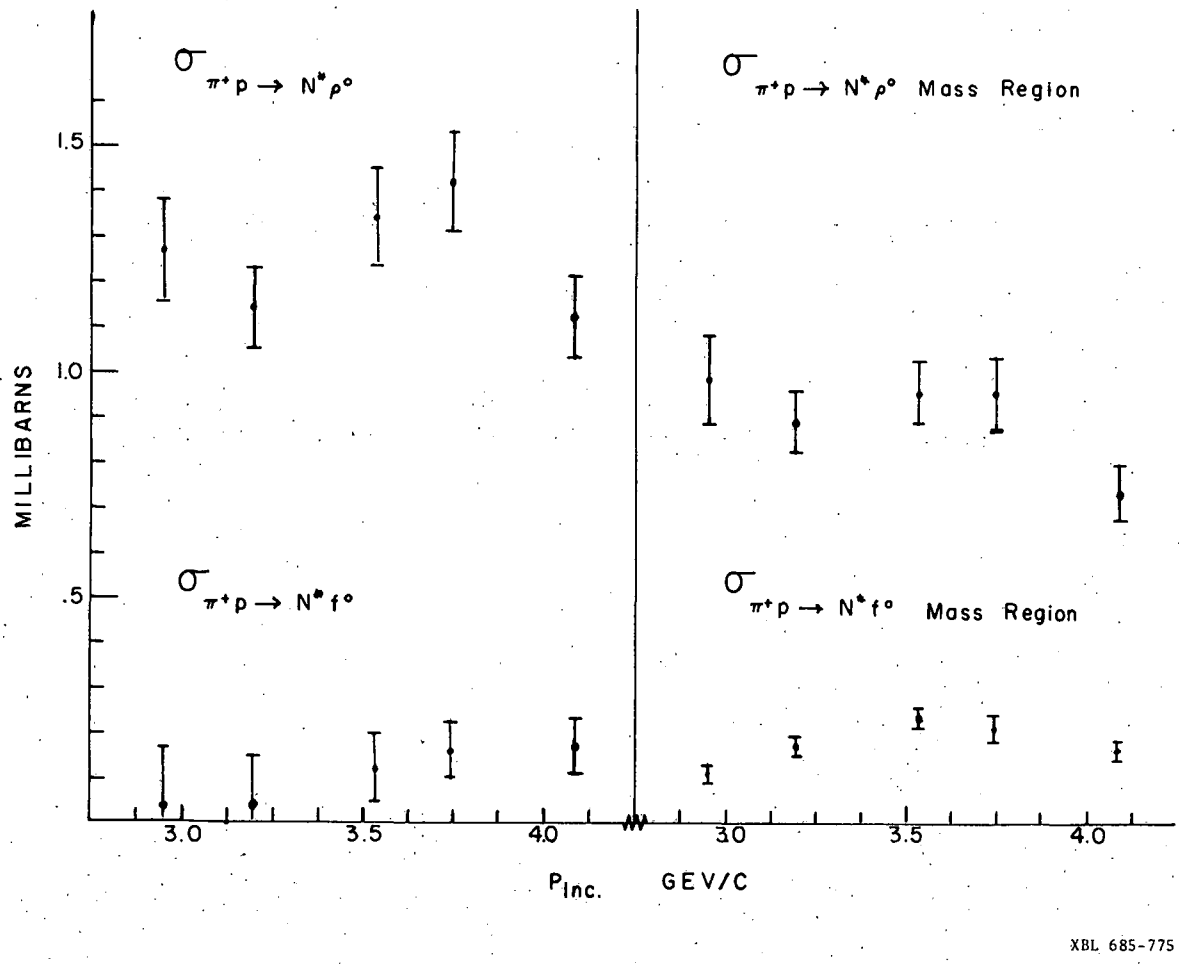

Fig. 53. Cross-sections for $N^*\rho$ and N^*f production and for production of events within the $N^*\rho$ and N^*f mass regions.

into $N^{*++}\rho^{\circ}$. The N^{*}f cross-section exhibits the expected near-threshold behavior, not being produced copiously until low momentum-transfer values are kinematically allowed.

For a more detailed analysis of the $N^{*}\rho$ final state it was necessary to choose selection criteria such that an enriched sample of $N^{*}\rho$ events would be obtained. Those events were taken with $M(\pi_i^+ p)$ lying between 1.12 and 1.32 GeV and $M(\pi_j^+\pi^-)$ between .68 and .86 GeV. Ambiguities were resolved on the basis of momentum transfer--i.e. if $M(\pi_j^+ p)$ and $M(\pi_i^+\pi^-)$ also lay within the requisite mass limits, the combination with the smaller momentum transfer from the proton to the "N^{*}" was chosen. That this is not a completely arbitrary procedure is seen in Fig. (54) where the invariant masses of the $\pi^+\pi^-$ and $\pi^+ p$ combinations with the smaller and larger momentum transfer are histogrammed. Clearly choosing the smaller momentum transfer leads to enhanced N^{*} and ρ signals. Further, fewer than 2% of the $N^{*}\rho$ events are effected so that there is a minimal bias to the sample.

The distribution in production angle is shown in Fig. (55). The extent of the forward peaking is manifest, with over 60% of the events lying within the 5% of the cosθ range greater than .9. Two other aspects of the data are noteworthy, however: 1) The "equatorial" region of cosθ is increasingly depleted as the energy increases. 2) There is a small backward peak at the highest momenta. Part of (1) is of course accounted for by the approximate e^{At} behavior of the forward peak which, for constant A, requires shrinkage in the cosθ peak with increasing energy. The effect persists, however, beyond the peak region. The percentage of events in each of five equally spaced intervals of cosθ, at each energy, is listed in Table (VI).

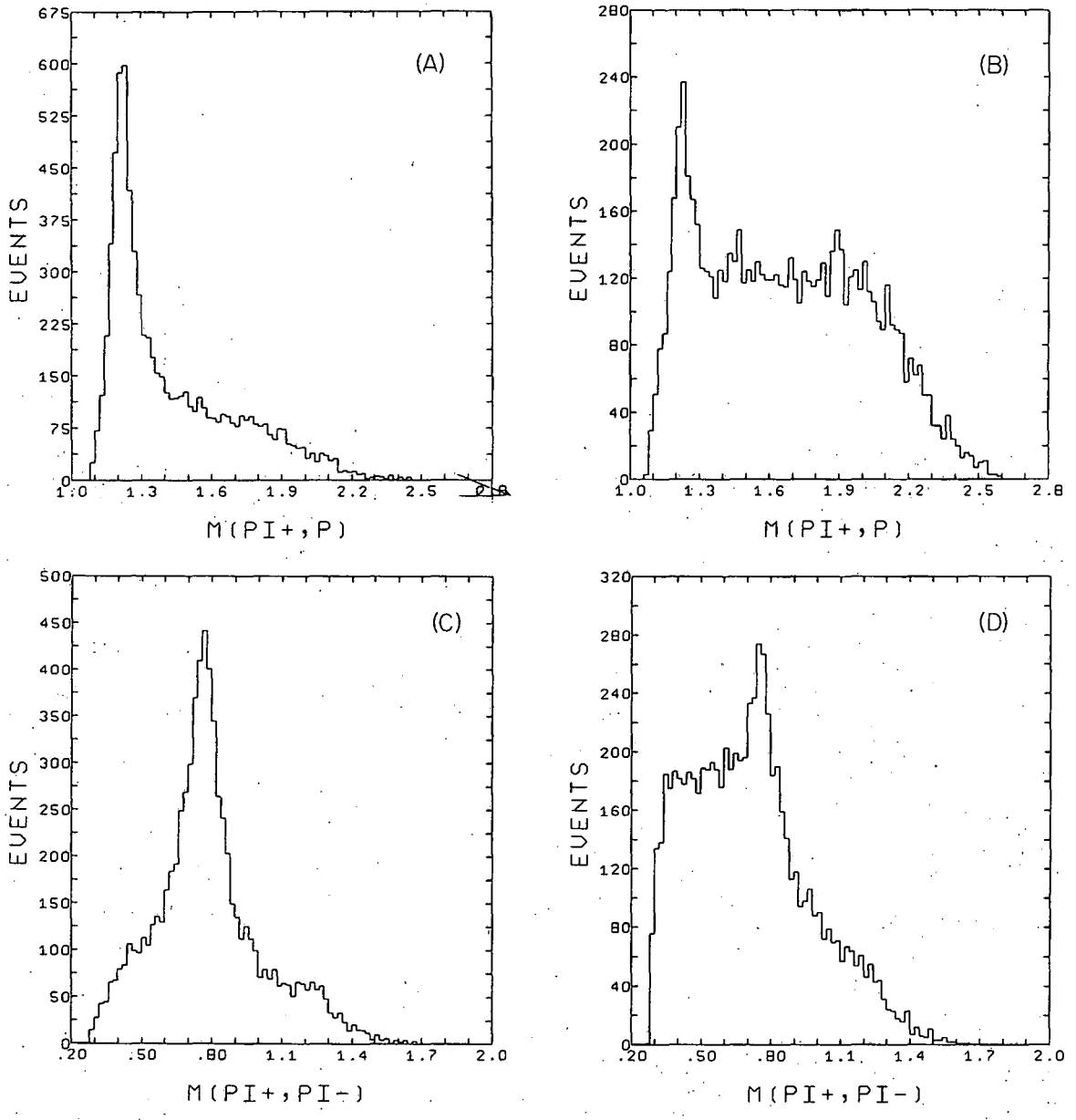

XBL 684-684

Fig. 54. π^+p (top) and $\pi^+\pi^-$ (bottom) invariant mass distributions for those combinations with the lesser (left) and greater (right) momentum transfer from the proton to the π^+p system.

Table VI. $N^{*}\rho$ Production Cosine Distribution

Momentum GeV/c	Total Number	$-1 < \cos\theta < -.6$ Number	%	$-.6 < \cos\theta < -.2$ Number	%	$-.2 < \cos\theta < .2$ Number	%	$.2 < \cos\theta < .6$ Number	%	$.6 < \cos\theta < 1.0$ Number	%
2.95	268	18	6.7	19	7.1	19	7.1	29	10.8	183	68.3
3.19	515	21	4.1	34	6.6	26	5.0	30	6.0	403	78.3
3.53	553	22	4.0	20	3.6	17	3.1	40	7.2	454	82.1
3.74	421	12	2.8	13	3.1	13	3.1	19	4.5	364	86.5
4.08	358	14	3.9	3	.8	5	1.4	11	3.1	325	90.8
ALL	2115	87	4.1	89	4.2	80	3.8	130	6.2	1729	81.7

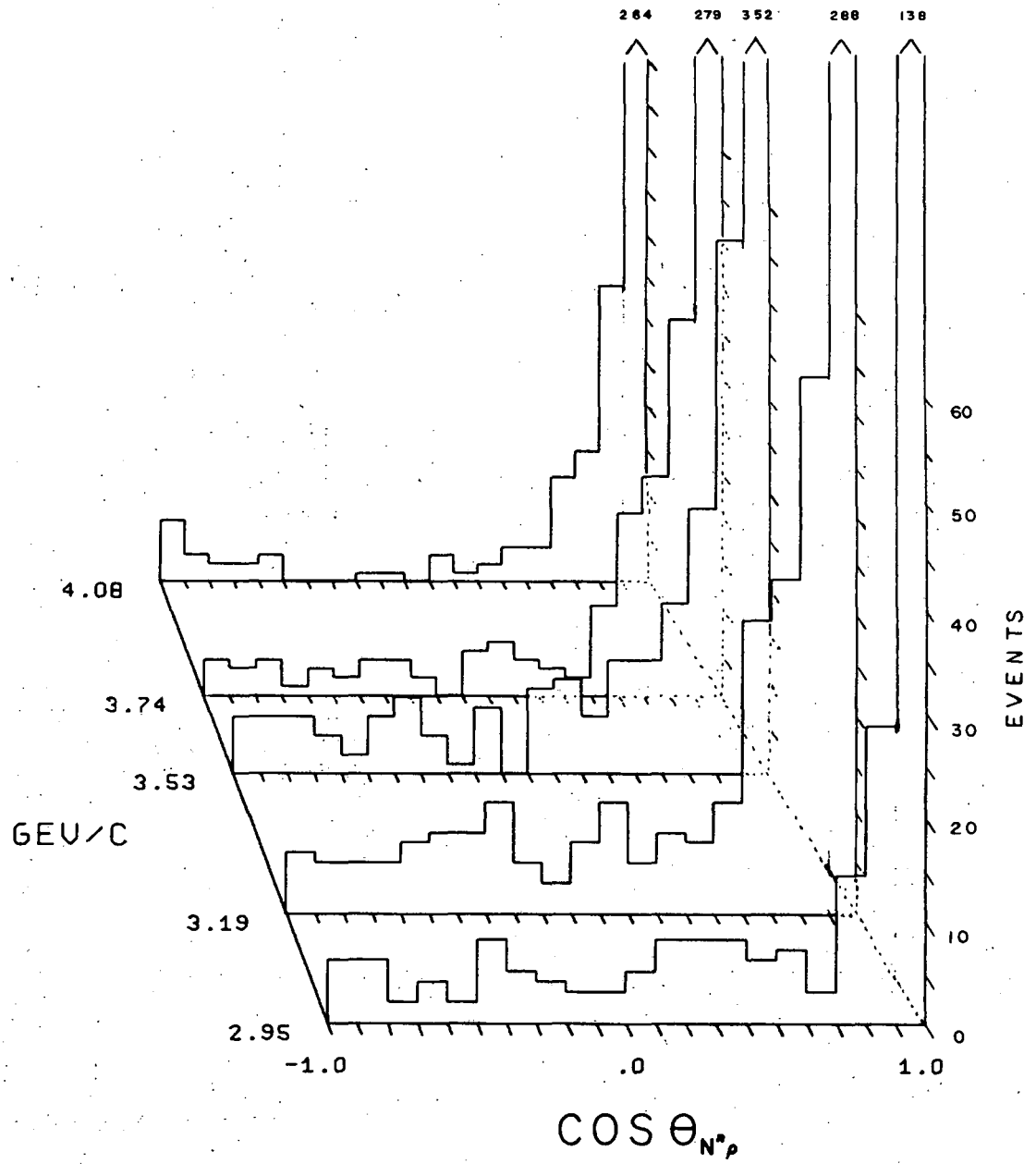

Fig. 55. $N^{*}\rho$ production cosine distributions at the five momenta. The forward peak is truncated and the number of events in it indicated above.

In terms of the momentum transfer (Fig. (56)) the most prominent feature of the forward peak is its nearly constant slope on a logarithmic scale. Table (VII) gives the results of the fits to this slope using (a) a conventional chi-square fit to the -t distribution and (b) an analysis based on the first two moments of -t -- i.e. $\langle -t \rangle$ and $\langle t^2 \rangle$ (Appendix (E)). The interval $.2 < -t < .5$ $(GeV/c)^2$ has been used, since the boundary region extends to .2 $(GeV/c)^2$ (at the lowest momentum), and a marked change in the slope occurs at about .5 $(GeV/c)^2$. The average value of the slope is found to be about $7.3 \pm .5$ and $7.5 \pm .5$ $(GeV/c)^{-2}$ by the two methods.

There is some slight evidence for shrinkage in the data -- i.e. for "A" being an increasing function of incident momentum, as the fitted value increases from 6.1 to 7.8 $(GeV/c)^{-2}$ in the interval studied. The evidence is hardly conclusive, however, since the highest value occurred at the central momenta and all of the values lie within errors of the average value.[28] Further, the values obtained for the central region of the $N^*\rho$ ($1.17 < M(\pi^+ p) < 1.27$ GeV, $.725 < M(\pi^+\pi^-) < .815$ GeV) do not demonstrate such a trend, although this is not surprising in view of the large errors accompanying them.

Although a simple exponential fits the data quite well between .2 and .5 $(GeV/c)^2$, outside this range of -t there are important discrepancies. In the vicinity of $-t = .5$ there is a radical change in slope (from $A = 7.3$ to $A \simeq 2$ $(GeV/c)^{-2}$ and perhaps even a "dip". Of course, in the tail of the distribution it is quite possible that background effects may be dominant. The definitely peripheral nature of much of the background considerably lessens the danger, however, that it will be very much proportionately greater at higher than low -t values.

The curve superimposed on the -t distribution of Fig. (55) is that given by an exponential distribution with $A = 7.3$ $(GeV/c)^{-2}$, integrated

Table VII. The logarithmic slope of the momentum transfer distribution from a) chi-square fit to the -t distribution, and b) a fit to the first two moments of t -- $.2 < -t < .5$ $(GeV/c)^2$.

	Method (a)		Method (b)	
$P_{Inc.}$ GeV/c	$A_{N^*\rho}$ $(GeV/c)^{-2}$	CL	$A_{N^*\rho}$ $(GeV/c)^{-2}$	$A_{N^*\rho(\text{central } N^*\rho)}$ $(GeV/c)^{-2}$
2.95	6.1 ± 1.3	.1	6.6	9.8
3.19	6.9 ± .9	.1	7.2	7.1
3.53	8.3 ± .8	.1	8.2	6.6
3.74	7.1 ± 1.2	.1	7.4	6.4
4.08	7.8 ± 1.0	1.0	7.7	8.8
ALL	7.3 ± .5	.25	7.5	7.5

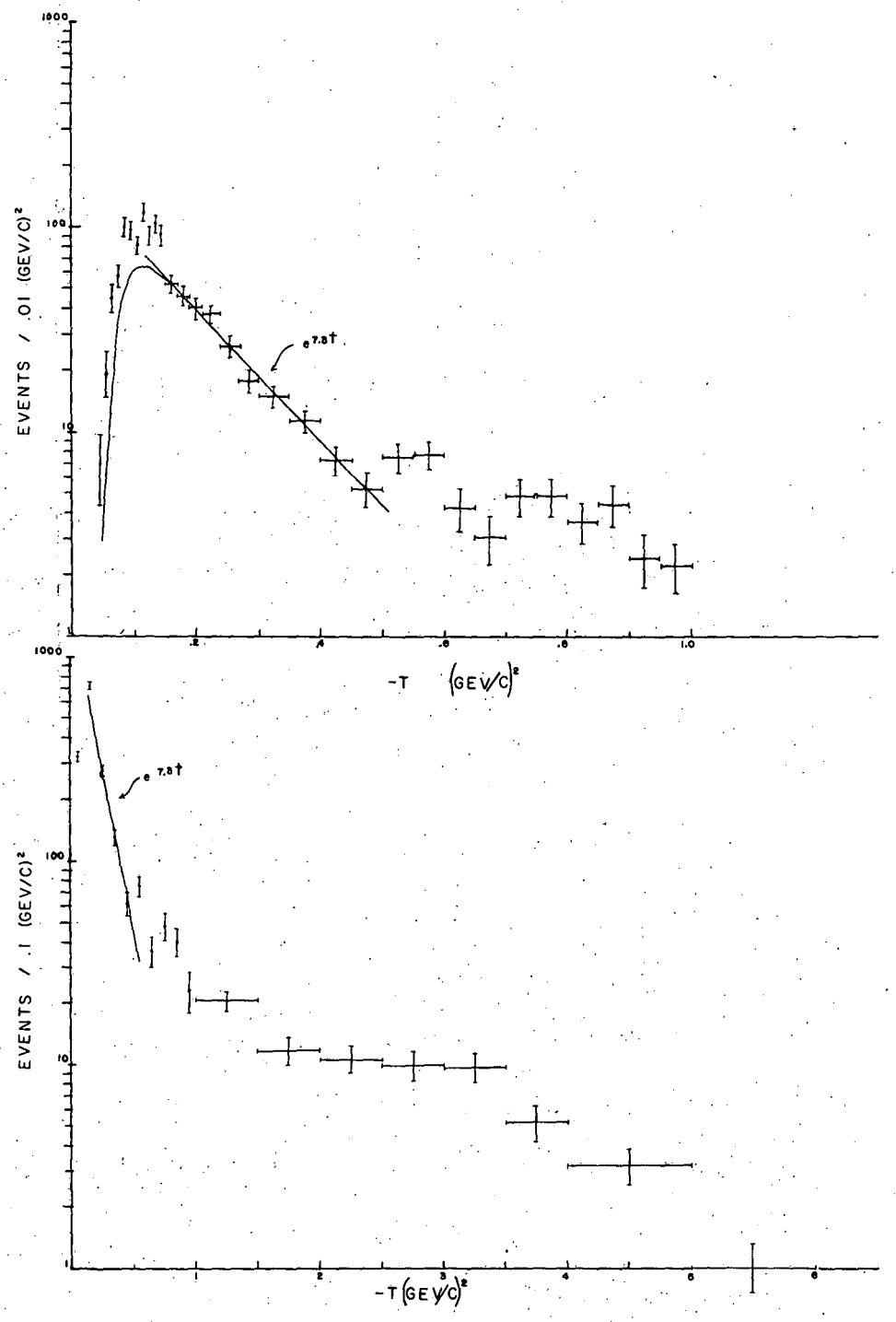

XBL 684-688

Fig. 56. The $N^*\rho$ momentum transfer distribution displayed over its entire range (bottom) and in fine detail (top).

over the $N^{*}\rho$ mass region (weighted by resonance Breit-Wigners) and summed over incident momenta (weighted as the number of events for $.2<-t<.5$ $(GeV/c)^2$). It illustrates the goodness of the exponential fit above the boundary region and its complete failure within that region. In the region where the operation of the kinematic limits would be supposed to reduce the cross-section, the experimental points lie in fact well above the extrapolation of a straight $e^{7.3t}$ dependence. For the region $0<-t<.15$ $(GeV/c)^2$ the experimental distribution contains 68% more events than predicted by the exponential fit. Of course, theoretically this is not unexpected. Both OPEA and OPEW models predict distributions which are more-than-exponentially peaked in -t. The data amply confirm this.

As seen above, momentum transfer is an inconvenient variable to use when wide resonances are studied because many of the events occur in the "boundary" region where interpretation of the data is difficult. In order to obviate this difficulty it has become fashionable recently to use the variable, $t' = |t-t_{min}|$ where t_{min} is calculated for each event and is the minimum value -t could assume, given the masses of the two final state systems for that event. Fig. (57) gives experimental t′ distributions together with the results of an exponential fit to the data. An exponential in t′ was also fit to each momentum separately, and the results are shown in Table (VIII). The fits are quite good all the way from $t' = 0$ to $.2$ $(GeV/c)^2$ and vary little from energy to energy. In the very forward direction, from $t' = 0$ to $.05$ $(GeV/c)^2$, the values of A obtained are poorly determined but definitely greater than those for the larger range of t′. Thus, neither the t nor t′ distributions lend credibility to recent predictions of a "turn over" in $d\sigma/dt$ at

Table VIII. The logarithmic slope of the t′ distribution for two intervals of t′.

$P_{Inc.}$ GeV/c	$0 < t' < .2$ $A_N^* \rho$ $(GeV/c)^{-2}$	CL	$0 < t' < .05$ $A_N^* \rho$ $(GeV/c)^{-2}$	CL
2.95	12.7 ± .7	.5	15.6 ± 4.5	.6
3.19	12.2 ± .9	.2	13.0 ± 6.6	.6
3.53	11.6 ± .8	.5	10.0 ± 4.0	.25
3.74	11.3 ± .8	.9	14.9 ± 4.8	.9
4.08	12.6 ± 1.1	.25	24.0 ± 4.8	.65
ALL	11.8 ± .4	.6	14.6 ± 2.0	1.0

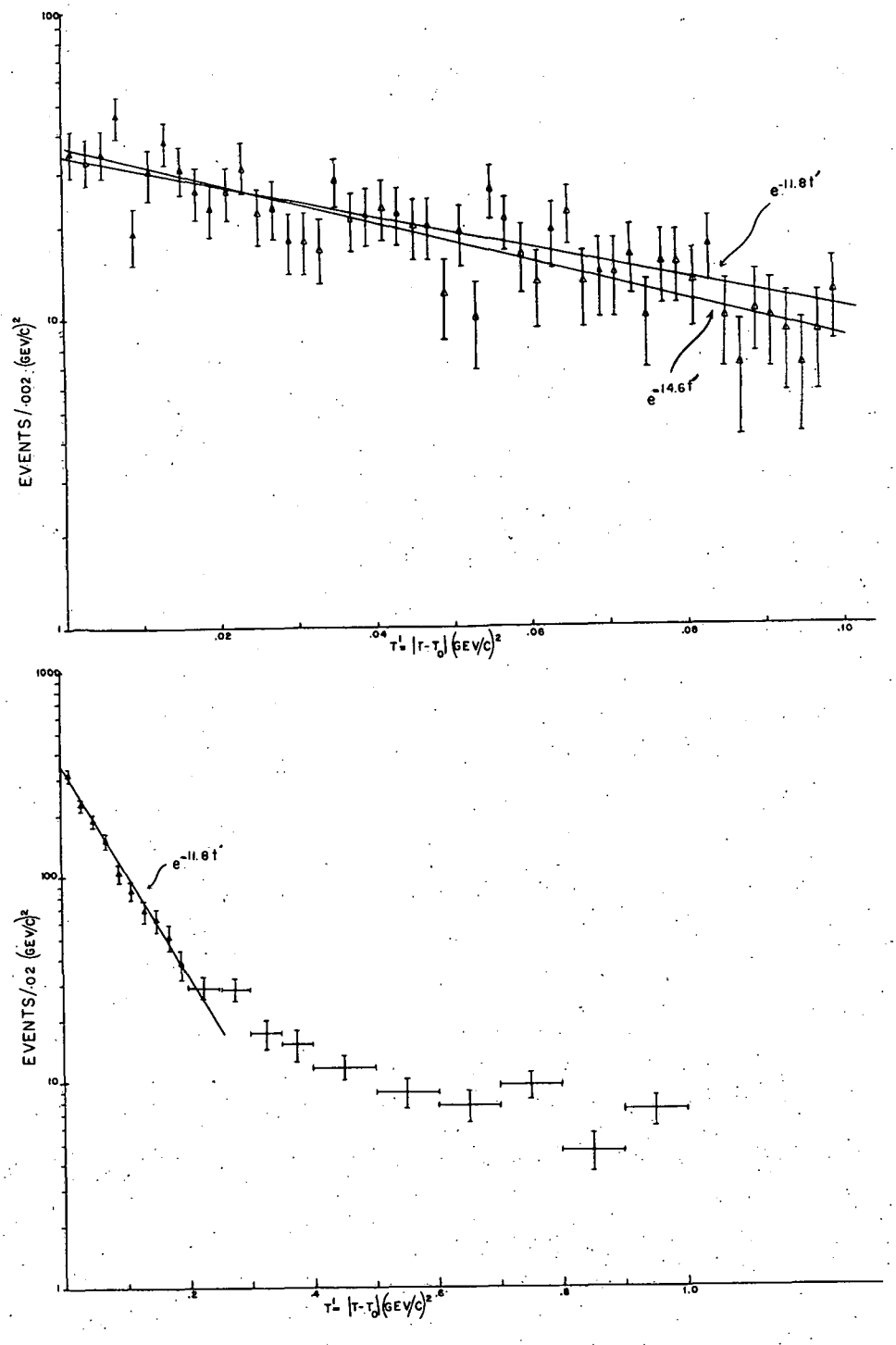

XBL 684-689

Fig. 57. The $N^*\rho$ t′ distribution displayed for $0 < t' < .1$ $(GeV/c)^2$ (top) and for $0 < t' < 1.0$ $(GeV/c)^2$ (bottom).

small t.[36]

In order to compare the momentum transfer distribution of Fig. (56) with OPEA and OPEW predictions, the experimental distribution must be suitably normalized. Both the background events within the mass cuts and the $N^*\rho$ tail outside must be taken into account before applying the mb/event ratios of Table IV. The background was estimated with the aid of the Monte-Carlo events previously used in fitting the π^+p -- $\pi^+\pi^-$ triangle plot. These were screened with the $N^*\rho$ selection criteria to determine the percentage of the five "background reactions" which would contaminate the $N^*\rho$ sample. This, together with the results of the fit (Table V), yielded a figure for background. This was also done for the $N^*\rho$ central region ($.725 < M(\pi^+\pi^-) < .815$ GeV, $1.17 < M(\pi^+p) < 1.27$ GeV) and for a background doughnut "control" region surrounding the $N^*\rho$ region (outer limits: $.50 < M(\pi^+\pi^-) < 1.04$ GeV, $.92 < M(\pi^+p) < 1.52$ GeV). The values obtained for the percentage of events accounted for by $N^*\rho$ production in each of these regions is given in Table IX.

Ideally the momentum transfer distribution should not just be multiplied by the simple scale factor obtained above, since the background distribution is not expected to be identical to that for $N^*\rho$ production. Because of the substantial widths of the resonances involved, and the mass dependence of the -t distribution, however, such special corrections were considered highly speculative and were ignored. Also, a factor for the "tail" contribution was not used in normalizing $d\sigma/dt$: as with the theoretical curves, $d\sigma/dt$ is given for $N^*\rho$ production within the stated mass limits.

In Fig. (58) OPEA, and OPEW curves are shown with the experimental distribution. The curves are the weighted averages of curves for the

Table IX. Percentage of $N^*\rho$ production in four event samples a) $N^*\rho$ cut: $.68 < M(\pi^+\pi^-) < .86$ GeV, $1.12 < M(\pi^+p) < 1.32$ GeV; b) Central $N^*\rho$: (subset of (a)) $.725 < M(\pi^+\pi^-) < .815$ GeV, $1.17 < M(\pi^+p) < 1.27$ GeV; c) $N^*\rho$ background: (Outer limits) $.50 < M(\pi^+\pi^-) < .104$ GeV, $.92 < M(\pi^+p) < 1.52$ GeV (The inner limits are those of (a)) d) $N^*\rho_B$ cut: (same as (a)); and, for (a) and (b) ((c) and (d)), if both combinations lay within the (a) ((c)) region, that with the lower $-t_{p,\pi^+p}$ was used.

Momentum GeV/c	(a) $N^*\rho$ %	(b) Central $N^*\rho$ %	(c) $N^*\rho$ background %	(d) $N^*\rho_B$ %
2.95	72	80	35	72
3.19	73	80	34	73
3.53	77	83	39	77
3.74	79	85	42	79
4.08	79	86	43	80
Combined	75	82	37	76

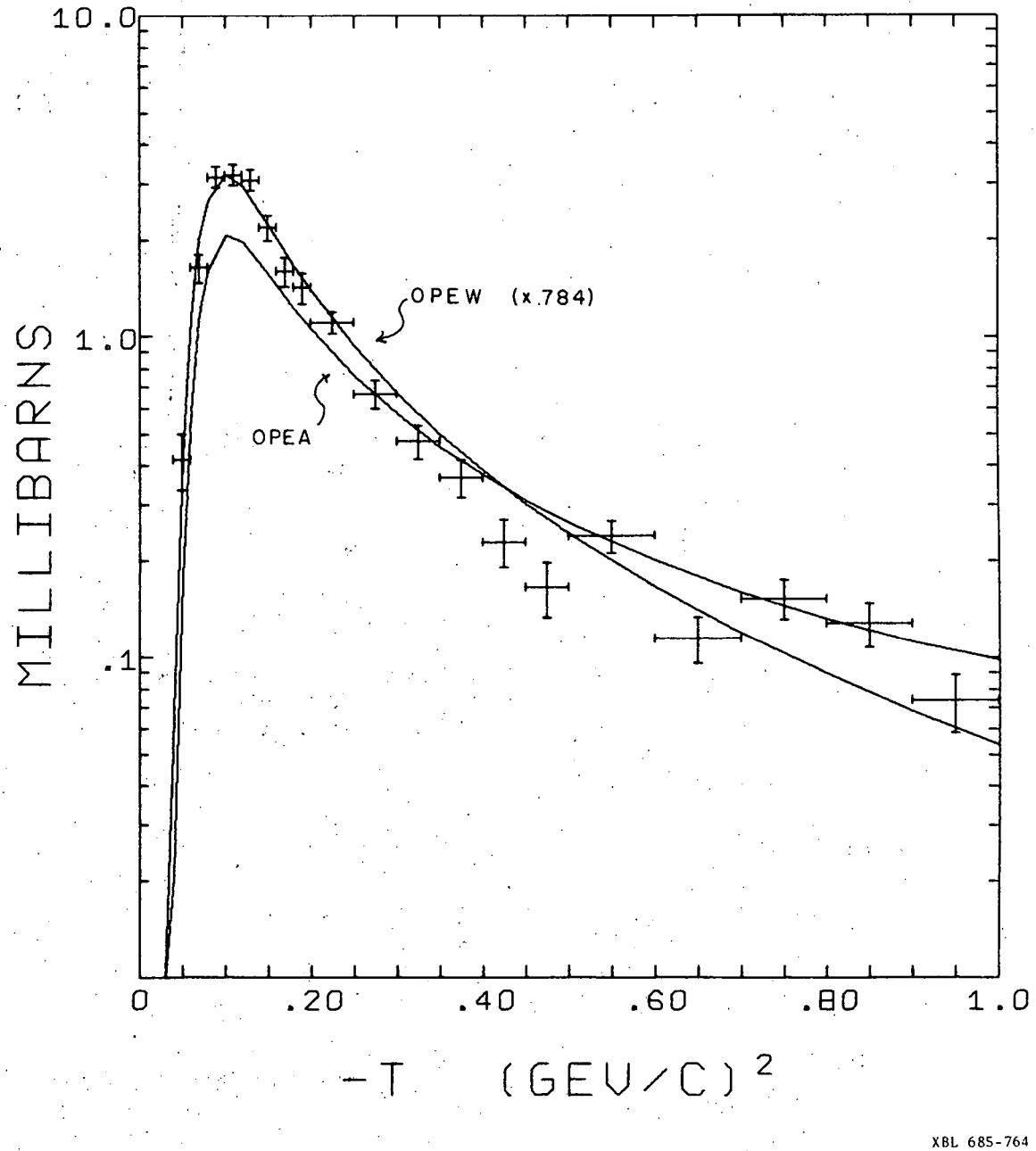

Fig. 58. $d\sigma/dt$ for $N^*\rho$ production in the $N^*\rho$ mass region showing OPEA and OPEW predictions as well as the experimental points.

five incident momenta (weighted so the area under each curve, for the region $0<-t<.5$ $(GeV/c)^2$, was equal to the number of events in that region at the corresponding momentum). Also, the OPEW curve is multiplied by .784 (the background correction factor), since it seems to fit the data much better without a correction for background. Only the form factor approach seems to yield a sufficiently steep slope for $d\sigma/dt$, although the OPEA gives a fair approximation to experiment. Further discussion of these models is given in Appendix (D), and as noted there the OPEA predictions are down by about a factor of three from those obtained by assuming the N^* and ρ to be stable (zero width) particles.

For the analysis of the decay distribution we use the formalism given by Donohue[26] and parameterize the $N^*\rho$ joint distribution as follows:

$$
\begin{aligned}
W(\theta_c,\varphi_c,\theta_d,\varphi_d) = 1/16\pi^2 \Big[& 1+1/2(1-3\rho^c_{00})(1-3\cos^2\theta_c)-1/2(1-4\rho^d_{33})(1-3\cos^2\theta_d) \\
& +R_8\,(1-3\cos^2\theta_c)\,(1-3\cos^2\theta_d) \\
& -3\,(\rho^c_{1,-1}\sin^2\theta_c\cos 2\varphi_c+\sqrt{2}\,\rho^c_{10}\sin 2\theta_c\,\cos\varphi_c) \\
& -2\sqrt{3}\,(\rho^d_{3,-1}\sin^2\theta_d\cos 2\varphi_d+\rho^d_{3,1}\sin 2\theta_d\,\cos\varphi_d) \\
& -3\,(1-3\cos^2\theta_d)\,(R_9\sin^2\theta_c\cos 2\varphi_c+1/\sqrt{2}\,R_{10}\sin 2\theta_c\,\cos\varphi_c) \\
& -\sqrt{3}\,(1-3\cos^2\theta_c)\,(R_{11}\sin^2\theta_d\cos 2\varphi_d+R_{12}\sin 2\theta_d\,\cos\varphi_d) \\
& +3\sqrt{3}\,(\sin^2\theta_c\sin^2\theta_d\,(R_{13}\cos(2\varphi_c+2\varphi_d)+R_{14}\cos(2\varphi_c-2\varphi_d)) \\
& \quad +\sin^2\theta_c\sin 2\theta_d\,(R_{15}\cos(2\varphi_c+\varphi_d)+R_{16}\cos(2\varphi_c-\varphi_d)) \\
& \quad +1/\sqrt{2}\,\sin 2\theta_c\sin^2\theta_d\,(R_{17}\cos(\varphi_c+2\varphi_d)+R_{18}\cos(\varphi_c-2\varphi_d)) \\
& \quad +1/\sqrt{2}\,\sin 2\theta_c\sin 2\theta_d\,(R_{19}\cos(\varphi_c+\varphi_d)+R_{20}\cos(\varphi_c-\varphi_d))\Big]
\end{aligned}
$$

a) θ_c, φ_c, θ_d, φ_d are the decay angles in either the helicity or

Jackson frames for the ρ° and N^{*++} respectively ($c \equiv \rho$, $d \equiv N^*$).

b) ρ^α_{ij} is the real part of the ij^{th} density matrix element for the α^{th} particle.

c) The R_k are combinations of joint density matrix elements given in Appendix (D). The above distribution is given in terms of orthogonal but not orthonormal functions and the terms in ρ^α_{ij} constitute the decay distribution of the α^{th} particle. The ρ^α_{ij} and R_k have been experimentally determined, by the method of moments, and are displayed in the figures which follow.

The joint-decay parameters are plotted as a function of momentum transfer in Fig. (59 and 60) for the helicity frame and given in Table X. The OPEA predictions are shown and seen to agree with the general features of the data, at least at small momentum transfer. The experimental values are listed in Table XI for the individual momenta, and for the parameters as a function of t′ rather than of t in Table XII.

A crude attempt has been made to take into account the background. Given two reactions, A and B, and two mass regions 1 and 2, with N^α_i the number of events in region i of reaction α and ρ^α_i a density matrix element corresponding to these events, then:

$$N_1 \rho_1 = N_1^A \rho_1^A + N_1^B \rho_1^B \qquad N_1 = N_1^A + N_2^B$$

$$N_2 \rho_2 = N_2^A \rho_2^A + N_2^B \rho_2^B \qquad N_2 = N_2^A + N_2^B$$

Then, to the extent that ρ, for a given process, does not depend upon the mass region for which it is obtained, one may solve for ρ^A (or ρ^B) in terms of the experimental parameters ρ_1 and ρ_2 and the percentages of the two reactions present in the respective regions.

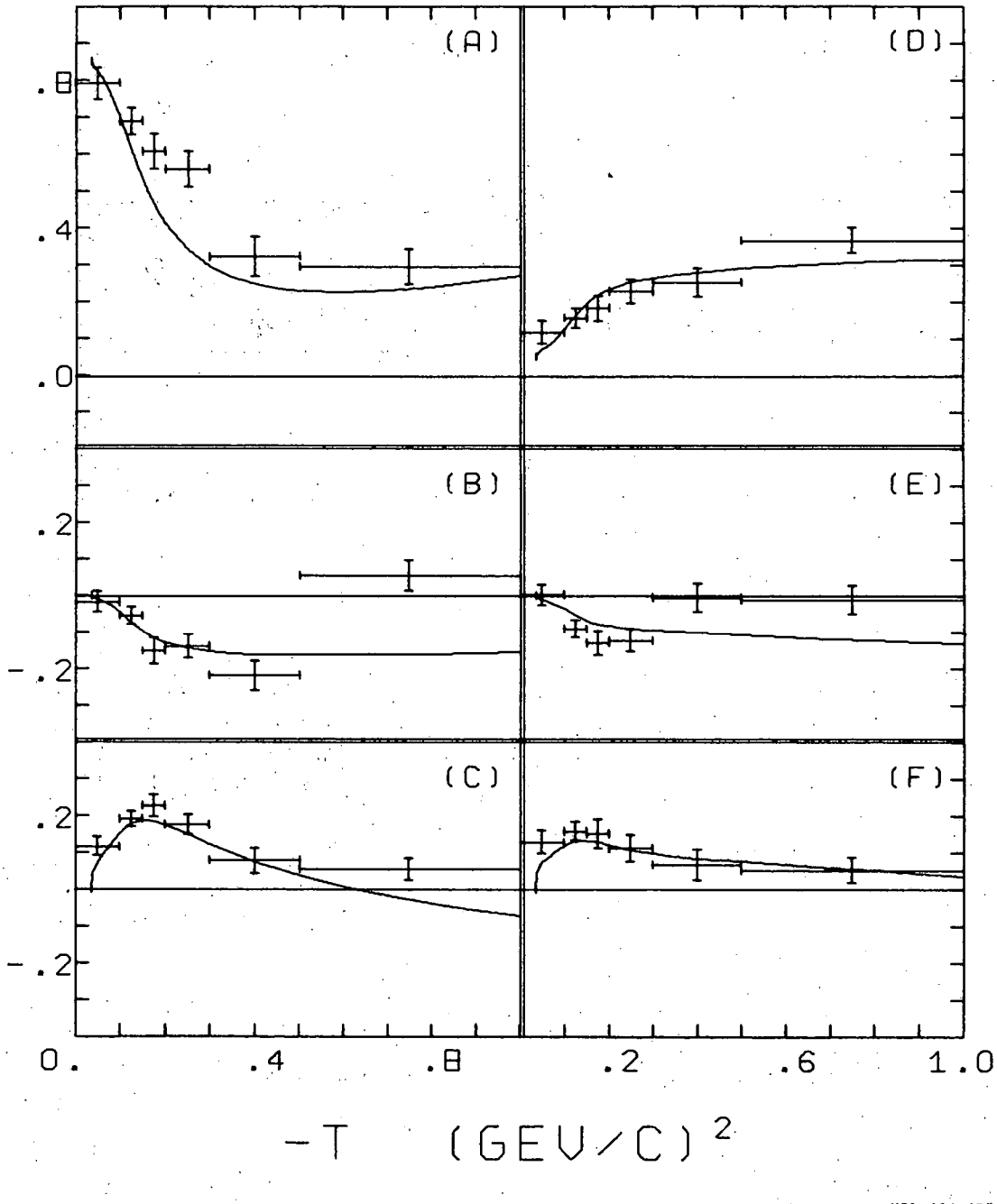

XBL 684-657

Fig. 59. $N^*\rho$ decay matrix elements as a function of momentum transfer, with the OPEA predictions being indicated by the solid line, for (A) $\rho^c_{0,0}$, (B) $\rho^c_{1,-1}$, (C) $\rho^c_{1,1}$, (D) $\rho^d_{3,3}$, (E) $\rho^d_{3,-1}$, (F) $\rho^d_{3,1}$ ($c \equiv \rho^\circ$, $d \equiv N^{*++}$).

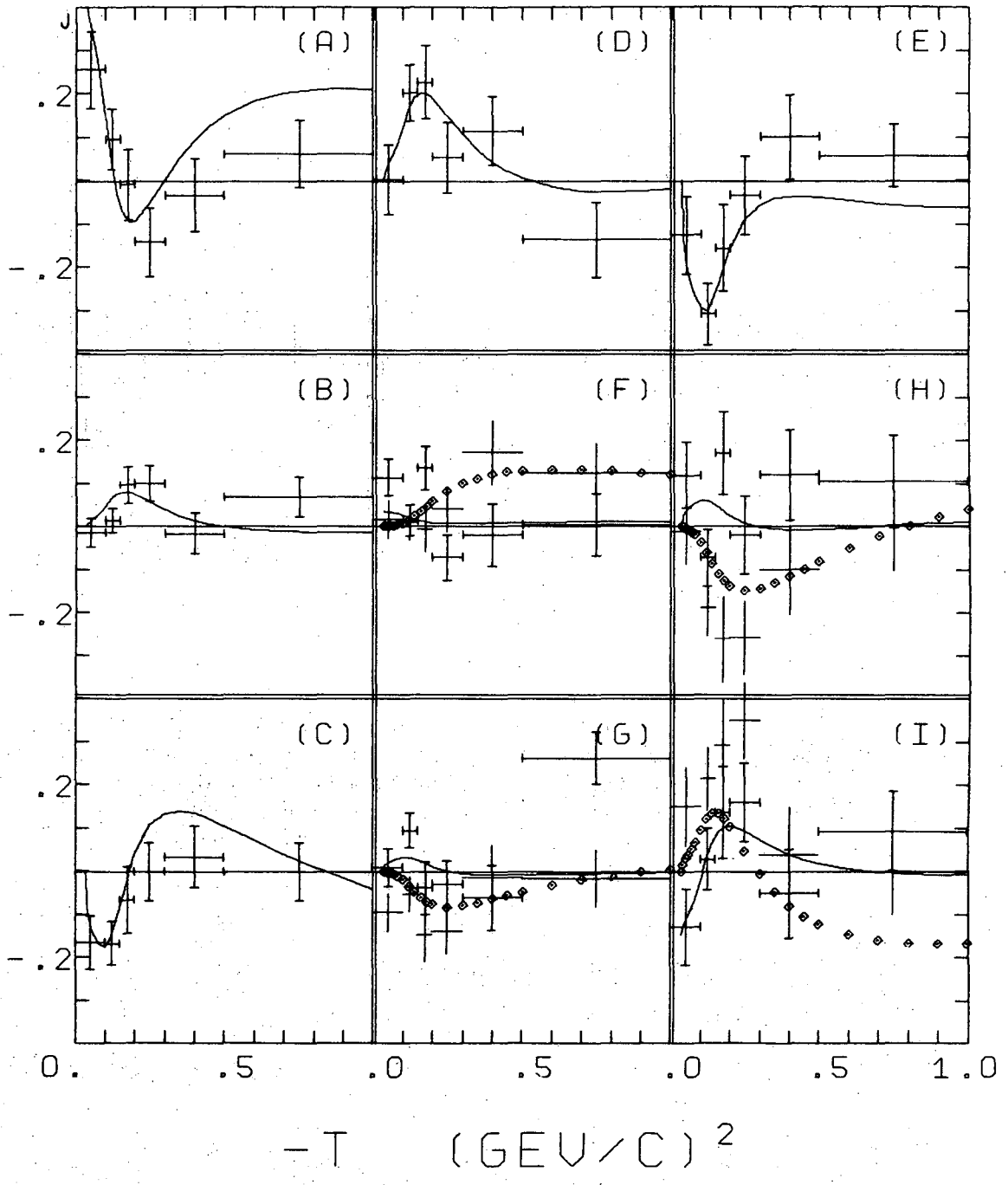

XBL 685-763

Fig. 60. $N^*\rho$ joint decay parameters as a function of momentum transfer, with the OPEA predictions being indicated by the solid (dotted) curves, for R_8 - R_{16} ((A)-(I)) using the solid curves, and R_{17}-R_{20} ((F)-(I))using the bare error bars and dotted curves.

Table X. $N^*\rho$ decay angular distribution parameters, (all momenta combined).

Parameter	$0<-t<.1$	$.1<-t<.15$	$.15<-t<.2$	$.2<-t<.3$	$.3<-t<.5$	$.5<-t<1.0$
$\rho^c_{0,0}$	.791±.044	.690±.036	.608±.049	.558±.048	.323±.054	.295±.047
$\rho^c_{1,-1}$	-.016±.028	-.054±.024	-.150±.035	-.138±.034	-.217±.041	.056±.044
$\rho^c_{1,0}$	.117±.025	.192±.020	.229±.031	.177±.028	.080±.035	.055±.031
$\rho^d_{3,3}$	.117±.032	.156±.027	.182±.036	.230±.034	.252±.039	.367±.034
$\rho^d_{3,-1}$	.003±.030	-.088±.025	-.129±.034	-.122±.031	-.004±.039	-.011±.041
$\rho^d_{3,1}$	.130±.031	.160±.027	.154±.040	.114±.036	.068±.042	.054±.035
R_8	.255±.089	.095±.070	-.010±.082	-.142±.079	-.034±.083	.062±.078
R_9	-.015±.034	.014±.029	.097±.043	.101±.042	-.016±.048	.069±.047
R_{10}	-.164±.062	-.166±.050	-.066±.079	-.001±.068	.033±.072	-.002±.067
R_{11}	.002±.081	.202±.065	.226±.084	.052±.082	.113±.079	-.137±.087
R_{12}	-.126±.090	-.309±.072	-.156±.099	-.035±.091	.099±.098	.055±.072
R_{13}	.114±.043	.014±.036	.136±.051	-.072±.053	-.020±.072	.004±.073
R_{14}	.016±.045	.008±.038	-.006±.051	.039±.051	.172±.074	.124±.069
R_{15}	.010±.044	.096±.041	-.039±.061	-.029±.054	-.062±.075	.262±.061
R_{16}	-.095±.044	-.052±.040	-.147±.061	-.139±.052	-.015±.077	-.016±.066
R_{17}	.119±.078	-.072±.066	.171±.097	-.019±.091	.120±.105	.104±.108
R_{18}	-.011±.077	-.187±.066	-.262±.099	-.258±.085	-.101±.104	.002±.106
R_{19}	-.128±.089	.028±.072	.136±.107	.160±.091	-.051±.102	.093±.093
R_{20}	.149±.090	.215±.073	.292±.105	.350±.088	.037±.113	-.001±.100
			(Jackson Frame)			
$\rho^c_{0,0}$	.826±.052	.671±.047	.625±.056	.276±.046	.199±.036	.586±.037
$\rho^c_{1,-1}$	-.041±.031	-.081±.033	-.066±.039	.047±.043	.047±.035	-.000±.026
$\rho^c_{1,0}$	-.058±.031	-.125±.029	-.004±.035	-.054±.032	-.063±.022	-.047±.022
$\rho^d_{3,3}$	.040±.040	.084±.035	.208±.040	.196±.040	.288±.027	.194±.026
$\rho^d_{3,-1}$	-.047±.032	-.037±.030	.021±.039	.088±.036	.036±.030	.024±.025
$\rho^d_{3,1}$	.012±.036	.008±.036	-.036±.041	-.075±.035	-.074±.028	.018±.026
R_8	.435±.120	.393±.091	.110±.103	.154±.084	.082±.058	.212±.066

Table XI. $N^*\rho$ decay angular distribution parameters (helicity frame) in the three -t intervals: a) 0.<-t<.15, b) .15<-t<.30, c) .30<-t<1.0 $(GeV/c)^2$.

Momentum		$\rho^c_{0,0}$	$\rho^c_{1,-1}$	$\rho^c_{1,0}$	$\rho^d_{3,3}$	$\rho^d_{3,-1}$	$\rho^d_{3,1}$	R_8
2.95	a.	.742±.092	.001±.055	.207±.046	.157±.072	-.055±.066	.113±.062	.373±.202
	b.	.549±.098	-.132±.072	.106±.057	.288±.071	-.119±.068	.157±.065	-.036±.172
	c.	.166±.104	-.174±.092	.084±.070	.357±.075	-.004±.092	-.050±.084	.064±.160
3.19	a.	.823±.061	-.041±.039	.145±.037	.074±.048	-.072±.039	.122±.047	.307±.139
	b.	.623±.069	-.188±.045	.270±.038	.161±.048	-.122±.044	.179±.051	-.098±.117
	c.	.334±.068	-.089±.061	-.005±.046	.293±.049	.049±.052	.052±.050	.104±.111
3.53	a.	.736±.054	-.032±.036	.143±.032	.249±.036	.015±.038	.108±.038	-.058±.096
	b.	.686±.068	-.127±.046	.146±.041	.301±.045	-.223±.045	.094±.052	-.139±.110
	c.	.438±.075	-.127±.055	.141±.046	.312±.051	-.023±.059	.058±.057	.068±.118
3.74	a.	.704±.059	-.016±.039	.160±.033	.135±.043	-.098±.042	.182±.044	.065±.108
	b.	.472±.072	-.117±.061	.232±.049	.187±.057	-.035±.054	.143±.061	-.103±.121
	c.	.206±.071	-.069±.068	.040±.049	.322±.056	-.061±.059	.164±.056	-.159±.117
4.08	a.	.663±.061	-.083±.042	.182±.034	.064±.044	-.066±.038	.203±.044	.300±.120
	b.	.498±.080	-.135±.061	.221±.053	.090±.059	-.082±.052	.085±.076	.032±.131
	c.	.289±.088	.135±.083	.102±.056	.310±.071	-.016±.070	.012±.066	-.010±.145
ALL	a.	.731±.028	-.038±.018	.162±.016	.140±.020	-.051±.019	.148±.020	.160±.055
	b.	.582±.034	-.143±.024	.201±.021	.208±.024	-.125±.023	.133±.027	-.081±.057
	c.	.308±.036	-.071±.031	.067±.023	.313±.026	-.008±.028	.061±.027	.017±.057

Table XII. $N^*\rho$ decay angular distribution parameters, as a function of t′ (all momenta combined).

Parameter	$0<-t<.02$	$.02<-t<.05$	$.05<-t<.1$	$.1<-t<.2$	$.2<-t<.5$	$.5<-t<1.0$
$\rho^c_{0,0}$	.826±.044	.742±.043	.599±.043	.530±.044	.367±.045	.232±.050
$\rho^c_{1,-1}$	.044±.028	-.067±.029	-.157±.029	-.140±.034	-.180±.033	.144±.048
$\rho^c_{1,0}$	.110±.025	.174±.025	.234±.024	.196±.027	.054±.029	.096±.031
$\rho^d_{3,3}$	.078±.032	.174±.033	.195±.030	.207±.032	.261±.032	.372±.037
$\rho^d_{3,-1}$	-.028±.029	-.050±.031	-.112±.029	-.119±.030	-.013±.032	-.018±.044
$\rho^d_{3,1}$	.087±.034	.189±.030	.207±.032	.082±.035	.055±.034	.076±.039
R_8	.275±.091	.145±.088	-.012±.074	-.148±.072	-.006±.070	.033±.080
R_9	-.055±.033	.006±.035	.099±.035	.110±.041	.009±.038	.007±.052
R_{10}	-.145±.062	-.167±.063	-.175±.062	.054±.066	-.005±.060	.010±.067
R_{11}	.054±.083	.186±.078	.160±.076	.154±.076	-.017±.067	-.062±.095
R_{12}	-.161±.096	-.263±.086	-.338±.083	.063±.084	.103±.078	.014±.079
R_{13}	.077±.041	.076±.044	.047±.046	-.049±.049	.024±.059	.018±.081
R_{14}	.020±.042	-.058±.046	.054±.046	.070±.047	.149±.060	.054±.077
R_{15}	.032±.047	.036±.045	.032±.050	-.006±.053	.020±.061	.290±.066
R_{16}	-.074±.047	-.080±.046	-.097±.048	-.168±.053	-.026±.060	.031±.073
R_{17}	.069±.077	-.016±.084	.052±.079	.003±.086	.178±.087	.000±.115
R_{18}	-.088±.078	-.116±.083	-.186±.078	-.288±.082	-.087±.085	.028±.116
R_{19}	-.195±.091	-.007±.087	.242±.086	.099±.088	-.026±.085	.095±.101
R_{20}	.093±.094	.278±.085	.269±.085	.344±.087	.020±.095	-.043±.099
			(Jackson Frame)			
$\rho^c_{0,0}$	.855±.043	.839±.039	.822±.041	.704±.046	.561±.045	.187±.049
$\rho^c_{1,-1}$	.058±.027	-.018±.026	-.045±.026	-.053±.031	-.084±.033	.122±.048
$\rho^c_{1,0}$	-.024±.026	-.058±.029	-.040±.027	-.114±.028	-.015±.029	-.091±.031
$\rho^d_{3,3}$	.057±.032	.052±.032	.006±.033	.112±.034	.204±.033	.190±.044
$\rho^d_{3,-1}$	-.016±.028	.020±.027	-.003±.027	-.064±.029	.019±.031	.086±.040
$\rho^d_{3,1}$	.006±.035	.048±.034	.017±.031	-.003±.034	-.028±.034	-.089±.038
R_8	.335±.092	.415±.089	.501±.095	.366±.093	.115±.080	.167±.094

$$\rho^A = \frac{N_1\rho_1 N_2^B - N_2\rho_2 N_1^B}{N_1^A N_2^B - N_2^A N_1^B} \quad , \qquad (\text{for } N_1^A/N_1^B \neq N_2^A/N_2^B)$$

$$\rho^A = \frac{\beta_2\rho_1 - B_1\rho_2}{\alpha_1\beta_2 - \alpha_2 B_1} \quad , \qquad \alpha_i = N_i^A/N_i, \; B_i = 1 - \alpha_i$$

Corrected density matrix elements have been calculated using this formula, with A being $N^*\rho$ production, B the background, and taking the relative fraction of each from Table IX. These are listed in Table XIII. This correction is seen not to materially alter the density matrix elements. Since the matrix elements are functions of the resonance masses, the differences between the "corrected" and "uncorrected" values may be largely a consequence of their being obtained in different mass regions. This is particularly true because of the large component of $N^*\rho$ "tail" in the background region.

It was noted several years ago[10] that the decays of the N^{*++} and ρ° were not independent, but that the ρ° decay cosine distribution was different for different regions of the N^* decay cosine and vice versa. This has led to a more general interest in the decay correlations of the $N^*\rho$ system.

In general, for a joint distribution $W(\theta_c, \varphi_c; \theta_d, \varphi_d)$ no correlation between the two decays occurs if the joint distrubution factors into a product of individual distributions:

$$1) \quad W(\theta_c, \varphi_c ; \theta_d, \varphi_d) = W_c(\theta_c, \varphi_c)\, W_d(\theta_d, \varphi_d)$$

The $N^*\rho$ joint distribution is of the form:

$$2) \quad W = k\Big(1 + \sum_i A_i^c f_i^c + \sum_i A_i^d f_i^d + \sum_{ij} B_{ij} f_i^c f_j^d + \sum_k A_k f_k\Big)(\theta_c, \varphi_c ; \theta_d, \varphi_d) \qquad (i,j = 1,3 \;\; k = 4,7)$$

Table XIII. $N^{*}\rho$ decay angular distribution parameters, corrected for background (all momenta combined).

Parameter	0<-t<.1	.1<-t<.15	.15<-t<.2	.2<-t<.3	.3<-t<.5	.5<-t<1.0
$\rho^{c}_{0,0}$	.896±.082	.676±.065	.547±.086	.467±.084	.259±.095	.266±.084
$\rho^{c}_{1,-1}$	-.008±.051	-.028±.045	-.166±.062	-.146±.060	-.253±.072	.104±.077
$\rho^{c}_{1,0}$	.175±.048	.247±.041	.246±.054	.136±.050	-.023±.062	-.029±.054
$\rho^{d}_{3,3}$	.039±.060	.184±.049	.183±.063	.254±.059	.293±.068	.367±.062
$\rho^{d}_{3,-1}$	.016±.053	-.122±.046	-.126±.060	-.130±.055	.004±.067	.027±.071
$\rho^{d}_{3,1}$	.150±.056	.175±.048	.137±.068	.092±.062	.020±.073	.019±.062
R_8	.359±.157	.061±.129	-.137±.146	-.294±.137	-.119±.148	.096±.140
R_9	-.050±.061	-.035±.054	.169±.077	.150±.075	-.110±.084	.097±.083
R_{10}	-.272±.113	-.232±.096	-.073±.138	.013±.119	.074±.124	-.108±.117
R_{11}	-.065±.143	.292±.118	.239±.149	-.033±.145	.172±.137	-.159±.154
R_{12}	-.035±.159	-.385±.130	-.092±.170	.140±.154	.125±.173	.107±.130
R_{13}	.249±.086	.034±.067	.170±.092	-.135±.095	-.084±.126	-.015±.128
R_{14}	-.024±.082	-.018±.070	-.088±.094	-.063±.091	.265±.130	.206±.125
R_{15}	-.025±.081	.104±.074	-.041±.106	-.069±.096	-.023±.130	.390±.112
R_{16}	-.087±.080	-.069±.074	-.233±.109	-.212±.095	.010±.134	-.051±.116
R_{17}	.193±.141	-.215±.126	.448±.185	.004±.158	.166±.180	.274±.188
R_{18}	.033±.140	-.367±.129	-.353±.178	-.342±.152	-.122±.176	.019±.178
R_{19}	-.200±.157	.075±.131	.165±.185	.206±.154	-.234±.179	.270±.167
R_{20}	.082±.159	.322±.134	.320±.182	.460±.152	-.017±.191	.010±.171
			(Jackson Frame)			
$\rho^{c}_{0,0}$	.956±.081	.884±.064	.808±.090	.594±.082	.554±.095	.243±.083
$\rho^{c}_{1,-1}$	.023±.048	.076±.044	-.036±.055	-.082±.057	-.106±.069	.093±.076
$\rho^{c}_{1,0}$	.006±.049	-.016±.042	-.033±.055	-.115±.052	.069±.061	.006±.055
$\rho^{d}_{3,3}$	-.009±.059	.043±.049	.058±.069	.110±.061	.256±.070	.245±.070
$\rho^{d}_{3,-1}$	.043±.050	-.040±.042	-.054±.057	-.048±.052	.025±.066	.097±.064
$\rho^{d}_{3,1}$	-.028±.060	.059±.051	-.024±.066	.013±.063	-.011±.071	-.065±.062
R_8	.387±.161	.556±.137	.337±.204	.409±.154	-.041±.177	.209±.152

where the A_i^{α} and B_{ij} are functions of the decay parameters and the f_i orthogonal functions of the relevant angles:

$$f_1(\theta, \varphi) = (1-3\cos^2\theta) \quad f_2(\theta, \varphi) = \sin^2\theta \cos 2\varphi \quad f_3(\theta, \varphi) = \sin 2\theta \cos\varphi$$

$$f_4(\theta_c \varphi_c ; \theta_d, \varphi_d) = \sin^2\theta_c \sin^2\theta_d \sin 2\varphi_c \sin 2\varphi_d$$

$$f_5 = \sin^2\theta_c \sin 2\theta_d \sin 2\varphi_c \sin\varphi_d$$

$$f_6 = \sin 2\theta_c \sin^2\theta_d \sin\varphi_c \sin 2\varphi_d$$

$$f_7 = \sin 2\theta_c \sin 2\theta_d \sin\varphi_c \sin\varphi_d$$

From (1) and (2) the conditions which must hold if there are to be no correlations are obvious:

$$B_{ij} - A_i^c A_j^d = 0 \qquad i, j = 1,3$$

$$A_k = 0 \qquad k > 3$$

The above thirteen equations determine a set of correlation parameters, whose divergence from zero would indicate the presence of decay correlations. More explicitly,

$$A_1^c = 1/2\,(1-3\,\rho_{00}^c) \qquad A_1^d = -1/2\,(1-4\,\rho_{33}^d)$$

$$A_2^c = -3\,\rho_{1,-1}^c \qquad A_2^d = -2\sqrt{3}\,\rho_{3,-1}^d$$

$$A_3^c = -3\sqrt{2}\,\rho_{1,0}^c \qquad A_3^d = -2\sqrt{3}\,\rho_{3,1}^d$$

and the correlation parameters are defined as follows:

$$C_1 = R_8 - A_1^c A_1^d$$

$$C_2 = R_9 + A_2^c A_1^d/3$$

$$C_3 = R_{10} + A_3^c A_1^d \sqrt{2}/3$$

$$C_4 = R_{11} + A_1^c A_2^d /\sqrt{3}$$

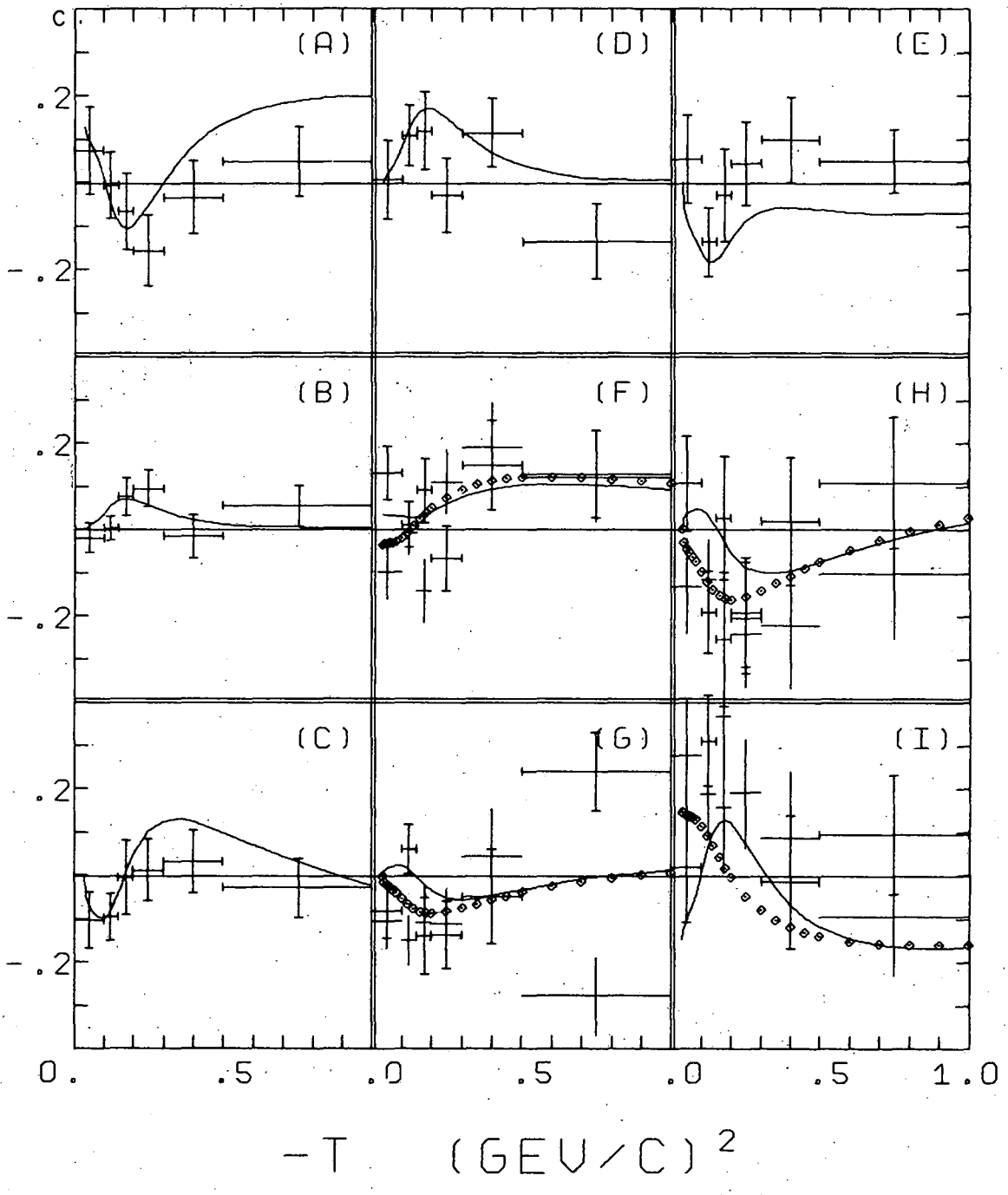

XBL 685-762

Fig. 61. $N^*\rho$ correlation parameters as a function of momentum transfer, with the OPEA predictions being indicated by the solid (dotted) curves, for C_1-C_9 ((A)-(I)) using the solid curves, and C_{10}-C_{13} ((F)-((I)) using the bare error bars and dotted curves.

Table XIV. $N^{*}\rho$ decay angular correlation parameters, (all momenta combined).

Parameter	$0<-t<.1$	$.1<-t<.15$	$.15<-t<.2$	$.2<-t<.3$	$.3<-t<.5$	$.5<-t<1.0$
C_1	.073±.101	-.006±.077	-.066±.088	-.156±.082	-.034±.084	.048±.080
C_2	-.019±.034	.004±.029	.077±.044	.095±.043	-.015±.051	.055±.048
C_3	-.102±.065	-.094±.055	-.004±.086	.013±.072	.033±.073	-.028±.069
C_4	.006±.091	.108±.070	.119±.091	-.030±.087	.114±.079	-.136±.087
C_5	.052±.101	-.137±.079	-.029±.107	.042±.096	.097±.099	.049±.073
C_6	.130±.062	.012±.053	.091±.074	-.066±.075	.150±.105	.129±.101
C_7	-.081±.064	.061±.058	-.140±.088	-.136±.077	-.047±.109	.240±.090
C_8	.107±.110	-.191±.095	.027±.143	-.191±.127	.020±.148	.109±.151
C_9	.019±.128	.311±.105	.547±.155	.595±.130	-.013±.153	.095±.137
C_{10}	-.097±.062	-.006±.053	-.142±.072	.111±.074	.192±.103	.120±.101
C_{11}	-.105±.063	-.148±.057	-.108±.087	-.109±.076	.046±.108	-.278±.090
C_{12}	-.130±.109	-.115±.093	-.433±.139	-.239±.125	-.221±.147	-.102±.151
C_{13}	.278±.126	.187±.102	.156±.150	.190±.127	.088±.152	-.094±.137
			(Jackson Frame)			
C_1	.036±.107	.123±.086	.124±.138	.225±.101	.073±.109	.164±.085
C_2	.007±.032	-.033±.028	.041±.041	-.081±.040	.073±.041	-.050±.050
C_3	-.033±.069	.091±.062	-.011±.090	.001±.078	-.028±.078	-.055±.078
C_4	.030±.085	.113±.067	-.055±.106	-.071±.080	-.003±.101	.084±.077
C_5	.117±.101	.041±.085	.001±.114	.114±.096	-.010±.106	-.154±.071
C_6	.099±.057	-.009±.045	.140±.067	-.009±.066	.079±.090	.069±.101
C_7	-.144±.063	-.021±.052	-.044±.077	.076±.078	-.095±.087	-.171±.095
C_8	-.017±.111	-.135±.091	.032±.120	-.058±.113	-.017±.149	.013±.135
C_9	-.107±.133	-.244±.110	-.355±.134	-.399±.140	-.167±.168	.024±.138
C_{10}	-.131±.057	-.076±.045	-.222±.067	.025±.066	.045±.090	-.040±.101
C_{11}	.009±.063	-.032±.052	.200±.077	.094±.078	.106±.087	.081±.095
C_{12}	.039±.111	.052±.091	.000±.120	.067±.112	-.128±.149	.390±.134
C_{13}	.323±.133	.274±.110	.300±.134	.324±.139	.298±.168	.149±.138

$$C_5 = R_{12} + A_1^c A_3^d / \sqrt{3}$$

$$C_6 = (R_{13} + R_{14}) - A_2^c A_2^d / (3\sqrt{3})$$

$$C_7 = (R_{15} + R_{16}) - A_2^c A_3^d / (3\sqrt{3})$$

$$C_8 = (R_{17} + R_{18}) - A_3^c A_2^d \sqrt{2}/(3\sqrt{3})$$

$$C_9 = (R_{19} + R_{20}) - A_3^c A_3^d \sqrt{2}/(3\sqrt{3})$$

$$C_{10} = R_{14} - R_{13}$$

$$C_{11} = R_{16} - R_{15}$$

$$C_{12} = R_{18} - R_{17}$$

$$C_{13} = R_{20} - R_{19}$$

These parameters are listed in Table XIV for each momentum and shown in Fig. (61) for the combined data. The OPEA predictions are again superimposed on the data and agree rather well with it. It is especially gratifying that for the $\cos\theta_\rho$ -- $\cos\theta_{N^*}$ correlation, experiment and theory are in reasonable agreement, since this is the most prominent of the correlations.

In all of the above no provision is made for any asymmetry in the $\cos\theta_\rho$ or $\cos\theta_{N^*}$ distributions. Given the general formula for the joint decay distribution no such asymmetry is permissable. It is well known, however, that such an asymmetry not only exists for the ρ meson but is very large.[10] Fig. (62) shows the $\cos\theta_\rho$ (and $\cos\theta_{N^*}$) distributions for $N^*\rho$ events, and Table XV lists values of $\langle\cos\theta_\rho\rangle$ and $\langle\cos^2\theta_\rho\rangle$ for the different momenta. The figure also shows these distributions for a tight $N^*\rho$ cut and for a background sample. The magnitude of the effect is seen by noting that the forward to backward ratio, $(E/B)_\rho$, for the $N^*\rho$ region is 2.3, implying a 30% excess of events in the forward

Table XV. The first two moments and forward-to-backward ratios of the N^* and ρ decay cosines for the $N^*\rho$ and central $N^*\rho$ regions.

Momentum	$\langle\cos\theta_\rho\rangle$	$\langle\cos^2\theta_\rho\rangle$	$\left(\frac{F-B}{F+B}\right)_\rho$	$\langle\cos\theta_{N^*}\rangle$	$\langle\cos^2\theta_{N^*}\rangle$	$\left(\frac{F-B}{F+B}\right)_{N^*}$
			Helicity frame -- $N^*\rho$ region			
2.95	.169±.036	.381±.019	.223±.060	.048±.035	.325±.019	.030±.061
3.19	.196±.027	.418±.014	.278±.042	.044±.026	.364±.013	.076±.044
3.53	.201±.026	.424±.014	.298±.041	.042±.024	.316±.012	.085±.042
3.74	.172±.030	.396±.015	.249±.047	.057±.029	.349±.014	.107±.048
4.08	.176±.032	.400±.016	.313±.050	.059±.033	.383±.016	.101±.053
ALL	.186±.013	.408±.007	.277±.021	.049±.013	.347±.006	.083±.022
			Helicity frame -- $N^*\rho$ Central region			
2.95	.120±.058	.402±.030	.148±.092	.172±.054	.359±.030	.200±.091
3.19	.219±.042	.388±.022	.330±.067	.058±.043	.366±.021	.107±.071
3.53	.241±.041	.411±.022	.336±.064	.036±.040	.346±.019	.047±.068
3.74	.236±.044	.398±.023	.363±.070	.044±.045	.360±.022	.084±.074
4.08	.243±.048	.413±.026	.368±.075	-.017±.051	.388±.024	.000±.081
ALL	.219±.020	.402±.011	.321±.032	.052±.021	.363±.010	.080±.034
			Jackson frame -- $N^*\rho$ region			
2.95	.139±.039	.427±.018	.231±.059	.094±.037	.379±.018	.112±.061
3.19	.208±.028	.460±.014	.262±.042	.074±.028	.397±.013	.080±.044
3.53	.193±.027	.433±.013	.267±.041	.063±.026	.391±.013	.103±.042
3.74	.148±.032	.461±.015	.235±.047	.062±.031	.408±.015	.088±.048
4.08	.156±.034	.451±.017	.218±.052	-.012±.034	.424±.016	-.039±.053
ALL	.175±.014	.448±.007	.249±.021	.057±.014	.400±.006	.071±.022

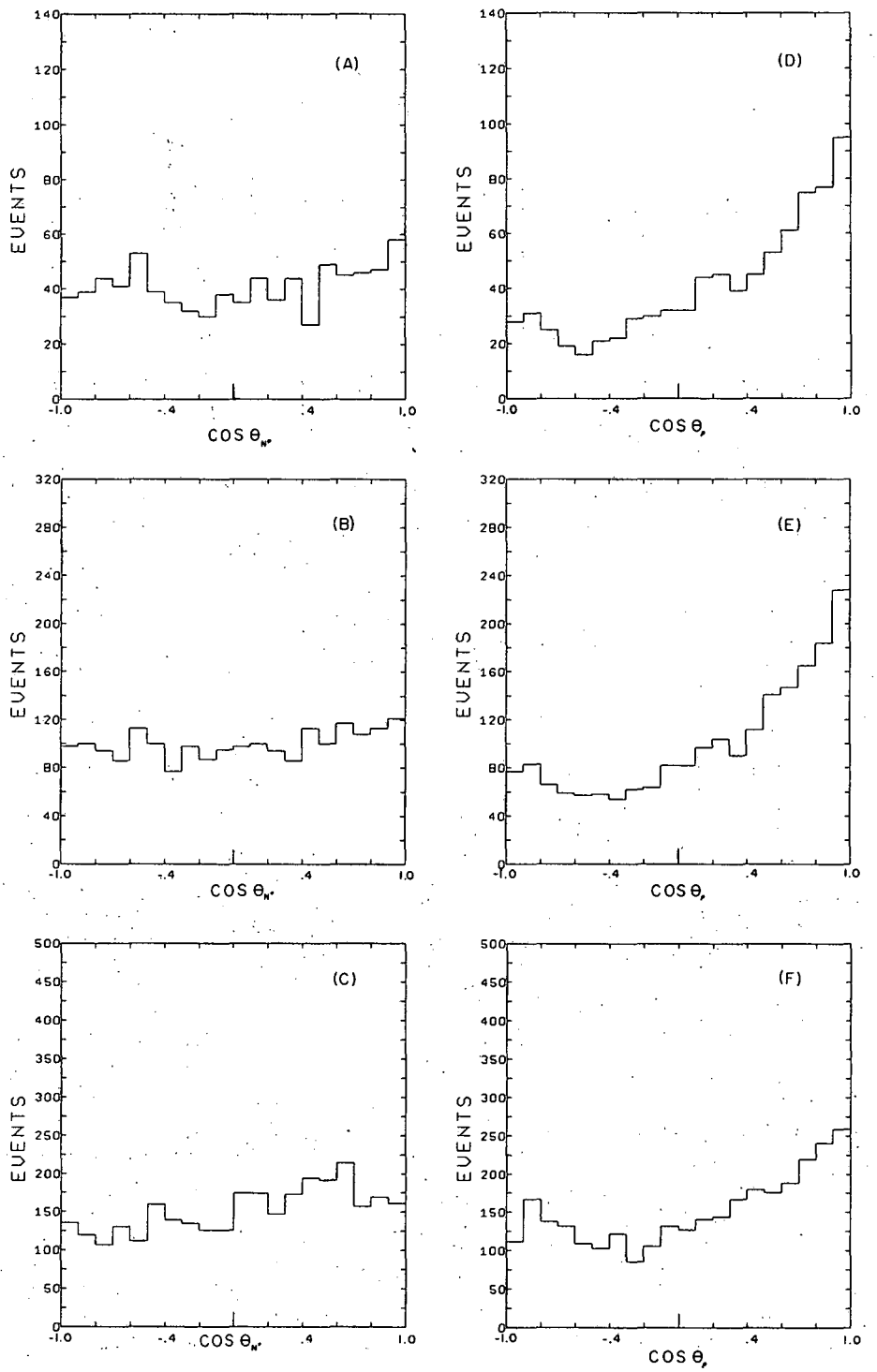

XBL 684-692

Fig. 62. N^* (left) and ρ (right) decay cosine distributions for the three following mass regions: Central $N^*\rho$--(A) and (D), $N^*\rho$ region--(B) and (E), Background region--(C) and (F).

direction. That the effect is associated with $N^*\rho$ production is confirmed by the fact that the effect is heightened in the central $N^*\rho$ region and diminished in the background region. Using the method of moments to obtain the decay parameters from formula (1) effectively involved folding the distribution about $\theta = \pi/2$ and ignoring the asymmetry.

B. $\underline{\pi^+ p \rightarrow N^{*++} f^\circ}$

N^*f production is evident at the three highest momenta. At those energies it accounts for from 3.6% to 5.9% of reaction (1), according to the fit of the $\pi^+\pi^-$ -- $\pi^+ p$ triangle plot. Its cross-section has already been presented in Fig. (53).

The behavior of the following variables will be discussed briefly in what follows: the momentum transfer, the production cosine, the f° decay cosine, and the N^* decay matrix elements. The event sample consisted of 312 events selected from the upper three momenta.

The N^*f cuts are as follows: $1.17 < M(\pi^+\pi^-) < 1.31$, $1.12 < M(\pi^+ p) < 1.32$ GeV, with the usual stipulation that double N^*f events are decided on the basis of the lower momentum transfer. An additional requirement was added in order to discriminate against $N^*\rho$ events. Neither of the $\pi^+ p$, $\pi^+\pi^-$ combinations was permitted to lie within the $N^*\rho$ region, as previously defined.

The background problem was quite severe. Using the above selection criteria it was estimated to be about 55%, 53%, and 41% at the three momenta. Therefore, considerable reliance is henceforward placed upon the background calculation outlined in the previous section. The outer limits on the background region for this calculation were set to be as follows: $1.08 < M(\pi^+\pi^-) < 1.40$ GeV, $1.02 < M(\pi^+ p) < 1.42$ GeV. Table XVI gives the background figures and numbers of events in the N^*f sample

Table XVI. Percentage of N^*f production in two event samples a) N^*f cut: $1.17 < M(\pi^+\pi^-) < 1.31$ GeV, $1.12 < M(\pi^+p) < 1.32$ GeV; b) N^*f background: (outer limits) $1.08 < M(\pi^+\pi^-) < 1.04$ GeV, $1.02 < M(\pi^+p) < 1.42$ GeV (The inner limits are those of (a)); and, for (a) ((b)), if both combinations lay within the (a) ((b)) region, that with the lower $-t_{p,\pi^+p}$ was used. Neither combination is allowed to lie within the $N^*\rho$ mass region.

Momentum GeV/c	(a) N^*f region %	# Events	(b) N^*f background %	# Events
2.95	15	30	8	40
3.19	14	101	6	145
3.53	34	138	13	173
3.74	47	92	18	133
4.08	59	82	25	118
Combined	36	443	14	609
Last Three	49	312	18	424

Table XVII. Logarithmic slopes of the -t and t′ distributions in N^*f production.

Momentum	% Exponential	A_{N^*f} $(GeV/c)^{-2}$	CL
a) Monte Carlo -t fit to phase space plus exponential			
3.53	38 ± 6	8 ± 1	.3
3.74	46 ± 8	6 ± 1.5	.004
4.08	72 ± 6	8 ± 1	.2
b) Fit to t′ distribution (N^*f region)			
3.53	100	2.89 ± .88	.6
3.74		2.48 ± .79	.6
4.08		7.14 ± .52	.5
Combined		4.21 ± .43	.9
c) Fit to t′ distribution (N^*f background region)			
3.53		3.58 ± .61	.1
3.74		4.21 ± .91	.15
4.08		4.56 ± .73	.9
Combined		4.15 ± .10	.9

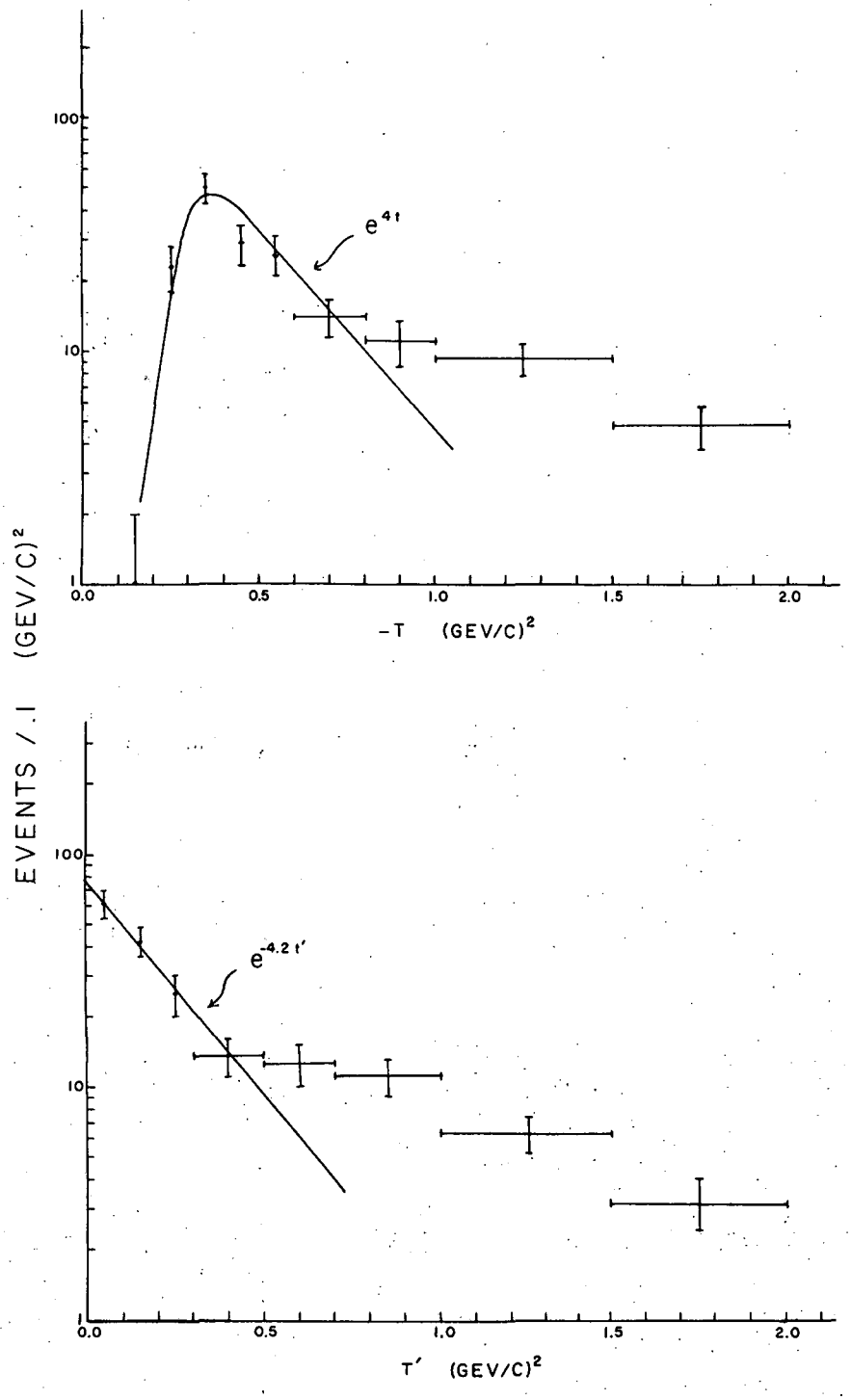

XBL 685-794

Fig. 63. The N^*f -t and t′ distributions for the events of the highest three momenta combined.

at each momentum.

The proximity of the N^*f region to the kinematic boundary renders a simple fit to the -t forward peak impossible. The boundary region extends to $-t = .64$ $(GeV/c)^2$, with the mass cuts used, and thus encompasses almost the entire forward region. This leaves two alternatives 1) One may Monte Carlo events according to different logarithmic slopes and compare with the data distribution or 2) One may use the variable t′ instead of t. The results of a rough fit to $(\alpha + \beta_e^{-6t} + \delta_e^{-8t})$ x phase space Monte Carlo events are shown in Table XVII. Values of between 6 and 8 (GeV/c) were found. The inclusion of a phase space background, of course, increases the value of A obtained over that which would be gotten from a simple fit of the -t distribution (~ 4 $(GeV/c)^{-2}$). Table XVII also shows the results of a fit to the t′ distribution, yielding $A = 4.21 \pm .43$ $(GeV/c)^{-2}$. The distribution is much more highly peaked at the highest momentum than at the other two. The -t and t′ distributions are displayed in Fig. (63) together with curves representing the above-mentioned exponential dependences.

The production cosine distribution is shown in Fig. (64). It is, as usual, very forward peaked and does not show any peaking in the backward direction. Thirty-one percent of the events have $\cos\theta > .9$ in comparison with the $N^*\rho$ mass region were over 60% lay beyond that point, and in comparison with the N^*f -background region where the corresponding figure is less than 24%.

The f° and N^{*++} decay cosine distributions are given, in the helicity frame, in Fig. (65) for the N^*f and N^*f -background regions. As with the $N^*\rho$ region, the N^* decay cosine distribution is nearly isotropic. However, for the f, the "$\pi^+\pi^-$" decay distribution shows considerably

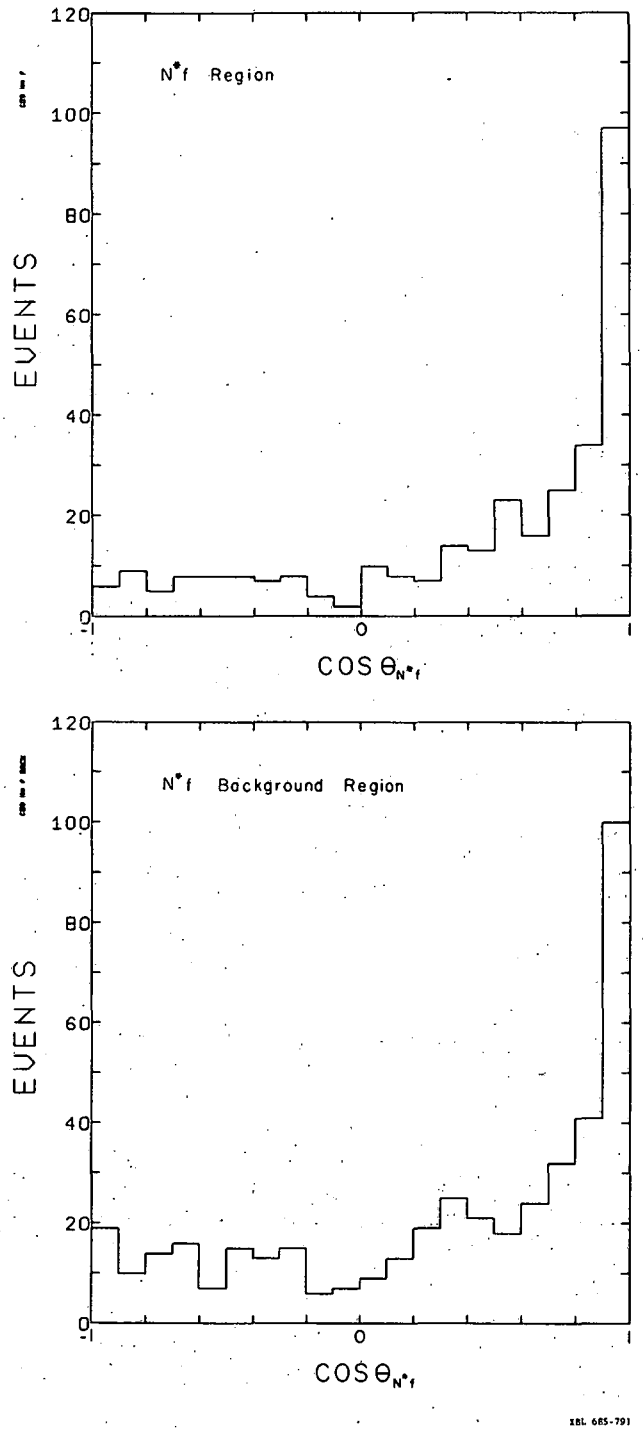

Fig. 64. The N^*f production cosine distribution for the N^*f region (top) and the N^*f - background region (bottom).

Table XVIII. N^{*++} decay density matrix elements and averages of the first eight Legendre polynomials of the f° decay cosine in $N^{*}f$ production for a) all t and b) $-t < .5$ $(GeV/c)^2$.

Parameter	$N^{*}f$ region (a)	$N^{*}f$ region (b)	Corrected for background (a)	Corrected for background (b)
$< p_1 >$	.065±.034	.009±.071	-.009±.104	-.004±.227
$< p_2 >$	.058±.026	.277±.045	-.002±.079	.148±.143
$< p_3 >$	-.050±.022	-.037±.044	-.205±.069	-.250±.144
$< p_4 >$	-.008±.019	.015±.039	-.056±.058	-.051±.123
$< p_5 >$	-.011±.017	-.030±.035	.000±.053	-.080±.112
$< p_6 >$	-.003±.016	.002±.033	.005±.049	-.041±.105
$< p_7 >$	.032±.016	.016±.032	.101±.047	.077±.100
$< p_8 >$	-.013±.014	.001±.029	-.036±.043	.047±.091
$\rho^{N^*}_{3,3}$	.196±.033	.188±.061	.132±.099	.169±.189
$\rho^{N^*}_{3,1}$	-.032±.030	-.101±.049	.031±.091	-.079±.153
$\rho^{N^*}_{3,-1}$	.053±.032	.134±.053	.175±.097	.237±.170

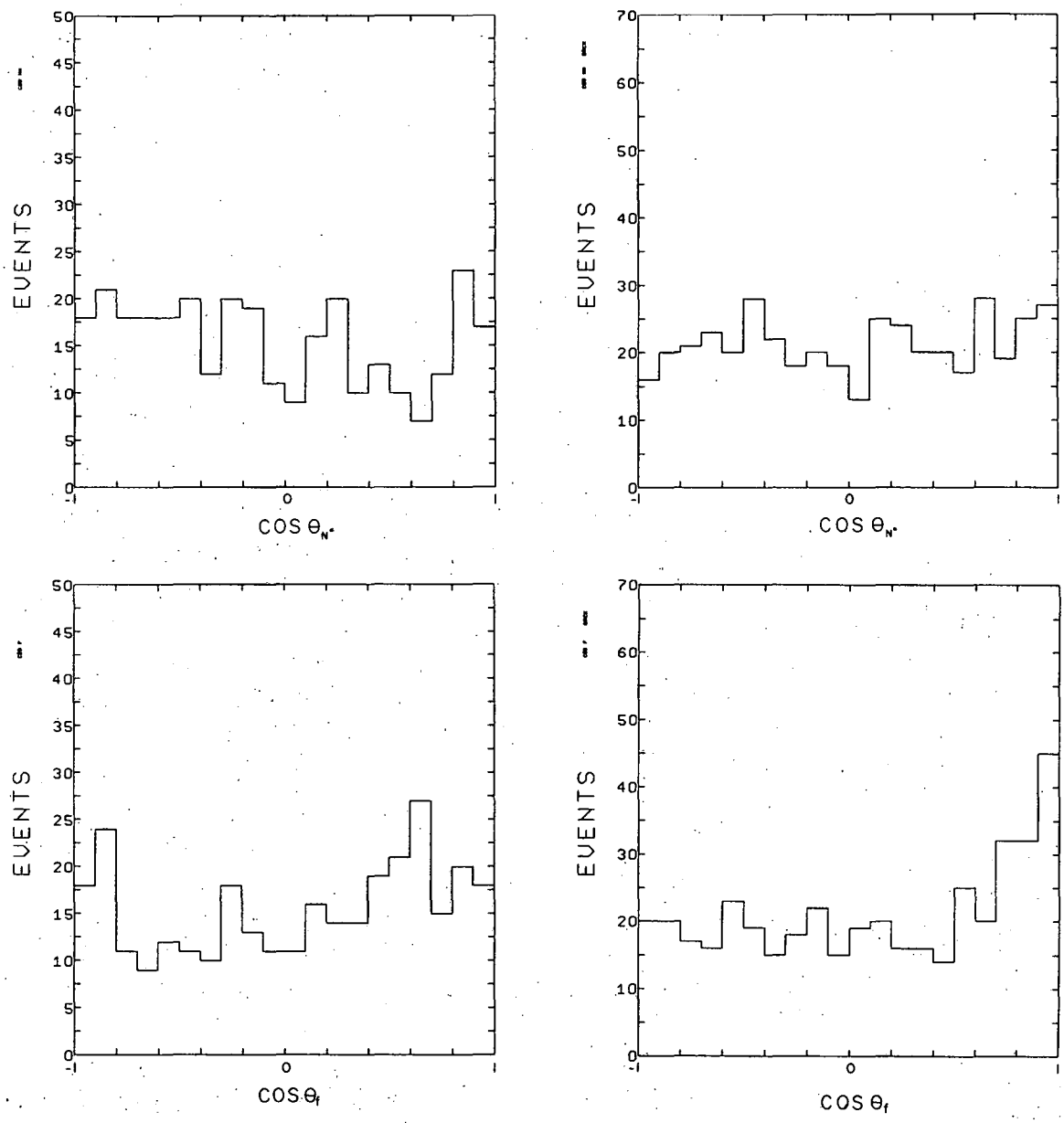

XBL 685-799

Fig. 65. The N^* (top) and f (bottom) decay cosine distributions, in the helicity frame, for the N^*f region (left) and the N^*f - background region (right).

less structure than for the ρ. In particular, the forward-backward asymmetry is very nearly absent, which is especially noteworthy in view of the strong forward peak in $\cos\theta_f$ in the background region. In order to give a better quantitative understanding of the decay distributions, the averages of the first eight Legendre polynomials in $\cos\theta_f$ and the three N^* density matrix elements are presented in Table XVIII.

C. $\pi^+ p \rightarrow N^{*++}\omega^\circ$

$N^*\omega$ production accounts for about 20% of reaction (2). The relevant triangle and Chew-Low plots are shown in Figs. (66-68) and show the magnitude and peripheral nature of this process. They also give evidence for strong ω and N^* signals outside of the double resonance region and, when compared with those for $N^*\rho$ production, are seen to demonstrate a much lesser degree of peripheralism. Comparisons will again be made between the experimental results and predictions of the CMEA. This model will be seen to be in rather poor agreement with experiment.

The fit to the $\pi^+\pi^-\pi^\circ$ -- $\pi^+ p$ triangle plot was less ambitious than that described previously for reaction (1). Because of the greater uncertainty in what processes might be contributing to the background, characteristics not immediately recognizable in the $\pi^+\pi^-\pi^\circ$ -- $\pi^+ p$ triangle plot were ignored. The Monte-Carlo program was used to generate events according to the following six final states:

1) $\pi^+ p \rightarrow \pi^+ p\, \pi^+\pi^-\pi^\circ$ (phase space)
2) $\pi^+ p \rightarrow N^{*++}\omega^\circ$ (e^{3t})
3) $\pi^+ p \rightarrow N^{*++}\eta^\circ$ (e^{3t})
4) $\pi^+ p \rightarrow N^{*++}\pi^+\pi^-\pi^\circ$ (e^{t})
5) $\pi^+ p \rightarrow \pi^+ p\, \omega^\circ$ (e^{t})
6) $\pi^+ p \rightarrow \pi^+ p\, \eta^\circ$ (e^{t})

The procedure is that previously used, except that for the ω and η it was not sufficient to use the "8030" resonance parameters, because the experimental resolution was large in comparison with the real widths.

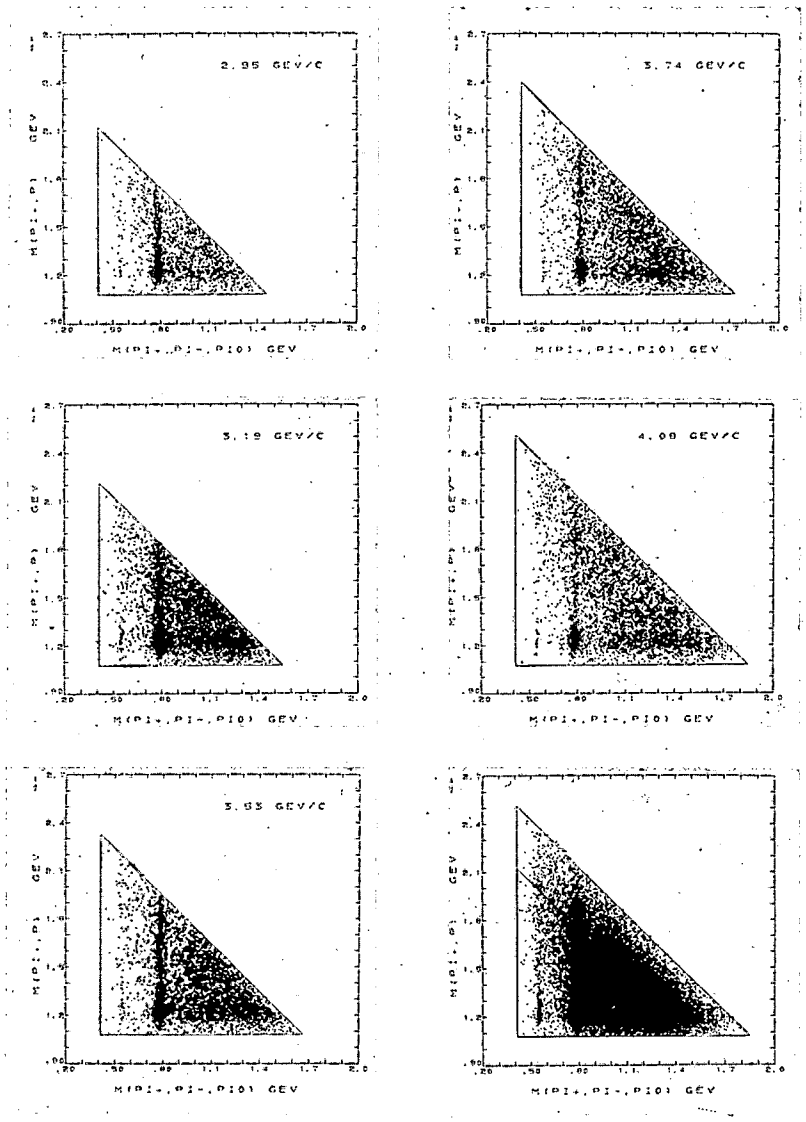

XBB 685-2617

Fig. 66. $\pi^+ p$ -- $\pi^+\pi^-\pi^0$ triangle plots for reaction (2) for the individual momenta and their sum. Both combinations are plotted for each event.

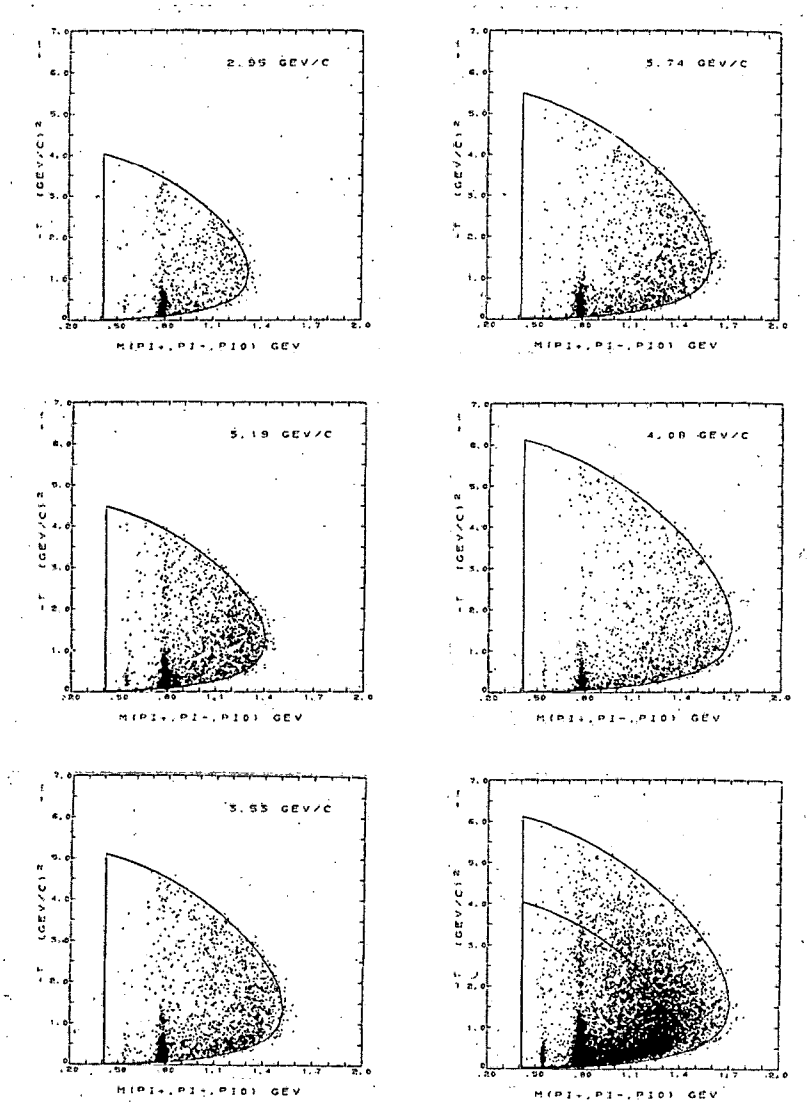

XBB 685-2618

Fig. 67. -t -- $\pi^+\pi^-\pi^0$ Chew-Low plots for events of reaction (1) lying within the N^* mass band. One combination per event is plotted (ambiguities are resolved on the basis of the lower momentum transfer).

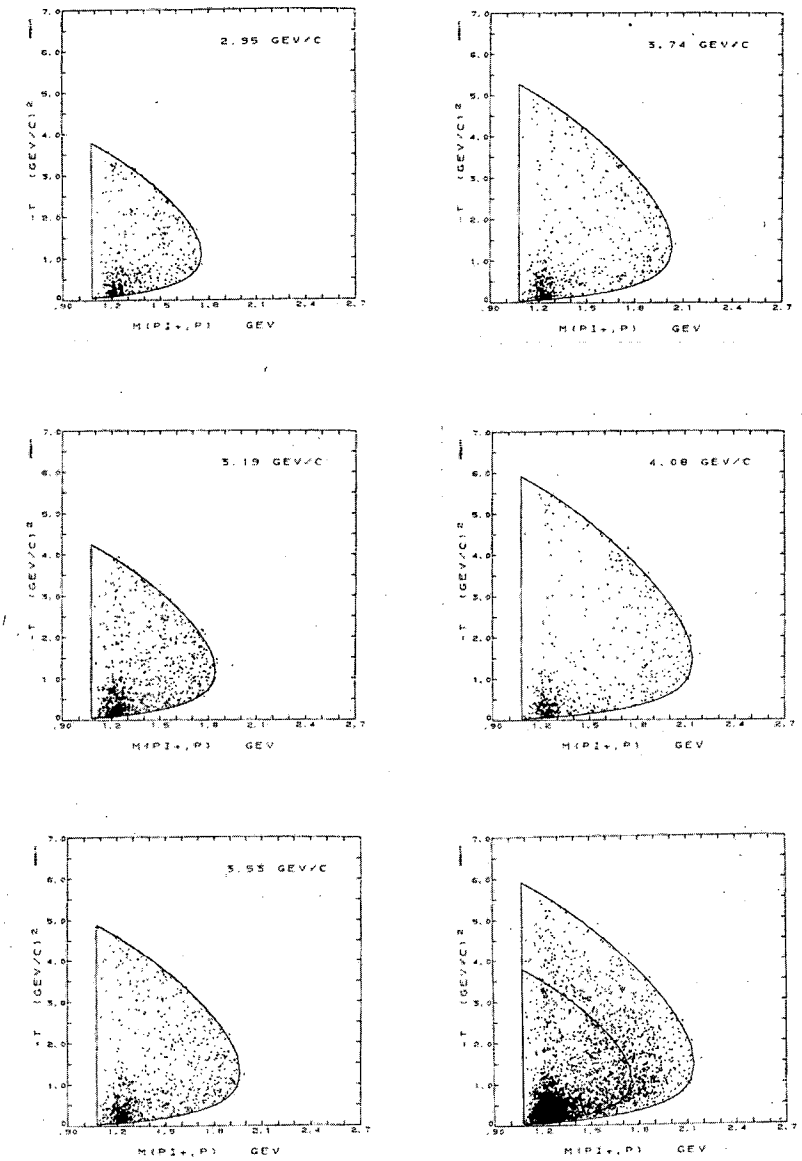

XBB 685-2616

Fig. 68. -t -- π^+p Chew-Low plots for events of reaction (1) lying within the omega mass band. One combination per event is plotted (ambiguities are resolved on the basis of the lower momentum transfer).

Table XIX. Results of a fit to the experimental $\pi^+\pi^-\pi^\circ$ -- π^+p triangle plot with events Monte-Carloed according to the six hypothetical reactions mentioned in the text.

Momentum	"Background" Reactions (%)				$N^*\omega$ and $N^*\eta$ Production (%)	
GeV/c	P.S.	N^*	ω	η	$N^*\omega$	$N^*\eta$
2.95	10.6±9.8	33.3±4.6	20.7±4.4	.1±6.0	33.7±2.6	2.0±.5
3.19	31.4±4.6	28.3±3.9	15.3±3.1	.6±.6	22.7±2.7	1.7±.2
3.53	32.5±3.7	28.9±3.3	16.6±2.5	.8±.0(?)	20.4±2.5	.9±.0(?)
3.74	35.1±3.7	30.0±3.4	12.9±2.9	.9±.5	20.4±2.8	.8±.4
4.08	33.6±2.0	26.2±.8	15.1±2.4	.4±1.3	23.9±2.0	.9±.4
Combined	33.6±1.9	27.9±1.7	14.6±1.3	.5±.4	22.2±1.3	1.2±.2

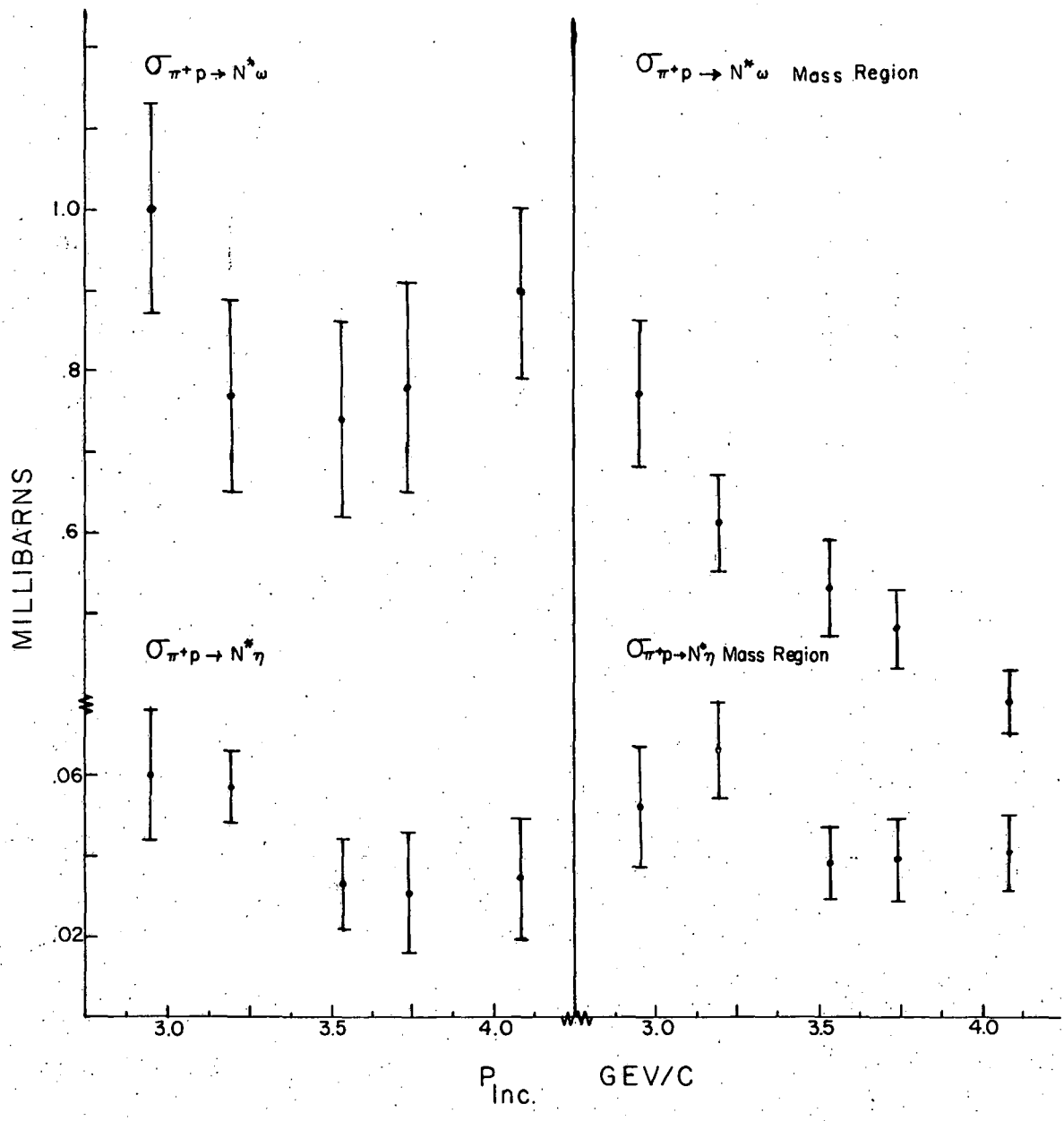

Fig. 69. Cross-sections for $N^*\omega$ and $N^*\eta$ production and for production of events within the $N^*\omega$ and $N^*\eta$ mass regions.

In a fit to the $M(\pi^+\pi^-\pi^\circ)$ distribution, values of 25.5 ± 1.3 MeV and 20.6 ± 34.6 MeV were obtained for the respective widths, yielding ~22 MeV for the experimental mass resolution.

The results of the fit are given in Table (XIX) and the resultant $N^*\omega$ and $N^*\eta$ cross-sections plotted in Fig. (69). Both the $N^*\omega$ and $N^*\eta$ cross sections are seen to decrease in this energy range. $N^*\eta$ production, in particular, decreases from 2% to less than 1% of reaction (2). It is interesting to note that at the first momentum (2.95 GeV/c) 54.4% of the events are associated with omega production, whereas at the other momenta this has shrunk to an average of about 37%.

The $N^*\omega$ mass region was chosen to lie within the bounds $.75 < M(\pi^+\pi^-\pi^\circ) < .81$ GeV, $1.12 < M(\pi^+p) < 1.32$ GeV. Again, double - $N^*\omega$ ambiguities were resolved on the basis of the lower momentum transfer. Since this reaction is less peripheral than $N^*\rho$ production, choosing the correct combination on the basis of the lower $-t_{p,N^*}$ is of less validity than before. It is an improvement over picking one of the combinations at random or averaging the two, however. As was seen in Fig. (49) and is displayed in Fig. (70), choosing the combination with the lower $-t_{p,N^*}$ clearly enhances the N^* and ω (and $N^*\omega$) signals. This affects only 1.1% of the events, fortunately.

The production cosine distribution is shown in Fig. (71). The usual forward peak is in evidence, but much less steep than for $N^*\rho$ production, and with only 34% of the events having $\cos\theta > .9$. Also, there is a distinct backward peak, less than 10% of the forward peak in magnitude, but definitely not merely a statistical fluctuation. It becomes more noticeable as the momentum is increased and the equatorial zone becomes denuded of events.

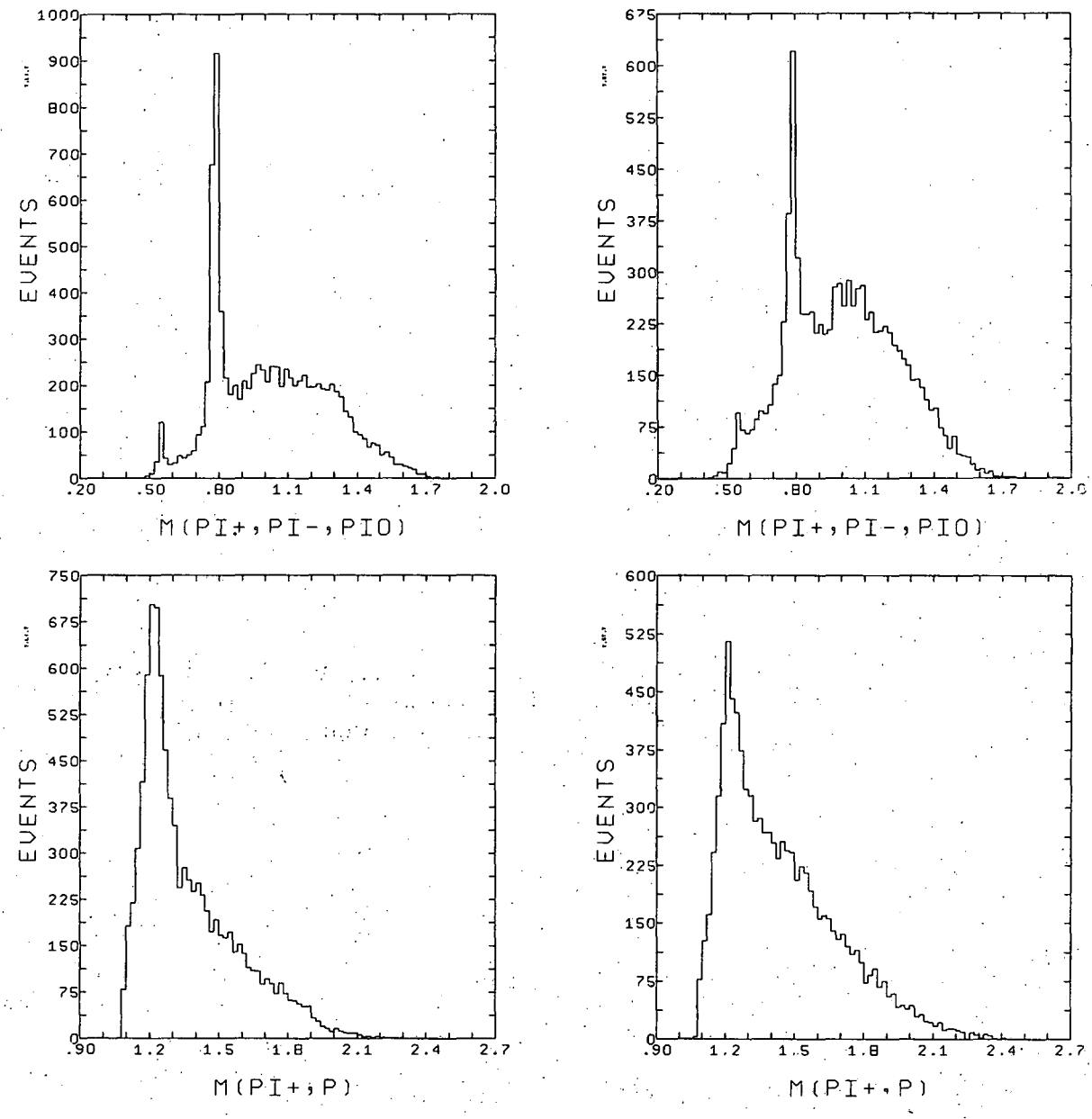

XBL 685-767

Fig. 70. $\pi^+\pi^-\pi^\circ$ (top) and π^+p (bottom) invariant mass distributions for those combinations with the lesser (left) and greater (right) momentum transfer from the proton to the π^+p system.

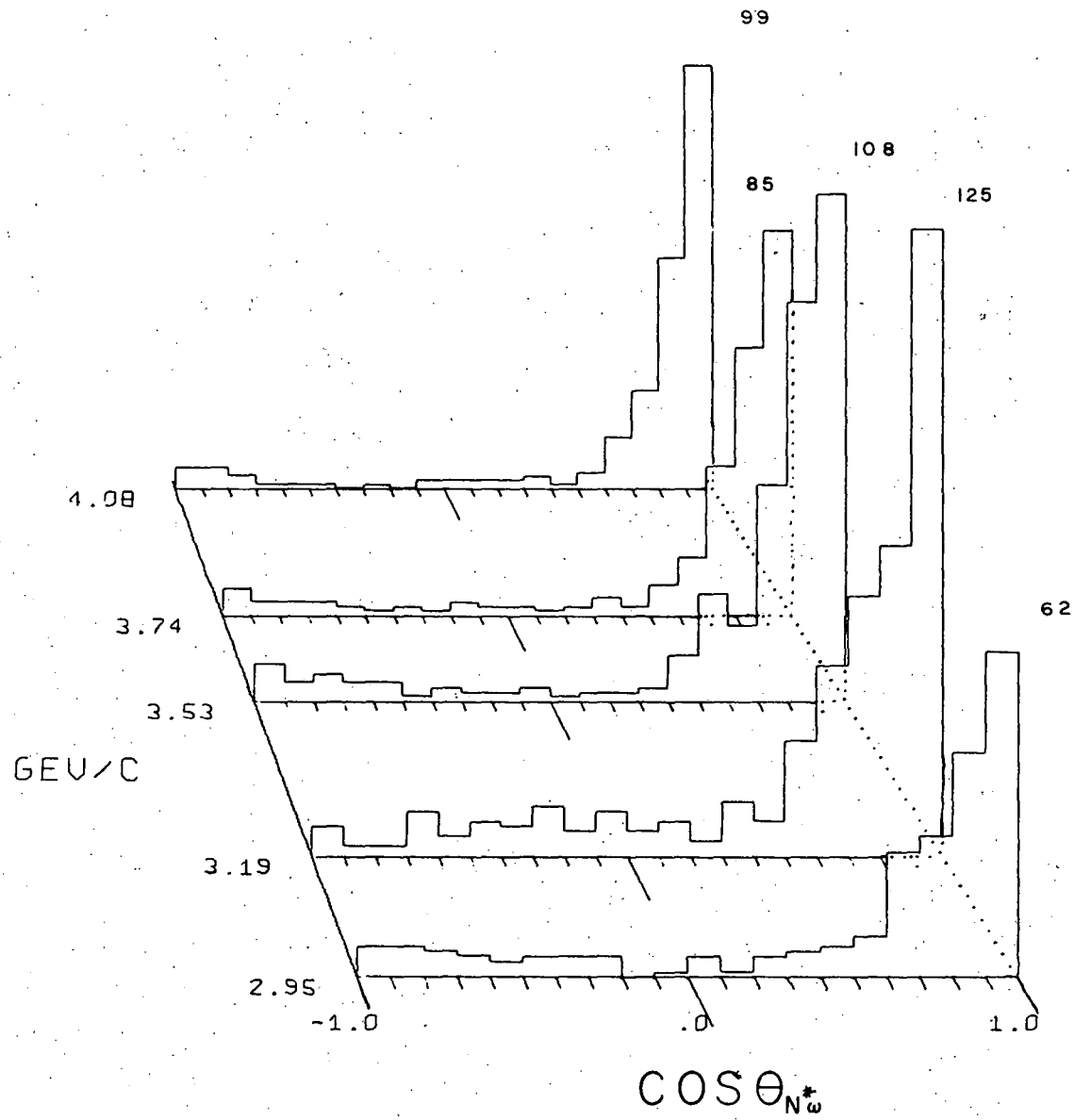

XBL 685-774

Fig. 71. $N^{*}\omega$ production cosine distributions at the five momenta. The number of events in the last bin are indicated.

The momentum transfer distribution is shown in Fig. (72). It is much less steeply peaked than was the corresponding $N^*\rho$ distribution. The peak was fit to an exponential and found to have a logarithmic slope of $2.31 \pm .06$ $(GeV/c)^{-2}$ over the interval $.2 < -t < 1.2$ $(GeV/c)^2$ with a confidence level of 35%. The N^* distribution has a simple exponential behavior over a much wider range of -t than did the $N^*\rho$ distribution, and in particular lacks the $N^*\rho$'s "anomalous" behavior in the boundary region. Looking at Figs. (56 and 72), it is interesting to note that whereas the $N^*\rho$ distribution is "concave" -- i.e. has a slope which decreases with increasing -t -- the $N^*\omega$ distribution appears to be even slightly convex, at least up to about $-t = 1.5$ $(GeV/c)^2$. There also appears to be some evidence for a dip at $-t = .8$ $(GeV/c)^2$.

The t′ distribution (Fig. (72)) was also fit to an exponential. The resultant slope, for the interval $0 < t' < 1$ $(GeV/c)^2$, was $A^{t'}_{N^*\omega} = 2.25 \pm .08$ $(GeV/c)^{-2}$.

The fitted values of the slopes for t and t′ are given in Table XX for each momentum separately. The values for the momentum transfer seem to indicate a definite shrinkage of the peak (increase in A) with energy.

In order to properly normalize the momentum transfer distribution the same procedure employed for the $N^*\rho$ was used. The background values for $N^*\omega$ (and $N^*\eta$) regions are shown in Table XXI and were used in conjunction with the mb/event figures of Table IV to obtain $d\sigma/dt$.

$d\sigma/dt$ is shown in Fig. (73) along with the OMEA predictions multiplied by a factor of four. The OMEA curve is seen to bear little resemblence to the experimental distribution. The scale factor of four, needed to normalize to the data peak, could be obtained by increasing the coupling constants and/or increasing the value of the absorption parameter γ_f.

Table XX. Logarithmic slopes of the -t and t′ distributions in $N^*\omega$ production. ($0.2 < -t < 1.2$ $(GeV/c)^2$, $0.0 < t' < 1.0$ $(GeV/c)^2$).

Momentum GeV/c	$A_{N^*\omega}^{-t}$ $(GeV/c)^{-2}$	CL	$A_{N^*\omega}^{t'}$ $(GeV/c)^{-2}$	CL
2.95	2.16 ± .25	.05	2.54 ± .14	.08
3.19	2.04 ± .19	.15	2.14 ± .17	.35
3.53	2.15 ± .17	.45	2.06 ± .15	.45
3.74	2.45 ± .22	.09	2.12 ± .18	.50
4.08	2.71 ± .28	.03	2.59 ± .20	.95
Combined	2.31 ± .06	.35	2.25 ± .08	.55

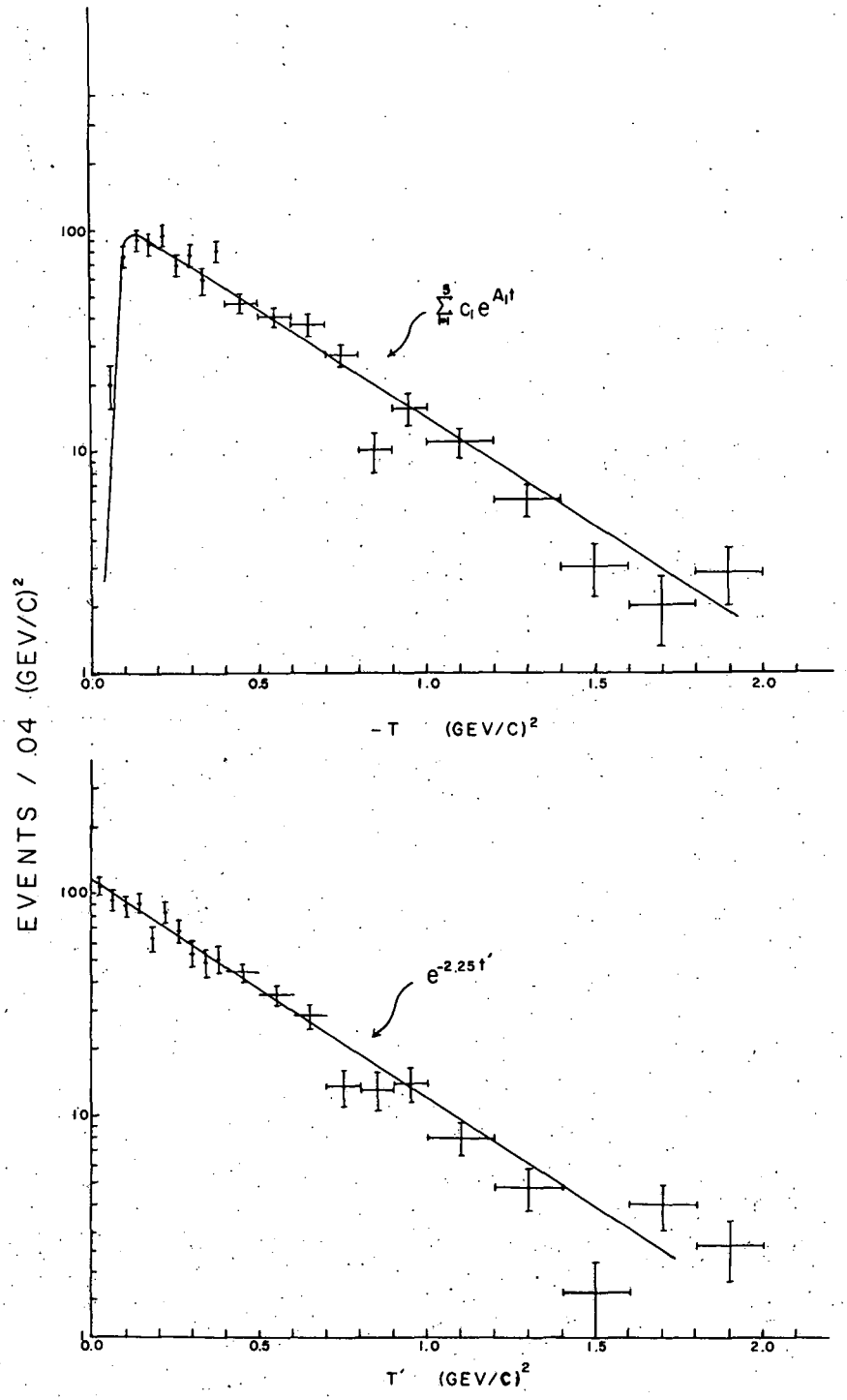

XBL 685-792

Fig. 72. The $N^*\omega$ -t and t′ distributions. The upper curve is the sum of curves at each momentum, using the logarithmic slopes of Table XX.

Table XXI. Percentages of $N^*\omega$ or $N^*\eta$ production in four mass regions of the $\pi^+\pi^-\pi^\circ$ -- π^+p triangle plot: a) $N^*\omega$ cut: $.75 < M(\pi^+\pi^-\pi^\circ) < .81$ GeV/c, $1.12 < M(\pi^+p) < 1.32$ GeV/c; b) $N^*\omega$ background: (Outer limits) $.69 < M(\pi^+\pi^-\pi) < .87$ GeV/c, $1.02 < M(\pi^+p) < 1.42$ GeV/c (The inner limits are those of (a)); c) $N^*\eta$ cut $.53 < M(\pi^+\pi^-\pi) < .57$ GeV/c, $1.12 < M(\pi^+p) < 1.32$ GeV/c; d) $N^*\eta$ background: (outer limits) $.49 < M(\pi^+\pi^-\pi) < .61$ GeV/c, $1.02 < M(\pi^+p) < 1.42$ GeV/c (The inner limits are those of (a)). In all cases ambiguities were resolved on the basis of the lower $-t_{p,\pi^+p}$ and for the $N^*\eta$ samples, no combination was allowed to lie within the $N^*\omega$ region.

Momentum GeV/c	(a) $N^*\omega$ %	(b) $N^*\omega$ background %	(c) $N^*\eta$ %	(d) $N^*\eta$ background %
2.95	76	42	88	42
3.19	74	37	80	36
3.53	76	42	75	30
3.74	82	46	75	28
4.08	87	59	81	49
Combined	79	43	80	35

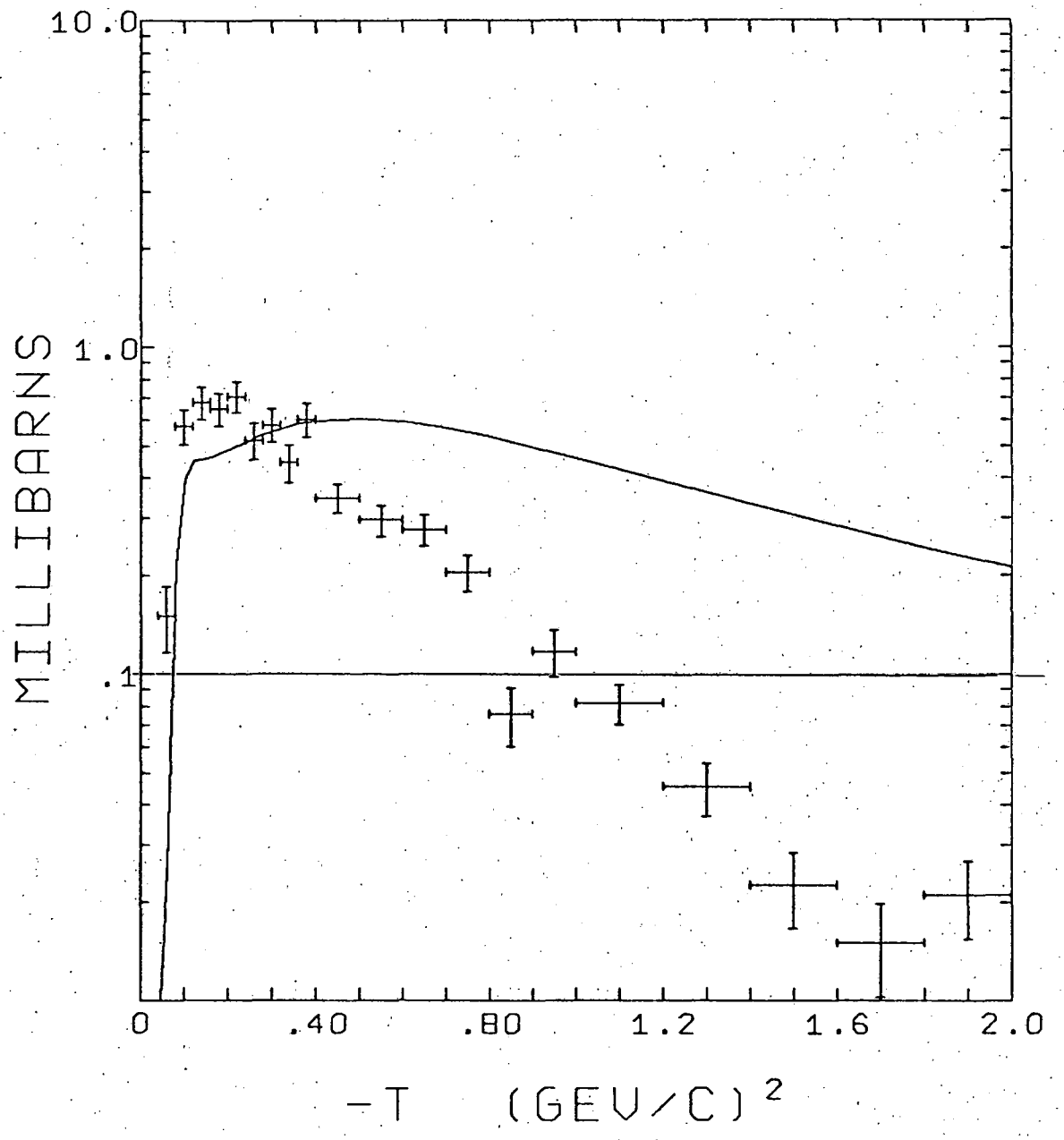

XBL 655-825

Fig. 73. $d\sigma/dt$ for $N^*\omega$ production in the $N^*\omega$ mass region, showing the OMEA predictions (x4.0) as well as the experimental points.

The very shallow slope of the curve would be affected by neither of these expedients; however, there are three coupling constants at the $N^{*++}\rho p$ vertex, and changing the ratios of these could effect the slope of $d\sigma/dt$. At least with the usual (relativistic Stodolsky-Sakurai) coupling, the ρ-exchange model, even with absorption, is seen to be in serious difficulty. Further, the Regge model with exchange of the ρ trajectory predicts a dip in $d\sigma/dt$ at $-t \simeq .55$ $(GeV/c)^2$.[37] There being no evidence in our data for such a dip, the validity of the ρ-exchange mechanism is again brought into question.

The angular decay parameters are treated for the $N^*\omega$ in precisely the same manner as they were for the $N^*\rho$. The only important distinction between the two cases is that the vector of interest in the meson decay frame is not the direction of one of the outgoing particles -- i.e. the π^+ for the ρ -- but is instead the normal to the ω decay plane. Otherwise, since the ρ and ω are both 1^- particles, the same parameterization is applicable for both the $N^*\rho$ and $N^*\omega$ systems. The decay parameters are presented in Tables XXII and XXV and in Figs. (74-76) are shown as a function of momentum transfer.

The curves superimposed upon the data points in Figs. (74-76) are the OMEA predictions. Obviously, the theoretical predictions are not at all well borne out by this experiment. The background calculation slightly improves this situation, but not sufficiently for the model to attain any real measure of success. Because of the previously mentioned uncertainty in the coupling constants used, however, this lack of agreement does not entirely invalidate the model.

Finally, the $\cos\theta$ and φ distributions for both the ω and N^* are shown in Fig. (77). They are all roughly isotropic. In particular the

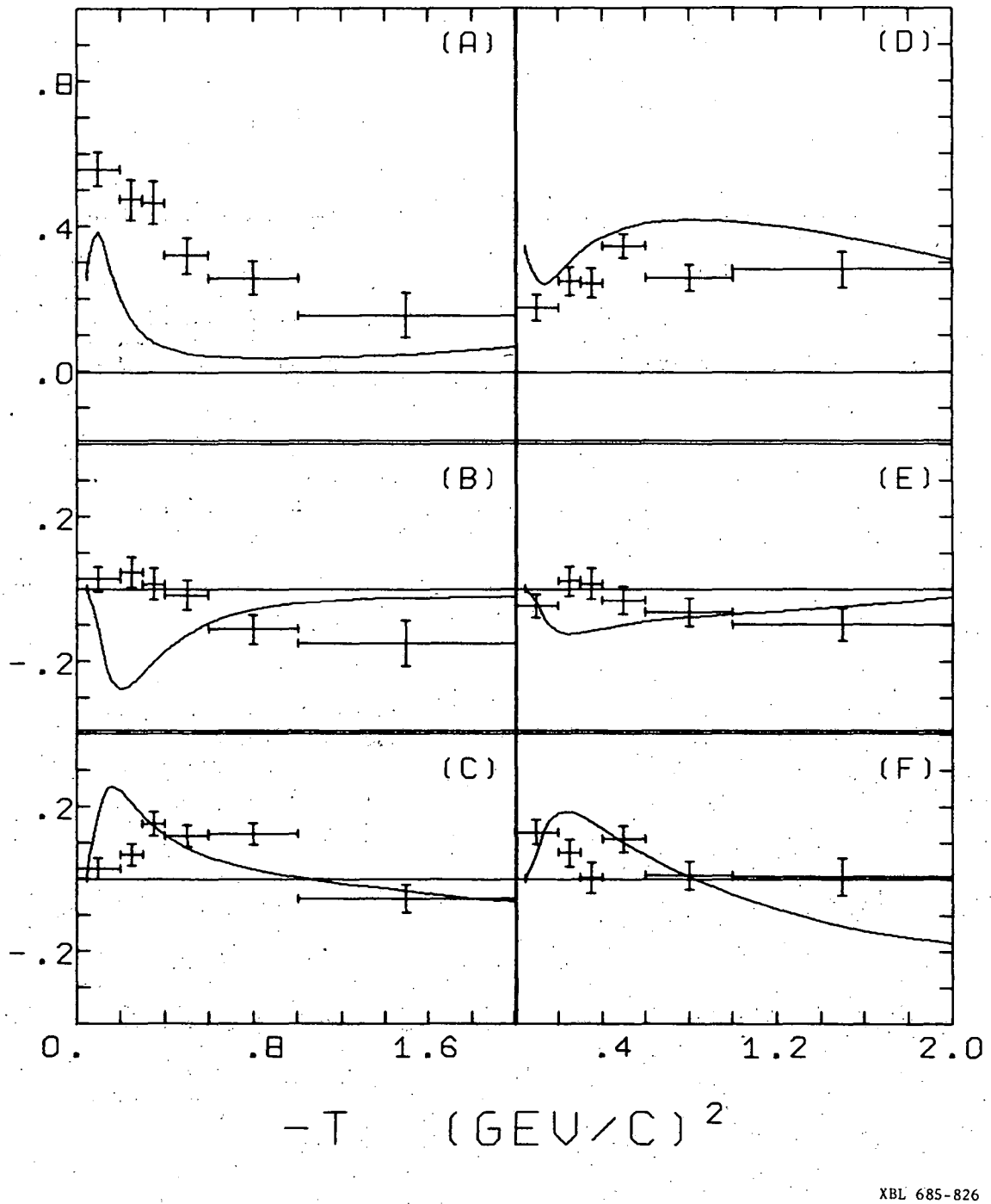

XBL 685-826

Fig. 74. $N^*\omega$ decay matrix elements as a function of momentum transfer, with the OMEA predictions being indicated by the solid line, for (A) $\rho^c_{0,0}$, (B) $\rho^c_{1,-1}$, (C) $\rho^c_{1,1}$, (D) $\rho^d_{3,3}$, (E) $\rho^d_{3,-1}$, and (F) $\rho^d_{3,1}$.

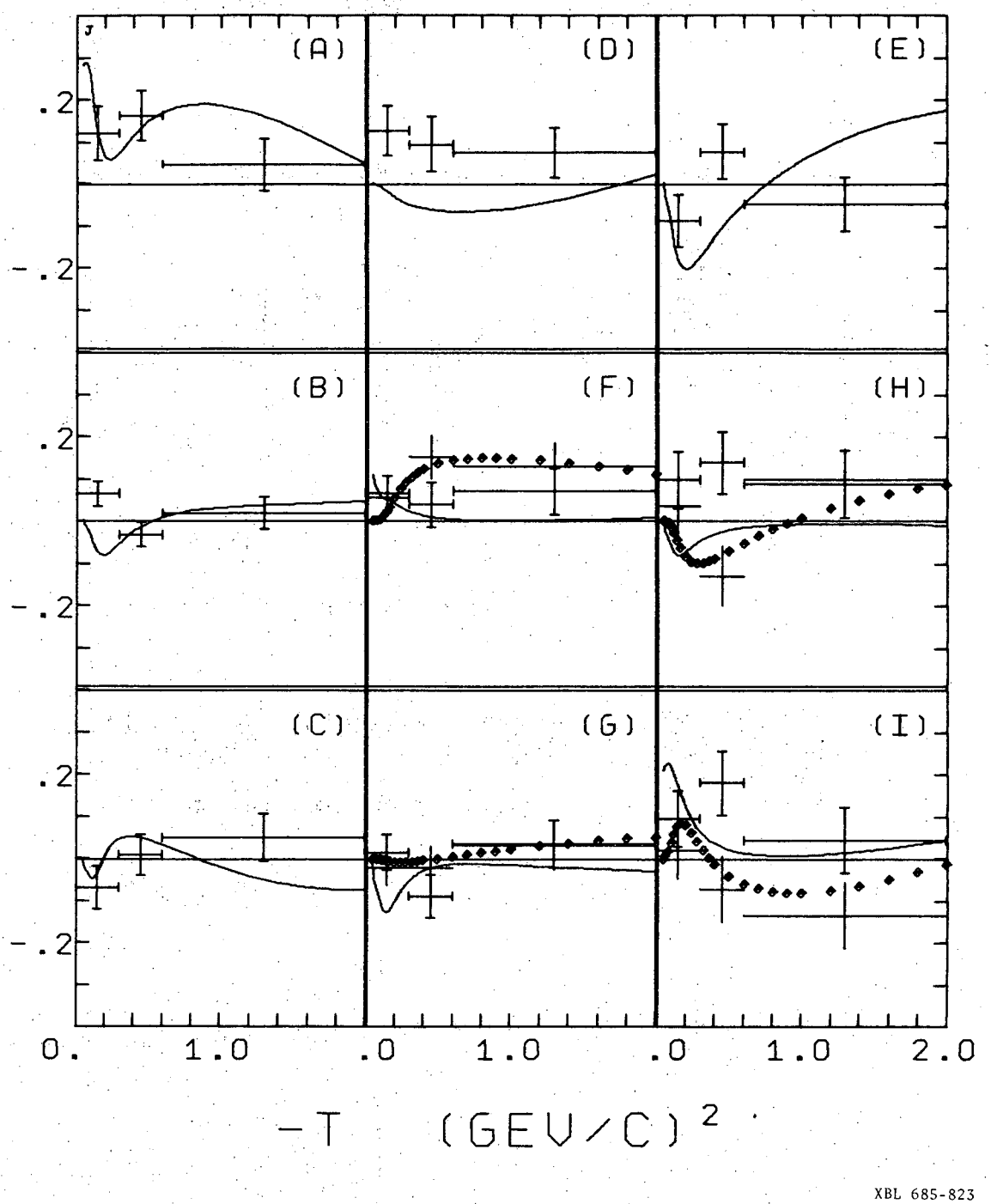

XBL 685-823

Fig. 75. $N^*\omega$ joint decay parameters as a function of momentum transfer, with the OMEA predictions being indicated, for R_8-R_{16} ((A)-(I)) with the solid curve, and R_{17}-R_{20} ((F)-(I)) with the bare error bars and dotted curve.

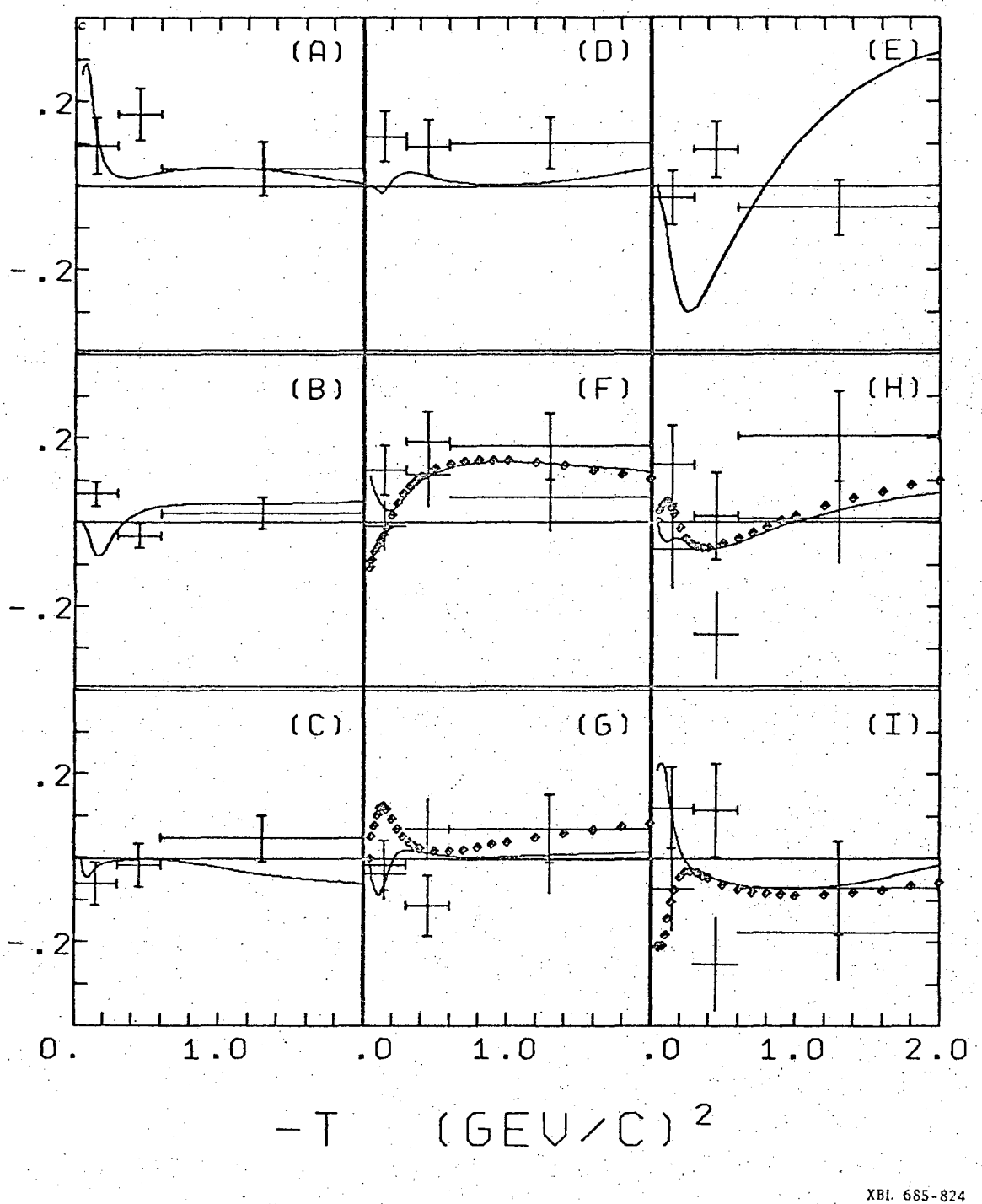

XBL 685-824

Fig. 76. $N^{*}\omega$ correlation parameters as a function of momentum transfer, with the OMEA prediction being indicated, for C_1-C_9 ((A)-(I)) with the solid curve, and C_{10}-C_{13} ((F)-(I)) with the bare error bars and dotted curve.

Table XXII. ω and N^* decay matrix elements (all momenta combined, c≡ω, d≡N^*).

Parameter	0<-t<.2	.2<-t<.3	.3<-t<.4	.4<-t<.6	.6<-t<1.0	1.0<-t<2.0
			(Helicity Frame)			
$\rho^c_{0,0}$	.558±.048	.473±.055	.466±.060	.320±.050	.257±.046	.154±.063
$\rho^c_{1,-1}$	.028±.035	.047±.041	.015±.044	-.017±.043	-.111±.041	-.150±.063
$\rho^c_{1,0}$	.029±.029	.068±.030	.153±.033	.121±.030	.126±.032	-.052±.040
$\rho^d_{3,3}$	.174±.036	.246±.040	.242±.040	.345±.034	.256±.036	.279±.051
$\rho^d_{3,-1}$	-.047±.033	.022±.040	.014±.044	-.031±.039	-.066±.039	-.098±.046
$\rho^d_{3,1}$	.130±.034	.073±.037	.003±.042	.110±.037	.010±.038	.009±.052
			(Jackson Frame)			
$\rho^c_{0,0}$	.480±.047	.364±.051	.424±.056	.395±.051	.430±.048	.559±.072
$\rho^c_{1,-1}$	-.011±.039	-.008±.043	-.006±.047	.021±.042	-.025±.040	.052±.054
$\rho^c_{1,0}$	-.087±.028	-.110±.031	-.162±.034	-.111±.031	-.150±.032	-.091±.041
$\rho^d_{3,3}$	.074±.037	.213±.039	.262±.044	.148±.039	.184±.041	.192±.045
$\rho^d_{3,-1}$	.011±.030	.041±.039	.003±.041	.083±.033	-.024±.035	-.048±.047
$\rho^d_{3,1}$	.000±.036	-.043±.039	-.025±.042	-.080±.038	-.020±.037	-.064±.056

Table XXIII. $N^*\omega$ decay angular distribution parameters, uncorrected and corrected for background (all momenta combined).

Parameter	$N^*\omega$ mass region 0<-t<.3	.3<-t<.6	.6<-t<2.0	$N^*\omega$ "corrected" 0<-t<.3	.3<-t<.6	.6<-t<2.0
$\rho^c_{0,0}$	.521±.036	.386±.039	.221±.037	.652±.074	.457±.070	.175±.066
$\rho^c_{1,-1}$	.036±.027	-.002±.031	-.125±.035	.051±.049	.015±.055	-.162±.061
$\rho^c_{1,0}$	.046±.021	.135±.022	.062±.025	.033±.038	.158±.040	.110±.044
$\rho^d_{3,3}$	.205±.027	.298±.026	.264±.030	.231±.049	.356±.050	.289±.051
$\rho^d_{3,-1}$	-.017±.026	-.010±.029	-.077±.030	-.042±.047	.001±.051	-.095±.052
$\rho^d_{3,1}$	.106±.025	.062±.028	.010±.031	.106±.045	.057±.049	.034±.053
R_8	.120±.065	.162±.060	.045±.063	.180±.119	.198±.107	.036±.112
R_9	.065±.030	-.031±.030	.019±.039	.049±.056	-.078±.056	.033±.067
R_{10}	-.069±.052	.009±.049	.051±.056	-.081±.094	.023±.089	.158±.102
R_{11}	.126±.060	.093±.066	.074±.061	.155±.110	.100±.114	.118±.108
R_{12}	-.089±.063	.075±.067	-.051±.065	-.208±.115	.122±.118	-.086±.113
R_{13}	.065±.042	.039±.053	.070±.056	.080±.077	.028±.093	.083±.097
R_{14}	.057±.041	.151±.052	.129±.057	.132±.078	.188±.092	.159±.099
R_{15}	.015±.043	-.090±.052	.035±.057	-.027±.080	-.136±.092	.027±.098
R_{16}	-.023±.040	-.022±.051	.031±.058	-.036±.074	-.003±.090	.052±.099
R_{17}	.099±.068	.138±.074	.087±.080	.156±.121	.129±.129	.140±.138
R_{18}	.036±.065	-.130±.072	.097±.073	.062±.115	-.183±.127	.171±.129
R_{19}	.095±.067	.180±.076	.044±.079	.157±.119	.234±.132	-.006±.133
R_{20}	.020±.070	-.073±.080	-.135±.078	.031±.122	-.100±.138	-.162±.130

Table XXIV. $N^*\omega$ decay angular distribution parameters (helicity frame) in the three -t intervals: a) $0<-t<.3$, b) $.3<-t<.6$, c) $.6<-t<2.0$ $(GeV/c)^2$.

Momentum		$\rho^c_{0,0}$	$\rho^c_{1,-1}$	$\rho^c_{1,0}$	$\rho^d_{3,3}$	$\rho^d_{3,-1}$	$\rho^d_{3,1}$	R_8
2.95	a.	.491±.090	-.032±.078	-.023±.062	.206±.077	-.065±.071	.044±.071	.336±.183
	b.	.357±.094	-.090±.070	.130±.057	.261±.066	-.055±.069	.122±.067	.094±.141
	c.	.162±.085	-.120±.090	.087±.063	.350±.070	.017±.081	-.009±.073	.286±.135
3.19	a.	.580±.068	.073±.049	.110±.038	.183±.051	-.073±.047	.098±.048	.265±.132
	b.	.409±.078	.026±.067	.130±.048	.311±.053	.011±.064	.015±.060	.251±.120
	c.	.306±.069	-.124±.056	.107±.046	.223±.052	-.043±.050	.050±.056	-.139±.110
3.53	a.	.502±.077	-.027±.052	.107±.043	.170±.060	.010±.056	.091±.051	.330±.139
	b.	.388±.076	.042±.058	.140±.041	.325±.048	.087±.059	.030±.052	.122±.117
	c.	.125±.074	-.205±.074	-.007±.051	.295±.055	-.186±.056	.010±.067	.067±.111
3.74	a.	.407±.080	.099±.070	-.073±.051	.235±.057	-.026±.063	.197±.063	.047±.116
	b.	.402±.097	.015±.074	.069±.051	.300±.059	-.039±.059	.122±.066	.181±.155
	c.	.289±.098	-.104±.088	.095±.067	.190±.086	-.101±.081	-.084±.073	.146±.196
4.08	a.	.582±.090	.046±.061	.035±.048	.252±.059	.075±.057	.094±.054	-.428±.143
	b.	.360±.092	-.044±.082	.218±.059	.270±.073	-.128±.072	.051±.073	.155±.159
	c.	.182±.100	-.011±.100	.018±.065	.292±.084	-.043±.083	.043±.078	.046±.196

Table XXV. $N^{*}\omega$ decay angular correlation parameters (all momenta combined).

Parameter	Helicity Frame 0<-t<.3	.3<-t<.6	.6<-t<2.0	Jackson Frame 0<-t<.3	.3<-t<.6	.6<-t<2.0
C_1	.095±.067	.170±.061	.040±.064	.173±.065	.174±.072	.081±.073
C_2	.068±.030	-.031±.030	.022±.040	.056±.034	.044±.036	.044±.036
C_3	-.061±.052	-.017±.051	.047±.057	.019±.054	-.054±.057	-.027±.062
C_4	.117±.062	.091±.066	.100±.063	.002±.053	-.075±.054	.109±.067
C_5	-.030±.065	.045±.067	-.054±.066	.074±.061	.047±.061	-.018±.073
C_6	.123±.059	.190±.074	.180±.080	.185±.061	.214±.070	.114±.068
C_7	-.016±.059	-.113±.073	.069±.082	-.065±.064	.020±.070	-.005±.074
C_8	.137±.094	.014±.105	.203±.109	.057±.089	.168±.105	-.230±.111
C_9	.119±.098	.113±.112	-.072±.111	-.107±.099	.084±.113	-.102±.122
C_{10}	-.008±.059	.112±.074	.058±.080	-.101±.061	-.177±.070	-.128±.068
C_{11}	-.038±.059	.068±.073	-.004±.082	-.028±.064	.139±.070	.020±.074
C_{12}	-.063±.094	-.269±.104	.009±.108	-.050±.088	-.185±.104	.040±.110
C_{13}	-.075±.097	-.253±.111	-.179±.111	.060±.099	.160±.112	.093±.121

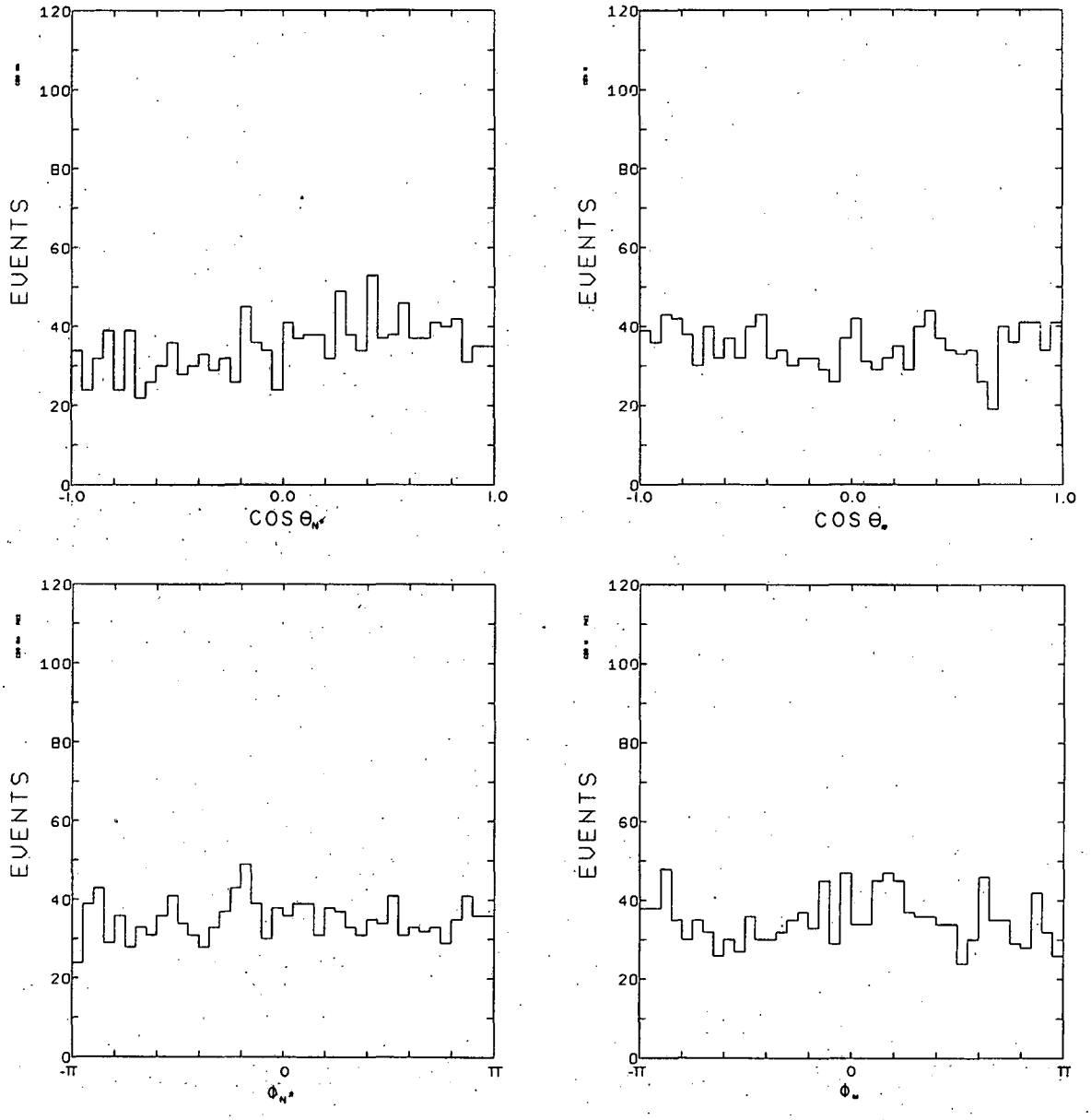

XBL 685-770

Fig. 77. N^* (left) and ω (right) decay angular distributions in the helicity frame.

$\cos\theta_\omega$ distribution bears no trace of anything similar to the asymmetry which dominates the corresponding ρ distribution.

D. $\pi^+ p \rightarrow N^{*++}\eta^\circ$

$N^{*++}\eta^\circ$ production accounts for only a very small percent (~1.2%) of reaction (2). Because of the small width of the η and the position of the $N^*\eta$ region near the kinematic boundary, however, a very clean sample of $N^*\eta$ events may be obtained. The mass selection criteria require $.53 < M(\pi^+\pi^-\pi^\circ) < .57$ GeV, $1.12 < M(\pi^+ p) < 1.32$ GeV, with no combination allowed in the $N^*\omega$ region, and ambiguities resolved on the basis of the smaller momentum transfer. For these criteria the background is at about the 20% level (Table XXI).

Since only 124 events pass the above $N^*\eta$ criteria, the different momenta are not considered separately. The sole exception to this rule is the $N^*\eta$ cross-section data, previously plotted in Fig. (69). Otherwise, the -t, t′ and $\cos\theta_{N^*\eta}$ distributions and the N^* decay parameters will be given only for the experiment as a whole.

The t and t′ distributions are shown in Fig. (78). Because the boundary region extends only to $-t = .067$ $(\text{GeV}/c)^2$, they are practically identical. They are very different from those previously encountered. Of the four double-resonance reactions studied, this is the only one with a turn-over in the t′ distribution. Neither remotely resembles an exponential distribution, so no logarithmic slope parameter "A" was obtained.

The $\cos\theta_{N^*\eta}$ distribution (Fig. (79)) further demonstrates the anomolous behavior of the forward peak. Not only do fewer than 26% of the events lie beyond $\cos\theta = .9$, there are actually over 40% more events in the neighboring $\cos\theta$ bin ($.8 < \cos\theta_{N^*} < .9$). Most of the events are,

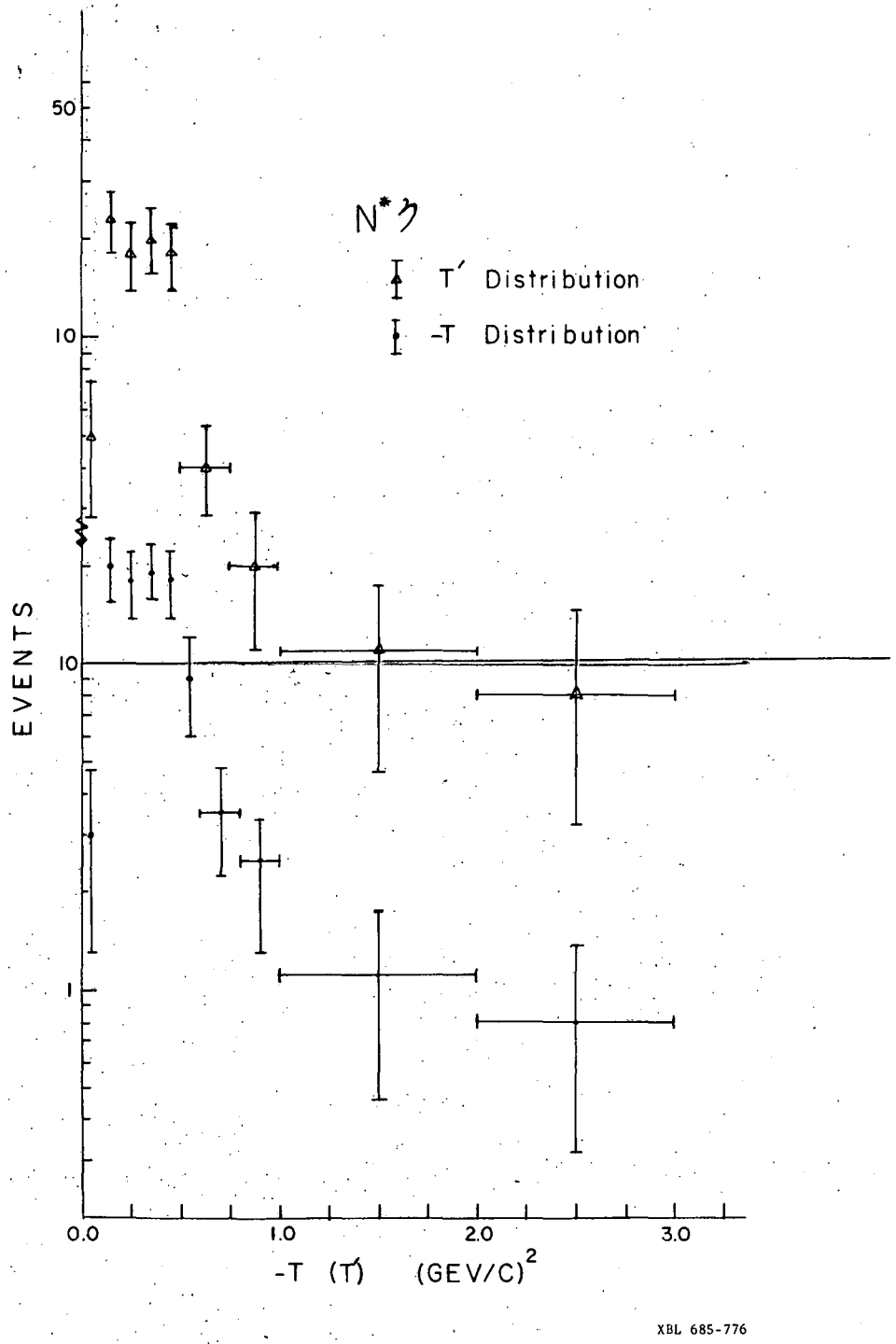

Fig. 78. $N^*\eta$ -t and t′ distributions.

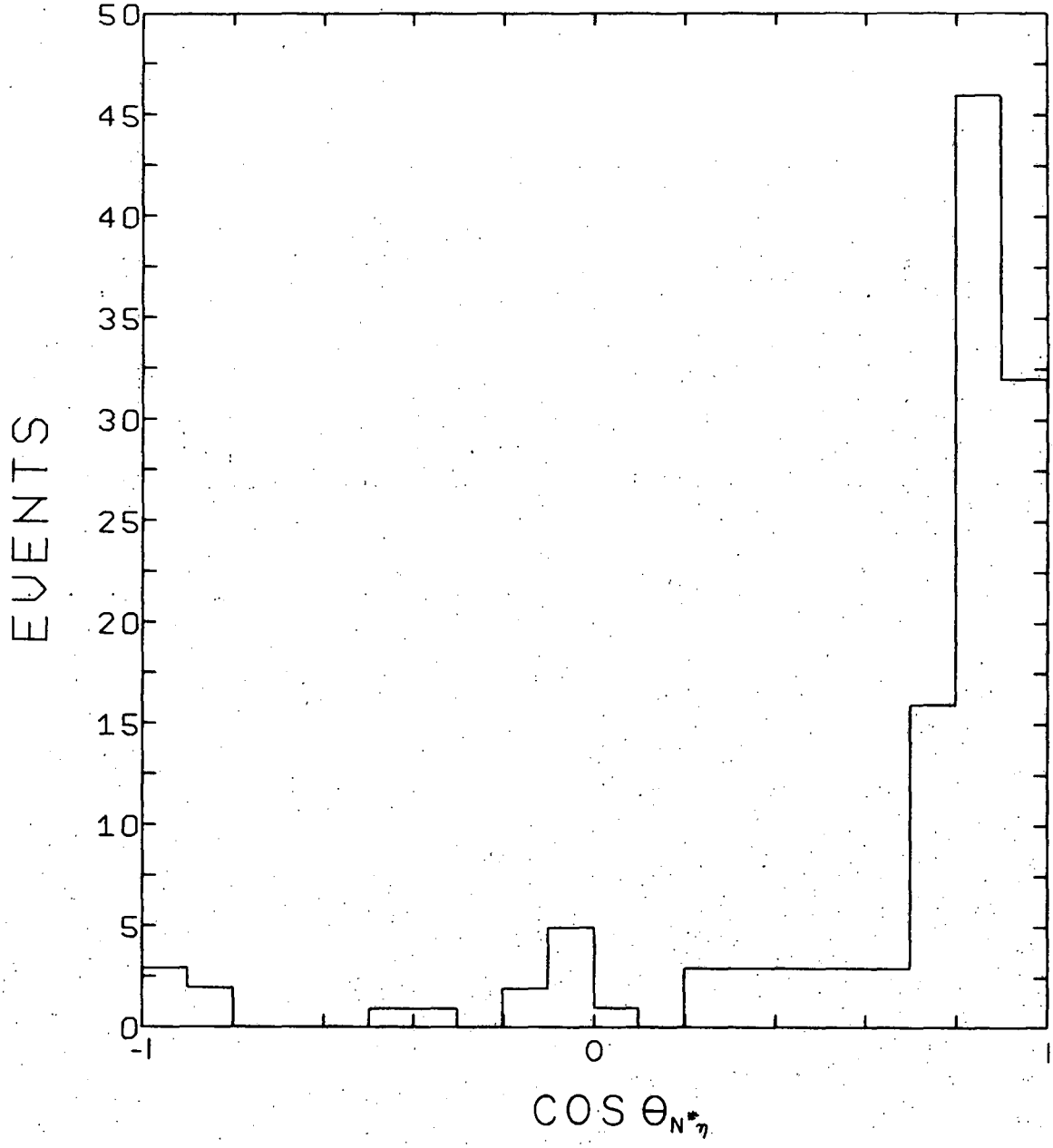

XBL 685-773

Fig. 79. $N^*\eta$ production cosine distribution.

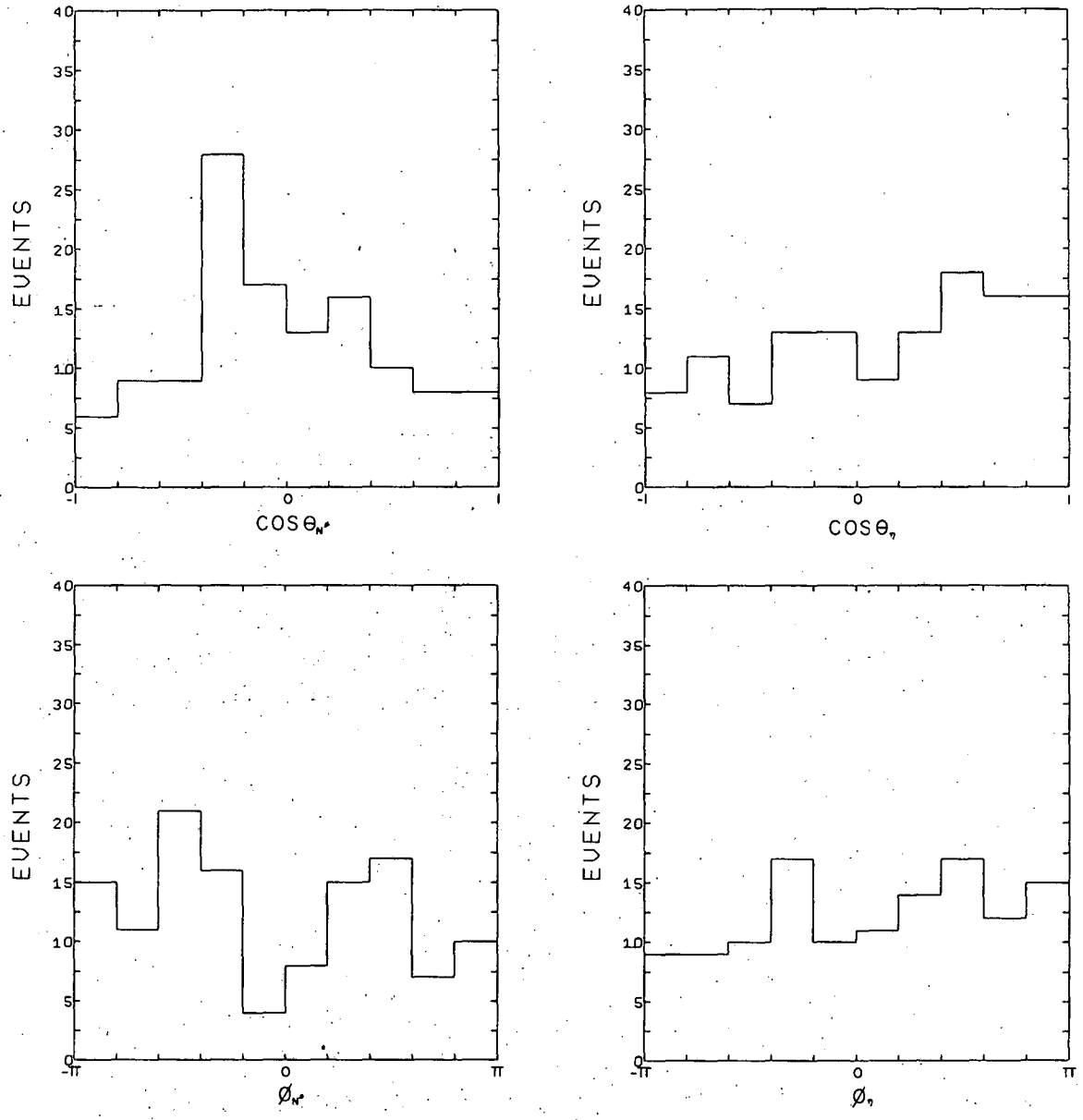

XBL 685-796

Fig. 80. N^* (left) and η (right) decay angular distributions in the helicity frame.

however, concentrated in the forward direction; although, there is some indication of a backward peak as well.

The decay angular distributions (helicity frame) are shown in Fig. (80), and the N^* decay parameters are listed below. The decay distributions are roughly compatible with isotropy with one exception. The exception is the $\cos\theta_{N^*}$ distribution, which displays a striking peak around $\theta = \pi/2$. The N^* decay parameters are as follows:

$$\rho^d_{3,3} = .435 \pm .044,\ .455 \pm .052 \quad (.441 \pm .068,\ .507 \pm .088)$$

$$\rho^d_{3,-1} = .202 \pm .054,\ .221 \pm .067 \quad (.282 \pm .088,\ .340 \pm .113)$$

$$\rho^d_{3,1} = -.008 \pm .042, -.008 \pm .052 \quad (-.001 \pm .066,\ .059 \pm .093)$$

where the background-corrected parameters are given in parenthesis, and the second member of each pair is for the region $-t < .5$ $(\text{GeV}/c)^2$. The value of $\rho^d_{3,3}$ is a measure of the deviation of the $\cos\theta_{N^*}$ distribution from isotropy, being roughly that for a $\sin^2\theta$ distribution (.5) and nearly twice that of an isotropic distribution (.25).

ACKNOWLEDGEMENTS

Many people have contributed to the development of my research. In particular I wish to thank the members of the Powell-Birge group for their help and friendship. I especially thank Professor Wilson M. Powell for ensnaring me into the group, and Dr. Robert W. Birge and Dr. George Gidal for making my stay here worthwhile.

Dr. Gidal has been primarily responsible for guiding my research program. I greatly appreciate his advice and counsel.

I would also like to thank Professor J. D. Jackson for several enlightening discussions of meson-exchange models.

I am indebted to the personnel of the scanning and measurement section under the direction of Mr. P. Wesley Weber. Without their work this project could not have been carried out. Special thanks are due Mrs. Lois Tinay and Mrs. Mattie L. Woodford for their careful scanning.

The data handling group, headed by Mr. Howard S. White was similarly indespensible. Mr. Loren Schulz was particularly helpful in obtaining information from the FAIR system.

I am extremely grateful to Mrs. Sandra Paciotti for her dilligent work in preparing this manuscript and for her encouragement in the hectic days preceding its completion. I would also like to thank Miss Kimberly Erle and Mr. Steven Pierce for assisting in the preparation of the figures.

This work was done under the auspices of the U. S. Atomic Energy Commission and the National Science Foundation.

Appendix A. NORMALIZATION INPUT PARAMETERS

In carrying out the normalization calculations of Section II, it was necessary to use cross-sections and differential cross-sections obtained in other experiments. Among these are the pp cross-sections used in finding the proton contamination (Fig. (A-1)) and the slopes of the elastic differential cross-sections used in correcting the π^+p and pp total cross-sections for scanning losses for events in the forward peak (Fig. (A-2)). As shown in those figures, a smooth curve was drawn through the data points, the intercepts of this curve with the five experimental momenta giving the values used in the analysis. With regard to Fig. (A-2), the values of A_{π^+p} of Coffin et al.[14] are not directly from the reference but from an exponential fit to the points given in the reference.

Values of the π^+p total cross-section were also used in the beam normalization. They were interpolated from those of Diddens et al.[23] and are 29.49 ± .23, 28.84 ± .22, 28.32 ± .22, 27.77 ± .22, and 27.40 ± .26 millibarns at the five momenta respectively.

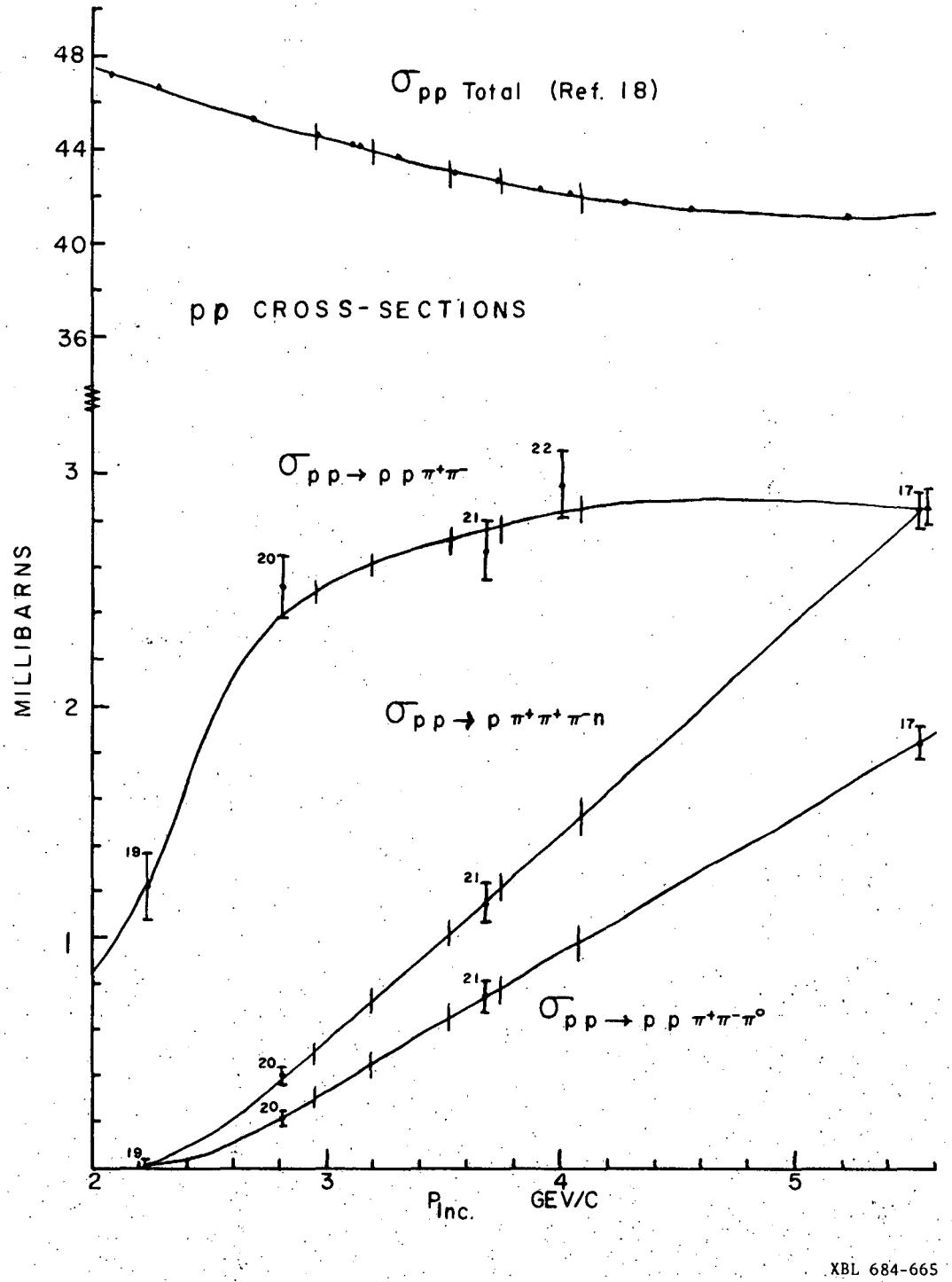

Fig. A-1. Cross-sections for pp reactions used in the beam normalization calculations.

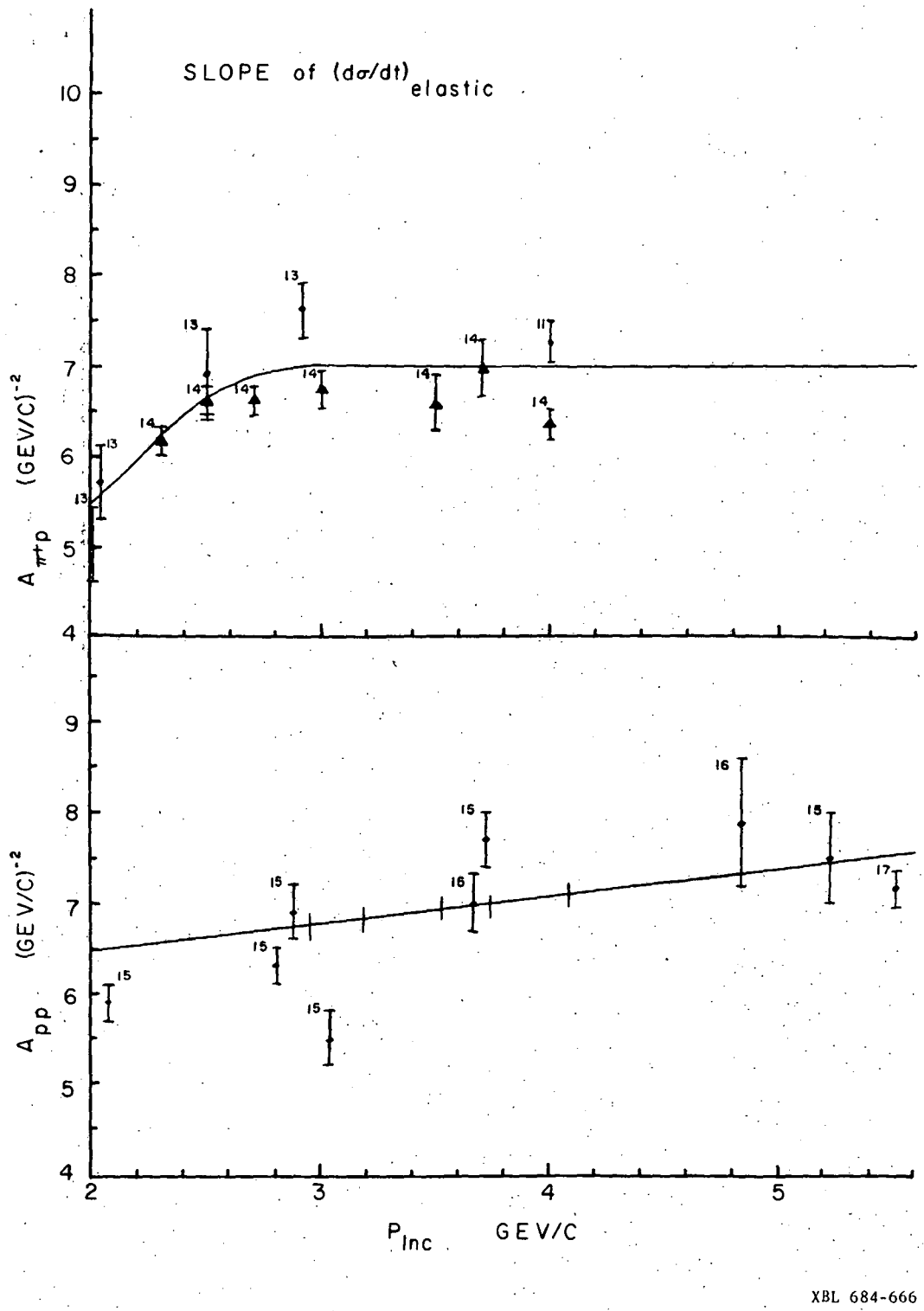

Fig. A-2. Logarithmic slopes of the $d\sigma/dt$ forward peak in π^+p and pp elastic scattering.

Appendix B. BREIT-WIGNER PARAMETERIZATION

In Sections III and IV Breit-Wigner factors were used in weighting Monte-Carlo events according to various resonance hypotheses. The Breit-Wigner form for a two-body decay, as given by Jackson,[25] was used:

$$f_{B.W.} = \frac{E}{q} \frac{\Gamma(E)}{(E_o^2 - E^2)^2 + E_o^2 \Gamma^2(E)}$$

$$\Gamma(E) = \Gamma_o (q/q_o)^{2\ell+1} R(E_o)/R(E)$$

where, in the resonance c.m., E is the energy of the two-particle system and q the momentum of the decay particles, E_o and q_o being these quantities at resonance. The form of R(E) and the values of E_o, Γ_o and ℓ are given in Table (B-1) for each of the resonances used in the analysis. All of the resonances except for the η and ω were assumed to decay into two particles. For the η and ω, a simpler form was used, putting $\Gamma(E) = \Gamma_o$, and setting the factor E/q equal to unity.

The weight for any event was the product of the suitable resonance terms divided by the maximum value this product could assume. The maximum value was not obtained analytically, however, but was the maximum value for any event in the sample. To avoid computational difficulties, a lower limit of .1 GeV/c was placed upon q.

Table B-1. Breit-Wigner parameters and form of R(E), where R(E) is of the type: I. $R = (q_o^2+q^2)$, II. $R = E(A^2+q^2)^{\ell}$ (A=.35 GeV/c), III. R = 1.0, IV. $R = q^{2\ell+1}$. In fitting the π^-n distribution of reaction (3), R_{II} was used in the N^{*-} B.W.; however, A = .35 GeV/c was found unsatisfactory and A = .175 GeV/c substituted. For the A1, A2, and $N^*(1700)$, which were assumed to decay into one stable particle and one resonance, the resonance mass was used in calculating q_o and the actual invariant mass of the two particle system making up the resonance was used in calculating q.

Symbol	Mass MeV	Width MeV	ℓ	R(E) Type	Decay Particle Masses GeV	GeV
ρ	770	130	1	I	.13958	.13958
f	1260	140	2	I	.13958	.13958
A1	1070	100	0	III	.13958	$M(\pi^+\pi^-)$:.77
A2	1305	90	2	III	.13958	$M(\pi^+\pi^-)$:.77
N^*	1236	120	1	II	.13958	.93826
N^*	1700	300	0	III	.13958	$M(\pi^+p)$:1.236
η	549	21		IV		
ω	783	26		IV		

Appendix C. MONTE-CARLO EVENT GENERATION

Monte-Carlo events were used extensively in the analysis of the experiment. These events were generated by a program having several advantages over conventional Monte-Carlo routines. The program, Bowl, generated four and five-body final states uniformly (unweighted) according to phase space times e^{At}. Without this feature, the effective number of events used with any peripheral process is greatly reduced from the number of events generated. Also, the program was so designed that events could be generated easily from any particular mass region--e.g. the $N^*\rho$ mass region. These options were implemented, however, at the cost of making the program somewhat bulky and rather slow.

As an example, the treatment of a four-body reaction thought to proceed via a highly peripheral quasi-two-body mechanism ($N^*\rho$ production) is outlined below. For the process,

$$1' + 2' \rightarrow \underset{\hookrightarrow a+b}{1} \quad \underset{\hookrightarrow c+d}{2}$$

the four body phase space integral may be written as,

$$1/64 \int (q_1 q_a q_c)/(M M_1 M_2)\, dM_1^2 dM_2^2 d\Omega_1 d\Omega_a d\Omega_c$$

where q_1, q_a, and q_c are the momenta of particles 1, a, and c in the overall c.m. and in the rest frames of particles 1 and 2 respectively, M is the total c.m. energy, and M_1 and M_2 are the masses of particles 1 and 2. Fixing the production plane removes the $d\varphi_1$ integral from $d\Omega_1$, and the remaining $d\cos\theta_1$ integral may be put in terms of the momentum transfer:

$$1/(32Mq_1') \int q_a q_c dM_1 dM_2 dt\, d\cos\theta_a d\cos\theta_c d\Omega_a d\Omega_c$$

$$1/(32Mq_1') \int dM_1 dM_2 dt d(q_a \cos\theta_a) d(q_c \cos\theta_c) d\varphi_a d\varphi_c \qquad (4)$$

Further, if the probability density is not unity (phase space), but contains a factor e^{At} one has:

$$\int_{t_{Min}(M_1,M_2)}^{t_{Max}(M_1,M_2)} e^{At} dt = \int_{u_{Min}(M_1,M_2)}^{u_{Max}(M_1,M_2)} du \quad (u = e^{At}/A) \qquad (5)$$

Thus, all kinematic factors have been cleared from the integrand. This is all that is required for the generation of unweighted events. Once variables have been found for which the integrand is unity, as in (4) and (5), a multi-dimensional cube may be constructed circumscribing the region of integration--i.e. the extreme upper and lower limits are found for each variable. Events are generated uniformly within this cube, and hence within the physical region as well, with those events lying outside the physical boundary subsequently being rejected.

A considerable amount of time is wasted, since the physical region occupies only a small portion of the volume of the cube. For example, a sample of 100 000 events of reaction (1) was generated by this method in 2051 seconds of C.D.C. 6600 C.P. time. Generated according to e^{8t} times phase space, the physical region occupied somewhat over 3% of the volume of the limiting cube at the lowest momentum (2.95 GeV/c) and less than 1% at the highest momentum (4.08 GeV/c).

Appendix D. ONE-MESON-EXCHANGE MODELS

In Section IV comparisons were made between experimental results and predictions of the one-meson-exchange-with-absorption model (OMEA)[26] and with a form factor approach of G. Wolf (OMEW).[29] In this appendix the method of computation with these models is described and a few additional comments made about them.

1. The OMEA

The OMEA calculations are based upon the treatment of John T. Donohue.[26] The relevant equations for computation with the OMEA are given in great detail in his thesis and will not be repeated here. A few general comments will be made, however, and corrections to typographical errors in the thesis noted.

In the OMEA it is assumed that for a single-particle exchange process, the partial-wave amplitude may be written,

$$M^j_{fi} = (S^j_{ff})^{1/2} B^j_{fi} (S^j_{ii})^{1/2}$$

--i.e. as the product of the Born amplitude with the square root of the elastic-scattering S-matrix elements in the initial and final states. Further, the elastic scattering S-matrix is assumed diagonal and independent of helicity indices. It is conventionally parameterized as,

$$S^j = 1 - Ce^{(-\gamma(j-1/2)^2)}$$

where C and γ are given by,

$$C = \sigma/(4\pi A), \qquad \gamma = 1/(2q^2 A)$$

σ being the total cross-section, A the slope of the forward diffraction peak, and q the c.m. momentum. Thus, C_i and γ_i are fixed by $\pi^+ p$ elastic scattering and total cross-section measurements; whereas C_f and γ_f are

not independently determined by experiment, since they involve the elastic scattering of resonances. From the values for σ and A of Appendix A, C_i is determined to be .86 ± .06, .84 ± .06, .83 ± .06, .81 ± .06, and .80 ± .06 at the five momenta respectively, and γ_i is .060 ± .004, .055 ± .004, .049 ± .003, .046 ± .003, and .042 ± .003. Values of C_f and γ_f will be considered later.

The B^j_{fi} are terms in the partial wave expansion of Born helicity amplitudes. The Born helicity amplitudes are given in Appendix C and the expansion discussion in Appendix D of Donohue's thesis. The following corrections were made to typographical errors in those appendices (with the help of Dr. J. D. Jackson):

1. Page 168: $\xi_\pm = \ldots E_b + m_b$ (not $E_d + m_b$)
2. Page 169: $B_{\lambda_c\lambda_d;\lambda_b} = \ldots (\sin(\theta/2))^{\lambda_c-\lambda_d+\lambda_b} (\cos(\theta/2))^{\lambda_c-\lambda_d-\lambda_b}$ (sign of λ_b switched)
3. Page 174: $b_{1/2;\pm 1/2} = \ldots)$ (add final parenthesis)
4. Page 174: $A = \ldots G_{B^*BP}$ (not $G^1_{B^*BV}$)
5. Page 175: $b_{0-1/2;\pm 1/2} = \ldots \xi_\mp$ (not $\xi_\pm$)
6. Page 175: $b_{1-1/2;\pm 1/2} = \ldots r_3($ (add parenthesis)
7. Page 176: $b_{1/2;\pm 1/2} = \ldots -2r_3(1\pm\cos\theta)(1\mp\cos\theta)\xi_\pm \mp (2E_d/m_d) \times (\cos\theta - v_d/v_b)\xi_\mp))$
8. Page 184: D.4 and D.6, $|\lambda-\mu|/2, |\lambda+\mu|/2$ (factor of ½ needed)

In addition, Donohue's statements, in his Appendix A, concerning the calculation of the d and e functions were studied and found to be correct. The only satisfactory method found for calculating the d functions was the forward recursion relation, and for the e functions,

it was necessary to run the recursion relation backward (All computing was done on the CDC 6600).

Having discussed the calculation of the helicity amplitudes, the expression for $d\sigma/dt$ and for the joint helicity density matrix will be given. The processes under consideration are of the type,

$$a + b \rightarrow c + d$$

where a and c are mesons and b and d baryons, and for which the spins and parities are 0^-, $\frac{1}{2}^+$, 1^-, and $3/2^+$ respectively. Thus, there is no helicity index for (a). Defining,

$$N = \sum_{\lambda_b \lambda_c \lambda_d} |M_{\lambda_c \lambda_d; \lambda_b}|^2$$

then, with q the initial c.m. momentum and s the square of the c.m. energy,

$$d\sigma/dt = N/(128\pi q^2 s)$$

$$R_{\lambda_c \lambda'_c; \lambda_d \lambda'_d} = 1/N \sum_{\lambda_b} M_{\lambda_c \lambda_d; \lambda_b} M^*_{\lambda'_c \lambda'_d; \lambda_b}$$

$$\rho_{\lambda_c \lambda'_c} = \sum_{\lambda_d} R_{\lambda_c \lambda'_c; \lambda_d \lambda_d}$$

where the R and ρ are joint helicity density matrix elements and helicity density matrix elements for the individual final-state particles respectively. As noted in the text, if the R and ρ are desired in some frame other than the helicity frame, a further rotation is necessary.

In Section IV-A the joint angular decay distribution was given in terms of the ρ_{fi} and certain parameters R_k. The relation of the R_k to the joint helicity density matrix elements is given in Table D-1. Also, the parameters were obtained experimentally by averaging certain functions of the decay angles over the distribution, and these functions are displayed explicitly in that table.

Table D-1. Relations between the angular distribution parameters and the helicity matrix elements, and their expression in terms of the decay angles. Only the real part of the helicity matrix elements contributes; so, for convenience, $R_{\lambda_c\lambda'_c;\lambda_d\lambda'_d}$ has been written for $\mathrm{Re}\left[R_{\lambda_c\lambda'_c;\lambda_d\lambda'_d}\right]$. (As used below, $k = 25\sqrt{3}/16$)

Parameter	Helicity matrix elements	Angular functions
$\rho^c_{0,0}$		$\frac{1}{2}\langle 5\cos^2\theta_c - 1\rangle$
$\rho^c_{1,-1}$	$\rho^c_{mm'} = \sum_n R_{mm';nn}$	$-(5/4)\langle \sin^2\theta_c \cos 2\varphi_c\rangle$
$\rho^c_{1,1}$		$-(5/4\sqrt{2})\langle \sin 2\theta_c \cos\varphi_c\rangle$
$\rho^d_{3,3}$		$(1/8)\langle 7 - 15\cos^2\theta_d\rangle$
$\rho^d_{3,-1}$	$\rho^d_{nn'} = \sum_m R_{mm;nn'}$	$-(5\sqrt{3}/8)\langle \sin^2\theta_d \cos 2\varphi_d\rangle$
$\rho^d_{3,1}$		$-(5\sqrt{3}/8)\langle \sin 2\theta_d \cos\varphi_d\rangle$
R_8	$\frac{1}{2}(R_{11;33}+R_{11;-3,-3}-R_{11;-1,-1}-2R_{00,33}+2R_{00;11}-R_{11;11})$	$(25/16)\langle (1-3\cos^2\theta_c)(1-3\cos^2\theta_d)\rangle$
R_9	$R_{1,-1;33}-R_{1,-1;11}$	$-(25/16)\langle (1-3\cos^2\theta_d)\sin^2\theta_c \cos 2\varphi_c\rangle$
R_{10}	$R_{10;33}+R_{10;-3,-3}-R_{10;11}-R_{10;-1,-1}$	$-(25/8\sqrt{2})\langle (1-3\cos^2\theta_d)\sin 2\theta_c \cos\varphi_c\rangle$
R_{11}	$R_{11;3,-1}+R_{11;1,-3}-2R_{00;3,-1}$	$-k\langle (1-3\cos^2\theta_c)\sin^2\theta_d \cos 2\varphi_d\rangle$
R_{12}	$R_{11;31}+R_{11;-1,-3}-2R_{00;31}$	$-k\langle (1-3\cos^2\theta_c)\sin 2\theta_d \cos\varphi_d\rangle$
R_{13}	$R_{1,-1;3,-1}$	$k\langle \sin^2\theta_c \sin^2\theta_d \cos(2\varphi_c+2\varphi_d)$
R_{14}	$R_{1,-1;-13}$	$k\langle \sin^2\theta_c \sin^2\theta_d \cos(2\varphi_c-2\varphi_d)$
R_{15}	$R_{1,-1;31}$	$k\langle \sin^2\theta_c \sin 2\theta_d \cos(2\varphi_c+\varphi_d)\rangle$
R_{16}	$R_{1,-1;13}$	$k\langle \sin^2\theta_c \sin 2\theta_d \cos(2\varphi_c-\varphi_d)\rangle$
R_{17}	$R_{10;3,-1}+R_{10;1,-3}$	$k\sqrt{2}\langle \sin 2\theta_c \sin^2\theta_d \cos(\varphi_c+2\varphi_d)\rangle$
R_{18}	$R_{10;-3,1}+R_{10;-13}$	$k\sqrt{2}\langle \sin 2\theta_c \sin^2\theta_d \cos(\varphi_c-2\varphi_d)\rangle$
R_{19}	$R_{10;31}-R_{10;-1,-3}$	$k\sqrt{2}\langle \sin 2\theta_c \sin 2\theta_d \cos(\varphi_c+\varphi_d)\rangle$
R_{20}	$R_{10;13}-R_{10;-3,-1}$	$k\sqrt{2}\langle \sin 2\theta_c \sin 2\theta_d \cos(\varphi_c-\varphi_c)\rangle$

A computer program was written to calculate $d\sigma/dt$ and the angular-distribution parameters, according to the OMEA procedure outlined above. Results for $N^*\rho$ and $N^*\omega$ production were checked with output furnished by Dr. Jackson and seen to agree with those of Donohue. Thus, there is good reason to believe that the OMEA curves which have been calculated are correct.

One feature which was added to Donohue's treatment, was integration over the double-resonance mass region. In most previous work the calculations were performed using the central values of the resonance masses in a "zero-width" approximation. These may be easily modified, however, to account for the finite resonance widths by adding a factor,

$$\left(\frac{\pi^{-1} M_o \Gamma(M)}{(M_o^2 - M^2)^2 + M_o^2 \Gamma^2(M)} \right) dM^2$$

where M is the invariant mass of the resonance system.[25] The resonance parameters used are those of Table B-1.

The remaining OMEA parameters whose values must be fixed are the coupling constants, C_f, and γ_f. The values of the coupling constants used are those of Donohue. For $N^*\rho$ production these are $G^2_{\rho\pi\pi}/4\pi = 2.0$ and $G^2_{\pi^+pN^*}/4\pi = .43$. Since this is a pion-exchange reaction, they appear only as overall multiplicative constants and only serve to scale $d\sigma/dt$. That is not true for $N^*\omega$ production. For vector meson exchange there are three coupling constants at the $p\rho N^{*++}$ vertex, and their ratios effect the density matrices as well as $d\sigma/dt$. The Donohue values (relativistic Stodolsky-Sakurai coupling) are $G^2_{\omega\rho\pi}/4\pi = 10$, $(G^1_{N^{*++}p\rho})^2/4\pi = 40$, $G^2_{N^{*++}p\rho} = G^1_{N^{*++}p\rho}$, $G^3_{N^{*++}p\rho} = 0$. C_f was chosen for maximum absorption, $C_f = 1.0$, and γ_f was set, somewhat arbitrarily, to $\frac{1}{4}\gamma_i$.

Figs. (D-1 and D-2) illustrate several of the basic features of the OMEA as applied to $N^*\rho$ production. Fig. (D-1) shows the differential cross-section. In (A), the simple Born-term curves are shown, (a) with and (b) without the zero-width assumption, along with the OMEA curves, likewise (c) with and (d) without that assumption. The effect of the integration over the $N^*\rho$ mass region is apparently to lower the curve by about a factor of three. It is also clear that even with absorption, the model does not account for the sharp forward peaking. In (B), the Born (a) and OMEA (b) curves are shown over the entire range of momentum transfer, with the data (as well as the curves) being for the central momentum. In (C), the dependence upon the incident momentum is studied, with curves at (a) 2.95 GeV/c and (c) 4.08 GeV/c being shown with the weighted sum of all the momenta (b). In (D), the effects of changing C_f and γ_f are shown, with (c) the normal curve at 3.53 GeV/c, (a) $\gamma_f = \frac{1}{2}\gamma_i$, and (b) $C_f = .9$. Thus, changing C_f radically effects the slope of $d\sigma/dt$, whereas changing γ_f primarily effects the height of the curve. In (E) the dependence upon the mass coordinates is demonstrated. Using the zero-width approximation, and arbitarily normalizing the data, curves at the center ((b): $M(\pi^+\pi^-) = .77$ GeV, $M(\pi^+p) = 1.22$ GeV) and at the extremities of the $N^*\rho$ mass region are shown ((c): $M(\pi^+\pi^-) = .86$ GeV, $M(\pi^+p) = 1.32$ GeV; (a): $M(\pi^+\pi^-) = .68$ GeV, $M(\pi^+p) = 1.12$ GeV). (F) illustrates one aspect of the OMEW model and is mentioned in Part 2.

Fig. (D-2) shows the ρ_{fi} for $N^*\rho$ production. The curves either have no symbol, or a small square, or a small diamond affixed to them at regular intervals. They will be referred to as curves (a), (b), and (c) respectively in what follows. Curves are always drawn for the central momentum (3.53 GeV/c), and the data is for all momenta combined.

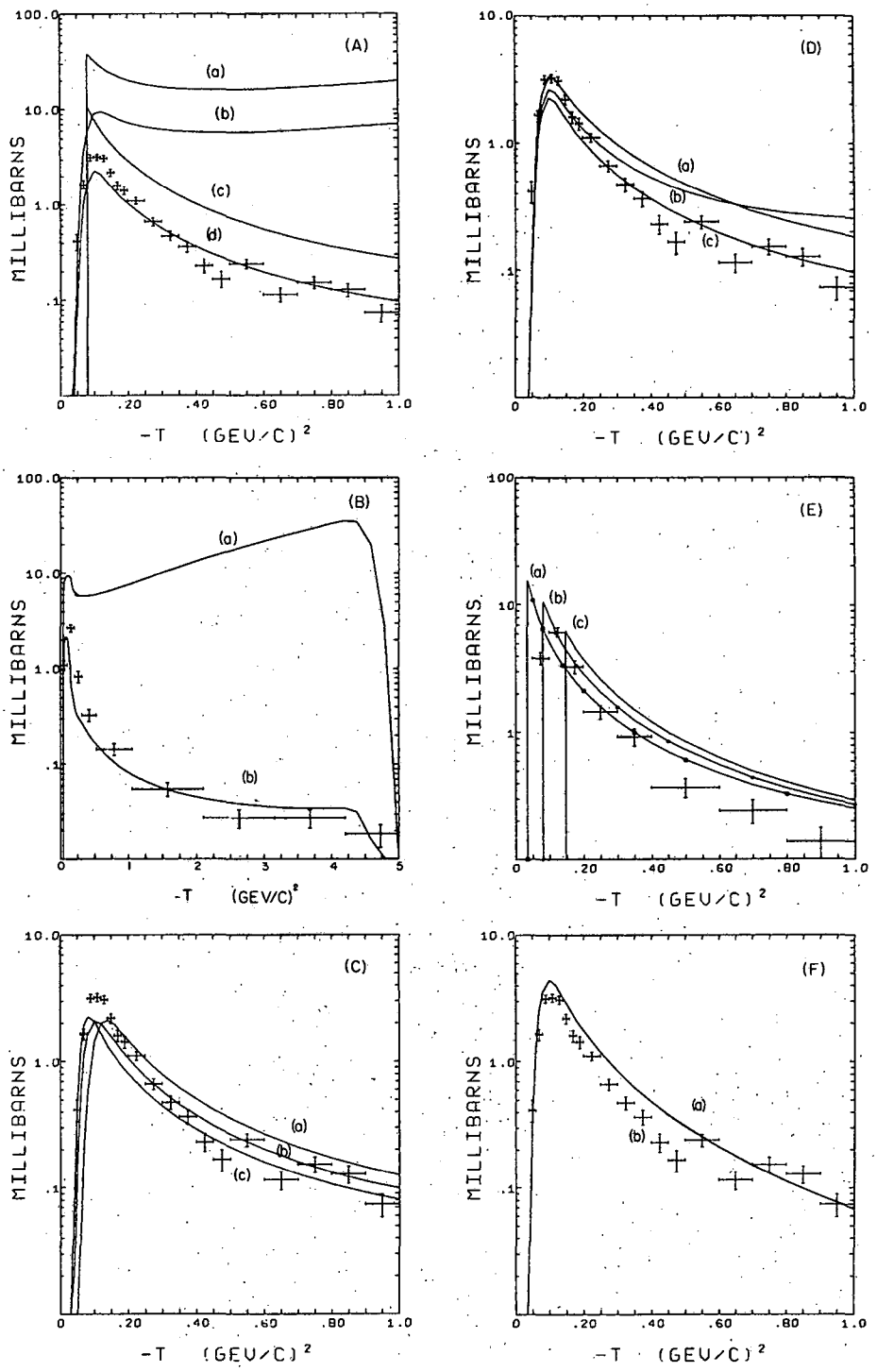

XBL 685-795

Fig. D-1. $d\sigma/dt$ for $N^*\rho$ production, with the various curves as described in the text.

In (A), (a) is the OMEA curve, (b) the OMEA unique-mass curve, and (c) the Born (integrated) curve. In the helicity frame the Born predictions are, of course, not the simple ones of the Jackson frame--e.g. $\rho^{c}_{0,0} = 1.0$, with the other ρ_{fi} being zero. The OMEA curves are seen to be in better agreement with the data in all cases, however. The unique-mass OMEA curve is seen to differ from the integrated OMEA one only slightly and there (in the t boundary region) to its own disadvantage. In (B), the background-corrected data points (bare error bars) are plotted along with the usual uncorrected points to display the slight differences between them. In (C), the momentum dependence is exhibited with curves at (a) 2.95 GeV/c, (b) 3.53 GeV/c, and (c) 4.08 GeV/c shown to differ only slightly from one another. In (D), the effects of changing C_f and γ_f are shown. The normal curve (a) and one with $\gamma_f = \frac{1}{2}\gamma_i$ (c) being nearly identical, whereas the curve with $C_f = .9$ (b) is much closer to the Born curve of (A). In (E), curves are drawn for the unique-mass OMEA for (a) $M(\pi^+\pi^-) = .86$, $M(\pi^+p) = 1.32$ GeV, (b) $M(\pi^+\pi^-) = .77$, $M(\pi^+p) = 1.22$ GeV, and (c) $M(\pi^+\pi^-) = .68$, $M(\pi^+p) = 1.12$ GeV. Quite substantial differences are seen for the different $N^*\rho$ mass values. In (F), the Jackson-frame predictions and data values are shown.

2. The OMEW

Calculation with the OMEW model is much simpler than for the OMEA. Of course, less information is obtained, since only $d\sigma/dt$ for $N^*\rho$ production is computed. The finite resonance widths are taken into account, however, and a correction is made for the T = 0,2 S-wave contribution to $\sigma_{\pi^+\pi^-}(m_\rho)$. The relevant equations are given in reference 29, and only a few comments concerning them will be made here.

The OMEW model for $N^*\rho$ production is a one-pion-exchange (Born term)

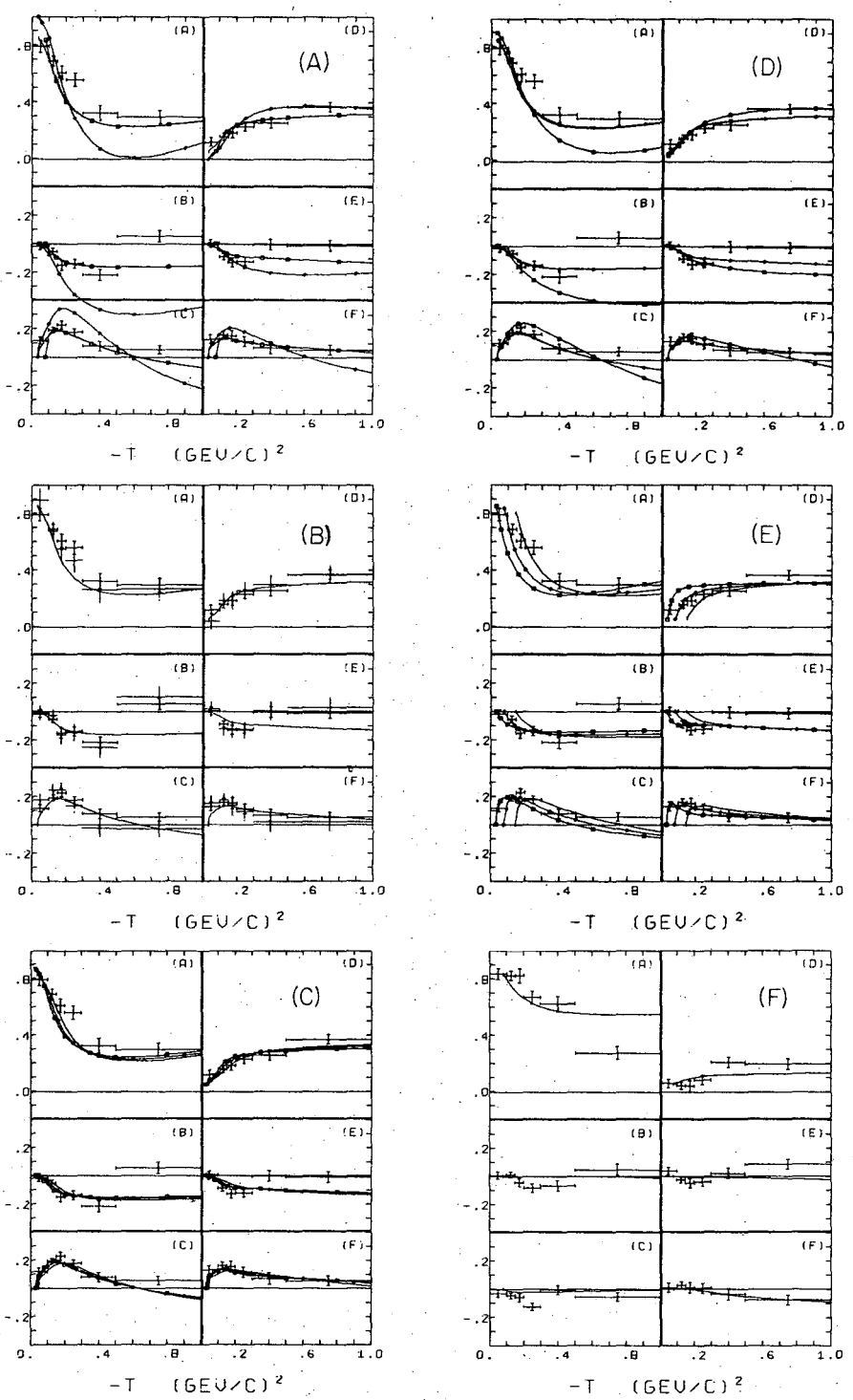

XBL 685-798

Fig. D-2. $N^*\omega$ decay matrix elements, with the various curves as described in the text. (In each sub-figure there are (A) $\rho^c_{0,0}$, (B) $\rho^c_{1,-1}$, (C) $\rho^c_{1,1}$, (D) $\rho^d_{3,3}$, (E) $\rho^d_{3,-1}$, and (F) $\rho^d_{3,1}$.)

model, modified by a form factor G(t):

$$G(t) = \frac{c-m^2}{c-t} \qquad (c = 2.29 \pm .27 \text{ GeV}^2)$$

Elastic scattering cross-sections, modified by off-mass-shell corrections, are used to describe the mass dependence of the differential cross-section.

The OMEW prediction for $d\sigma/dt$ is plotted in Fig. (D-1:F). As is noted in the text, when the background correction is made to the data, the OMEW curve lies well above the data points. This probably reflects the way in which the parameter c in G(t) was obtained, and is not necessarily a defect inherent in the model.

To examine the effect of the correction for T = 0,2 S-wave contributions, the OMEW program was run without that correction. The resultant curve was plotted on the previously mentioned figure, and is indistinguishable from the normal OMEW curve.

Appendix E. METHOD OF MOMENTS AS APPLIED TO $d\sigma/dt$

The usual procedure in parameterizing the momentum transfer distribution is to make a chi-square fit to the distribution, varying the parameters involved. One defect in this procedure is the dependence of the results upon the particular binning scheme used, especially when there are few events. In an attempt to circumvent this difficulty, a procedure employing the method of moments was investigated.

For any normalized distribution $f(t,A)$ the following are true by definition:

$$1 = \int f(t,A)dt \tag{1}$$

$$\langle t^k \rangle = \int t^k f(t,A)dt \tag{2}$$

where the integral is over the full range of t in question. In principle, for any hypothetical $f(t,A)$ one can solve the above set of integral equations for the parameters of the distribution (A) in terms of the experimentally observed $\langle t^k \rangle$. In practice, of course, that is not an easy task.

For the momentum transfer distribution, the following density function was used:

$$f(t,A) = ke^{At}$$

As mentioned in the text, the interval $.2 < -t < .5$ $(GeV/c)^2$ was used, so the mass dependence of the lower limit of integration was eliminated. Equations (1) and (2) become:

$$1 = -\int_1^2 ke^{At}dt = -k/A\Big|_1^2 e^{At}$$

$$= k/A(e^{At_1} - e^{At_2}) \qquad 0 < -t_1 < -t_2$$

$$\langle t \rangle = \int_1^2 kte^{At}dt = -k/A\Big|_1^2 e^{At}(-t+1/A)$$

$$= k/A^2(e^{At_1} - e^{At_2}) - k/A(t_1e^{At_1} - t_2e^{At_2})$$

$$= 1/A - (t_1 - t_2e^{-A\Delta t})/(1-e^{-A\Delta t}) \quad \Delta t = |t_2 - t_1|$$

This equation was easily solved numberically for A (using the Varmit minimization program) and, as noted, in the text, gave results compatible with those of a chi-square fit to the data. When the method was used in an attempt to gain further information; however, the result was completely unsatisfactory.

Since $d\sigma/dt$ for $N^*\rho$ production has a decreasing logarithmic slope, a second parameter was added to the density function:

$$f(t,A,B) = ke^{At + Bt^2}$$

Using the first two moments of t with this function, the minimization routine failed to find a suitable solution. Unfortunately, it is not clear to what the failure is due. The function is not directly integrable, and various expedients were employed in carrying out the integration numberically, so that the fault may lie with these or with the limited range of t or with the limited number of moments of t used or limited number of events in the sample studied.

REFERENCES

1. H. Foelsche and H. Kraybill, Multiple Pion Production in Interactions of Positive Pions with Protons Near 1 BeV, Phys. Rev. 134, B1138 (1964).
2. J. K. Kopp, A. Shapiro, and A. Erwin, π^+- Proton Scattering at 990 MeV, Phys. Rev. 123, 301 (1961).
3. P. Daronian, A. Daudin, M. Jabiol, C. Lewin, C. Kochowski, B. Ghidini, S. Mongelli, and V. Picciarelli, π^+p Interactions at 1.6 GeV/c, Nuovo Cimento 41A, 503 (1966).
4. J. A. Johnson and H. L. Kraybill, Inelastic Nonstrange π^+p Interactions at 1.65 BeV, Bull. Am. Phys. Soc. 9, 70 (1964).
5. F. E. James and H. L. Kraybill, Interactions of π^+ Mesons with Protons at 2.08 BeV/c, Phys. Rev. 142, 896 (1966).
6. N. Gelfand, Production of Pionic Resonances in π^+p Interactions around 2.5 BeV/c (Ph.D. thesis), CU-1932-239 Nevis-137, June 1965.
7. N. Armenise, B. Ghidini, V. Picciarelli, A. Romano, G. Kayas, J. Laberrigue-Frolow, J. Tridon, L. Vigneron, and T.P. Yiou, Exchange Mechanism for $\pi^+p \rightarrow N^{*++}\rho^\circ$ Reaction at 2.75 GeV/c, Nuovo Cimento 41A, 159 (1966).
8. S. Yamamoto, J. Smith, D. Rahm, and J. Lloyd, Double Resonance Production by 2.77-BeV/c π^+ Mesons on Hydrogen, Phys. Rev. 140, B730 (1965).
9. M. Abolins, R. Lander, W. Mehlhop, N. Xuong, and P. Yager, Production of Multi meson Resonances by π^+p Interaction and Evidence for a $\pi\omega$ Resonance, Phys. Rev. 11, 381 (1963).
10. B. Shen, Resonance Production in Pion-Proton Interactions at 3.65 BeV/c and 3.7 BeV/c (Ph.D. thesis), UCRL-16170, September 1965.

11. Aachen-Berlin-Birmingham-Bonn-Hamburg-London (I.C.)-Munchen Collaboration, $\pi^+ p$ Interactions at 4 GeV/c, Phys. Rev. 138, B897 (1965).

12. M. Deutschmann, R. Schulte, H. Weber, W. Woischnig, C. Grote, J. Klugow, S. Nowak, S. Brandt, V. Cocconi, O. Czyzewski, P. Dalpiaz, G. Kellner, and D. Morrison, Resonance Production by 8 GeV/c Positive Pions on Protons, Phys. Letters 12, 356 (1964).

13. D. E. Damouth, L. Jones, and M. Perl, Pion-Proton Elastic Scattering at 2.00 GeV/c Phys. Rev. Letters 11, 287 (1963).

14. C. T. Coffin, N. Oidmen, L. Ettlinger, D. Meyer, A. Saulys, K. Terwilliger, and D. Williams, Elastic Differential Cross Sections for $\pi^{\pm}$ + p Scattering from 2.3-6.0 BeV/c, Phys. Rev. 159, 1169 (1967).

15. M. L. Perl, L. W. Jones, and C. C. Ting, Pion-Proton Elastic Scattering from 3 GeV/c to 5 GeV/c, Phys. Rev. 132, 1252 (1963).

16. Y. Akimov, L. Zolin, A. Kalinin, V. Nikitin, V. Pantuev, L. Rob, V. Sviridov, and M. Khachaturyan, Measurement of the pp- and pd-Scattering Differential Cross Section at 4.0 BeV by Means of Semiconductor Detectors, Soviet Journal of Nuclear Physics 4, 63 (1967).

17. G. Alexander, O. Benary, G. Czapek, B. Haber, N, Kidron, B. Reuter, A. Shapira, E. Simopoulou, and G. Yekutieli, Proton-Proton Interactions at 5.5 GeV/c, Phys. Rev. 154, 1284 (1967).

18. D.V. Bugg, D. Salter, G. Stafford, R. George, K. Riley, and R. Tapper, Nucleon-Nucleon Total Cross Sections from 1.1 to 8 GeV/c, Phys. Rev. 146, 980 (1966).

19. A. Eisner, E. Hart, R. Louttit, and T. Morris, Proton-Proton Scattering at 1.48 BeV, Phys. Rev. 138, B670 (1965).

20. E. Pickup, D. Robinson, and E. Salant, p-p Interactions at 2 BeV II. Multiple-Pion Production, Phys. Rev. 125, 2091 (1962).

21. E. L. Hart, R. Louttit, D. Luers, T. Morris, W. Willis, and S. Yamamoto, Multiple Meson Production in Proton-Proton Collisions at 2.85 BeV, Phs. Rev. 126, 747 (1962).

22. J. Kidd, L. Mandelli, V. Pelosi, S. Ratti, A. Sichirollo, L. Tallone, F. Conte, and G. Tomasini, A Possible Y = 2, S = 0 $pp\pi^+$ Resonance at 2520 MeV, Phys. Letters 16, 75 (1965).

23. A. N. Diddens, E. Jenkins, T. Kycia, and K. Riley, Structure in the Pion-Proton Total Cross Section between 2 and 3 BeV, Phys. Rev. Letters 10, 262 (1963).

24. M. Bardadin-Otwinowska, M. Danysz, T. Hofmokl, S. Otwinowski, H. Piotrowska, R. Sosnowski, M. Szeptycka, and A. Wroblewski, Evidence for the Production of $N^*(2830)$ in π^+-p Interactions at 8 GeV/c, Physics Letters 21, 357 (1966).

25. J. D. Jackson, Remarks on the Phenomenological Analysis of Resonances, Nuovo Cimento 34, 1644 (1964).

26. J. T. Donohue, Calculations on Production Reactions Using the Absorptive Peripheral Model (Ph.D. thesis), University of Illinois, 1967.

27. A. H. Rosenfeld, N. Barash-Schmidt, A. Barbaro-Galtieri, L. Price, P. Soding, C. Wohl, M. Roos, and W. Willis, Data on Particles and Resonant States, UCRL-8030 Rev., January 1968.

28. L. D. Jacobs, A Study of Resonance Production and Decay and Elastic Scattering in π^-p Two-prong Interactions 2.05 to 3.22 GeV/c, (Ph.D. thesis), UCRL-16877, August 1966, indicates that "A" may be expected to increase in the region of an S-channel resonance.

29. G. Wolf, Shrinkage Effects and One-pion Exchange, Phys. Rev. Letters 19, 925 (1967).

30. W. Jackson, R. Bacastow, S. Y. Fung, And R. Pu (University of California at Riverside) carried out most of the δ-ray normalization work. A reference for the theory is F. S. Crawford, Jr., Pion-Electron Scattering Cross Section at 1.12 BeV/c, Phys. Rev. 117, 1119, (1960).

31. G. Borreani, and D. Hall, Calibration of F.S.D. Ionization Measurement in Hydrogen, LRL Physics Note PB-119, November 1967.

32. W. Jackson, R. Bacastow, S. Y. Fung, and R. Pu (University of California at Riverside) are currently working on an analysis of the A meson.

33. A. Citron, W. Galbraith, T. Kycia, B. Leontic, R. Phillips, A. Rousset, and P. Sharp, Structure in the Pion-Proton Total Cross Section Between 2 and 7 GeV/c, Phys. Rev. 144, 1101 (1966).

34. G. Gidal, D. Brown, R. W. Birge, R. Bacastow, S. Y. Fung, W. Jackson, and R. T. Pu, Resonance Production in $\pi^+ p$ Interactions Between 3 and 4 GeV/c, UCRL-17984, December 1967 (Athens Topical Conference on Recently Discovered Resonant States, 3rd (1967)-to be published).

35. S. Y. Fung, W. Jackson, R. T. Pu, D. Brown, and G. Gidal, Evidence for the Kinematic Origin of the H Enhancement, UCR-34P 107-64, March 1968.

36. M. LeBellac, Pion Conspiracy in $\pi N \rightarrow \rho\Delta$, Physics Letters 25, B524 (1967).

37. F. Arbab and C. B. Chiu, Association Between the Dip in the $\pi^- p \rightarrow \pi^0 n$ High-Energy Angular Distribution and the Zero of the ρ Trajectory, Phys. Rev. 147, 1045 (1966).

38. D. Brown, G. Gidal, R. W. Birge, R. Bacastow, S. Fung, W. Jackson, and R. Pu, Quasi-Two-Body Final States Produced in $\pi^+ p$ Interactions Between 3 and 4 GeV/c, Phys. Rev. Letters 19, 664 (1967).

39. M. Morley, Exp. 36-41 Scanning Instructions, LRL Physics Note PB-79, March 1966. A general reference for the 72" bubble chamber is: J. D. Gow and A. H. Rosenfeld, Berkeley 72" Hydrogen Bubble Chamber, Proceedings of the International Conference on High-Energy Accelerators and Instrumentation: CERN, 1959.

40. H. White, S. Buckman, D. Hall, E. Hurwitz, L. Meissner, J. Smith, and F. Stannard, The Fog, Cloudy and Fair Programs for Bubble Chamber Data Reduction, UCRL-9457, August 1960. A more comprehensive reference is: A. Rosenfeld and W. Humphrey, Analysis of Bubble Chamber Data, Ann. Rev. Nucl. Sci. 13, 103 (1963).